Multiscale Modeling of Carbon Nanotube-Epoxy Nanocomposites

by

Nicholas A. Fasanella

A dissertation submitted in partial fulfillment
of the requirements for the degree of
Doctor of Philosophy
(Aerospace Engineering)
in the University of Michigan
2016

Doctoral Committee:

Associate Professor Veera Sundararaghavan, Chair
Associate Professor Donald J. Siegel
Associate Professor Henry Sodano
Professor Anthony M. Waas, University of Washington

A man either lives life as it happens to him, meets it head-on and licks it, or he turns his back on it and starts to wither away.

GENE RODDENBERRY, *STAR TREK*

2016

To my parents.

ACKNOWLEDGMENTS

I first and foremost would like to thank my adviser, Professor Veera Sundararaghavan, for all of his support throughout my time at Michigan. His guidance extended beyond academics, and has helped bring me to where I am today personally and professionally. I am very appreciative of Professors Anthony Waas, Donald Siegel, and Henry Sodano for joining my committee and offering helpful feedback regarding my research. I have had a number of academic mentors that have helped me reach this point, and in particular I would like to express my gratitude to Professors Assimina Pelegri and Ioannis Chasiotis for their support and mentoring throughout my studies.

I would like to thank my MSSL lab mates for the assistance I have received over the years: Abhishek, Adam, Jiangyi, Pinar, Shang, Shardul, Siddhartha and Sriram. Thank you to my office mates: Adam, Dave, Edgar and Jonathan for brightening even the most difficult of days.

I would like to acknowledge the Boeing Company and the Defense Threat Reduction Agency for funding my research. Thank you to the Rackham Graduate School, the College of Engineering, and the Department of Aerospace Engineering for facilitating my studies.

Finally, I am grateful to my family and friends for their encouragement throughout my life. I would like especially thank my parents; Cindy and Guy, my brothers; Andy and Vinny, and my best friends; Darrin and Werner.

TABLE OF CONTENTS

LIST OF FIGURES

LIST OF TABLES

ABSTRACT

Multiscale Modeling of Carbon Nanotube-Epoxy Nanocomposites

by

Nicholas A. Fasanella

Chair: Associate Professor Veera Sundararaghavan

Epoxy-composites are widely used in the aerospace industry. In order to improve upon stiffness and thermal conductivity; carbon nanotube additives to epoxies are being explored. This dissertation presents multiscale modeling techniques to study the engineering properties of single walled carbon nanotube (SWNT)-epoxy nanocomposites, consisting of pristine and covalently functionalized systems. Using Molecular Dynamics (MD), thermomechanical properties were calculated for a representative polymer unit cell. Finite Element (FE) and orientation distribution function (ODF) based methods were used in a multiscale framework to obtain macroscale properties.

An epoxy network was built using the dendrimer growth approach. The epoxy model was verified by matching the experimental glass transition temperature, density, and dilatation. MD, via the constant valence force field (CVFF), was used to explore the mechanical and dilatometric effects of adding pristine and functionalized SWNTs to epoxy. Full stiffness matrices and linear coefficient of thermal expansion vectors were obtained. The Green-Kubo method was used to investigate the thermal conductivity as a function of temperature for the various nanocomposites. Inefficient phonon transport at the

ends of nanotubes is an important factor in the thermal conductivity of the nanocomposites, and for this reason discontinuous nanotubes were modeled in addition to long nanotubes.

To obtain continuum-scale elastic properties from the MD data, multiscale modeling was considered to give better control over the volume fraction of nanotubes, and investigate the effects of nanotube alignment. Two methods were considered; an FE based method, and an ODF based method. The FE method probabilistically assigned elastic properties of elements from the MD lattice results based on the desired volume fraction and alignment of the nanotubes. For the ODF method, a distribution function was generated based on the desired amount of nanotube alignment; and the stiffness matrix was calculated. A rule of mixture approach was implemented in the ODF model to vary the SWNT volume fraction. Both the ODF and FE models are compared and contrasted. ODF analysis is significantly faster for nanocomposites and is a novel contribution in this thesis. Multiscale modeling allows for the effects of nanofillers in epoxy systems to be characterized without having to run costly experiments.

CHAPTER 1

Introduction

Carbon nanotubes (CNTs) have been researched extensively in the last 20 years because of their outstanding mechanical [1–3], electrical [4–6] and thermal properties [7, 8]. Due to these exceptional properties and very high aspect ratios, forming CNT-polymer nanocomposites has become an attractive option to improve the properties of the polymer. This work will focus in particular on single walled carbon nanotubes (SWNTs). SWNTs are an atom thick single layer of graphene with a cylindrical structure and an elastic modulus around 1 TPa [9]. Atomistic simulation methods allow the effects the effects of nanoparticles in a composite system to be characterized without running costly experiments.

Polymer-matrix composite materials are widely used in aerospace, automotive, marine and other high-performance applications due to their high specific strength, high specific stiffness, fatigue resistance, and ease of manufacturing. Thermoset polymers are the most predominant type of matrix system, and epoxies specifically are preferred for aerospace grade components due to their superior mechanical properties and resistance to environmental degradation due to moisture. The thermomechanical properties of nanocomposites are highly dependent on the interface between the CNT and epoxy. It is experimentally difficult to characterize this interface, making molecular modeling an essential tool for relating molecular interfacial structure to bulk thermomechanical properties. In Chapter 2, Molecular Dynamics (MD) was used in order to explore the effects on the mechanical and dilatometric properties by adding pristine and covalently functionalized SWNTs to crosslinked polymers. MD allows for the effects of mechanical and thermal loading to be isolated and visualized in regions of interest where it may not be possible with experiments.

Epoxies are generally limited to low temperature applications, and this is in part due to their low thermal conductivity of $\sim$.24 W/mK at room temperature [10]. It is of great interest to improve the heat conduction in epoxies in order to remove excess heat, and boost reliability and performance. CNTs have very high thermal conductivity, with SWNTs having a thermal conductivity of 1750-5800 W/mK [8, 11] and high aspect ratios. For this reason, SWNTs were investigated as an additive to improve the thermal conductivity of the

epoxy via the formation of functionalized and pristine SWNT-polymer nanocomposites. Inefficient phonon transport between nanotubes at discontinuities (i.e. the nanotube ends) is an important factor in the thermal conductivity of SWNT-epoxy nanocomposites, and so discontinuous nanotubes were modeled to study this. In Chapter 3, MD was used to study the use of the Green-Kubo integral of the heat flux autocorrelation function to model the full 3D thermal conductivity of SWNT-epoxy nanocomposites.

Molecular Dynamics has a well-known length scale problem, with the dimension of the sides of the MD lattice in Chapters 2 and 3 being $\sim$40 Å. Even with periodic boundary conditions, ways to upscale the simulations to better compare with continuum results are desired. To this achieve this, multiscale modeling was considered in Chapter 4 to give better control over the volume fraction of SWNT. Multiscale modeling also allowed the effects of SWNT alignment to be considered, and this was done in Chapter 5. Two different multiscale approaches were used; a Finite Element based method, and an ODF based method. For the Finite Element method, elements were probabilistic assigned elastic properties from the MD lattice results based on the desired volume fraction of nanotubes, and the alignment of the nanotubes. For the ODF method, an orientation distribution function was generated for the desired amount of nanotube alignment, and the stiffness matrix was calculated. To vary the volume fraction of nanotubes, a rules of mixture approaches was implemented in the ODF approach. Multiscale modeling allows for the effects of nanofillers in epoxy systems to be better characterized on a contiuum-level without having to run experiments.

The problems outlined above can be broken down into a few major categories: Atomistic modeling for thermomechanical properties, atomistic modeling for thermal conductivity, and multiscale modeling for elastic properties of SWNT-epoxy nanocomposites. Relevant experimental and computational literature is reviewed for the thermomechanical results in Section 1.1, thermal conductivity in Section 1.2, and multiscale modeling in Section 1.3. The goal of this thesis is to create methods that allow the effects of nanofillers in a polymer network to be characterized without having to run physical experiments. SWNT-epoxy systems are studied in this this work, but the methodology is applicable to any number of various fillers and polymers.

1.1 Thermomechanical Properties of CNT-Polymer Nanocomposites

There have been a numerous experimental studies on the effects to mechanical properties or thermal dilatation from adding SWNTs to various polymers. To fully take advantage of

the mechanical and thermal properties of carbon nanotubes, attempts have been made to functionalize the nanotubes. Functionalization allows for better dispersion and interfacial bonding of the carbon nanotube to the polymer matrix, and has shown to give significantly improved mechanical properties [12–21]. Polyacrylonitrile (PAN) fibers were created containing 10 wt% SWNTs, which saw a 100% improvement in tensile modulus, reduction in thermal shrinkage, and increased glass transition temperature of 40° C over control fibers, indicating strong interaction between PAN and SWNTs [22, 23]. In [24], SWNT-polyacrylonitrile (PAN) composite films were created which show massive reduction in the coefficient of thermal expansion (CTE) above and below the glass transition temperature (T_g), and large raises in tensile strength (80%) and Young's modulus (300%) at 40 wt% SWNT when compared to pure PAN. In [25], fluorinated SWNTs are used to evaluate the effect of nanotube sidewall functionalization on the mechanical properties of polyethlene composites. It was seen that the fluorination disrupts the larger SWNT rope structure and allows covalent bonding to occur between the polyethylene and SWNT; increasing interfacial characteristics and mechanical properties over pure SWNT-polyethylene composites. In [26] and [27], polypropylene-CNT composites were investigated. In [26], polypropylene containing 0.8 wt% SWNT exhibits faster crystallization rate compared to pure polypropylene, but does not show improvements in mechanical properties due to poor dispersion. In [27], SWNTs were added, and the maximum increase in mechanical properties was seen at 0.75 wt%, with an increase of 39% in Young's modulus and 27% in yield strength over neat polypropylene. This study demonstrated that for effective reinforcement, good nanotube dispersion is necessary. It was seen in [28] that the elastic modulus and yield strength of SWNT-PMMA composite fibers increased with nanotube loading and draw ratio, even up to high loadings of 8 wt% SWNT. A significant increase in the impact strength was seen in [29] by adding CNTs, though very little increase in the elastic modulus was seen for either SWNTs or MWNTs. In [30], the elastic modulus increased with increasing SWNT loading, with a maximum increase of a 90% for purified SWNT-PMMA with 2 wt% SWNTs. In [31] large increases in Young's modulus, toughness and tensile strength were seen at 0.1 wt% doped SWNT over pristine PMMA, though pristine SWNTs show very little improvement due to defects in the samples.

Chemical functionalization allows for efficient load transfer between the fillers and matrix in the composite. Geng et. al showed that SWNT-poly(ethyele oxide)(PEO) composites with improved uniformity and dispersion can be formed using chemically functionalized carbon nanotubes, with significant enhancement of the mechanical properties. A 300% increase in the Young's modulus and yield strength over pure PEO, was obtained at a nanotube loading of 1 wt% [21]. In [20], composites of poly(vinyl alcohol) (PVA)

containing pristine and functionalized nanotubes were tested in tension. It was found that the mechanical properties of these nanocomposite were significantly improved compared to the polymer, with a maximum increase of 55% in the modulus and yield strength for a 5 wt% SWNT, functionalized SWNT-PVA composite. Functionalization allowed for good distribution of the nanotubes in the matrix, and good interfacial bonding between the functionalized carbon nanotubes and hosting polymer matrix, leading to increased strength. Functionalized SWNT-PVA composites are also investigated in [19], where it is seen functionality improves uniformity and dispersion of the SWNTs. In another study, significant improvements were seen in the mechanical properties for SWNT/PVA composites, with the tensile strength and Young's modulus continuing to increase with increasing wt%, and the highest measured values were a 43% improvement in Young's modulus over neat PVA, and a 55% improvement in yield strength [20]. In [32], the thermal expansion is measured for various vol% of SWNT in poly(vinylidene fluoride) (PVDF). The coefficient of thermal expansion continues to decrease at higher vol%, with the minimum value being a 35% decrease over neat PVDF at 49 vol% SWNT. These experiments demonstrate the potential of CNTs, especially functionalized CNTs, as reinforcement agents in nanocomposites.

Of most relevance to this work, there have been numerous experiments where SWNTs have been added to form composites with various epoxies, and the thermomechanical properties of the subsequent nanocomposite have been calculated. In [33], the role of nonionic surfactant in improving the interfacial interaction in CNT-epoxy composites was considered. The epoxy used is bisphenol A epoxy resin with hydroxylated polyamine hardener H-917. With the surfactant, T_g increased from 63°C to 88°C, and the elastic modulus increased by more than 30% with 1 wt% CNT. Without the surfacant, the pure nanotubes have only moderate effects on thermomechanical properties. In [17], covalent functionalization of SWNTs via an optimized H_2S_4/70% HNO_3 acid treatment and subsequent fluorination to epoxy EPON 862 (DGEBA) with curing agent EPI-CURE W was considered. The functionalized nanotubes were shown to be well dispersed in the composite, and the elastic modulus and the tensile strength were increased by 30% and 18% over neat epoxy, respectively. The pristine SWNT-epoxy fracture surfaces showed nonuniform dispersion, and sliding of SWNTs in the epoxy matrix, and therefore composites showed little improvement in mechanical properties over neat epoxy. In [13], functionalization of a SWNT and EPON 862 (DEGBA) with curing agent EPI-CURE W was studied. Functionalization was accomplished via the reaction of terminal diamines with alkylcarboxyl groups attached to SWNTs during the course of a dicarboxylic acid acyl peroxide treatment. The resulting covalently functionalized system showed large improvements in mechanical properties over neat epoxy, with a 65% increase in elastic modulus for 4 wt% SWNT and a 25% in

yield strength for 1 wt% SWNT. In [14], functionalized and pristine SWNT-epoxy systems were studied, where the epoxy was EPON 862 (DEGBA) with curing agent EPI-CURE W. Functionalization of the SWNTs was done by grafting epoxy polymer curing agent, EPI-W to the SWNTs through diazotization. At 0.5 wt% SWNTs, the elastic modulus of the functionalized system was enhanced by 24.6%, while the pristine SWNT system improved by only 3.2% over neat epoxy. In [34], composites of SWNT and Epoxiber-20 with IB-72 were studied, where Epoxiber-20 is a low viscosity epoxy resin formed by condensation between Bisphenol A and Epichlorhydrin. After purifying and dispersing the SWNTs, an improvement of up to 16.3% was seen at 0.1 wt% SWNT. Functionalized and non-functionalized SWNT-epoxy composites were studied in [12] where the epoxy resin is EPIKOTE 862 resin (DEGBA), with curing agent EPIKURE W. Improvements of 27% in Young's modulus and 17% in tensile strength were seen, however these were less than expected and the authors suggest improved dispersion and prevention of the curling of SWNTs may be necessary to fully realize the potential of SWNT and epoxy nanocomposites. In [35], an Epon 862 based composite with curing agent DETDA was mixed with CNTs functionalized via covalent and noncovalent bonding approaches. The coefficient of thermal expansion (CTE) was reduced by up to 52% below T_g for nanocomposites with a 1 wt% loading of SWNTs. Above T_g however, the CTE increases substantially due to phonon modes vibration and Brownian motion of the SWNTs. In [16], functionalization of SWNT was again explored by grafting epoxide onto single-walled carbon in order to better integrate the SWNT into the epoxy. Mechanical testing demonstrated an increased Young's modulus by 60% and yield strength by 40% at 1 wt% SWNT relative to neat epoxy, showing that load transfer from the epoxy to the SWNT was achieved via epoxide-grafting. In [18] plasma fluorinated SWNTs were used to react with a primary aliphatic amine in order to create functionalized SWNT-epoxy composites. This caused crosslinking to occur between the epoxy and amino-functionalized SWNTs, leading to an improvement in mechanical strength with respect to samples prepared with pristine nanotubes. In [36], nanocomposites of SWNT-epoxy resin with aligned nanotubes were created by a solution casting technique and subsequent stretching of the semi-dried mixture along one direction at a draw-ratio of 50. The epoxy used in this study was a bisphenol-A type epoxy resin (E51) and hardener N,N-dimethylbenzylamine (BDMA). Higher electrical conductivity and mechanical properties were demonstrated along the stretched direction than perpendicular to it, with improvements of 103% in Young's modulus and 164% in tensile strength in the stretch direction over neat epoxy. In [15], m-chloroperbenzoic acid-epoxidized CNTs were used to form composites with epoxy resin Epon 862. The epoxidized CNTs-modified epoxy composites showed a 50% increase in the Young's modulus and 32% improvement in the

tensile strength with 1 wt% loading when compared to neat epoxy. In [37], the thermal dilatation was measured of .25 wt% carboxylated SWNTs without covalent functionalization. The epoxy resin was diglycidyl ether of bisphenol A (DGEBA) with hardener Aradur HY 956. The addition of the SWNTs reduced the linear coefficient of thermal expansion by 29%. In [38], SWNT-epoxy composites with a very high nanotube loading of up to 39.1 wt% were fabricated, where the epoxy was diglycidyl ether of bisphenol-A (DGEBA) with a mixed curing agent consisting of a room temperature curing agent (molar ratio of 2:1 of triethylenetetramine to O,O'-bis(2-aminopropyl)polypropyleneglycol 2000) and a high temperature curing agent (p-diaminodiphenylsulfone, DDS). The mechanical properties were enhanced greatly due to the incorporation of SWNTs, with the Young's modulus increasing by 408% and the tensile strength by 183% when compared to neat epoxy.

Molecular Dynamics has been used previously to analyze the elastic properties of various polymer-SWNT systems such as polyethylene [39,40]. In [39], classical MD was used to study the thermal expansion and diffusion characteristics of SWNT-polyetlene composites using Brenner's potential for intra-nanotube interactions, and van der Waals forces for polymer-nanotube interface. It was found T_g, as well as the CTE and diffusion coefficients for the composite increased relative to pure polyethylene. In [41], a comparison was made between the mechanical response of SWNT/polyethylene composites with continuous nanotubes replicated via periodic boundary conditions, and composites containing discontinuous nanotubes. Both composites are loaded along, and transverse to the axis of the nanotube, and it was found that the continuous nanotube system showed an increased in stiffness along the nanotube direction relative to neat polyethylene, though no substantial improvement in the transverse direction was seen. The discontinuous system did not show improvement over the polymer in either direction, and the authors believe this to be due to the low aspect ratio of SWNTs. In [42], the compliance matrix was generated for short and an infinite carbon nanotubes embedded into a polyethylene matrix. Two different models were employed, and both gave similar results due to the lack of bonding between matrix and SWNT; the first used Brenner's potential for the whole system, and second Brenner's potential for the nanotube, but a united-atom potential for the polyethylene matrix. The infinite nanotubes gave substantial improvement in stiffness properties along the nanotube direction, while the short nanotubes produced improvements of $\sim$100%, but substantially less than that of the infinite tubes. Neither system produced a substantial improvement over neat polyethylene in the direction transverse to the SWNT. In [40] MD was used to investigate the interfacial characteristics of SWNT-polyethylene composites. The interface strength was described by the critical interfacial shear stress (CISS) and the steady interfacial shear stress (SISS) as function of the MD simulation model size, sliding velocity of

CNTs, radius of CNTs, and polymer chain length. It was found that the CISS and SISS decrease as the CNT radius increased, and increase as the polymer chain length increased. In [43], a SWNT (10,10) was added to two amorphous polymers, poly(methyl methacrylate) (PMMA) and poly(m-phenylenevinylene)-co-[(2,5-dioctoxy-p-phenylene) vinylene] (PmPV) with different volume fractions. A constant-strain energy minimization method was used to calculate elastic moduli of the composite system along, and transverse to the nanotube axis. It was seen that the modulus along the nanotube axis increased with increasing volume fraction of SWNT of up to 28% for both composites. Increases in the transverse direction were minor for all volume fractions considered. In [44], mechanical properties of adding a SWNT to poly (phenylacetylene) (PPA) were investigated via the AIREBO potential for interaction between carbon atoms in the SWNT, Lennard-Jones potential for interactions between PPA and the SWNT, and the AMBER potential for interactions between PPA atoms. It was once again seen that the longitudinal Young's modulus along the nanotube direction is improved drastically, However, transverse moduli did not see significant improvement relative to pure polymer.

The results of [41–44] demonstrates that functionalization is likely necessary to strengthen the interface and impart the properties of the SWNT to the polymer in the direction transverse to the SWNT, as well as in the direction along the nanotube for discontinuous tubes, as the van der Waal interactions are insufficient for load transfer. To take full advantage of the mechanical and thermal properties of the SWNTs, experimental attempts described earlier have covalently functionalized the nanotube to the epoxy [12–21]. A few studies have used MD to investigate the effects of covalent bonding on SWNT-polyethylene systems. In [45], the interfacial sliding of a SWNT chemically bonded to a chain of polyethylene was simulated. The functionalization results in higher interfacial shear strengths and higher interfacial viscosities than in the non-bonded composite, demonstrating better incorporation of the nanotube into the polymer network. In [46], changes in the bulk elastic properties due the addition SWNT to polyethylene with and without covalent functionalization were considered. For 1% volume fraction of SWNT, chemical functionalization causes the Young's and shear moduli of the random composites, and the longitudinal Young's modulus of the aligned composites to reduce by 11%. When the nanotube length is held fixed at 400 nm, and various nanotube volume fractions are considered, functionalizion causes the Young's and shear moduli of the random, and the longitudinal Young's modulus of the aligned composites to reduce by 12%. However, functionaliation caused the transverse Young's modulus and the transverse shear modulus of the aligned composites to increase by up to 45%. This study highlights one of the potential drawbacks of functionalization, as chemical bonding to the nanotube creates defects and may decrease the inherent stiffness

of the SWNT.

Epoxies have an amorphous structure and building complex crosslinked molecular configurations with realistic properties is challenging, and so attempts to study the thermomechanical properties of SWNT-epoxy systems via Molecular Dynamics are limited. Liang et. al used MD to study the molecular interactions between a (10,10) SWNT and EPON 862 (DGEBF) resin and EPI-CURE W (DETDA) curing agent [47]. They found that the Epon 862 resin and DETDA molecules both have attractive interactions with a (10,10) SWNT. The aromatic ring planes of both Epon 862 and DETDA molecules try to align towards the surface of the SWNT and wrap around it, and so good wetting properties were predicted between the (10, 10) SWNT and Epon 862 resin/DETDA agent. Gou et. al. expanded this work and studied affinities between a (10, 10) SWNT and two epoxy systems, EPON 862/EPI-CURE W curing agent (DETDA) and DGEBA (diglycidylether of bisphenol A)/diethylenetriamine (DETA) curing agent. In agreement with [47], they found that EPON 862 and DETDA had strong attractive interactions with a (10,10) SWNT. It was seen DGEBA also had a strong attractive interaction, and conversely, DETA had a repulsive interaction [48]. In [49], interfacial bonding strength was calculated for a composite consisting of EPON 862 epoxy resin and EPICURE W curing agent embedded with a (10,10) SWNT. This was done via a pullout test, where the interfacial shear strength between the nanotube and the cured epoxy resin was calculated to be up to 75 MPa. The authors indicate this may be sufficient for effective stress transfer from the epoxy to the SWNT. However, other simulations directly measuring the mechanical results of SWNT-polymer composites have not shown this to be true for composites lacking functionalization [41–44]. Zhu et. al studied SWNT-EPON 862 composites, and found stress-strain relations in the longitudinal direction, parallel to the nanotube, for continuous nanotubes that span the entire simulation cell and become infinite with periodic boundary conditions applied, as well as discontinuous CNTs. They found that the long, continuous CNTs greatly enhance the Young's modulus in the longitudinal direction ($\sim$1000%) over neat epoxy. The short, discontionous CNTs show a much smaller improvement of 20% compared to neat epoxy [50]. Mohan et. al. predicted the effects of carbon vacancy defects on the Young's modulus of a SWNT and EPON 862 crosslinked with DETDA composite using MD [51]. For a composite with 7-12 wt% SWNT, two carbon vacancy defects in the SWNT reduces the Young's modulus by 13-18%, while four carbon vacancy defects in the SWNT reduced the Young's modulus of the composite by 21-30%. To the author's knowledge, there had not previously been MD simulations of SWNT-epoxy nanocomposite systems that were able to extract the bulk elastic properties of the system by calculating the full elastic stiffness matrix.

Molecular scale simulations provide the ability to isolate the effects of the SWNT on the

composite system in greater detail than experimentation. Epoxies have an amorphous structure and building complex crosslinked molecular configurations with accurate properties is challenging [52]. Using an amorphous crosslinked structure that has been experimentally verified [53], MD will be used in Chapter 2 to obtain full elastic stiffness matrices and thermal expansion vectors for pristine SWNT and covalently functionalized SWNT composite systems. The effects of randomly oriented SWNT-epoxy composites were simulated by rotating and averaging the properties in every direction [54, 55].

1.2 Thermal Conductivity of CNT-Polymer Nanocomposites

MD has been used previously to study the thermal conductivity of simpler systems, such as metals, ionic salts and non-crosslinked amorphous polymers [56–58]. It is difficult to create accurate models for crosslinked polymers, and only recently has MD been used to study the thermal conductivity of these systems [59, 60]. Thermal conductivity is generally calculated using equilibrium or non-equilibrium MD approaches. For equilibrium MD, the Green-Kubo method is used, which relates fluctuations of the thermal current to the thermal conductivity via the fluctuation-dissipation theorem [61]. For non-equilibrium MD (NEMD) methods, a long slab of polymer is constructed and a difference in temperature is established between a heat source and a sink at the ends of the slab, and the flux is calculated. The epoxy in this study is built using the dendrimer growth approach which builds a cubic unit cell, and so is well suited for the Green-Kubo method. A comparison between the equilibrium Green-Kubo approach and NEMD method for an epoxy model built using multi-step crosslinking, found the two methods result in comparable values of thermal conductivity [59].

MD studies of SWNT-polymer composites to this point have focused on the interfacial thermal conductance or resistance of SWNT-polymer systems. Shenogin et. al studied the effects of functionalization on the transverse thermal transport properties of a SWNT/octane system using equilibrium MD. It was found that functionalization via chemical bonding greatly reduced the SWNT-matrix interfacial thermal resistance, and approximately doubled the effective composite conductivity. However, they found that the addition of chemical bonding to the SWNT reduced the intrinsic tube conductivity [62]. Clancy and Gates used MD to study the effects of functionalization on the interfacial thermal resistance of a SWNT and bulk non-crosslinked poly(ethylene vinyl acetate) composite by grafting linear hydrocarbon chains to the surface of the SWNT. They found the interfacial thermal

resistance decreased as the degree of functionalization (grafting density) and chain length of the grafted linear hydrocarbon chains increased. An analytic model using the calculated interfacial thermal resistance was used to obtain the effective thermal conductivity of the composite, which saw very large increases in thermal conductivity, approaching 100 W/mK for high grafting densities (.12 Å^2) of long nanotubes (100 μm) with high volume fractions (5%), and greater than 10 W/mK for many other combinations [63]. Huxtable et. al combined MD and experiments on a CNT-Octane system and found the thermal conductivity of the composite to be restricted by a low interfacial thermal conductance ($\sim$12 MW/m^2K), leading to results much lower than predicted at a given volume fraction considering the SWNT's intrinsic thermal conductivity [64]. Xu and Buehler used MD to show that the thermal resistance at the junctions of two CNTs can be reduced by modifying the interfacial molecular structure via polymer wrapping of polyethylene chains to improve the matching of phonon spectra and phonon mode coupling, and found improvements of up to 40% in thermal conductivity [65]. Alaghemandi et. al studied a composite of CNTs and polyamide-6,6 using reverse non-equilibrium MD and found that the thermal conductivity of the composite increased slightly parallel to the nanotube and decreased perpendicular to the nanotube. They concluded that the high interfacial thermal resistances, in the absence of chemical modification or any other alteration, hinders heat transfer from the polymer to the nanotubes [66]. Varshney et. al. used non-equilibrium MD to investigate the interfacial thermal conductance in functionalized CNT-epoxy composite system for crosslinked and non-crosslinked systems. The interfacial thermal conductance was 20% higher for the crosslinked system, due to reduction in volume and increased structural rigidity during curing. The increase in interfacial thermal conductance was shown to be linear with increasing degree of functionalization for both systems [67]. SWNTs that span the entire MD cell become infinite when periodic boundary conditions are applied. This, or the use of NEMD methods, has limited all of the aforementioned studies, with exception of Alaghemandi et. al., to measuring the conductivity/resistance perpendicular to the nanotube axis. These studies have identified the interfacial thermal resistance as the primary reason for lower than expected increases in the composite thermal conductivity [62, 65, 66].

Experimentally, there have been a number of studies investigating the potential increase in thermal conductivity from adding SWNTs to epoxy. These studies have generally shown a monotonic increase in the effective thermal conductivity as the loading of nanotubes increases when considering weight fractions of SWNTs. Gojny et. al studied SWNT-epoxy, DWNT-epoxy and MWNT-epoxy composites, and the effects of functionalization on the DWNT and MWNT nanocomposites where the epoxy is a modified DGEBA-based resin (L135i) with amine hardener (H137i) [68]. A 20% increase in thermal conductivity was

seen at 0.5 wt%, though they found results to be limited due to strong phonon boundary scattering at the CNT interfaces, as well as scattering at lattice defects. Biercuk et al. studied epoxy samples, Epon 862 epoxy resin and Ancamine 2435 dimethane-amine, with 1 wt% SWNT and saw a 125% increase in thermal conductivity at room temperature, and a 70% increase at 40 K. [69]. Liu and Fan showed that for 2 wt% CNT (95% multi-wall), chemical modification can reduce the interfacial thermal impedance in CNTs-plydimethylsiloxanerubber nanocomposites, but have negative effects on the thermal conductivity of the CNT itself [70]. At higher nanotube loading, 3 wt% SWNT, Choi et. al saw thermal conductivity increase by up to 300% over neat epoxy (Thixotropic/PR2032 epoxy resin). They found the effective thermal conductivity can be further enhanced another 10% via magnetic alignment [71]. At 10% SWNTs by volume in a epoxy-SWNT composite, where the epoxy was Epon 828 with crosslinker EpiKure 3234, Byring et. al. saw up to 64% improvement in thermal conductivity [72]. The reviewed literature does not show the existence of a thermal peculation threshold, where thermal transport properties are drastically increased at a certain CNT loading, even at very high nanotube loading. This is in stark contrast to the electrical conductivity of CNT/epoxy composites where orders of magnitude increases are seen at the electric percolation threshold, which for SWNT-epoxy composites is only 0.05 wt% SWNT [73]. Experimental results have yielded results far lower than what one would estimate from a rule of mixtures calculations given the high inherent CNT thermal conductivity.

Thus far, experimental results have not seen the improvements in thermal conductivity simulations have predicted possible, and inefficient phonon transport between nanotubes is likely the limitation [74]. The ends of the SWNT are discontinuities, and the phonon mean free path is approximately 0.5 μm for SWNTs at room temperature [75]. It can therefore be expected phonon scattering will be significant at the free ends for nanotubes shorter than this length. Previous MD studies have been limited to calculating the interfacial thermal resistance or conductivity due to the lack of a free boundary. This will prevent boundary scattering, and the only scattering mechanism will be phonon-phonon interactions. In Chapter 3, equilibrium MD simulations were performed on the an epoxy model created using the dendrimer growth approach. Functionalized and pristine nanotube-epoxy composites were created for various nanotube lengths, and the thermal conductivity of the systems was calculated via the Green-Kubo formulation in 3D. Covalent functionalization was explored to improve the interfacial thermal conductivity, though it was expected to decease the inherent SWNT conductance [62]. The methods used to create the material systems are given in detail in Section 2.3. For systems with short-range pair interactions, such as the Lennard-Jones or embedded atom potential, the heat flux expression in the integrand

of the Green-Kubo is well know. Electrostatic forces between partial charges on atoms in crosslinked systems lead to long range interactions. Hence, the per-atom energy to compute the heat flux vector in the case of long range interatomic interactions is calculated on a periodic domain using the standard or mesh-based particle-particle-particle-mesh (PPPM) Ewald methods [76]. In Section 3.2, 'k-space' or 'reciprocal' modeling of electrostatic energy is explored. Results with and without this long range correction are shown and compared with experiments, along with the nanocomposite results. To the author's best knowledge, this study was the first time MD was used to study discontinuous nanotubes in epoxy composites to factor in the nanotube end effects to the thermal conductivity of SWNT-epoxy nanocomposites [77, 78].

1.3 Multiscale Modeling of Polymer-Based Nanocomposites

Molecular Dynamics has well-known limitations regarding time scale and length scales. The time step of an MD simulation are typically on the order of femtoseconds. It is defined by the fastest motion in the system and vibrational frequencies are up to 3000 cm^{-1}, corresponding to period on the order of 10 fs [79]. The limiting factor of the length scale is the number of atoms that can be included in the simulation, on the order of 10^3-10^8 atoms, and this is on the order of 10-100 nanometers [79]. To address these issues, multiscale modeling techniques have been formulated to solve for the continuum properties of SWNT-polymer nanocomposites.

A number of different approaches have been implemented by various researchers to model SWNT-polymer nanocomposites. Li and Chou examined the effect of interfacial load transfer on the stress distribution in a CNT-polymer composites. A SWNT was modeled on an atomstic scale using the molecular structural mechanics method they created. The polymer matrix was treated as a continuum, and the Finite Element method was adopted for modeling its deformation [80]. Namilae and Chandra also studied interfacial properties and developed a hierarchical multiscale methodology to link Molecular Dynamics and the Finite Element method through atomically informed cohesive zone model parameters. The developed methodology was used to study the effect of interface strength on the stiffness of the CNT-based composite via pullout tests [81]. Li and Chou later modeled of the compressive behavior of CNT-polymer composites. The buckling forces of SWNT-polymer composites at different nanotube lengths and diameters are computed by assuming the CNT and polymer matrix interact via van der Waals interactions at the interface. The re-

sults indicate that continuous nanotubes most effectively enhance the composite's buckling resistance [82]. Liu et. al. used a multiscale approach to study the effect functionalization of CNTs has on the damping characteristics of SWNT-polymer composites. The interfacial shear strength between the SWNT and epoxy was calculated via pull out test. The strength values obtained from MD were then applied to a micromechanical damping model of an RVE of a SWNT-epoxy composite under cyclic loading, showing functionalization increases interfacial shear strength [83].

Seidel and Lagoudas calculated the effective elastic properties for CNT reinforced composites through a variety of micromechanics techniques. The effective properties of CNTs were calculated via a composite cylinders micromechanics technique, and these effective properties were then used in the self-consistent and Mori-Tanaka methods to obtain effective elastic properties of composites consisting of aligned single or multi-walled carbon nanotubes embedded in a polymer matrix [84]. Spanos and Kontos developed a multiscale Monte Carlo and Finite Element model for the effective elastic properties of SWNT-polymer nanocomposites. This models allowed for non-uniform dispersion and distribution of SWNT in polymers to be factored into the macroscopic behavior of the nanocomposites via a multiscale homogenization approach [85]. Tserpes et. al used a multiscale RVE for modeling the tensile behavior of CNT-reinforced composites to integrate nanomechanics and continuum mechanics. Isolated CNTs were modeled using a progressive fracture model based on the modified Morse potential, and FE was used for modeling the matrix and building the RVE. Stiffness was calculated for a unidirectional nanotube/polymer composite using the RVE [86]. Ionita used multiscale modeling via atomistic and mesoscale simulations to study SWNT-epoxy composites. The models were used to determine the effects of diameter and weight fraction of SWNTs on thermomechanical properties. The Young's modulus, glass transition temperature and solubility parameter of the composites were calculated via MD, and the dissipative particle dynamics method and Flory-Huggins theory was employed to predict SWNT-epoxy morphologies [87]. Yang et. al. developed a sequential multiscale bridging model to characterize the CNT size effects and weakened bonding effects at the interface of CNT-polyproplyene composites using MD and continuum micromechanics. Using the proposed multiscale model, the elastic modulus for nanocomposites at various volume fractions and CNT sizes was estimated [88]. They later investigated a nonlinear two-step multiscale modeling approach for the elasoplastic behavior of a CNT-polymer composite via MD simulations and a continuum nonlinear micromechanics based on the secant moduli method. The imperfect interface between the CNT and polymer and the interphase formed by the adsorbed polymer molecules to the surface of CNT were considered. It was found that the weakened interface and polymer-

densified interphase both play important roles the elastoplastic behavior, and they cancel each other out according to the CNT volume fraction [89].

In Chapter 4, multiscale modeling approaches via molecularly informed Finite Element and ODF-based models are used to calculate the effective elastic properties of functionalized and pristine SWNT-epoxy composites at various volume fractions of SWNTs. As the literature above highlights, multiscale approaches for effective properties of SWNT-epoxy systems are limited, and no one has yet considered functionalized systems. In Chapter 5, the effects of varying nanotube alignment are considered for the pristine and functionalized SWNT-epoxy nanocomposites via a multiscale framework, for the first time in literature.

CHAPTER 2

Thermomechanical Modeling

The thermomechanical properties of nanocomposite materials are highly dependent on the interface between the epoxy and the CNT. It is experimentally difficult to characterize this interface, and therefore molecular modeling is a useful tool for linking molecular interfacial structure to bulk thermomechanical properties. In this chapter, MD was used in order to explore the effects on the mechanical and dilatometric properties by adding pristine and covalently functionalized SWNTs to crosslinked polymers. MD allows for the effects of mechanical and thermal loading to be isolated and visualized in regions of interest where it may not be possible with experiments. Epoxies have an amorphous structure, which makes building complex crosslinked molecular configurations with accurate properties is challenging [52]. Using an amorphous crosslinked structure that has been experimentally verified [53], MD was used to obtain full elastic stiffness matrices and thermal expansion vectors for pristine SWNT-epoxy and covalently functionalized SWNT-epoxy composite systems. The effects of randomly oriented nanotube/epoxy composites was simulated by rotating and averaging the properties in every direction.

2.1 Overview of Molecular Dynamics

Molecular Dynamics (MD) is a simulation technique that predicts the time evolution of a system of interacting particles, such as atoms or molecules. [90–94] The particles are given a realistic set of initial conditions, positions, and velocities, such that particles are in physically feasible positions (i.e no overlapping atoms). The motion of an individual atom is determined through interactions with other particles in the system, commonly contained in an interaction potential, which will be discussed at length in Section 2.1.1. MD is a deterministic method; the evolution of the system is completely determined from the given initial positions and velocities, aside from uncertainty introduced via computational errors. For each time step, the velocities and positions of each atom are obtained, though it gener-

ally is macroscopic properties of materials that are primary of interest, and not the motion of individual atoms. Statistical distribution functions are used to describe the configurations generated by the simulation, and so MD can also be viewed as a statistical mechanics method. In statistical mechanics, macroscopic thermodynamic quantities of interest can be computed, in an average sense, by averaging over all of the configurations, as shown below as a function of position (**r**) and momentum (**p**) for quantity A:

$$\langle A \rangle_{r,p} = \int_p \int_r A(\mathbf{r, p}) P(\mathbf{r, p}) d\mathbf{r} d\mathbf{p}. \tag{2.1}$$

Eq. 2.1 is known as the ensemble average of quantity A, where P is a probability density determined by the selected fixed macroscopic properties, or ensemble. Instantaneous values of a property are based on the position and velocity at a given time, and will fluctuate around the ensemble average. For N particles, a thermodynamic ensemble contains $6N$-dimensional phase space $(\mathbf{r}, \mathbf{p})$ data subjected to some thermodynamic constraint (i.e. fixed energy and volume for an NVE ensemble). If all possible configurations of velocity and position of an ensemble are considered, the ensemble average will yield the true value of a bulk property. MD is often used to find time-averaged macroscale quantities, shown below for A:

$$\langle A \rangle_t = \frac{1}{\tau} \int_0^\tau A\big[\mathbf{r}(t), \mathbf{p}(t)\big] dt. \tag{2.2}$$

The ergodic hypothesis states that an ensemble averaged over many configurations, or a phase space ensemble, will be equivalent to an average over time of a single configuration, or a time ensemble.

$$\langle A \rangle_{r,p} = \langle A \rangle_t. \tag{2.3}$$

This is generally valid provided the simulation is run long enough to generate sufficient configurations, and the trajectory is able to cover all of phase space.

The evolution of a system in time is found by solving Newton's equations of motion for all the particles. For a particle i, the equation of motion is given as:

$$m_i \mathbf{a}_i = m_i \frac{d^2 \mathbf{r}_i}{dt^2} = \mathbf{F}_i(\mathbf{r}_i, ..., \mathbf{r}_n), \tag{2.4}$$

where $\mathbf{F}_i$ is a function of position of the other particles in the simulation. For N particles, N trajectories need to be computed. In any MD simulation, it is required to be able to model how the particles interact, via the force term in Eq. 2.4. It is also necessary to have methods for analyzing the data to calculate the desired properties.

The basic steps of any MD simulation are as follows: first the system needs to be initialized by selecting permissible initial positions and velocities. Next, the forces on all the particles are computed, and Newton's equations of motions are integrated. These steps take up the bulk of the simulation. Finally, it it necessary to compute averages of the measured quantities. If there are N total atoms in a system, the force acting on the i^{th} atom can be obtained from an interatomic potential, $U(r_1, r_2, ..., r_N)$, which is a function of the positions of all other atoms as follows:

$$\mathbf{F}_i = -\nabla_i U(r_1, r_2, ..., r_N). \tag{2.5}$$

2.1.1 Interatomic Potential

In constructing an interatomic potential, electrons are treated classically, and the atoms interact via a prescribed analytical model. This has the advantage of allowing longer simulation times with more particles over ab initio (quantum) methods, but means the potentialss are often limited to the applications they were constructed for. An interatomic potential should be able to accurately capture the nature of the bonding (i.e covalent bonding, metallic bonding, ect., and be able to replicate experimental results for macroscopic quantities of interest. For a system containing N interacting atoms, the potential energy can be divided up into various terms depending on single atoms, pairs of atoms, atom triplets, and so on:

$$U = \sum_i v_1(\mathbf{r}_i) + \sum_i \sum_{j>i} v_2(\mathbf{r}_i, \mathbf{r}_j) + \sum_i \sum_{j>i} \sum_{k>j>i} v_3(\mathbf{r}_i, \mathbf{r}_j, \mathbf{r}_k) + ... \,. \tag{2.6}$$

The summation for the higher order terms is restricted such that counting bonds more than once is prevented. The first term in Eq. 2.6 is the one-body term, which takes into account the effects of an external field. The second term is known as the pair potential, and generally contributes the most towards the total potential energy. It describes the interaction between two particles, and depends on the magnitude of the distance between the two particles, $\mathbf{r}_{ij}$. The third team in Eq. 2.6 is an angular term that describes triplets of particles. These terms depend on the orientations of the three atoms, and are very important for covalent systems [95]. Higher order terms or many-body potentials are typically negligible due to their low contributions to the total potential energy.

In order to accurately fit various bonding scenarios, a number of different modeling approaches are used for different types of systems. The most simple potential is the Lennard-Jones potential, also known as the 12-6 potential, which is a pair potential for van der Waals interactions that works well for noble gases:

$$v_2 = 4\epsilon\Big[\Big(\frac{\sigma}{r_{ij}}\Big)^{12} - \Big(\frac{\sigma}{r_{ij}}\Big)^{6}\Big], \tag{2.7}$$

where ϵ is the depth of the well and σ is the distance of the repulsive wall from the origin. The first term in Eq. 2.7 is a strong repulsive term due to electron overlap as atoms get too close together. The second term is an attractive term that arises from dipole-dipole interactions.

For ionic materials, it is necessary to include long-range interactions [90]. This is generally done by summing short-range and long-range terms to describe the interactions between the ions. A Coulomb charge-charge potential is commonly used to describe the attractive long-range interactions, and a repulsive term is added to keep the atoms from getting too close together:

$$v_2 = \frac{q_i q_j}{4\pi\epsilon_o r_{ij}} + Ae^{\beta r_{ij}}, \tag{2.8}$$

where q_1 and q_2 are charges on ions 1 and 2 respectively, ϵ_o is the permittivity of free space, and r_{12} is the separation distance of ions 1 and 2. The first term is the Coulomb potential, which will be attractive if the ion is of opposite charge, and the second term is the repulsive term.

While the simple potentials discussed earlier work well for certain systems, they do not for metal or covalent systems. Pair potentials are insufficient for metals due to the nature of metallic bonding, where valence electrons are shared by the metal ions in the material and bonding is non-directional. The embedded atom method is a multibody potential used to model metallic systems, where every atom is viewed as being embedded in a pool of delocalized electrons. Unlike Lennard-Jones and ionic systems, the bonding in covalent systems is highly directional, meaning they have orientational preferences. Covalent bonds are formed by atoms sharing electrons, forming a strong chemical bond. There is an overlap of electron clouds of the two atoms bonded, and same electrons fill the valance shells of both atoms [96]. This leads to an angular dependence, thus making a three-body term very important for nearest neighbors. Additionally, covalent bonds are short-ranged and are very stiff along the bond direction. An example of a covalent potential is the Stillinger-Weber, often used for Silicon [95], where the two body term in Eq. 2.6 is:

$$v_2(r_i, r_j) = \begin{cases} (Br_{ij}^{-4} - A)e^{\frac{1}{r_{ij}-1}} & \text{if } r_{ij} < a \\ 0 & \text{if } r_{ij} \geq a, \end{cases} \tag{2.9}$$

where the Br_{ij}^{-4} term is a repulsive term, and the A term is an attractive term. As r ap-

proaches 0, v_2 will diverge as r^{-4}, and as r approaches a, v_2 will go to zero as $e^{\frac{1}{r_{ij}-1}}$. The three-body term, which is essential due the orientation dependence of covalent bonds, is given as:

$$v_3(r_i, r_j, r_k) = \lambda e^{\left[\frac{\gamma}{r_{ij}-a}+\frac{\gamma}{r_{ik}-a}\right]}\left(\cos\theta_{ijk} + \frac{1}{3}\right)^2. \tag{2.10}$$

Here, it is seen that Eq. 2.10 will go to zero if θ_{ijk} =109.47, which is the minimum energy for tetrahedral bonding. The total expression give five parameters for fitting experimental data: A, B, a, λ and γ.

2.1.2 Integration Schemes

With initial conditions and the interatomic potential defined, the equations of motion can be solved numerically via a number of different integration schemes. The resulting solutions are the position and velocities of all atoms as a function of time, $\mathbf{r}_i$(t) and $\mathbf{v}_i$(t). For a system with N atoms, $3N$ 2$^{\text{nd}}$ order differential equations given by Eq. 2.4 need to be solved. Finite difference approaches are used in order to solve these equations step-by-step. Given the relevant dynamic information at time t, such as molecular velocities and positions, the dynamic information is then found at later time, $t + \delta t$. The time interval, δt, is chosen such that an acceptable amount of accuracy is achieved, and is generally much smaller than the time a particle takes to travel its own length [90]. Ideally, the integration scheme should posses certain attributes such as: the ability to satisfy conservation laws for energy and momentum, time reversibility, allow for a long time step (δt), run fast, and require small amounts of memory. In practice, not all these attributes are required and many popular integration schemes do not satisfy all of them.

The most simple, widely used finite difference algorithm to solve Eq. 2.4 is the Verlet method [97, 98]. It solves the positions at the next time step $r(t + \delta t)$ based on the current positions $r(t)$, accelerations $a(t)$, and the position at the previous time step, $r(t - \delta t)$:

$$\mathbf{r}(t + \delta t) = 2\mathbf{r}(t) - \mathbf{r}(t - \delta t) + \frac{\mathrm{d}^2\mathbf{r}}{\mathrm{d}t^2}\delta t^2 + O(\delta t^4). \tag{2.11}$$

The velocities do not appear in Eq. 2.11, as they have been canceled out by summing the Taylor expansion about $\mathbf{r}(t)$:

$$\mathbf{r}(t + \delta t) = \mathbf{r}(t) + \frac{\mathrm{d}\mathbf{r}}{\mathrm{d}t}\delta t + \frac{1}{2}\frac{\mathrm{d}^2\mathbf{r}}{\mathrm{d}t^2}(\delta t)^2 + \frac{1}{6}\frac{\mathrm{d}^3\mathbf{r}}{\mathrm{d}t^3}(\delta t)^3 + O(\delta t^4) \tag{2.12}$$

$$\mathbf{r}(t-\delta t) = \mathbf{r}(t) - \frac{\mathrm{d}\mathbf{r}}{\mathrm{d}t}\delta t + \frac{1}{2}\frac{\mathrm{d}^2\mathbf{r}}{\mathrm{d}t^2}(\delta t)^2 - \frac{1}{6}\frac{\mathrm{d}^3\mathbf{r}}{\mathrm{d}t^3}(\delta t)^3 + O(\delta t^4). \tag{2.13}$$

From Eq. 2.12 and 2.13, it can be seen that Eq. 2.11 is a third order method, even though it does not contain third order derivatives, and that it is time-reversible. As shown, the error due to truncation is of the order δt^4. The velocities can be extracted from the old and new positions, and are important for energy calculations. The error for the velocities however, is of the order δt^2. The expression for velocity is:

$$\mathbf{v}(t) = \frac{\mathbf{r}(t+\delta t) - \mathbf{r}(t-\delta t)}{2\delta t} + O(\delta t^2). \tag{2.14}$$

Some improvements have been made to the Verlet method, and a very common scheme is known as the "Velocity Verlet" algorithm, which calculates positions, velocities and accelerations at time t [99]. The error is of the same basic order than the original Verlet method, but has less error due to round off. The expressions for position and velocity are given respectively as:

$$\mathbf{r}(t+\delta t) = \mathbf{r}(t) + \frac{\mathrm{d}\mathbf{r}}{\mathrm{d}t}\delta t + \frac{1}{2}\frac{\mathrm{d}^2\mathbf{r}}{\mathrm{d}t^2}\delta t^2 \tag{2.15}$$

$$\mathbf{v}(t+\delta t) = \frac{\mathrm{d}\mathbf{r}(t)}{\mathrm{d}t} + \frac{1}{2}\left[\frac{\mathrm{d}^2\mathbf{r}(t)}{\mathrm{d}t^2} + \frac{\mathrm{d}^2\mathbf{r}(t+\delta t)}{\mathrm{d}(t+\delta t)^2}\right]. \tag{2.16}$$

There are numerous integration schemes, and another well-known Verlet-like method is the "leap frog" scheme. Additionally, higher order schemes that allow longer time steps or better accuracy at the expense of memory requirements are sometimes used. These employ higher order derivatives, and a popular type of higher order algorithm are "predictor-corrector" schemes [98, 100, 101]. In general, these work by predicting values for position, velocity and acceleration at time $t+\delta t$ using data at time t, evaluating forces at time $t+\delta t$, and correcting the predicted positions, velocities, and forces based on the evaluation step.

For finite difference based integration algorithms, error can be broken down into two distinct categories: round-off errors and truncation errors [93]. Round-off errors result from computer implementation of an algorithm. Truncation errors are inherent to the algorithm and result from errors created by the finite difference method, such as the where the Taylor expansion is truncated. These errors, no matter how small, will lead to exponential divergence from the true trajectory over time. This is known as the Lyapunov instability [91]. This can be more formally formulated by considering the position of a particle N at time t:

$$\mathbf{r}_i(t) = f\Big(\mathbf{r}_n(0), \mathbf{p}_N(0); t\Big), \tag{2.17}$$

where $\mathbf{r}$ and $\mathbf{p}$ are position and momentum, respectively. If the initial conditions are perturbed slightly by an amount ϵ this gives:

$$\mathbf{r}_p(t) = f\Big(\mathbf{r}_n(0), \mathbf{p}_N(0) + \epsilon; t\Big). \tag{2.18}$$

So, if $\Delta\mathbf{t}$ is defined as $\mathbf{r}_i(t) - \mathbf{r}_p(t)$, $\Delta\mathbf{t}$ will only be linear in ϵ for a short time period. For longer time periods:

$$|\Delta\mathbf{r}(t)| \sim \epsilon \exp(\lambda t), \tag{2.19}$$

where λ is the Lyapunov exponent, and represents the exponential divergence of the two trajectories with time. This is not a huge issue for Molecular Dynamics, as typically MD is used for statistical predictions and the trajectories are close enough for meaningful results.

2.1.3 Periodic Boundry Conditions

Molecular Dynamics simulations are typically limited in how many atoms they can contain, $O(10^3 - 10^8)$, which is far below the number of atoms seen in a continuum, which is on the order of Avogadro's number $O(10^{23})$. This means that an unrealistically high percentage of the atoms in an MD simulation will lie on the surface or subsurface, where atoms are known to behave differently. To alleviate surface effects and better model a continuum, periodic boundary conditions (PBCs) are often used [92]. In practice, an MD simulation using PBCs will have one primary cell, which is then replicated infinitely in space to create a lattice. The movement of particles within every cell is identical. This can be better illustrated pictorially, where Fig. 2.1 shows 2D PBCs where the yellow cell is the primary cell. The blue particles are the particles from the primary cell, and the red particles are the repeated images. Different shapes represent different particles. It can be seen that particles are free to move across the boundary into a different cell, and when this happens an equivalent particle will enter the vacated cell, keeping the number of atoms fixed in a cell. The use of PBCs eliminates surface atoms by having no walls or barriers at the boundary of the primary cell. Potential energy in the primary cell is given as:

$$U_{PC} = \frac{1}{2} \sum_{i}^{N_{PC}} \sum_{j \neq i}^{N_{PC}} u(r_{ij}^{o}). \tag{2.20}$$

Eq. 2.20 does not factor in interactions across the cell boundaries, so if interactions are long enough, the above expression will not be accurate. In this case, the image atoms must also be counted:

$$U_{PC} = \frac{1}{2} \sum_{\boldsymbol{\alpha}} \sum_{i}^{N_{PC}} \sum_{j \neq i}^{\boldsymbol{\alpha}} u\Big(|\mathbf{r}_i - (\mathbf{r}_j + L\boldsymbol{\alpha}\Big), \tag{2.21}$$

where $\boldsymbol{\alpha}$ is a vector which specifies the periodic cell ($\boldsymbol{\alpha} = \mathbf{0}$ is the primary cell), i designates an atom within the box selected, and j sums over all the other particles. A 2D example of $\boldsymbol{\alpha}$ is shown in Fig. 2.2. The potential energy of each image of an atom, m, are identical. If particle m is assumed to be in the primary cell, and m' is in an image cell (in 2D), $\boldsymbol{\alpha} = (1, 1)$, then the potential energy for m and m' are:

$$U_m = \frac{1}{2} \sum_{\boldsymbol{\alpha}} \sum_{j \neq i}^{N_\alpha} u\Big(|\mathbf{r}_m^o - (\mathbf{r}_j^o + L\boldsymbol{\alpha}\Big), \tag{2.22}$$

$$U_{m'} = \frac{1}{2} \sum_{\boldsymbol{\alpha}} \sum_{j \neq i}^{N_\alpha} u\Big(|\mathbf{r}_m^{(1,1)} - (\mathbf{r}_j^o + L\boldsymbol{\alpha}\Big). \tag{2.23}$$

It is known that $\mathbf{r}_m^{(1,1)} = \mathbf{r}_m^o$, and therefore $U_m = U'_m$, and likewise $F_m = F'_m$. Therefore, the forces, energy and other quantities of interest need only be evaluated over the particles in the primary cell. PBCs need to be used carefully however, and it is important that a simulation cell is large enough such that a given particle will not interact with its own image particles. In practice, interactions are usually truncated by a given cut-off radius, r_c, and so the length of the cell, L, needs to satisfy $r_c \leq \frac{L}{2}$ as shown in Fig. 2.3.

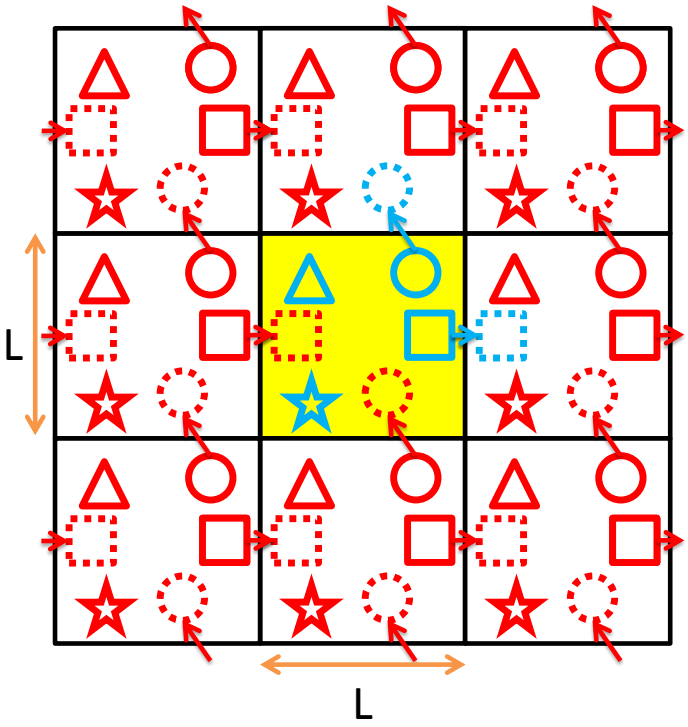

Figure 2.1: PBCs shown where main cell is the yellow box, original particles are shown in blue, and periodically repeated particles are shown in red.

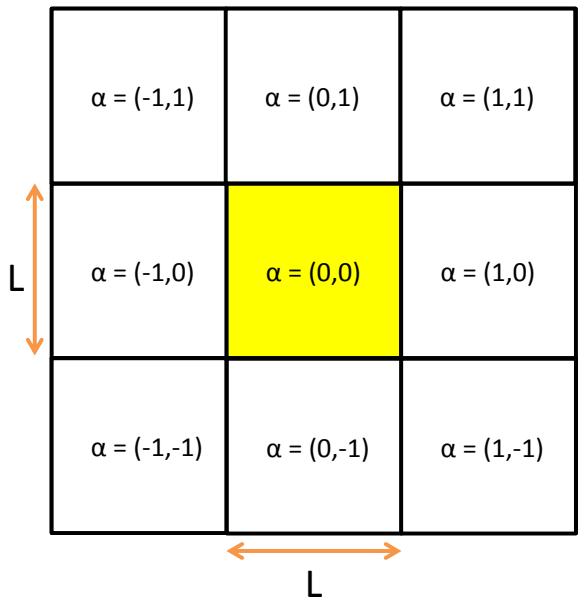

Figure 2.2: 2D example of using α to select a periodic image, where the primary cell is in yellow.

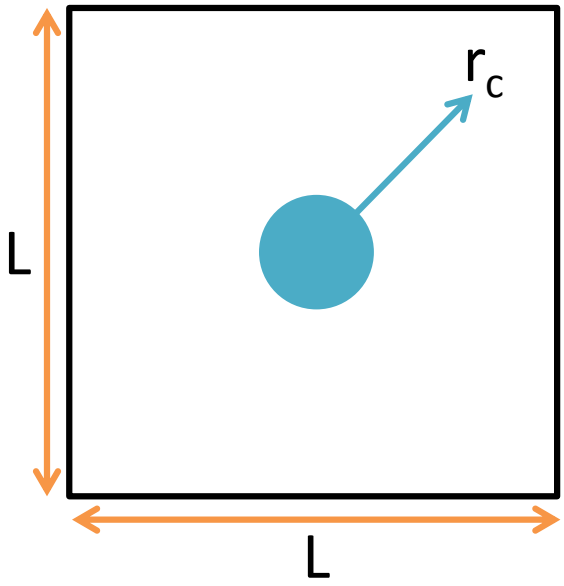

Figure 2.3: For periodic boundry conditons to be used, the simulation cell must be large enough such that the interaction cut-off radius satisfies $r_c \leq \frac{L}{2}$.

2.1.4 Ensembles

MD makes heavy use of statistical mechanics to find average macroscopic properties of interest from the microscopic states that are distributed by an ensemble [102]. Some of the most commonly used ensembles consist of the microcanonical (NVE) ensemble, canonical ensemble (NVT), and isothermalisobaric ensemble (NPT). The microcanonical ensemble is an isolated, adiabatic system where the number of particles (N), the size of the simulation cell (V) and the total energy (E) are held fixed. The canonical ensemble is isothermal using a thermostat to control the temperature (T). The number of particles (N), and the size of the simulation cell (V) are also held constant. The isothermalisobaric ensemble is, as the name implies, isobaric and isothermal. A thermostat and barostat are used to control temperature and pressure, respectively. The number of particles (N), pressure (P), and temperature (T) are held constant. There are several methods in order to control temperature in an MD simulation that can be broken down to: stochastic methods, velocity re-scaling methods, and extended system methods [90]. Stochastic methods include the Andersen thermostat, which uses impulses on random particles to change their velocity in order to maintain a desired temperature [103]. Velocity re-scaling methods, such as the Berendsen thermostat, couple the system with a constant temperature heat bath in order to adjust velocities such that a constant temperature is maintained [104]. Extended system methods, such as the Nosé and Nosé-Hoover thermostats, which consider a heat bath by adding an artificial

variable with a ”mass”, determining the coupling between the system and the heat bath, and a velocity, which acts time-scaling parameter [105–107]. These thermostats are among the most accurate and commonly used methods for constant temperature Molecular Dynamics.

2.2 Materials

Diglycidyl ether of bisphenol A (DGEBA) is the epoxy chosen for this study. The epoxy molecules were crosslinked with curing agent 3-3’ diamino diphenyl sulfone (DDS). The structure of the epoxy and the amine can be seen in Figs. 2.4a and 2.4b, respectively. Each epoxide has a crosslinking functionality of one towards the amine curing agents. The epoxy monomer has two epoxide (oxirane ring) groups leading to a total functionality of two. Each amine group has a functionality of two towards epoxy molecules. The DDS monomer has two amine groups for a total functionality of four. A typical amine stoichiometric ratio for synthetic epoxy is approximately 2:1 or 33.3 mol% amine. The polymer is formed by bonding of the epoxide group in DGEBA and the amine groups in the DDS. To form a crosslink, the primary amine group reacts with the epoxide group, creating a bond between the terminal carbon of the epoxide group and the nitrogen of DDS. The carbon-oxygen bond breaks between the terminal carbon and the oxygen from the epoxide, and forms and alcohol (-OH) link. The crosslinked structure seen in Fig. 2.5a can undergo another reaction with a different epoxy molecule, forming the final crosslinked structure seen in Fig. 2.5b.

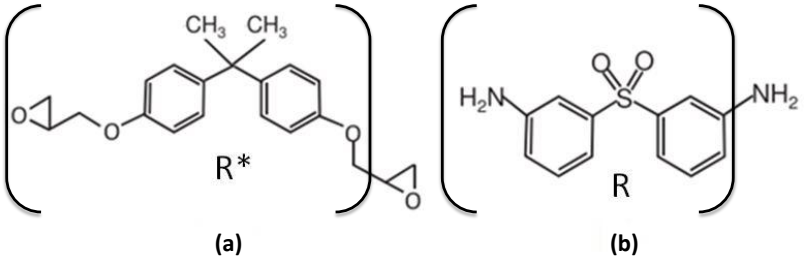

Figure 2.4: a. Chemical structure of epoxy resin, Diglycidyl ether of bisphenol A (DGEBA). b. The amine monomer diamino diphenyl sulfone (DDS). Brackets give the notation for R and R* in Fig. 2.5.

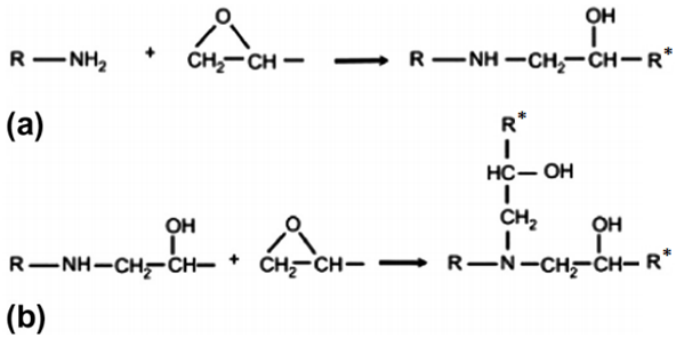

c points

Figure 2.5: Epoxy-amine cross-linking through reaction of epoxide group and amine group

2.3 Material Modeling

A major hurdle in creating accurate models for molecular simulation of industrial grade epoxies is attaining realistic crosslinking densities, where a conversion percentage of 70-95% is typically seen when measured through Near-Infrared (NIR) Spectroscopy [108]. A number of approaches have been used to build polymer networks with greater than 70% crosslink conversions. The majority of these approaches can be characterized based on whether unreacted monomer mixtures are crosslinked all-at-once (one-step) or over time (multi-step). For one-step crosslinking, sites are first randomly selected and then pairs of sites within a capture radius are crosslinked together [109, 110]. One-step methods lead to artificially high network strains. In multi-step crosslinking, every reactive pair that satisfies a length criteria are crosslinked iteratively, with equilibration and the length criteria increasing with every iteration [111]− [112]. Multi-step methods prevent and relieve network strains, but they are computationally expensive. A new method was introduced by Christensen in 2007 to build epoxy networks using a 'dendrimer' growth approach [52, 113]. In this method, the thermoset resin is modeled by starting with a single monomer and then crosslinking a second layer of monomers around it. In the next step, a third layer of monomers are crosslinked to the second layer. In this way, generations (layers) of monomers are added to a seed structure that grows in size at every pass. An example is shown in Fig. 2.6, where on the left the seed structure is shown in red, with a second layer in blue. The subsequent images show a third and fourth layer being grown to the seed structure in green and orange, respectively. The principal advantages of the dendrimer growth method are the complete avoidance of artificial network strain during curing and the low computational cost of the growing procedure.

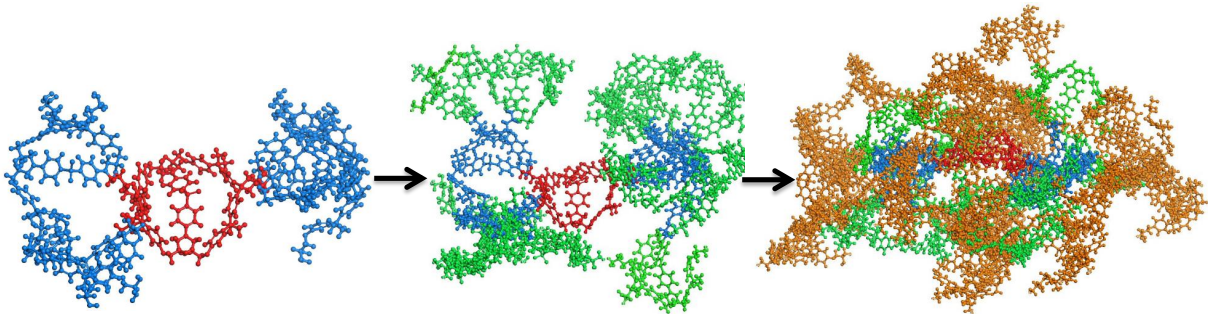

Figure 2.6: Dendrimer growth process: left image shows initial seed in red and a second layer in blue. A third and fourth layer shown in green and orange are subsequently grown.

The 'dendrimer' growth approach was used to build the epoxy network in Materials Studio [114] containing 36 amine groups and 71 epoxy groups, as seen in Fig. 2.7. The system contains 4601 atoms and is sufficiently complex to accurately capture the amorphous nature of the polymer. All simulations in this work are performed under periodic boundary conditions, and the Consistent Valance Force Field (CVFF) [115] potential was used for bonded and non-bonded interactions in LAMMPS [116]. This force-field has been used in previous studies to accurately predict thermodynamic properties of epoxy [59, 60]. 75% of available epoxy sites were crosslinked, which is representative of many structural epoxies. To verify the accuracy of the initial dendrimer structure; the dilatometric curve simulated by MD has been compared to experimental results, and the full elastic stiffness matrix was generated by conducting tensile and shear tests via MD to verify the structure is isotropic.

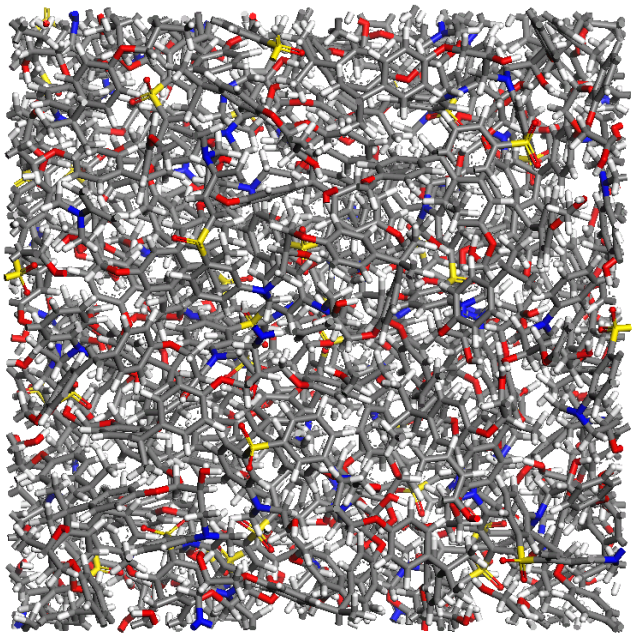

Figure 2.7: The dendrimer structure of epoxy after energy minimization.

Equilibration of the structure was necessary, as the initial density of the dendrimer, seen in Fig. 2.8, is far too low due to the growth process. To achieve density convergence, the annealing protocol shown in Table 2.1 was followed. The structure was further optimized during the "Minimization" step via a sequence of energy minimization and annealing. This was done by first minimizing the energy via conjugate gradient (CG) for 10000 iterations. Next, MD was then performed over several annealing cycles using an NPT ensemble. Dynamics was first performed well above T_g (600 K and 1 atm) for 500 ps. Dynamics was then run well below T_g (1 K and 1 atm) for 500 ps, followed by CG. After ten cycles, the potential energy was sufficiently minimized such that density converged to within 0.5% across consecutive annealing steps. Progressive density convergence is shown in Fig. 2.9, and final density of 1.17 g/cc at 1 atm and 1 K was obtained after convergence.

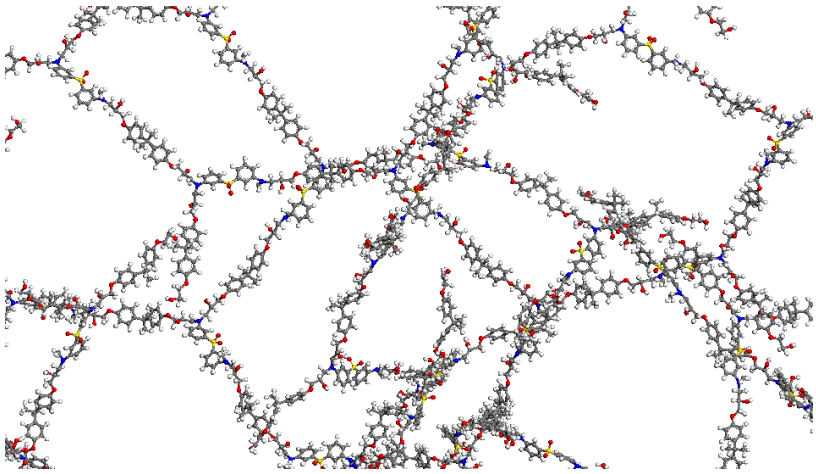

Figure 2.8: Initial epoxy structure after dendrimer growth approach.

Table 2.1: Annealing protocol for equilibrating the epoxy structure [117].

NVT for 50 ps at 650 ^{o}K (Equilibration)
NPT for 50 ps at 650 ^{o}K and 0.1 GPa (Initial compaction)
NVT for 50 ps at 500 ^{o}K (Equilibration)
NPT for 50 ps at 500 ^{o}K and 0.25 GPa (Additional compaction)
NVT for 50 ps at 450 ^{o}K (Equilibration)
NPT for 50 ps at 400 ^{o}K and 0.0001 GPa (Reduce to 1 atm)
NVT for 50 ps at 300 ^{o}K (Equilibration)
NPT for 50 ps at 300 ^{o}K and 0.0001 GPa (Equilibration)
Minimization until density within $< 0.5\%$ across consecutive steps

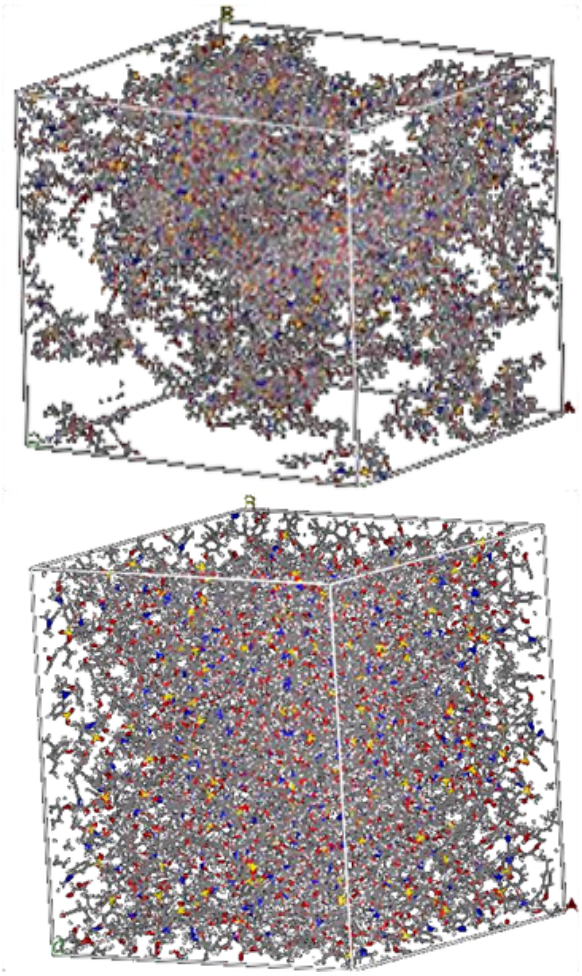

Figure 2.9: Density showing convergence after energy minimization and annealing

To build the CNT/Epoxy nanocomposites, a vacancy was created in the epoxy by moving atoms radially outward from a chosen point, and an single-walled armchair nanotube (4,4) was inserted in the space. Moving atoms caused many bonds to be displaced from their equilibrated length, so the same minimization process ran previously via a sequence of conjugate gradient (CG) minimization and dynamics above and below T_g was used to minimize potential energy until the density converged. Images of the equilibrated structure can be seen normal to the nanotube direction (x-y plane) in Fig. 2.10, and along the nanotube (x-z plane) in Fig. 2.11. A functionalized SWNT-epoxy composite was created by covalently bonding the nanotube to the DDS molecule. One of the four functional sites of the DDS was attached to the SWNT, as shown in Fig. 2.12. The other functional sites react with the epoxide, as shown earlier in Fig. 2.5. The degree of crosslinking for the epoxy is unaffected, as sites that were previously not reacted with the epoxy were selected to bond covalently to the nanotube. Again, minimization was performed via a sequence of

the conjugate gradient (CG) minimization and annealing until the density was seen to converge. The functionalized system containing four covalent bonds to the epoxy can be seen in Fig. 2.13b. Experimentally, carbon nanotubes with amino groups covalently bonded to their side walls have been prepared by use of fluorinated SWNTs [17, 18, 118, 119].

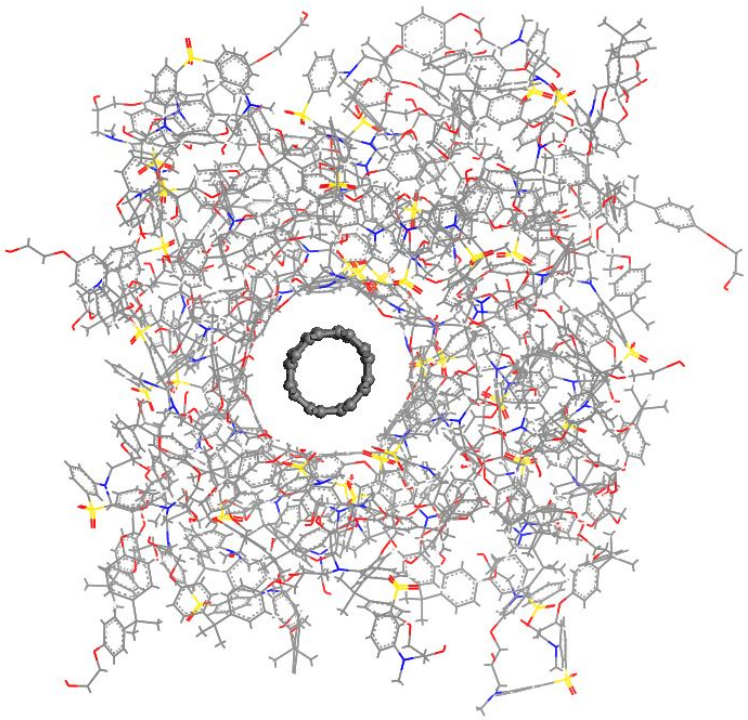

Figure 2.10: Pristine SWNT and epoxy nanocomposite after reaching equilibrium in x-y plane.

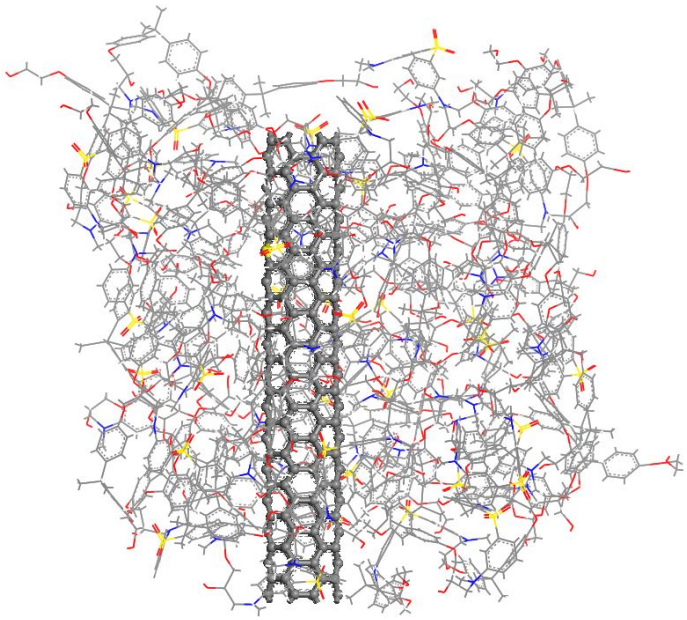

Figure 2.11: Pristine SWNT and epoxy nanocomposite after reaching equilibrium in x-z plane.

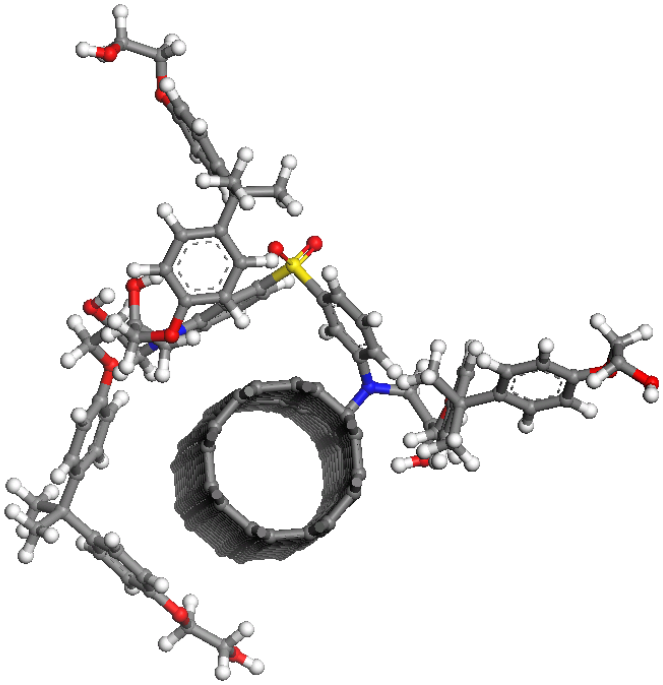

Figure 2.12: Nanotube functionalization to amine and subsequent crosslinking to epoxy.

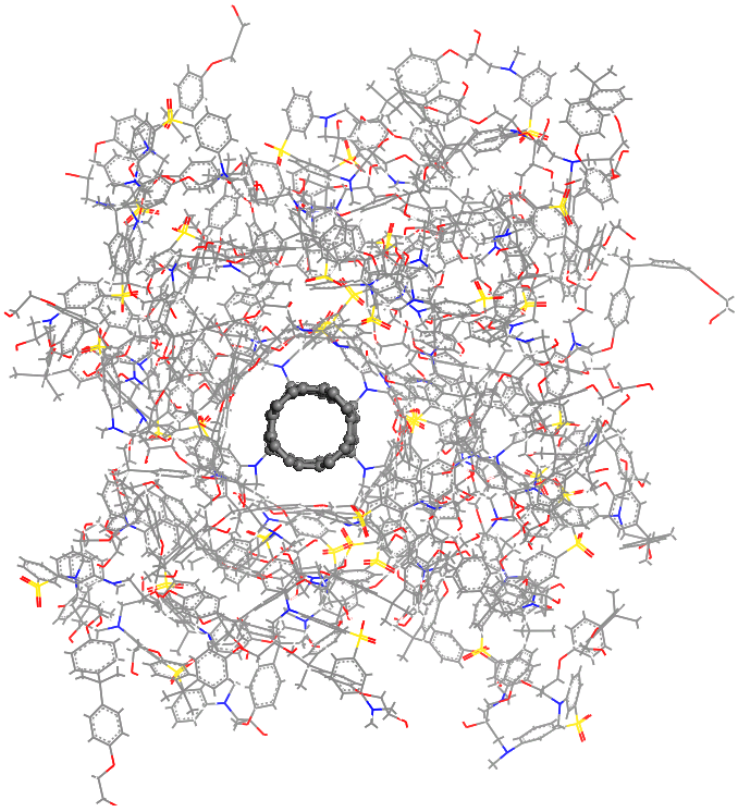

Figure 2.13: Functionalized SWNT and epoxy nanocomposite.

2.4 Model Verification

Tension (x, y and z directions) and shear tests (xy, yz and xz in the positive and negative directions) were performed via MD to obtain the stiffness matrices at various temperatures. Strains were applied and the stress was averaged over three samples. These results were used to solve for the 36 constants in the elastic stiffness matrix. The epoxy was verified to be isotropic by rotating the resulting stiffness matrix in all directions, using the transformation law for a fourth-order tensor, as shown in Fig. 2.14. Rotation tensors were chosen such that they took into account all independent rotations of a transversely isotopic system when accounting for symmetries. The isotropic properties of epoxy can be seen in Fig. 2.15. These were obtained using a strain rate of $10^6 \frac{1}{s}$, however the deformation was only applied once every 1000 time steps. This leads to an effective strain rate of $10^3 \frac{1}{s}$, and allowed the system 500 time steps to relax before stress data was collected and averaged. It has been measured experimentally that for a DGEBA-DDS resin system with an 80% degree of curing, the tensile elastic modulus is 3.1 GPa at room temperature (300 K) [120]. Additionally, for tests in compression at room temperature and quasi-static loading rates, a Poisson's ra-

tio of 0.37 has been measured experimentally [121]. The Young's modulus and Poisson's ratio at 300 K are found to be 3.0 GPa and 0.35 respectively, which compares well with the experimental results and show the relaxation steps allow for quasi-static results to be obtained.

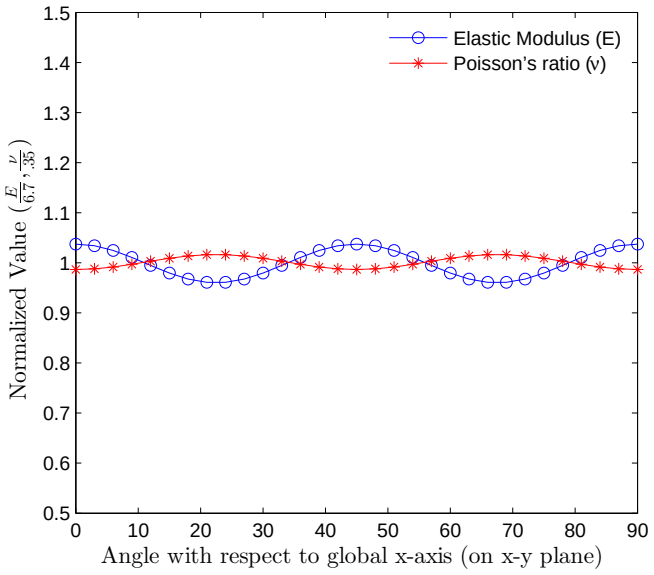

Figure 2.14: Variation of elastic properties by rotating with respect to the x-axis.

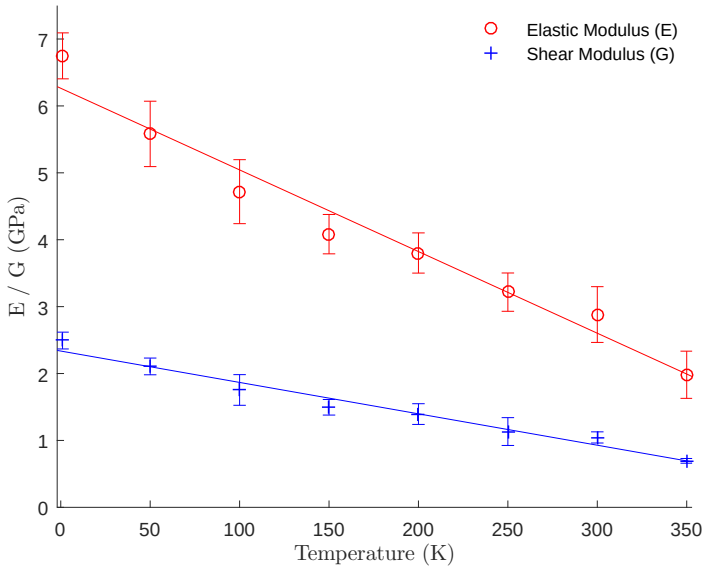

Figure 2.15: Young's modulus and shear modulus for epoxy model.

The thermal expansion coefficient for the neat epoxy was obtained via an NPT simulation. The change in cell length with varying temperature was plotted with an experimentally measured dilatometric curve in Fig. 2.16 [122]. The MD calculated data is seen to be in very good agreement with the experimental curve. The linear coefficient of thermal expansion (CTE) between -50^oC to 150^oC was measured to be 54.4 $\pm$ 2.7 $\mu/^oC$ from this figure, with error bars shown later in Fig. 2.25. Thermal expansion at higher temperatures was plotted in Fig. 2.17 to show the glass transition temperature, which falls within the experimental range of 425-495 K for DGEBA/DDS [122].

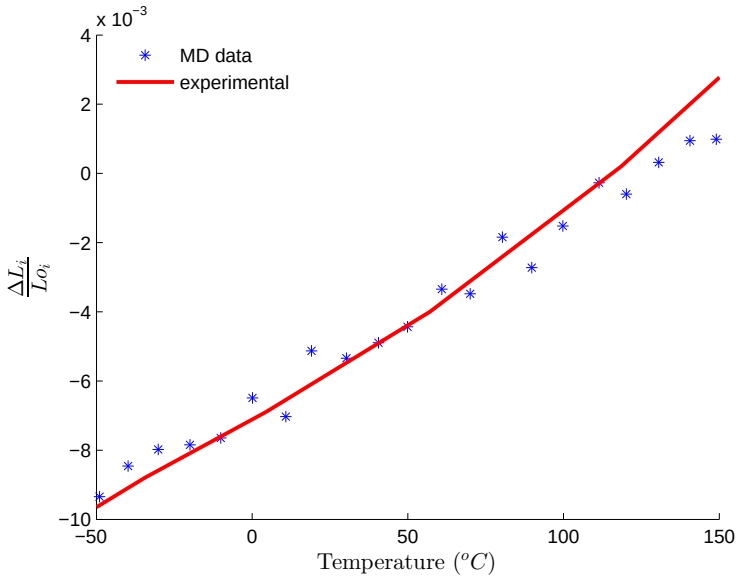

Figure 2.16: MD calculation of thermal expansion is superposed with an experimentally measured dilatometric curve reported in [122].

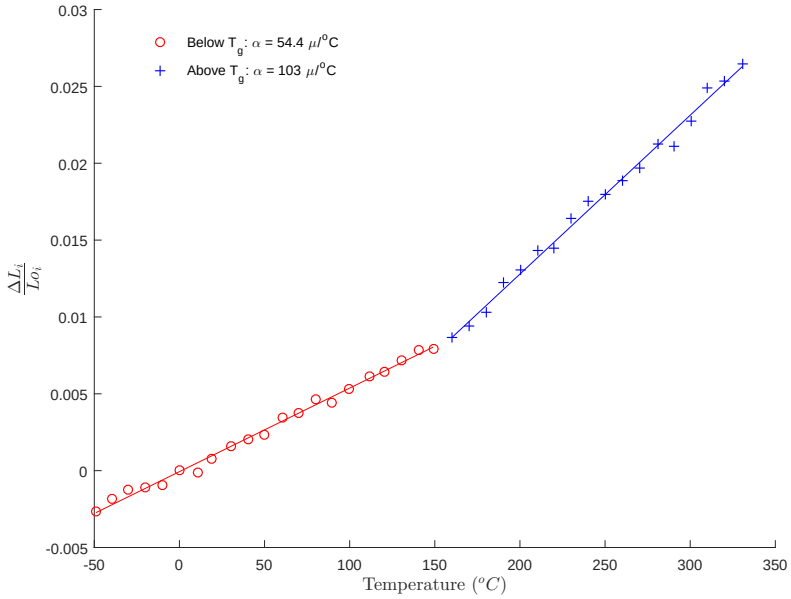

Figure 2.17: Thermal expansion for neat epoxy showing the glass transition temperature.

2.5 Results

2.5.1 Elastic Results

Similar to epoxy, tension and shear tests were run for the pristine and covalently functionalized SWNT-epoxy composite systems to obtain the full stiffness matrices. Both nanocomposite systems were found to be transversely isotropic and the properties of the pristine SWNT-epoxy system and the covalently functionalized SWNT-epoxy systems are seen in Table 2.2 and Table 2.3, respectively. As expected, both systems see dramatically increased stiffness in the nanotube direction E_{zz}, demonstrated in Fig. 2.18a due to the inclusion of the nanotube. By comparing the properties of the covalently functionalized SWNT-epoxy composite to that of the pristine SWNT-epoxy composite, it is seen that the functionalized nanocomposite becomes much more stiff in the direction transverse to the nanotubes (E_{xx}), demonstrated in Fig. 2.18b, and highlighted in Fig. 2.19. It can be readily seen here that the directions transverse to the nanotube show substantial improvement due to functionalization (40% at 1 K), where the pristine nanotube system only sees minor improvements in transverse stiffness due to van der Waals effects (7% at 1 K) over neat epoxy [24]. It is worth noting that functionalization causes sp^3 hybridization carbon sites on the sidewalls of the nanotube, and this lowers the stiffness of the composite system along the nanotube (E_{zz}), as seen in Tables 2.2 and 2.3. It has been shown theoretically, however, that even a high degree of functionalization on the sidewall of the SWNT will only decrease the me-

chanical strength by 15% [123]. There are negligible differences in the in-plane Poisson's ratio (υ_{xy}) between the functionalized and non-functionalized systems. There is a clear reduction in the out of plane Poisson's ratio (ν_{zx}), meaning that there will be less contraction in the plane of isotropy (x-y) when the system is pulled along the nanotube direction (z) due to the nanotube functionalization. Finally, the shear modulus in the z-direction, (G_{xz}) has noticeably increased due to the covalent bonding to the SWNT. The mechanical properties of discontinuous nanotubes was also studied, and the results are shown in Section 2.5.6

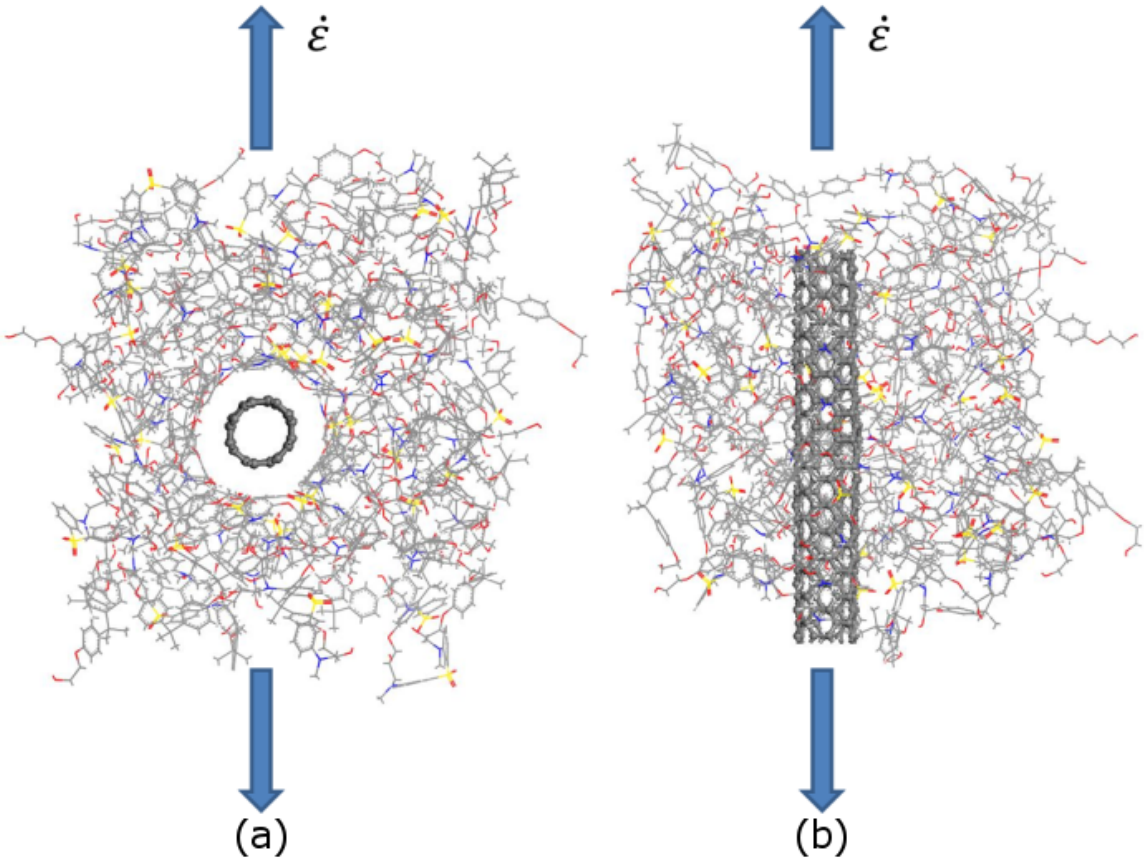

Figure 2.18: Tension tests in the a. z-direction, along the nanotube direction and b. plane of isotropy (x-y) perpendicular the nanotube direction.

Temperature (K)	$E_{xx}(GPa)$	$E_{zz}(GPa)$	ν_{xy}	ν_{zx}	$G_{xz}(GPa)$
1	7.2	72	0.49	0.32	2.4
50	6.2	71	0.52	0.32	2.1
100	5.9	70	0.54	0.36	2.0
150	5.1	70	0.55	0.36	1.7
200	4.7	69	0.59	0.37	1.5
250	3.7	68	0.67	0.40	1.3
300	2.7	68	0.75	0.43	.87
350	2.0	67	0.75	0.45	.77

Table 2.2: Material properties: pristine SWNT-epoxy composite.

Temperature (K)	$E_{xx}(GPa)$	$E_{zz}(GPa)$	ν_{xy}	ν_{zx}	$G_{xz}(GPa)$
1	9.4	70	0.49	0.30	3.3
50	8.7	69	0.50	0.30	2.9
100	8.0	69	0.54	0.31	2.8
150	6.6	68	0.54	0.31	2.5
200	6.0	67	0.57	0.32	2.2
250	4.9	66	0.58	0.35	1.8
300	4.0	66	0.63	0.38	1.6
350	3.0	65	0.67	0.38	.86

Table 2.3: Material properties: covalently functionalized SWNT-epoxy composite.

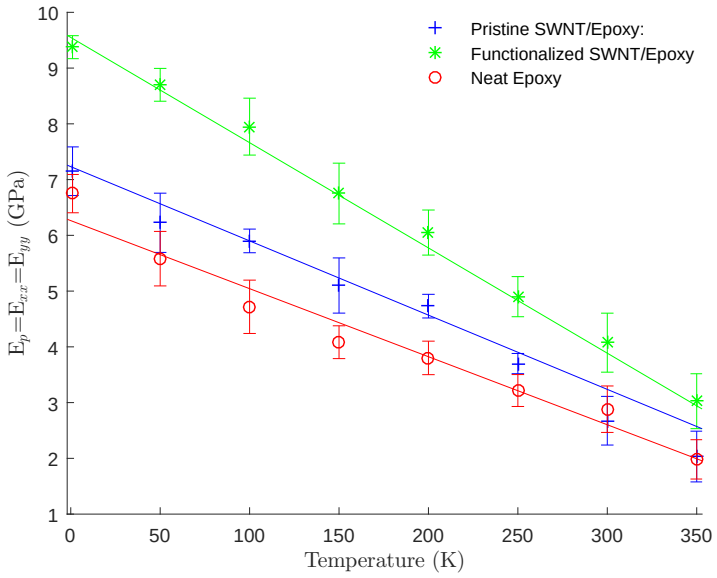

Figure 2.19: Elastic modulus in the plane of isotropy for the composite systems and neat epoxy (fully isotropic).

A tension test in the plane of isotropy (x-y), where each atoms was colored by its per-atom stress at various strain levels, is shown for the covalently functionalized SWNT-epoxy nanocomposites in Fig. 2.20a, and for the pristine SWNT-epoxy nanocomposite in Fig. 2.20b. MD results are statistical, and so the stress evolution of an individual atom is meaningless. However, when considering the stresses of every atom in the system at lower strain levels, the high stress (red) and low stress (blue) atoms tend to cancel, where at higher strain levels there are less low stress (blue) atoms. When averaging over all of the atoms and accounting for the volume, the average stress increases linearly with increasing strain. Fig. 2.20a shows that at higher strains, the atoms bonding the epoxy to the nanotube experience higher average stresses, demonstrating that stress is being transferred to the nanotube, leading to the higher stiffness levels seen in Fig. 2.19 when comparing the covalently functionalized SWNT-epoxy nanocomposite to the pristine SWNT-epoxy nanocomposite.

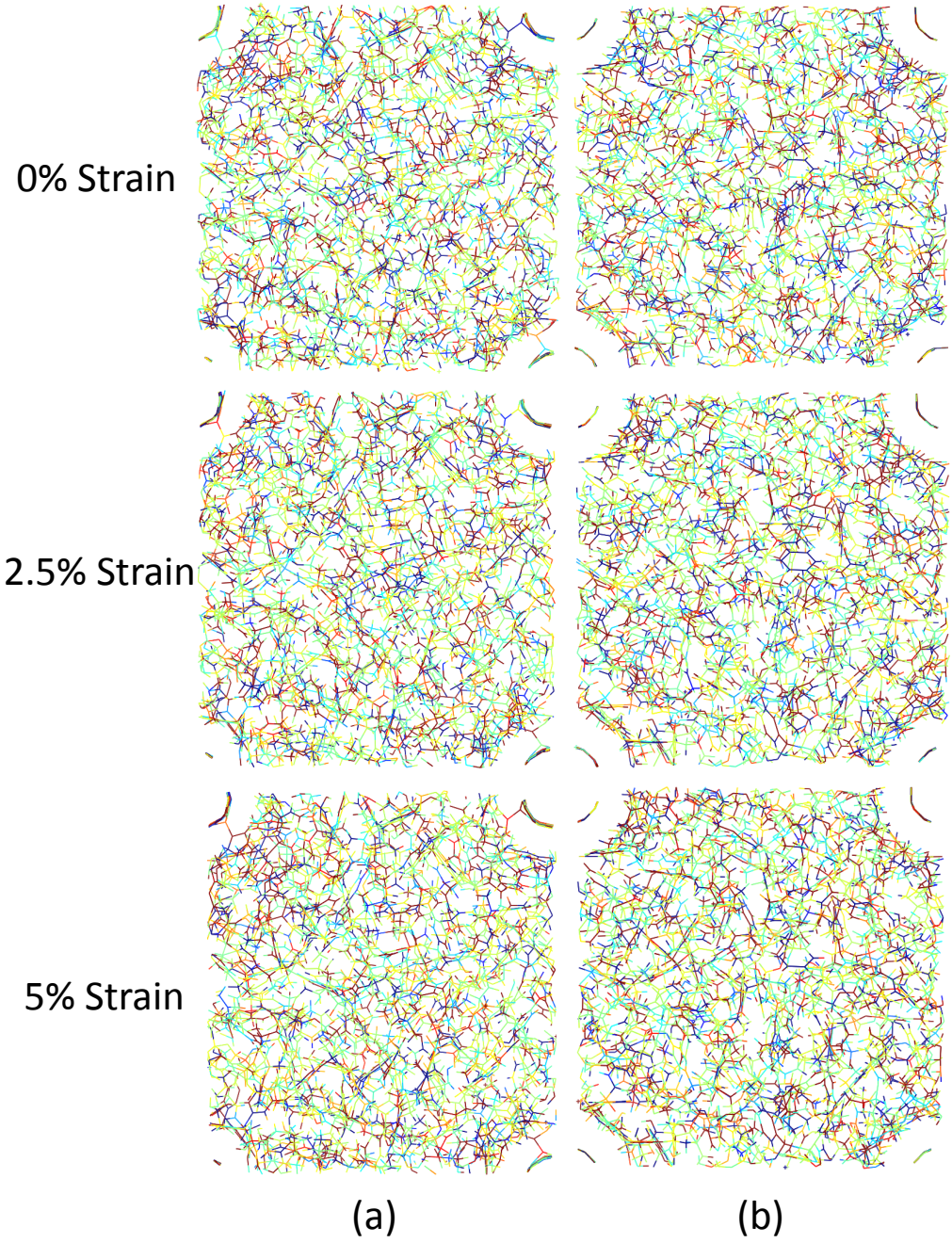

Figure 2.20: Atoms colored by high stress (red) and low stress (blue) at various strain levels for the a. covalently functionalized SWNT-epoxy nanocomposite and b. pristine SWNT-epoxy nanocomposite.

2.5.2 Thermal Expansion Results

The thermal expansion vectors were found via MD for the SWNT-epoxy composite systems. The thermal expansion in the plane of isotropy (x-y) and nanotube (z) directions for the SWNT-epoxy composite with pristine nanotubes are shown in Fig. 2.21. Since the structure is transversely isotropic, the results in the x and y directions are identical and the linear CTE was measured to be 55.3 $\pm$ 5.1 $\mu/^oC$, which approximately the CTE of neat epoxy. This result is expected since there was no functionalization to the nanotube, so the epoxy is free to expand in the x-y plane. The expansion in the z-direction was found to be 6.9 $\pm$ 1.4 $\mu/^oC$, where the thermal expansion was constrained by the nanotube, which has a longitudinal coefficient of thermal expansion of -1.2 $\mu/^oC$ [124]. For the covalently functionalized SWNT-epoxy composite, the thermal expansion in the plane of isotropy (x-y) and nanotube (z) directions can be seen in Fig. 2.22. There is a negligible effect of the covalent bonding for thermal expansion in the x-y plane. However, even with only four covalent bonds, the thermal expansion was reduced to 4.3 $\pm$ 1.2 $\mu/^oC$ in the nanotube direction. This represents a 42% reduction when compared to the pristine SWNT-epoxy composite.

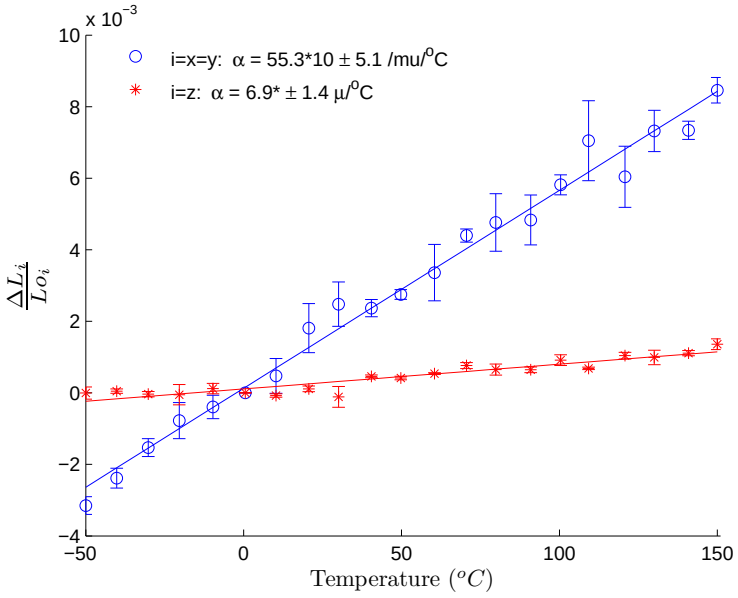

Figure 2.21: Thermal expansion for pristine SWNT-epoxy nanocomposites along the SWNT (z-direction) and transverse to the nanotube (x-y plane).

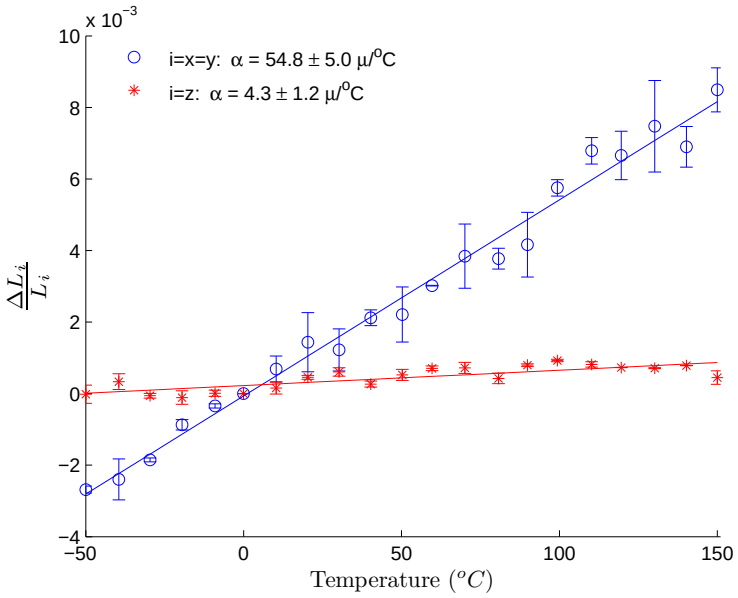

Figure 2.22: The thermal expansion for the covalently functionalized SWNT-epoxy nanocomposites along the SWNT (z-direction) and transverse to the nanotube (x-y plane).

2.5.3 Equivalent Isotropic System

To create an isotropic composite epoxy system, the effects of randomly oriented nanotubes in the epoxy were explored. To achieve this, the stiffness tensor and thermal expansion vector were rotated and averaged over all possible orientations using the ODF model, which will be discussed in detail in Section 4.2.1. The resulting system was isotropic and so can be compared with epoxy, done for the Young's modulus in Fig. 2.23, shear modulus Fig. 2.24, and the linear CTE in Fig. 2.25. Adding randomly oriented nanotubes results in a very large increase in the elastic modulus for both the functionalized nanotube epoxy composite (200% increase at 1 K) and pristine nanotube epoxy composite (180% increase at 1 K) when compared to neat epoxy. The coefficients of thermal expansion were seen to be reduced by 30% to 39.3 $\pm$ 2.0 $\mu/^oC$ for the pristine SWNT-epoxy composite system and 32% to 37.2 $\pm$ 1.4 $\mu/^oC$ for the covalently functionalized SWNT-epoxy composite system.

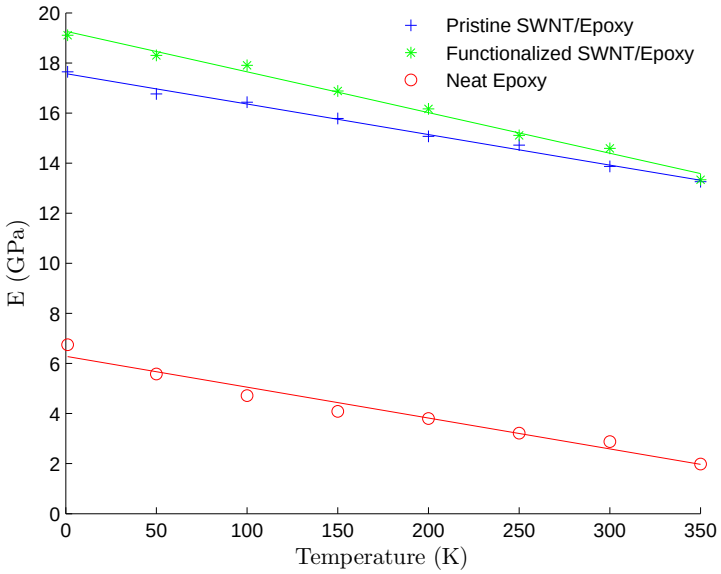

Figure 2.23: Young's modulus for an isotropic, pristine SWNT-epoxy composite, an isotropic, functionalized SWNT-epoxy composite and neat epoxy.

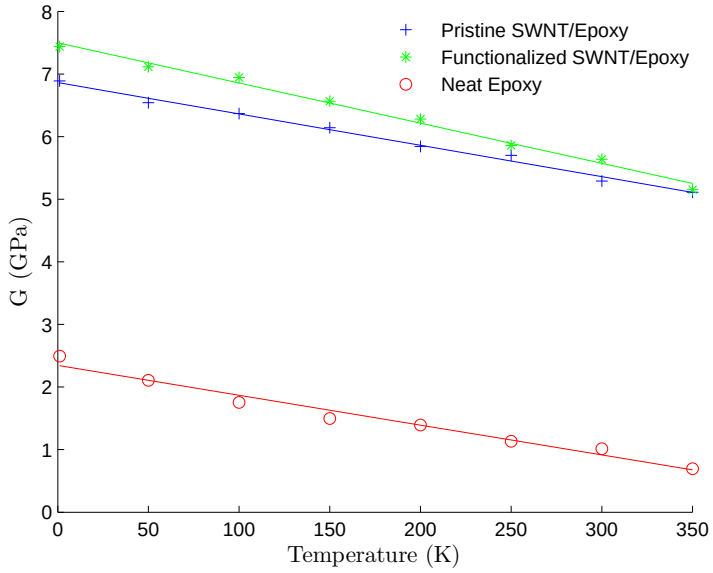

Figure 2.24: Shear modulus for an isotropic, pristine SWNT-epoxy composite, an isotropic, functionalized SWNT-epoxy composite and neat epoxy.

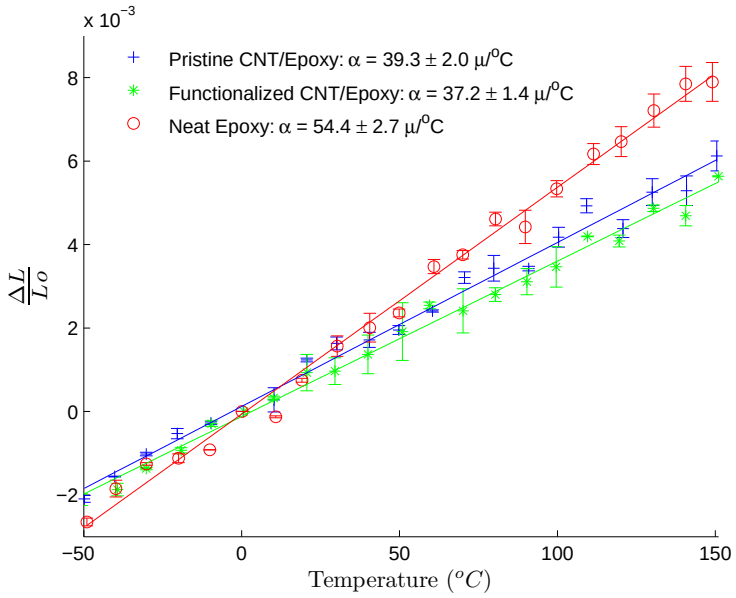

Figure 2.25: Thermal expansion for an isotropic, pristine WWNT/epoxy composite, an isotropic, functionalized SWNT-epoxy composite and neat epoxy.

2.5.4 Error

For all of the MD results shown in this Chapter, three different equilibrated structures were averaged, and properties for each structure were averaged across multiple time steps. This leads to two different types of uncertainty due to averaging: time step averaging and sample-to-sample averaging. For the thermal expansion results, the variances for both sources of error are summed and the resulting standard deviations lead to the range of values reported. For the transversely isotropic thermal expansion in Figs. 2.21 and 2.22, the cell length in the plane of isotropy and nanotube directions were used to calculate the linear coefficient of thermal expansion. For the thermal expansion of the equivalent isotropic systems, seen in Fig. 2.25, volume data was used to calculate the linear coefficient of thermal expansion. This leads to a smaller standard division than if the individual cell lengths were multiplied and their variances combined. The magnitude of the standard deviations show that the cumulative effects of the error due to averaging is small.

2.5.5 Experimental Comparison

Experimentally, it has been found that covalent functionalization of the SWNT to the epoxy will increase the tensile modulus when compared to neat epoxy [17, 18]. Pristine nanotube and epoxy composite systems show a lesser improvement in mechanical properties

than functionalized nanotubes due a lack of interfacial bonding across atomically smooth carbon nanotube surfaces [12–14] Functionalization allows the load to be transferred to the nanotube from the polymer matrix and prevent slipping between the nanotube and the polymer [125]. It is important to note that the MD results shown here thus far represent a material with a very high weight percentage of nanotubes (8 wt% SWNT) with perfectly dispersed, continuous nanotubes due to periodic boundary conditions. Multiscale modeling will be used in Chapters 4 and 5 to reduce the wt%, or volume fraction of the SWNTs, and discontinuous nanotubes will be investigated in Section 2.5.6. Studies have shown that an increasingly large wt % of nanotubes continues to increases the modulus of polymer/SWNT composites [13, 20, 70]. In particular, Zhu et. al saw a $\sim$30% increase with 1 wt% functionalized SWNT in a EPON 862 and Curing Agent W system, and a $\sim$70% increase with 4 wt% SWNT [13]. Wang et. al showed an increase of 60% in the modulus with just a 1 wt% nanotubes that are covalently functionalized [16]. It has been shown at very high loading of non-covalently functionalized SWNTs, 20.5 wt% and 39.1 wt%, tensile modulus increases by 166% and 408% respectively [38].

Pizzutto et.al. measured the thermal dilatation of .25 wt% carboxylated single-walled carbon nanotubes without covalent functionalization. In the linear region of 25^o C to 65^o C, the linear CTE was measured to be 62 $\mu/^oC$ for the neat epoxy, and 44 $\mu/^oC$ for the SWNT-epoxy composite [37]. Adding in the SWNTs reduced the linear CTE by 29%. For the MD simulation of the pristine SWNT-epoxy system, as seen in Fig. 2.25, the linear coefficient of thermal expansion has decreased from 55.2 $\mu/^oC$ for the neat epoxy to 39.1 $\mu/^oC$, a similar reduction of 30%. Wang et al. studied functionalized SWNT-epoxy composites, and in the linear region of 50^o C to 120^o C, saw reduction in thermal expansion from 60 $\mu/^oC$ for pure epoxy to 40 $\mu/^oC$ for oxidated SWNTs with covalent functionalization, a reduction of 33% [35]. This is very similar to the 32% reduction seen for the functionalized SWNT-epoxy composite in this study. A summary of experimental comparisons to the MD results for thermal dilatation is shown in Fig. 2.26.

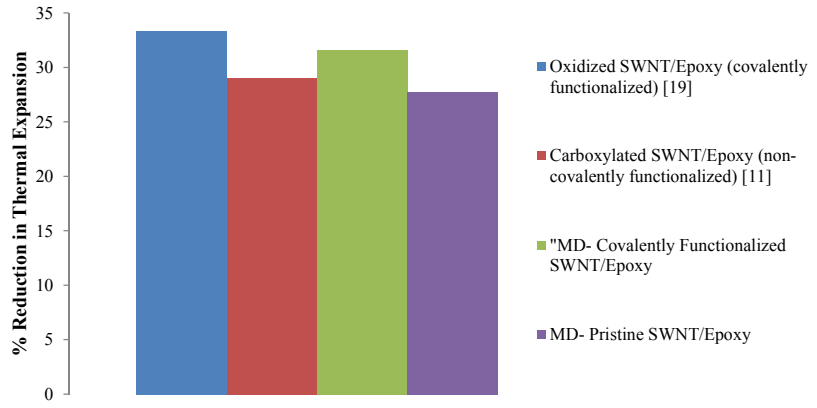

Figure 2.26: Percent reduction in linear coefficient of thermal expansion due to the addition of nanotubes to epoxy [35, 37]

2.5.6 Discontinuous SWNTs

When the SWNT spans the entire simulation cell, the use of periodic boundary conditions leads to the creation of an essentially infinite nanotube, which is shown in Fig. 2.27a, where two periodic cells are shown in the y and z directions. Realistically, the ends of the nanotubes interact with the epoxy, and for this reason, nanotubes that do not span the entire cell were also created using this same method, and the equilibrated structure in Fig. 2.27b shows epoxy filling in the space between the periodic nanotubes. The elastic properties of a few different discontinuous systems were studied. The nanotube that spans the entire simulation cell contained 15 'repeat units', so nanotubes with only 11 and 13 'repeat units' were investigated. Pristine and functionalized SWNTs were investigated, and the resulting transversely isotropic properties can be seen in Tables 2.4-2.7. It is clear from these results that the reduction of the nanotube length leads to a massive reduction in stiffness along the SWNT axis (z-direction). The effects of discontinous nanotubes on the elastic properties will be further studied in Chapters 4 and 5.

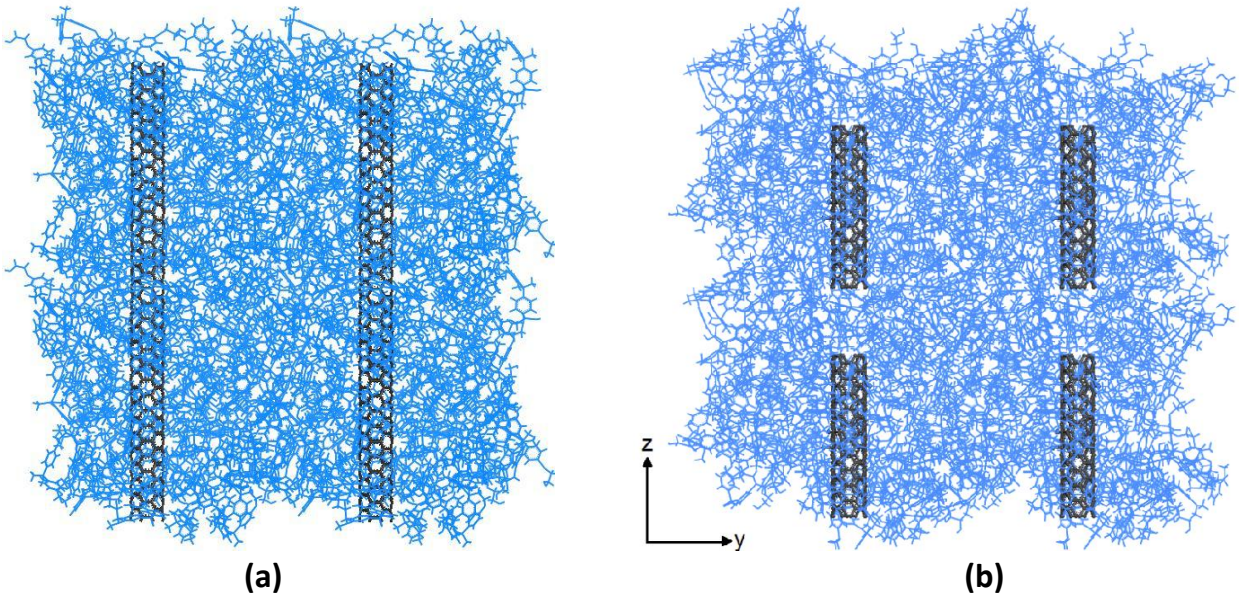

Figure 2.27: Two periodic cells are shown in the z-direction and y-direction to show nanotube spacing for a. SWNTs that span the entire cell that effectively become infinite and b. discontinuous SWNTs that span 11/15 of the cell.

Temperature (K)	$E_{xx}(GPa)$	$E_{zz}(GPa)$	ν_{xy}	ν_{zx}	$G_{xz}(GPa)$
1	6.8	8.2	0.38	0.33	3.1
50	6.2	7.3	0.40	0.34	2.7
100	5.8	6.3	0.39	0.35	2.6
150	5.9	6.0	0.39	0.35	2.2
200	5.0	5.8	0.40	0.36	2.0
250	4.5	4.5	0.40	0.39	1.6
300	3.8	4.5	0.42	0.40	1.4
350	3.4	3.1	0.41	0.40	1.2

Table 2.4: Material properties: pristine SWNT-epoxy composite, 11 repeat units.

Temperature (K)	$E_{xx}(GPa)$	$E_{zz}(GPa)$	ν_{xy}	ν_{zx}	$G_{xz}(GPa)$
1	6.7	8.2	0.37	0.33	3.1
50	6.1	7.3	0.41	0.35	2.6
100	5.8	6.4	0.41	0.36	2.5
150	5.3	6.1	0.40	0.34	2.2
200	4.8	5.7	0.41	0.36	2.0
250	4.5	4.7	0.41	0.38	1.6
300	3.8	4.2	0.47	0.39	1.4
350	3.3	3.5	0.48	0.37	1.3

Table 2.5: Material properties: pristine SWNT-epoxy composite, 13 repeat units.

Temperature (K)	$E_{xx}(GPa)$	$E_{zz}(GPa)$	ν_{xy}	ν_{zx}	$G_{xz}(GPa)$
1	8.1	7.5	0.30	0.34	3.3
50	7.0	6.6	0.35	0.34	3.0
100	6.5	6.3	0.32	0.35	2.8
150	5.4	5.8	0.33	0.35	2.6
200	5.0	4.8	0.35	0.37	2.4
250	4.5	4.1	0.38	0.36	2.0
300	3.7	3.7	0.41	0.38	1.6
350	3.4	3.2	0.41	0.36	1.4

Table 2.6: Material properties: functionalized SWNT-epoxy composite, 11 repeat units.

Temperature (K)	$E_{xx}(GPa)$	$E_{zz}(GPa)$	ν_{xy}	ν_{zx}	$G_{xz}(GPa)$
1	8.2	8.0	0.31	0.35	3.5
50	7.4	7.5	0.32	0.37	3.2
100	7.0	6.7	0.32	0.35	2.8
150	6.1	5.8	0.35	0.35	2.5
200	5.0	5.4	0.36	0.34	2.2
250	4.5	5.3	0.35	0.36	1.9
300	3.8	4.5	0.36	0.36	1.6
350	3.4	4.0	0.38	0.34	1.4

Table 2.7: Material properties: functionalized SWNT-epoxy composite, 13 repeat units.

2.6 Conclusions

Molecular Dynamics was used to analyze the thermal and mechanical properties of SWNT-epoxy nanocomposites created by adding functionalized and pristine carbon nanotubes to epoxy. The epoxy model was built using a 'dendrimeric' growth approach, which was verified by obtaining the correct density, showing the system to be isotropic, and by comparing the thermal expansion to experiments. The change in the mechanical and thermal expansion properties was studied along and perpendicular to the nanotube for both epoxy/SWNT nanocomposites, and the full stiffness matrices and thermal expansion vectors were obtained. As expected, there was a large increase in stiffness along the nanotube direction for both the pristine SWNT-epoxy and functionalized SWNT-epoxy composites. The direction transverse to the nanotube saw a 40% increase in stiffness due to covalent functionalization over neat epoxy at 1 K whereas the pristine nanotube system only saw a 7% increase due to van der Waals effects. The thermal expansion along the nanotube was significantly decreased due to the negative coefficient of thermal expansion of a SWNT. An additional 42% reduction in thermal expansion in the direction of the nanotube was realized for the covanently functionalized SWNT-epoxy composite when compared to the pristine SWNT-epoxy composite. The thermal expansion transverse to the nanotube showed negligible change compared to the neat epoxy for both nanocomposite systems. The stiffness matrices and thermal expansion vectors were rotated over every possible configuration to simulate the effects of an isotropic system consisting of randomly oriented nanotubes in the epoxy. The equivalently isotropic nanocomposite systems showed substantial improvements over

the neat epoxy in terms of higher stiffness (200% for the covalently functionalized SWNT-epoxy composite) and lower thermal expansion (32% reduction for the covalently functionalized SWNT-epoxy composite). The reduction in thermal expansion was verified by comparison with experiments.

CHAPTER 3

Thermal Conductivity

Despite their wide use in aerospace grade materials, epoxies are generally limited to low temperature applications, and this is in part due to their low thermal conductivity of $\sim$.24 W/mK at room temperature [10]. It is of great interest to improve the heat conduction in epoxies in order to remove excess heat, and boost reliability and performance. Carbon nanotubes (CNTs) have very high thermal conductivity, with single wall carbon nanotubes (SWNTs) having a thermal conductivity of 1750-5800 W/mK [8, 11] and high aspect ratios. For this reason, SWNTs were investigated as an additive to improve the thermal conductivity of the epoxy via the formation of functionalized and pristine SWNT/polymer nanocomposites. Inefficient phonon transport between nanotubes at discontinuities (i.e. the nanotube ends) is an important factor in the thermal conductivity of SWNT-epoxy nanocomposites. For this reason, the discontinuous nanotubes outlined in Section 2.5.6 are studied in addition to long SWNTs. The Green-Kubo integral of the heat flux autocorrelation function was used via MD to model the full 3D thermal conductivity of SWNT-epoxy nanocomposites.

3.1 Materials

The same epoxy and amine system described in Section 2.2 was used in this chapter; diglycidyl ether of bisphenol A (DGEBA) crosslinked with curing agent 3-3' diamino diphenyl sulfone (DDS). The 'dendrimer' growth approach was used to build the epoxy network in Materials Studio shown previously in Fig. 2.7. The network contained 36 amine groups and 71 epoxy groups, leading to a total of 4601 atoms. In Section 2.4, the system was shown to be sufficiently complex to accurately capture the amorphous nature of the polymer by matching the dilatometric curve to experimental results, matching the experimental glass transition temperature, verifying the structure was isotropic by generating the full elastic stiffness matrix, and obtaining the proper density. All simulations in

this Chapter are performed under periodic boundary conditions, and the Consistent Valence Force Field (CVFF) [115] potential was used for bonded and non-bonded interactions in LAMMPS [116]. CVFF has been used in previous studies to accurately predict thermodynamic properties of epoxy [59, 60]. 75% of available epoxy sites were crosslinked, which is realistic for many structural epoxies.

The structure was equilibrated via a sequence of energy minimization and annealing. The dendrimer structure was optimized by minimizing the energy via conjugate gradient (CG) minimization for 10000 iterations. Next, MD was used to anneal the structure using an NPT ensemble. Dynamics was first performed well above glass transition temperature (600 K and 1 atm) for 500 ps. Next, dynamics was run well below T_g (1 K and 1 atm) for 500 ps, followed by CG. After ten cycles, the density converged to within 0.5% across consecutive annealing steps. A density of 1.17 g/cc at 1 atm and 1 K was obtained after convergence. SWNT-epoxy nanocomposites were built by creating a vacancy in the epoxy by radially moving atoms outward and inserting a SWNT (4,4) into the space. Moving atoms caused bonds to displaced from their equilibrated length, so it was necessary to equilibrate the structure via the same annealing process ran previously via a sequence of CG minimization and dynamics above and below T_g.

Functionalization of the SWNT-epoxy composites was achieved by creating a covalent bond between the SWNT and the amine. The DDS molecule contains two amine groups, one of which was bonded to the SWNT. As seen previously Fig. 2.12, the nanotube is attached to the DDS, and the functional sites bond with the epoxide. Functional sites that were previously unreacted were chosen to bond to the SWNT, so this method of functionalization did not effect the epoxy's degree of crosslinking. Again, bonds were displaced from their equilibrium length so equilibration was performed via a sequence of the conjugate gradient (CG) minimization and annealing until the density was seen to converge. The functionalized system contains four covalent bonds, and the equilibrated structure was seen previously in Fig. 2.13. When the nanotube spans the entire cell, the use of periodic boundary conditions leads to the creation of an infinite nanotube, shown in previously in Fig. 2.27a, where two periodic cells are shown in the y and z directions. Realistically, nanotubes are not infinite and so end effects are important. For this reason, nanotubes that do not span the entire cell were also created using this same method, and the equilibrated structure in Fig. 2.27b shows epoxy filling in the space between the periodic nanotubes.

3.2 Green-Kubo Method for Predicting Thermal Conductivity

The Green-Kubo method is an equilibrium MD approach that calculates the thermal conductivity (K) from the fluctuations of the heat current along a direction, J_x, via the fluctuation-dissipation theorem [61, 126]. The thermal conductivity is given by:

$$K = \frac{V}{k_B T^2} \int_0^\infty \langle J_x(t) J_x(0) \rangle dt, \tag{3.1}$$

where V and T are the volume and temperature of the system respectively, and k_B is the Boltzmann constant. $\langle J_x(t) J_x(0) \rangle$ is the heat current auto correlation function (HCACF).

For an isotropic material, a scalar conductivity is obtained by averaging across all three directions. For neat epoxy in the present study, the following formula is employed where the factor of three in the denominator arises due to the averaging across the x, y, and z directions:

$$K = \frac{V}{3k_B T^2} \int_0^{t_c} \langle \boldsymbol{J}(t) \boldsymbol{J}(0) \rangle_{t_s} dt. \tag{3.2}$$

In the above expression, $\boldsymbol{J}$ is the heat current vector, t_c stands for the finite correlation time over which the integration is carried out, and t_s is the sampling time for which the ensemble average for computing HCACF is accumulated. Since the nanocomposite systems are not isotropic, it is not possible to average over all three directions and so the thermal conductivity is calculated for each direction individually.

The heat current vector is defined in a number of different ways [127]. It is most commonly defined as:

$$\boldsymbol{J} = \frac{1}{V} \frac{d}{dt} \sum_{i=1}^{N} \boldsymbol{r}^i e^i, \tag{3.3}$$

where, $\boldsymbol{r}^i$ and e^i are the position vector and total energy of atom i, respectively. The summation is done over the total number of atoms in the system, N. The energy of atom i, e^i, is obtained by summing the potential energy (PE) and kinetic energy (KE):

$$e^i = \frac{1}{2} m^i \|\boldsymbol{v}^i\|^2 + U^i, \tag{3.4}$$

where m^i and $\boldsymbol{v}^i$ are the mass and velocity of atom i, respectively. U^i is the potential energy of atom i. It is dependent on the form of interaction potential (including bonded and non-bonded interactions) used in the simulations. In the CVFF potential, the total

energy is computed as a sum of pair interactions (U_{pair}), Coulombic interactions ($U_{coulomb}$), energies that accounts for changes in bond lengths (U_{bond}), bond angle (U_{angle}), dihedral angle ($U_{dihedral}$), and improper dihedral angle ($U_{improper}$) in the following form:

$$U = U_{pair} + U_{coulomb} + U_{bond} + U_{angle} + U_{dihedral} + U_{improper}. \tag{3.5}$$

The per-atom energy (U^i) is computed by averaging the energy contributions and distributing an equal portion to each the atom the interaction set. For example, a quarter of the dihedral energy is assigned to each of the four atoms in the dihedral term:

$$\begin{aligned} U^i = & \left[\frac{1}{2}\sum_{n=1}^{N_p} U_{pair}(\boldsymbol{r}^i, \boldsymbol{r}^2) + \frac{1}{2}\sum_{n=1}^{N_b} U_{bond}(\boldsymbol{r}^i, \boldsymbol{r}^2) + \frac{1}{3}\sum_{n=1}^{N_a} U_{angle}(\boldsymbol{r}^i, \boldsymbol{r}^2, \boldsymbol{r}^3)\right] \\ & + \left[\frac{1}{4}\sum_{n=1}^{N_d} U_{dihedral}(\boldsymbol{r}^i, \boldsymbol{r}^2, \boldsymbol{r}^3, \boldsymbol{r}^4) + \frac{1}{4}\sum_{n=1}^{N_i} U_{improper}(\boldsymbol{r}^i, \boldsymbol{r}^2, \boldsymbol{r}^3, \boldsymbol{r}^4 + \frac{1}{2}\sum_{n=1}^{N_c} U_{coulomb}(\boldsymbol{r}^i, \boldsymbol{r}^2)\right]. \end{aligned} \tag{3.6}$$

The first term in the above expression is the pairwise energy contribution, where n goes over the N_p atoms neighboring atom i, and $\boldsymbol{r}^i$ and $\boldsymbol{r}^2$ are the positions the two atoms in the pairwise interaction. The second term is a bond contribution of similar form for the N_b bonds containing atom i. The third, fourth, and fifth terms are expressions for the N_a angle, N_d dihedral, and N_i improper interactions, respectively, that atom i is part of. The sixth term, $U_{coulomb}$, is the contribution from long-range Coulombic interactions and are handled differently using the standard or PPPM Ewald methods described in the next section.

Substituting Eq. 3.4 in Eq. 3.3 and differentiating with respect to time, the microscopic heat current vector $\boldsymbol{J}$ is obtained as:

$$\boldsymbol{J}(t) = \frac{1}{V}\sum_{i=1}^{N} \boldsymbol{v}^i e^i + \sum_{i=1}^{N} \boldsymbol{S}^i.\boldsymbol{v}^i. \tag{3.7}$$

The first term is the diffusive part of the heat current which is caused by motion of atoms. The second term is the interaction part of the heat current which represents the transfer of energies due to interatomic interactions, where $\boldsymbol{S}^i$ is the per atom stress tensor. For the CVFF potential, $\boldsymbol{S}^i$ is given by the following expression, where a and b iterate over the values x, y , and z to generate the 6 components of the symmetric tensor:

$$
\begin{aligned}
V\boldsymbol{S}^i_{ab} = &\left[\frac{1}{2}\sum_{n=1}^{N_p}(\boldsymbol{r}^i_a\boldsymbol{F}^i_b + \boldsymbol{r}^2_a\boldsymbol{F}^2_b) + \frac{1}{2}\sum_{n=1}^{N_c}(\boldsymbol{r}^i_a\boldsymbol{F}^i_b + \boldsymbol{r}^2_a\boldsymbol{F}^2_b) + \frac{1}{2}\sum_{n=1}^{N_b}(\boldsymbol{r}^i_a\boldsymbol{F}^i_b + \boldsymbol{r}^2_a\boldsymbol{F}^2_b)\right] \\
&+ \left[\frac{1}{3}\sum_{n=1}^{N_a}(\boldsymbol{r}^i_a\boldsymbol{F}^i_b + \boldsymbol{r}^2_a\boldsymbol{F}^2_b + \boldsymbol{r}^3_a\boldsymbol{F}^3_b) + \frac{1}{4}\sum_{n=1}^{N_d}(\boldsymbol{r}^i_a\boldsymbol{F}^i_b + \boldsymbol{r}^2_a\boldsymbol{F}^2_b + \boldsymbol{r}^3_a\boldsymbol{F}^3_b + \boldsymbol{r}^4_a\boldsymbol{F}^4_b)\right] \\
&+ \left[\frac{1}{4}\sum_{n=1}^{N_i}(\boldsymbol{r}^i_a\boldsymbol{F}^i_b + \boldsymbol{r}^2_a\boldsymbol{F}^2_b + \boldsymbol{r}^3_a\boldsymbol{F}^3_b + \boldsymbol{r}^4_a\boldsymbol{F}^4_b)\right]. \qquad (3.8)
\end{aligned}
$$

In the first three terms, $\boldsymbol{F}^i$ and $\boldsymbol{F}^2$ are the forces resulting from two atoms interacting. Similarly, there are forces due to the angle, dihedral, and improper interactions of atom i. The above stress tensor contains only the virial terms and does not include the kinetic energy contribution.

3.2.1 Computation of Long Range Coulombic Interactions

In crosslinked polymers, there are long range interatomic interactions due to electrostatic forces between partial charges on atoms. In this case, the energy contribution per atom required for the computation of the heat current vector is more conveniently calculated on a periodic domain using the standard or mesh-based PPPM Ewald methods. In these methods, a 'real-space' component of electrostatic energy is computed within a small cut–off distance, beyond which the slow decay is modeled using the 'k-space' or 'reciprocal' part, which decays with the inverse distance. The Ewald expression for potential energy $U_{coulomb}$ and its contribution to the stress tensor are computed in this section. In the Ewald approach, the electrostatic potential energy of a neutral distribution of N atoms with point charges q_i can be written as [128]:

$$
\begin{aligned}
4\pi\epsilon_0 U_{coulomb} &= \frac{1}{2}\sum_{i=1}^{N}\sum_{\substack{j=1\\ j\neq i}}^{N}\frac{q_i q_j}{r_{ij}} \\
&= \frac{1}{2}\sum_{i=1}^{N}\sum_{\substack{j=1\\ j\neq i}}^{N}\frac{q_i q_j}{r_{ij}}\,\mathrm{erfc}(\kappa r_{ij}) + \frac{2\pi}{V}\sum_{k\neq 0}\frac{exp(k^2/4\kappa^2)}{k^2}\sum_{i=1}^{N}\sum_{\substack{j=1\\ j\neq i}}^{N} q_i q_j \exp(i\boldsymbol{k}.\boldsymbol{r}_{ij}).
\end{aligned} \qquad (3.9)
$$

In Eq. 3.9, ϵ_0 is the electric permittivity of free space, and $r_{ij} = |\boldsymbol{r}_j - \boldsymbol{r}_i|$ is the distance between charges i and j. The complimentary error function of the distance, $\mathrm{erfc}(\kappa r_{ij})$

is multiplied by a convergence factor κ, and the second term on the right-hand side is the Fourier expansion of the difference between the first term and the full electrostatic potential energy. The Fourier expansion in terms of wave vectors $k_\alpha = \frac{2\pi n_\alpha}{L}$ (α = x,y,z) is used where L is the periodic box size. The k-space part of the electrostatic potential energy and the stress tensor, in addition to a sum over wave vectors $\boldsymbol{k}$, contains double sums over all pairs of atoms i, j; $i \neq j$. Observing that $\boldsymbol{r}_{ij} = \boldsymbol{r}_j - \boldsymbol{r}_i$, this double sum can be written as a single sum over N charges which speeds up the computation N-fold [129]:

$$\sum_{i=1}^{N}\sum_{\substack{j=1\\ j\neq i}}^{N} q_i q_j \exp(i\boldsymbol{k}.\boldsymbol{r}_{ij}) = \sum_{i=1}^{N} q_i \exp(i\boldsymbol{k}.\boldsymbol{r}_i)\sum_{j=1}^{N} q_j \exp(-i\boldsymbol{k}.\boldsymbol{r}_j) - \sum_{i=1}^{N}(q_i)^2$$

$$= \Theta(\boldsymbol{k})\Theta(-\boldsymbol{k}) - \sum_{i=1}^{N}(q_i)^2. \tag{3.10}$$

Here, $S(\boldsymbol{k})$ is the structure factor given as $\Theta(\boldsymbol{k}) = \sum_{i=1}^{N} q_i \exp(i\boldsymbol{k}.\boldsymbol{r}_i)$. The sum of the squared charges is subtracted because the first term on the right-hand side contains the self–interaction term with $i = j$. With the use of the transformation Eq. 3.10, the expression for the electrostatic potential energy is:

$$4\pi\epsilon_0 U_{coulomb} = \frac{1}{2}\sum_{i=1}^{N}\sum_{\substack{j=1\\ j\neq i}}^{N}\frac{q_i q_j}{r_{ij}}\operatorname{erfc}(\kappa r_{ij}) - \frac{\kappa}{\pi^{1/2}}\sum_{i=1}^{N}(q_i)^2 + \frac{2\pi}{V}\sum_{k\neq 0}\frac{\exp(k^2/4\kappa^2)}{k^2}\Theta(\boldsymbol{k})\Theta(-\boldsymbol{k}). \tag{3.11}$$

The subtracted term $(\frac{\kappa}{\pi^{1/2}})\sum_{i=1}^{N}(q_i)^2$, corresponding to i=j, is the contribution due to self-interaction. The per atom version of the potential energy contribution is calculated using a per atom structure factor $\Theta^i(\boldsymbol{k})$, defined as $\Theta^i(\boldsymbol{k}) = q_i \exp(i\boldsymbol{k}.\boldsymbol{r}_i)$, as follows:

$$4\pi\epsilon_0 (U^i)_{coulomb} = \frac{1}{2}\sum_{\substack{j=1\\ j\neq i}}^{N}\frac{q_i q_j}{r_{ij}}\operatorname{erfc}(\kappa r_{ij}) - \frac{\kappa}{\pi^{1/2}}(q_i)^2 + \frac{2\pi}{V}\sum_{k\neq 0}\frac{\exp(k^2/4\kappa^2)}{k^2}\Theta^i(\boldsymbol{k})\Theta(-\boldsymbol{k}). \tag{3.12}$$

The elements of the Coulombic part of the stress tensor are obtained by the differentiation of Eq. 3.11 with respect to components of $\boldsymbol{r}_{ij}$. The resulting electrostatic part of the stress tensor $(\boldsymbol{S}_{ab})_{coulomb}$ is given as follows, where a and b take on values x ,y, and z to generate

the 6 components of the symmetric tensor [130]:

$$
\begin{aligned}
4\pi\epsilon_0 V(\boldsymbol{S}_{ab})_{coulomb} &= \frac{1}{2}\sum_{i=1}^{N}\sum_{\substack{j=1\\ j\neq i}}^{N}\frac{q_i q_j}{r_{ij}^3} r_{ija} r_{ijb} \\
&= \frac{1}{2}\sum_{i=1}^{N}\sum_{\substack{j=1\\ j\neq i}}^{N} q_i q_j \left[\frac{\operatorname{erfc}(\kappa r_{ij})}{r_{ij}^3} + \frac{2\kappa}{\pi^{1/2}}\frac{\exp(-\kappa^2 r_{ij}^2)}{r_{ij}^2}\right] r_{ija} r_{ijb} \\
&+ \frac{2\pi}{V}\sum_{k\neq 0}\frac{\exp(k^2/4\kappa^2)}{k^2}\left[\delta_{ab} - 2\left(\frac{1}{k^2}+\frac{1}{4\kappa^2}\right)k_a k_b\right]\Theta(\boldsymbol{k})\Theta(-\boldsymbol{k}),
\end{aligned}
\tag{3.13}
$$

where $\delta_{\alpha\beta}$ is the Kronecker symbol. The per atom stress tensor is computed using the per atom structure factor as:

$$
\begin{aligned}
4\pi\epsilon_0 V(\boldsymbol{S}_{ab})^i_{coulomb} &= \frac{1}{2}\sum_{\substack{j=1\\ j\neq i}}^{N}\frac{q_i q_j}{r_{ij}^3} r_{ija} r_{ijb} \\
&= \frac{1}{2}\sum_{\substack{j=1\\ j\neq i}}^{N} q_i q_j \left[\frac{\operatorname{erfc}(\kappa r_{ij})}{r_{ij}^3} + \frac{2\kappa}{\pi^{1/2}}\frac{\exp(-\kappa^2 r_{ij}^2)}{r_{ij}^2}\right] r_{ija} r_{ijb} \\
&+ \frac{2\pi}{V}\sum_{k\neq 0}\frac{\exp(k^2/4\kappa^2)}{k^2}\left[\delta_{ab} - 2\left(\frac{1}{k^2}+\frac{1}{4\kappa^2}\right)k_a k_b\right]\Theta^i(\boldsymbol{k})\Theta(-\boldsymbol{k}).
\end{aligned}
\tag{3.14}
$$

The PPPM solver employs the same approach as the standard Ewald approach described above except that atomic charges are mapped to a 3D mesh and fast Fourier transforms (FFTs) are used to compute the structure factors, and is more accurate [131].

3.3 Results

3.3.1 Sampling and Correlation Times

A preliminary convergence study was done using a Lennard-Jones/Coulomb interaction cutoff of 12.5 Å to find the necessary sampling and correlation times. The structures were equilibrated at the temperature being studied for 0.5 ns, followed by further equilibration and collection of heat current data used for calculation of the autocorrelation function. A

correlation time of 8 ps was initially used, and the sampling interval was taken as the size of the time step (1 fs). Convergence of the HCACF at 298K and 1 atm for neat epoxy at various sampling times is shown in Fig. 3.1. Sampling times longer than 0.8 ns were carried out but showed no significant further convergence of the HCACF. Fig. 3.1b shows a zoomed in section of Fig. 3.1a, and here it can be seen that the variation in the HCACF is very small at 0.8 ns for neat epoxy. The effect of temperature on the HCACF convergence for a sampling time of 0.8 ns is shown in Fig. 3.2a. Even at higher temperatures, such as 423 K, good convergence of the HCACF was seen. Fig. 3.2b shows the convergence error for the HCACF by comparing the value at the current sampling time with the HCACF value at a sampling time of 0.1 ns. As the time step exceeds 0.8 ns, the error flattens out and the HCACF converges. Fig. 3.1 and Fig. 3.2 show that a correlation time of 8 ps and a sampling time of 0.8 ns are sufficient for convergence of the HCACF in the temperature range of interest for neat epoxy. For the pristine and functionalized SWNT-epoxy nanocomposites, a correlation time of 16 ps is used because the HCACF did not show sufficient convergence for a correlation time of 8 ps. Convergence of the HCACF for the pristine SWNT-epoxy nanocomposite and functionalized SWNT-epoxy nanocomposite are shown in Fig. 3.3 and Fig. 3.4, respectively. Here, sampling times of 0.032 ns to 1.6 ns are compared. Convergence is seen to occur by 1.6 ns in Fig. 3.3b and Fig. 3.4b for the pristine SWNT-epoxy nanocomposite and functionalized SWNT-epoxy nanocomposite, respectively. This convergence study allowed the necessary correlation and sampling times to be determined for the various systems investigated.

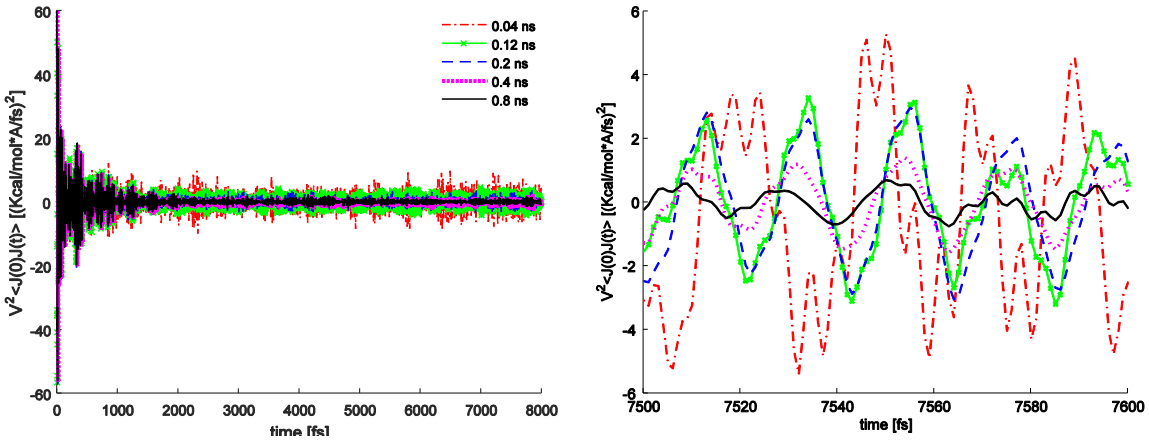

Figure 3.1: a. HCACF for neat epoxy at T = 298K, P = 1 atm at different sampling times. b. Zoomed HCACF for neat epoxy at T= 298K, P = 1 atm to show convergence

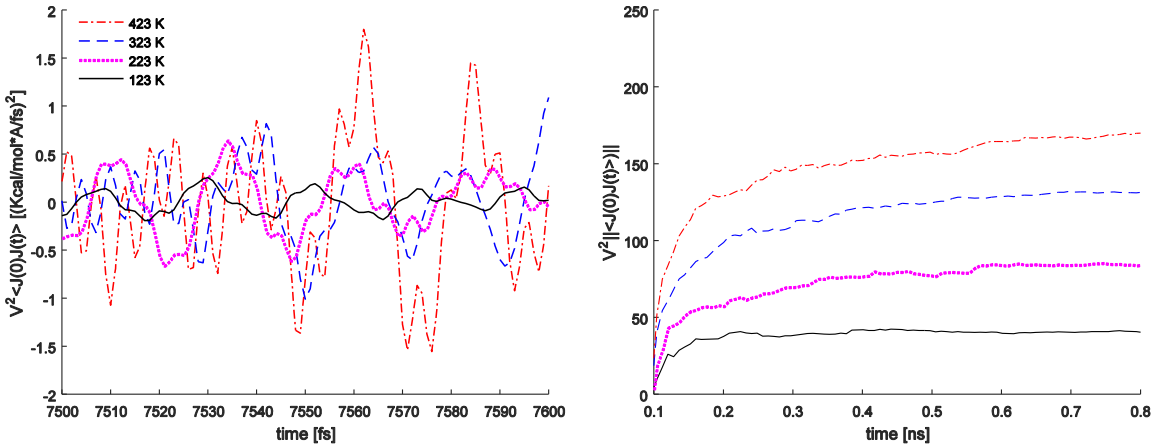

Figure 3.2: a. Zoomed in HCACF of neat epoxy for sampling time of 0.8 ns at various temperatures and P = 1 atm. b. Convergence of HCACF at various temperatures and P = 1 atm.

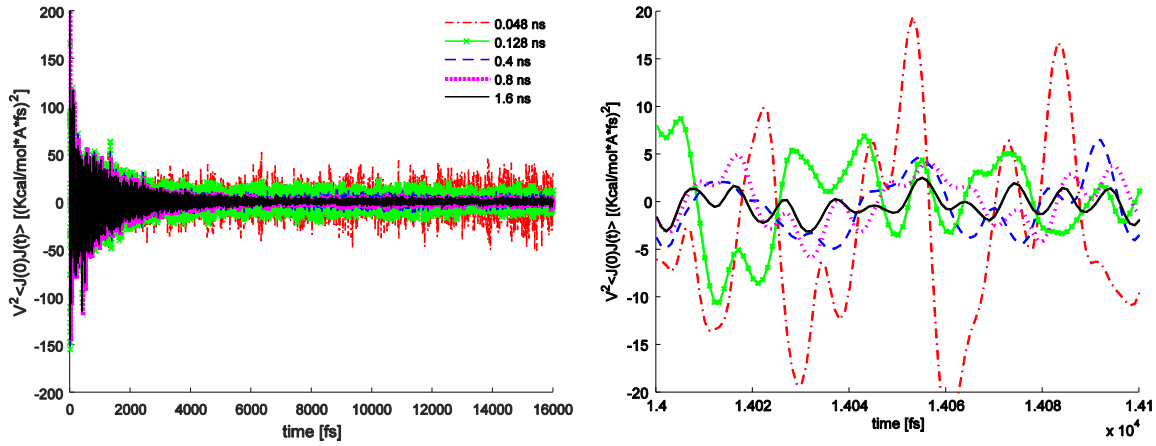

Figure 3.3: a. HCACF of pristine SWNT-epoxy nanocomposite at T= 298K, P = 1 atm. b. Zoomed HCACF of pristine SWNT-epoxy nanocomposite at T= 298K, P = 1 atm to show convergence.

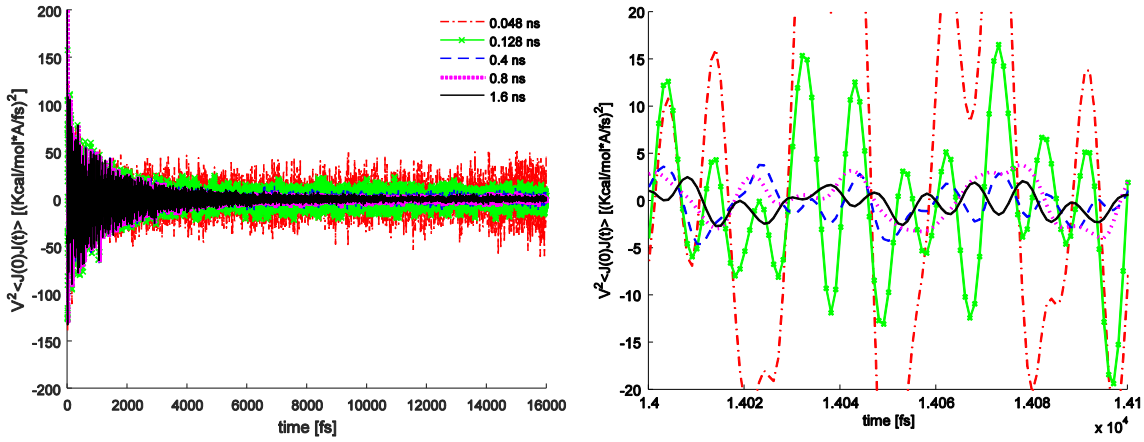

Figure 3.4: a. HCACF of functionalized SWNT-epoxy nanocomposite at T= 298K, P = 1 atm. b. zoomed HCACF of functionalized SWNT-epoxy nanocomposite at T= 298K, P = 1 atm to show convergence.

3.3.2 Thermal Conductivity of Epoxy

Thermal conductivity for the epoxy as a function of temperature with and without long range corrections is shown in Fig. 3.5. The data labeled 'No Long Range Correction' was a real–space algorithm and therefore did not include any long range Coulombic interactions. The red line, labeled 'With Long Range Correction' included the 'k-space' component electrostatic energy. The free parameters such as the grid size, and convergence acceleration factor are determined by specifying an accuracy value [132]. Here, an accuracy value was taken as 10^{-4}, meaning the error will be 1/10000 of the force two unit point charges with a 1 Å separation exert on one other. Due to oscillations in the thermal conductivity results, all the reported values of thermal conductivity were averaged over 0.2 ns. Both measures of thermal conductivity, with and without long-range electrostatic forces have virtually identical slopes. However, at room temperature the PPPM method matches the experimental value of epoxy, while the LJ–cutoff overestimates it by approximately 50%. Fig. 3.6a shows the convergence of thermal conductivity to 0.24 W/mK for a PPPM simulation, which is in excellent agreement with experimental values for DGEBA-based epoxy at room temperature [10, 59, 60]. Sampling times as long as 3.2 ns have been investigated, but due to the numerical integration of the HCACF in the thermal conductivity calculation, there will be a steady drift after convergence. This is shown in Fig. 3.6b, where convergence occurred between 0.8 ns and 1.4 ns. As the sample time moves past the converged region, the thermal conductivity is seen to steadily drift upwards away from the converged value.

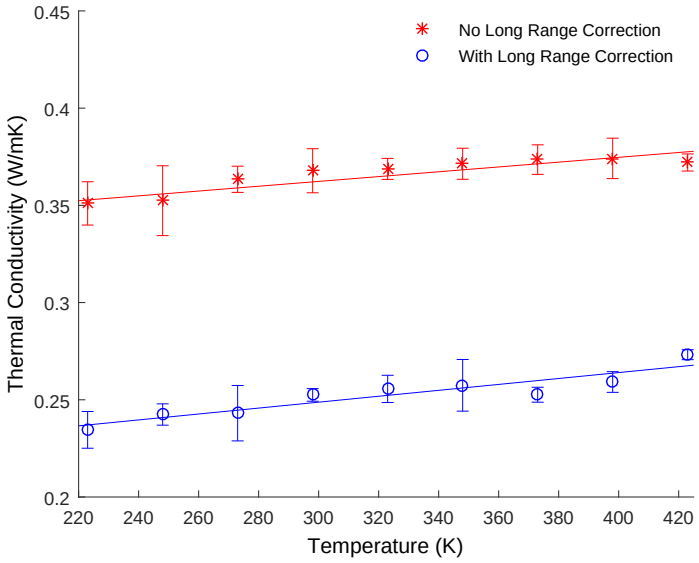

Figure 3.5: Thermal conductivity for neat epoxy with and without long range electrostatic interactions for various temperatures at P=1 atm.

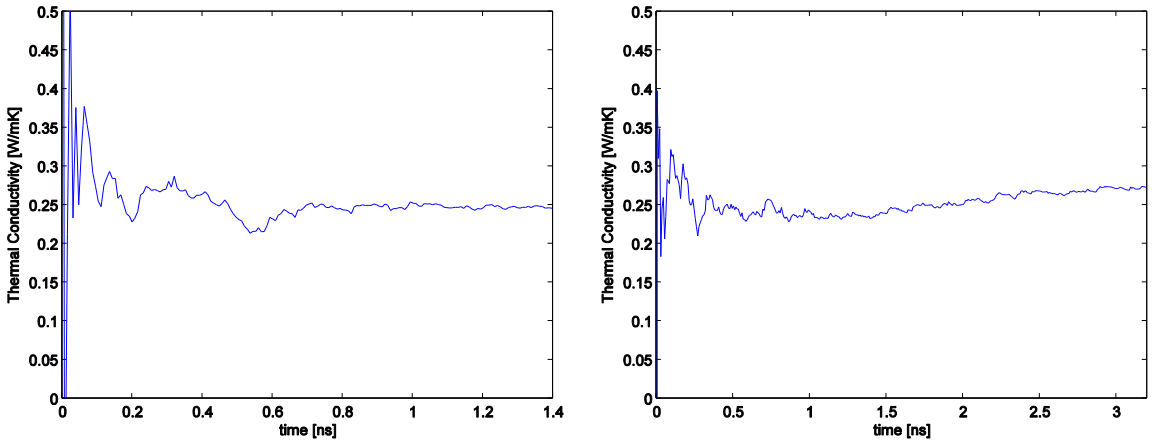

Figure 3.6: a. Convergence of the thermal conductivity at T= 298K, P = 1 atm. b. Drift in thermal conductivity at T= 298K, P = 1 atm due to numerical integration of HCACF at larger sampling times.

3.3.3 Thermal Conductivity of Nanocomposites

Fig. 3.5 shows the necessity of including long range interactions; and how they allow the thermal conductivity to accurately capture experimental values. The PPPM method was used to calculate the thermal conductivity of pristine and functionalized SWNT-epoxy

nanocomposites. The first system investigated was an isolated SWNT that spanned the entire simulation cell. The thermal conductivity of a nanotube of length 36.89 Å with the application of periodic boundary conditions making the SWNT effectively infinite is shown in Fig. 3.7. As expected, the nanotube shows decreasing thermal conductivity with increasing temperature [133]. Compared to many studies, the thermal conductivity of the nanotube along the nanotube length is significantly lesser [8, 11]. It has been seen previously that there is a length dependence in the thermal conductivity of nanotubes even with periodic boundary conditions [134]. Longer nanotubes allow additional modes with smaller wave vectors. Smaller wave vectors are longer lived than the higher frequency modes due to a lower probability of Umklapp scattering, and generally have higher group velocities, leading to an increased thermal conductivity [134].

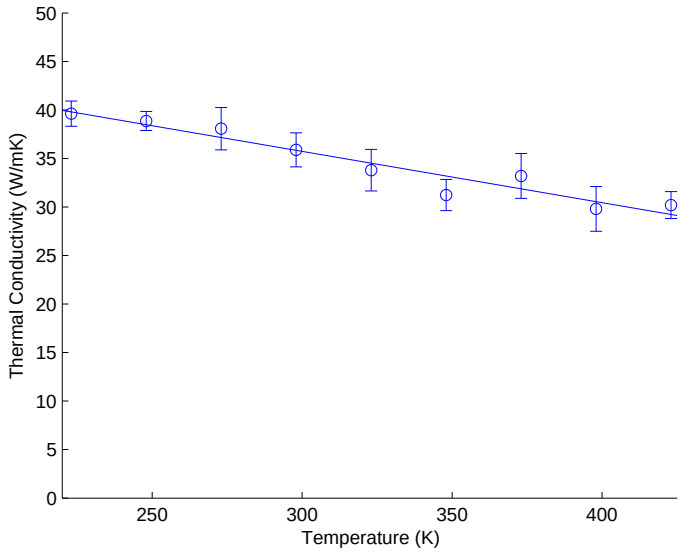

Figure 3.7: Thermal conductivity for a SWNT of length 36.89 Å with periodic boundary conditions applied for various temperatures at P = 1 atm.

The thermal conductivity in the plane perpendicular to the nanotube (x-y) for both the pristine and functionalized nanocomposites systems, compared with neat epoxy is shown in Fig. 3.8. The pristine SWNT-epoxy nanocomposite's thermal conductivity does not show much variation with temperature, and is reduced by 27% at room temperature in the x-y plane when compared to isotropic neat epoxy. This reduction is due to there being less degrees of freedom per unit volume available for heat transport, since this occurs predominately in the polymer and is therefore hindered by the inclusion of the nanotube [66]. The van der Waal forces are inefficient in thermal transport across the SWNT-epoxy interface, and most of the heat flux occurs in the polymer because heat transfer is slow through the

hallow tube. The thermal conductivity of the functionalized SWNT-epoxy system shows a stronger temperature dependence, and is greater than that of neat epoxy over the entire temperature range, with a 64% improvement at room temperature. The increase in the thermal conductance in the interface direction is due to an improved thermal coupling between the SWNT and the epoxy. The creation of sp^3 hybridization defects in functionalization creates scattering sites for phonons along the SWNT, allowing energy to be transferred from the epoxy to the SWNT.

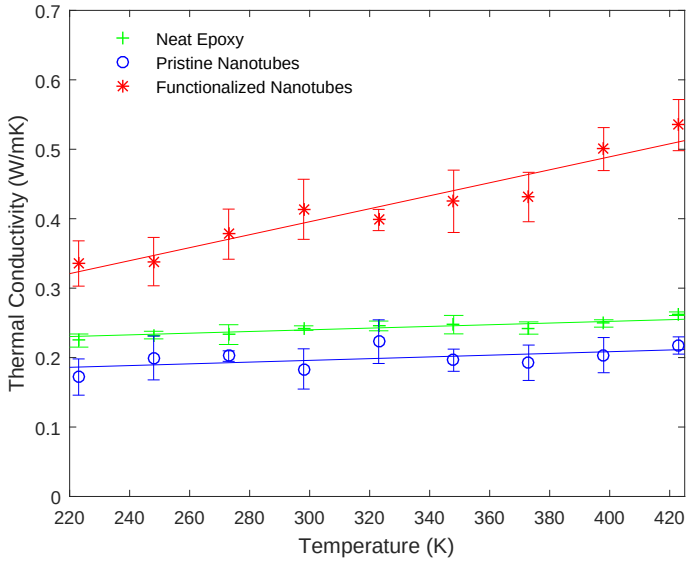

Figure 3.8: Thermal conductivity in the directions perpendicular the nanotube axis (x-y plane) for functionalized and pristine SWNT-epoxy nanocomposites compared with neat epoxy.

The thermal conductivity parallel to the nanotube (z-direction) for the pristine SWNT-epoxy and functionalized SWNT-epoxy nanocomposites are shown in Fig. 3.9 and Fig. 3.10. Fig. 3.9 shows very large improvements along the nanotube direction for the pristine SWNT-epoxy system over neat epoxy, much more so than the functionalized system. The pristine SWNT-epoxy system demonstrates a thermal conductivity along the SWNT direction equivalent to that of an isolated nanotube, as demonstrated above in Fig. 3.7. The functionalized SWNT-epoxy system showed significant improvement ($\sim$700%) over neat epoxy in the nanotube direction, as seen in Fig. 3.10, but a whole order magnitude lesser than that of the pristine SWNT-epoxy system. Experimenents and simulations have shown that the defects to the nanotube introduced by functionalization decrease the inherent tube thermal conductivity, since they act as scattering points for thermal energy. [62, 70]. For

this reason, it is clear that in regards to overall system thermal conductivity there is a trade-off between the greater improvements along the nanotube direction for the pristine SWNT system, and the improvements perpendicular to the SWNT for the functionalized SWNT system. Shenongin et. al proposed that functionalization is only useful for SWNT-epoxy composites containing shorter aspect ratio nanotubes, because reduction in tube conductance is greater in higher aspect ratio SWNTs. [62]

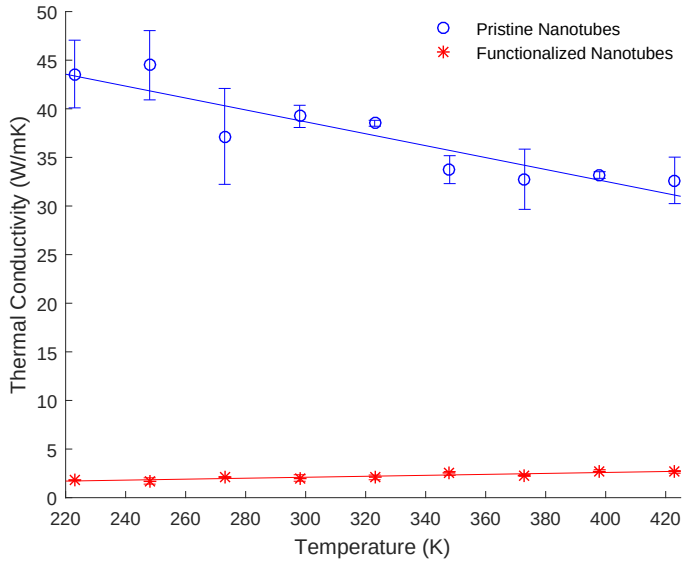

Figure 3.9: Thermal conductivity along the nanotube axis (z-direction) for the pristine SWNT-epoxy nanocomposites compared to functionalized nanocomposite

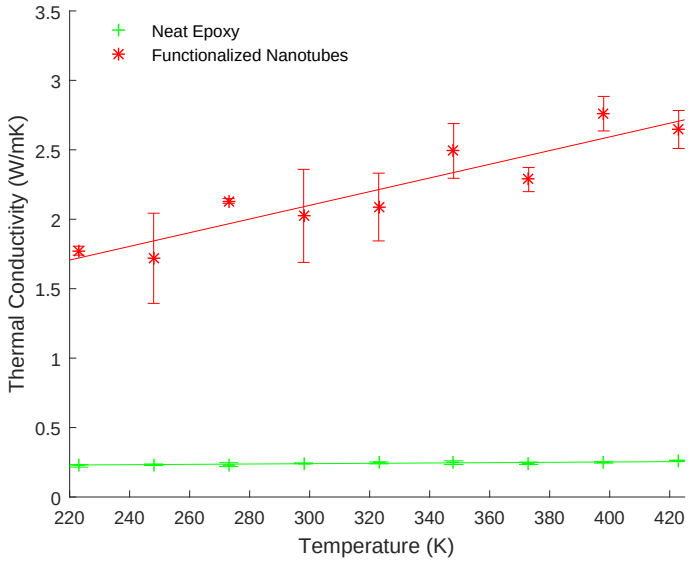

Figure 3.10: Thermal conductivity along the nanotube axis (z-direction) for the functionalized SWNT-epoxy nanocomposite compared to neat epoxy.

As discussed previously, experimental data has not matched the improvements predicted by simulations, with the likely limitation being inefficient phonon transport between nanotubes. In realistic systems, nanotube ends act as phonon scattering sites, and so discontinuous nanotubes were modeled in this study. This was done by creating nanotubes that did not span the entire simulation cell length. Periodic boundary conditions were still applied, but there is epoxy in-between the nanotubes as shown earlier in Fig. 2.27b. SWNTs of that span 11/15 of the simulation cell, and 13/15 of the simulation cell were considered. While these are very short SWNTs, they allowed the end effects to be investigated as desired. The results for the short nanotubes compared to the infinite systems and neat epoxy, perpendicular to the nanotube axis (x-y plane), and along the nanotube axis (z-direction) in the temperature range of 248-348 K are shown in Fig. 3.11 and Fig. 3.12, respectively. From Fig. 3.11, it is seen that the discontinuous functionalized nanotubes have only a slight reduction in thermal conductivity when compared to the infinite, functionalized SWNT-epoxy system, and the nanotubes spanning 11/15 and 13/15 of the cell show an improvement of 42% over neat epoxy. The discontinuous SWNT-epoxy systems display higher thermal conductivity compared to the infinite system, and both discontinuous systems are approximately equal to the thermal conductivity of isotropic neat epoxy. This further illustrates that heat transfer to the epoxy perpendicular to the pristine nanotube was poor, and the discontinuous nanotubes allow a larger path, and more epoxy per unit volume for the heat flux to travel around the nanotube. The results along the nanotube axis in Fig. 3.12 show that for the

discontinuous nanotubes there is great improvement over neat epoxy, 103% and 115% for the 11/15 and 13/15 cell length pristine SWNT-epoxy systems, and 91% and 103% for the 11/15 and 13/15 cell length functionalized SWNT-epoxy systems. However, gains in thermal conductivity are significantly less than that of the infinite, functionalized SWNT-epoxy system. The infinite pristine SWNT-epoxy system is not shown because it yet another order of magnitude greater. This shows that including SWNT end effects drastically lowers the prediction of the thermal conductivity of the SWNT-epoxy nanocomposites. It is further demonstrated that there is a trade-off between the greater improvements along the nanotube direction for the pristine SWNT system, and the improvements perpendicular to the SWNT for the functionalized SWNT system, towards the overall system thermal conductivity.

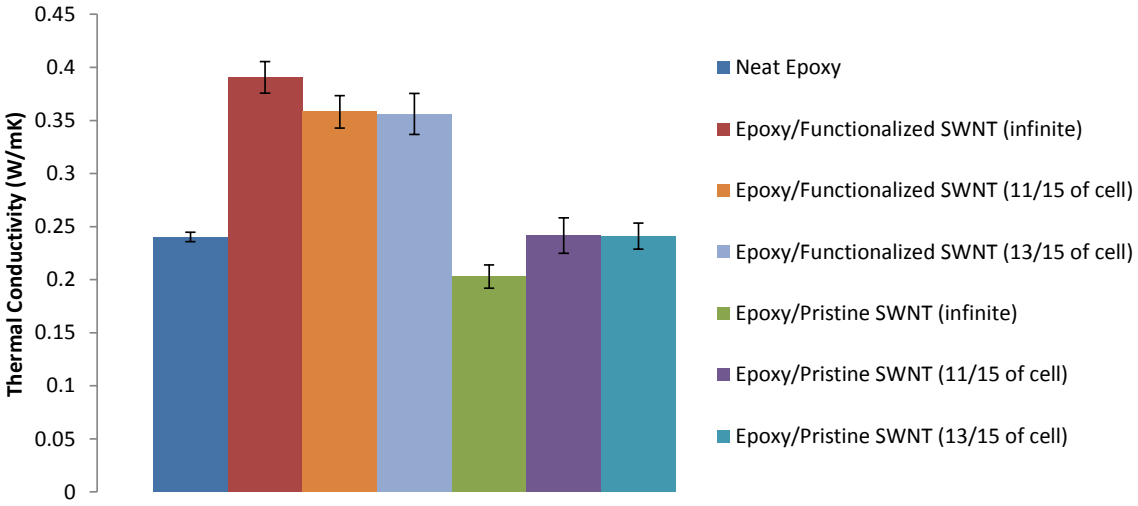

Figure 3.11: Thermal conductivity in the temperature range of 248-348 K in the directions perpendicular to the nanotube axis for the various short and infinite SWNT-epoxy nanocomposites studied.

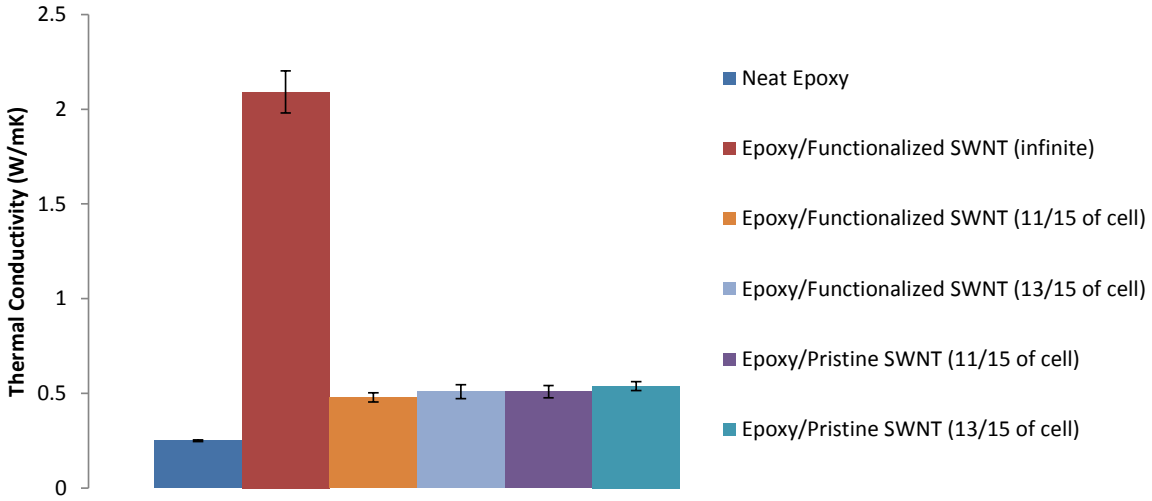

Figure 3.12: Thermal conductivity in the temperature range of 248-348 K along the nanotube axis for the various short and infinite SWNT-epoxy nanocomposites studied. Epoxy-Pristine SWNT (infinite) is omitted since its average value is 38.6 W/mK in this temperature range.

3.3.4 Equivalent Isotropic Results

To simulate an equivalent isotropic system consisting of randomly oriented nanotubes, the thermal conductivity tensors are rotated and averaged over every possible orientation accounting for symmetry using the ODF method described later in Section 4.2.1, and the results are shown in Fig. 3.13 for the various nanocomposites. It is highlighted here that for the discontinuous SWNTs, the functionalized system showed a greater improvement in thermal conductivity. The improvements along the nanotube axis are essentially equivalent for the discontinuous pristine and functionalized SWNT-epoxy systems, so the thermal conductivity perpendicular to the SWNT axis being significantly improved by functionalization makes that system superior. However, for the infinite systems, the pristine SWNT-epoxy composite showed much greater improvement, with an equivalent isotropic thermal conductivity of 13 W/mK. For the long nanotubes, there was a huge reduction in inherent tube conductivity via functionalization. It is expected that the end effects will be of lesser importance for long nanotubes that extend beyond the length of the phonon mean free path, and so inclusion of these effects in the long nanotubes studied is of less importance. This suggests a certain length where the optimum improvement in thermal conductivity transitions from functionalized to pristine SWNTs.

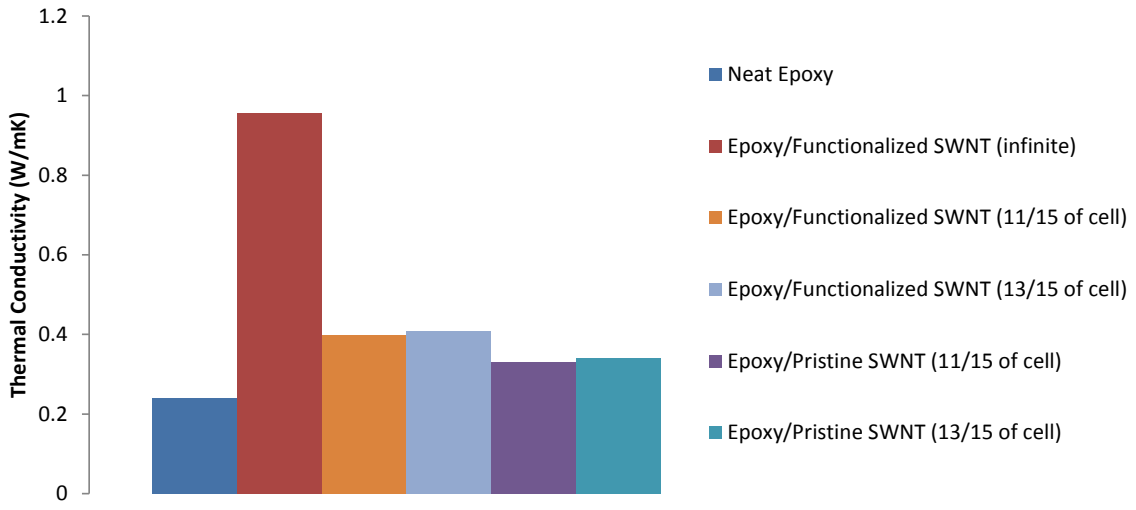

Figure 3.13: Thermal conductivity of an equivalent isotropic systems created by rotating thermal conductivity tensor over all possible orientations. Epoxy-Pristine SWNT (infinite) is omitted since its equivalent isotropic thermal conductivity is 13 W/mK.

3.3.5 Experimental Comparisons

Calculating the equivalent isotropic systems allows a comparison to be done with experiments, since the majority of work has been done with randomly oriented SWNTs. Fig. 3.14 shows the MD results for discontinuous SWNT-epoxy composites at the two different mass fractions compared with experimental data at various mass fractions. [72]. The curve shown is from the effective medium theory fit to the experimental data. Both sets of data were normalized by the value of neat epoxy. The discontinuous nanotubes that span 11/15 and 13/15 of the simulation cell account for mass fractions of 0.06 and 0.07 respectively. The trend shown by increasing the mass faction is in excellent agreement with the experimental data. This confirms that modeling the end effects of the SWNTs is essential to obtaining a realistic prediction of thermal conductivity.

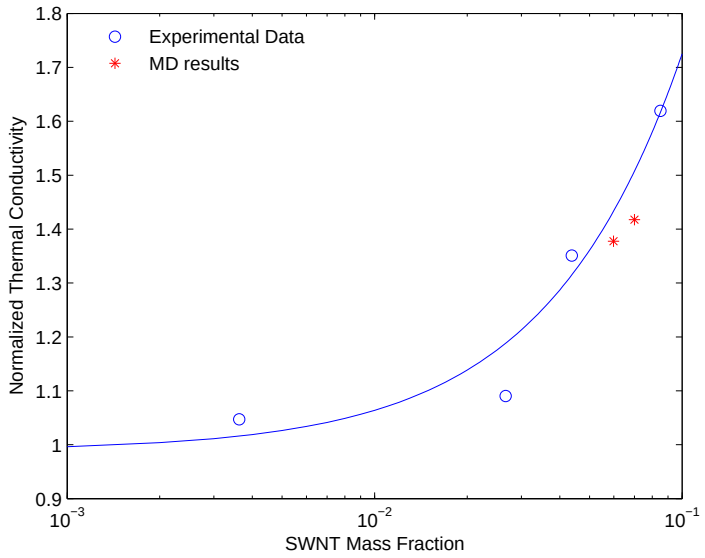

Figure 3.14: Experimental comparison of discontinuous, pristine SWNT-epoxy composite results at a given mass fraction [72].

The MD data points in Fig. 3.14 can be expanded over a larger range of mass fractions by combining the ODF model with the parallel (Voigt) and series (Reuss) rule of mixtures, which again will be discussed in much more detail in Section 4.2.1. This was done in Fig. 3.15 for the pristine, discontinuous nanotubes for the parallel model in green and the series model in red. The rule of mixtures results were calculated for each of the two MD points using both models, and those results were averaged and plotted along with the normalized experimental data points from [72]. The figure shows that the multiscale ODF model can allow the MD calculations, which are very limited in the range of possible mass fractions, to be inexpensively extrapolated over a wide range of mass fractions that match up well with experimental results.

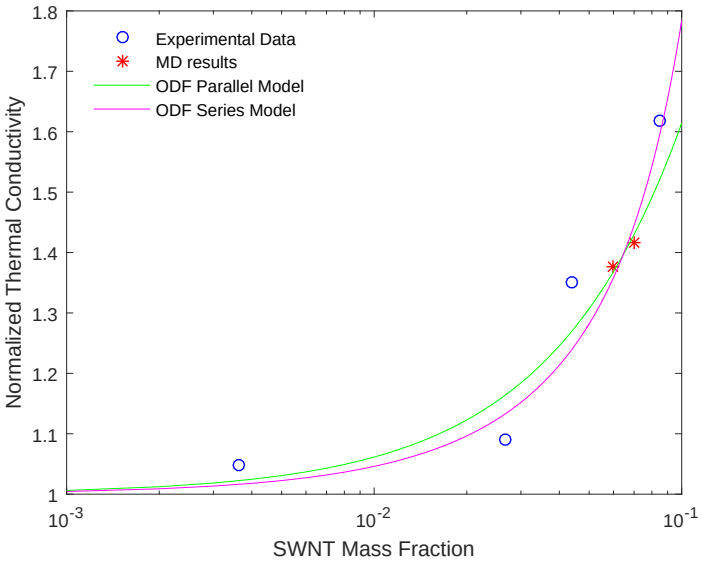

Figure 3.15: ODF parallel and series models of discontinuous, pristine SWNT-epoxy composite results based on the MD results, compared to experimental results at a given mass fraction [72].

3.4 Conclusions

The thermal conductivity of crosslinked epoxy and SWNT-epoxy nanocomposites was investigated using MD via the Green-Kubo integral of the heat current auto correlation function. The epoxy network was built using the dendrimer growth approach, and the inclusion of long-range Coulombic interactions via a 'k–space' component of electrostatic energy allows the thermal conductivity to match the experimental value of .24 W/mK at room temperature. The use of non-equilibrium methods and periodic boundary conditions had limited many previous studies to calculating interface thermal conductance. In this study, thermal conductivity was calculated in the plane perpendicular to the nanotube, as well as along the nanotube direction. For the pristine, long SWNT-epoxy system, the thermal conductivity along the nanotube direction is equivalent to that of an isolated SWNT, but in the plane perpendicular to the nanotube there is a reduction of 27% when compared to neat epoxy. The functionalized, long SWNT-epoxy system showed a very large increase along the nanotube axis ($\sim$700%), though it is an order of magnitude less than that displayed by the pristine SWNT-epoxy system. The plane perpendicular to the nanotube shows a 64% improvement in thermal conductivity at room temperature when compared to neat epoxy. Inefficient phonon transport between nanotubes at the ends is an impor-

tant factor in the thermal conductivity of SWNT-epoxy nanocomposites, and for this reason discontinuous nanotubes were investigated. The discontinuous nanotubes showed a large improvement over neat epoxy along the nanotube axis: 103%–115% for the pristine SWNT-epoxy, and 91%–103% for the functionalized SWNT-epoxy systems. The discontinuous, functionalized systems also showed a 42% improvement in the plane perpendicular to the nanotube walls, while the discontinuous, pristine SWNT-epoxy systems display no improvement over epoxy. The thermal conductivity tensor was rotated over all possible orientations to allow for experimental comparison, and the results are in excellent agreement for the discontinuous, pristine SWNT-epoxy nanocomposite. For the short nanotubes investigated, functionalization provides greater improvement in overall composite conductivity than pristine nanotubes. For the long nanotubes investigated, the massive increase in the thermal conductivity along the tube boosted composite conductivity much greater than the added improvements in the plane perpendicular to the nanotube due to functionalization when considering deterioration of the inherent tube conductivity. These simulations demonstrate there is a SWNT length threshold where the best improvement for a composite system with randomly oriented nanotubes would transition from functionalized SWNTs to pristine SWNTs.

CHAPTER 4

Multiscale Modeling of Nanocomposites

Molecular Dynamics has a well-known length scale problem, with the dimension of each side of the MD lattice described in Chapter 2 being ∼40 Å. Even with periodic boundary conditions, ways to upscale the simulations to better compare with continuum results are desired. To this achieve this, multiscale modeling was considered to give better control over the volume fraction of SWNT, and allow the effects of nanotube alignment to be studied. Two methods were used: a finine element based method, and an ODF based method. For the Finite Element method, which is described in more detail in Section 4.1, elements were probabilistically assigned elastic properties from the MD lattice results based on the desired volume fraction and alignment of the nanotubes. NIST code NISTIR 6269 was used to run the Finite Element analysis [135]. For the ODF method, described in detail in Section 4.2, an orientation distribution function was generated for the desired amount of nanotube alignment, and the stiffness matrix was calculated. To vary the volume fraction of nanotubes, a rules of mixture approaches was implemented.

4.1 FEM Multiscale Method

4.1.1 Overview of the Finite Element Method

The Finite Element method is formulated using a variational method which requires a functional, which is an integral expression implicitly containing the governing differential equation, to exist for the problem being solved. This integral expression is often referred to as the weak form of a differential equation, while the governing differential equations with the boundary conditions is considered the strong from. The strong form requires that its conditions are true at every point, while the weak form only requires that these conditions are satisfied in an average sense [136]. The Finite Element method is based on an approximate version of the weak form of the governing differential equation plus boundary conditions.

Described below is an energy approach for elastic problems to derive the Finite Element governing equations [136, 137]. To do this, the principle of stationary potential energy is applied to the functional for potential energy, Π_p. The principle of stationary potential energy dictates that at equilibrium, the potential energy is minimized: $d\Pi_p = 0$.

First, a functional for the potential energy for an elastic body is needed in order to carry out the Finite Element method. The total potential energy is a combination of the strain energy from the elastically deformed body, U, and energy of the applied loads, Ω:

$$\Pi_p = U + \Omega. \tag{4.1}$$

The total strain energy for an elastic body is found by integrating the strain energy density, written here in the absence of initial stresses and strains, over the volume of the material:

$$U = \frac{1}{2}\int \{\boldsymbol{\sigma}\}^T\{\boldsymbol{\epsilon}\}dV = \frac{1}{2}\int \{\boldsymbol{\epsilon}\}^T[\mathbf{E}]\{\boldsymbol{\epsilon}\}dV, \tag{4.2}$$

where $\{\boldsymbol{\epsilon}\} = \{\epsilon_x\ \epsilon_y\ \epsilon_z\ \gamma_{xy}\ \gamma_{yz}\ \gamma_{xz}\}$ is an array of strains, and $[\mathbf{E}]$ is the 6x6 the constitutive matrix that relates stress, $\{\boldsymbol{\sigma}\}$ to strain $\{\boldsymbol{\epsilon}\}$.

The applied loads, or work potential, can be written as:

$$\Omega = -\int \{\mathbf{u}\}^T\{\mathbf{F}\}dV - \int \{\mathbf{u}\}^T\{\mathbf{T}\}dS + \sum_i \{\mathbf{u}_i\}^T\{\mathbf{P}_i\}, \tag{4.3}$$

where $\{\mathbf{u}\}$ is the displacement vector, $\{\mathbf{F}\}$ represents the body forces, and the term containing it is integrated over the volume. $\{\mathbf{T}\}$ represents the surface traction, and is integrated over the surface the traction is applied. The last term, $\{\mathbf{u}_i\}^T\{\mathbf{P}_i\}$ is due to point loads applied at point i, and so $\{\mathbf{u}_i\}$ is the displacement at that point. For the Finite Element formulation, it will be assumed these loads are applied at nodes, where $\{\mathbf{d}_i\}$ is the displacement vector of node i. Eqs. 4.2 and 4.3 are general expressions for an elastic body, and this domain is discretized into finite elements with specified degrees of freedom. The global potential energy is then a summation of energies of all the elements, e:

$$\Pi_p = \sum_e \frac{1}{2}\int_{V_e} \{\boldsymbol{\epsilon}\}^T[\mathbf{E}]\{\boldsymbol{\epsilon}\}dV - \sum_e \int_{V_e} \{\mathbf{u}\}^T\{\mathbf{f}\}dV - \sum_e \int_{A_e} \{\mathbf{u}\}^T\{\mathbf{T}\}dA + \sum_i \{\mathbf{d}_i\}^T\{\mathbf{P}_i\}. \tag{4.4}$$

In a typical problem solved using Finite Elements, there are numerous degrees of freedom, D_i, and our potential energy is a function of these degrees of freedom, $\Pi_p = \Pi_p(D_1, D_2, ..., D_n)$. Applying the principle of stationary potential energy yields:

$$d\Pi_p = \frac{\partial \Pi_p}{\partial D_1} dD_1 + \frac{\partial \Pi_p}{\partial D_2} dD_2 + ... + \frac{\partial \Pi_p}{\partial D_n} dD_n = 0. \tag{4.5}$$

For any zero or nonzero value of dD_1, dD_2, dD_n, then $d\Pi_p = 0$ for the principle of stationary energy to hold, and so it is required that all $\frac{\partial \Pi_p}{\partial D_i}$ must go to zero, and so for $i = 1, 2, .., n$:

$$\frac{\partial \Pi_p}{\partial D_i} = 0 \tag{4.6}$$

.

In the Finite Element method, Eq. 4.6 is solved for the various degrees of freedom, which are determined by the type of finite element chosen. Hexahedron elements, or "brick" elements are used in this formulation, and can be seen in Fig. 4.1. This element contains three degrees of freedom for every node: x-displacement (u), y-displacement (v), and z-displacement (w). The origin of the element is in the bottom left corner, giving u, v and w a range of 0 to 1. This is different than the usual convention, where formulations in natural coordinates typically have ξ, η, and ζ range from -1 to 1 [137,138]. The 3D location of each node inside a specific element can be seen in Table 4.1, where the node numbers correspond to Fig. 4.1. With the given coordinates, the eight shape functions obtained for the hexahedron element are:

$$\begin{aligned}
N_1 &= (1-x)(1-y)(1-z) \\
N_2 &= x(1-y)(1-z) \\
N_3 &= xy(1-z) \\
N_4 &= (1-x)y(1-z) \\
N_5 &= (1-x)(1-y)z \\
N_6 &= x(1-y)z \\
N_7 &= xyz \\
N_8 &= (1-x)yz.
\end{aligned} \tag{4.7}$$

The hexahedron elements are sometimes referred to as "trilinear" elements, since the shape functions consists of the product of three linear functions. The displacements are determined at the nodes, and are interpolated linearly over the element using the shape functions:

$$\{\mathbf{u}\} = [\mathbf{N}]\{\mathbf{d}\}, \tag{4.8}$$

where $\{\mathbf{u}\}$ is the displacements interpolated over an element, $[\mathbf{N}]$ is a matrix of the shape functions from Eq. 4.7, and $\{\mathbf{d}\}$ is a vector of the nodal displacements. For the hexahedron element, expanding Eq. 4.8 yields:

$$\begin{Bmatrix} u \\ v \\ w \end{Bmatrix} = \begin{bmatrix} N_1 & 0 & 0 & N_2 & 0 & 0 & N_3 & 0 & 0 & \dots \\ 0 & N_1 & 0 & 0 & N_2 & 0 & 0 & N_3 & 0 & \dots \\ 0 & 0 & N_1 & 0 & 0 & N_2 & 0 & 0 & N_3 & \dots \end{bmatrix} \begin{Bmatrix} u_1 \\ v_1 \\ w_1 \\ u_2 \\ v_2 \\ w_2 \\ \vdots \\ w_8 \end{Bmatrix}. \quad (4.9)$$

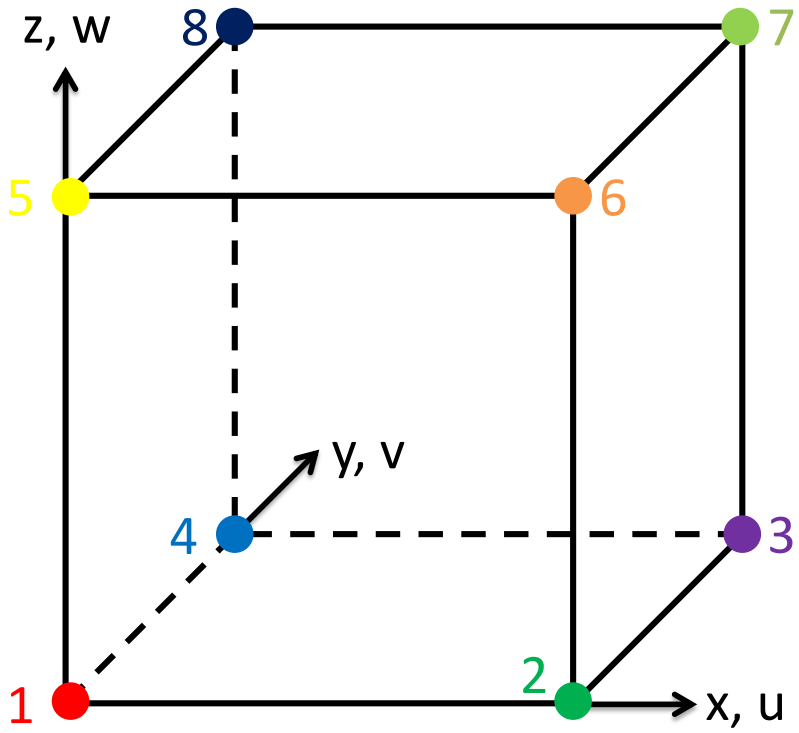

Figure 4.1: Hexagonal element with node labeling.

Node Number	u	v	w
1	0	0	0
2	1	0	0
3	1	1	0
4	0	1	0
5	0	0	1
6	1	0	1
7	1	1	1
8	0	1	1

Table 4.1: The location of each node in 3D for a given element, where the node numbers correspond to Fig. 4.1.

Ultimately, strain is needed for Eq. 4.2, and this can be obtained using the shape functions for individual elements and the vector of the nodal displacements, $\{\mathbf{d}\}$ via the strain-displacement matrix, [**B**]:

$$\{\boldsymbol{\epsilon}\} = [\boldsymbol{\partial}][\mathbf{N}]\{\mathbf{d}\} = [\mathbf{B}]\{\mathbf{d}\}. \tag{4.10}$$

From Eq. 4.10, where [**N**] is the matrix of shape functions shown in Eq. 4.8, and $[\boldsymbol{\partial}]$ in 3D is given as:

$$[\boldsymbol{\partial}] = \begin{bmatrix} \frac{\partial}{\partial x} & 0 & 0 \\ 0 & \frac{\partial}{\partial y} & 0 \\ 0 & 0 & \frac{\partial}{\partial z} \\ \frac{\partial}{\partial y} & \frac{\partial}{\partial x} & 0 \\ 0 & \frac{\partial}{\partial z} & \frac{\partial}{\partial y} \\ \frac{\partial}{\partial z} & 0 & \frac{\partial}{\partial x} \end{bmatrix}. \tag{4.11}$$

From the strain-displacement matrix and the constitutive matrix, [**E**], the stiffness matrix for a single element is defined as:

$$[\mathbf{k}^e] = \int_{V_e} [\mathbf{B}]^T [\mathbf{E}][\mathbf{B}] dV. \tag{4.12}$$

In the FE routine applied here, the integral to calculate stiffness matrix is evaluated using Simpson's rule. No term integrated is higher than quadratic in x, y, or z, and therefore

applying Simpson's rule gives an exact solution. It is now possible to write the strain energy, previously formulated in Eq. 4.4, in terms of the stiffness matrix and the nodal displacements:

$$U_e = \frac{1}{2}\{\mathbf{d}\}^T[\mathbf{k}^e]\{\mathbf{d}\}. \tag{4.13}$$

With the expression for U_e in Eq. 4.13, the strain energy for a single element is known, and can be summed to give the global strain energy, U. This, combined with the nodal values of the applied loads, Ω, will yield the global potential energy. Shape functions are used to distribute the body forces into elemental body forces, $\mathbf{f}^e$, and surface forces into elemental traction forces, $\mathbf{T}^e$, from Eq. 4.4 to obtain:

$$\int_{V_e} \{\mathbf{u}\}^T\{\mathbf{f}\}dV = \{\mathbf{d}\}^T\{\mathbf{f}^e\} \tag{4.14}$$

$$\int_{A_e} \{\mathbf{u}\}^T\{\mathbf{T}\}dA = \{\mathbf{d}\}^T\{\mathbf{T}^e\}. \tag{4.15}$$

In order to link the local energy to the global energy, a global number scheme is used for every node in the mesh. Every node is part of eight different elements, and is given a global number according to the following [135]:

$$m = nx \cdot ny \cdot (k-1) + nx \cdot (j-1) + i, \tag{4.16}$$

where nx, ny, and nz are the total number of nodes in the x, y and z directions respectively. The global location of the node is represented by i, j and k. For an example of a single element, the node labeled "3" in Fig. 4.1 would have $i = 1$, $j = 1$, $k = 0$. The range of i will therefore go from 0 to nx with intervals of 1, and similarly j and k will go to ny and nz, respectively.

From Eq. 4.16, every node will have a global value, and it is possible to keep track of nodes with respect to their surrounding elements. The elemental matrix values $\mathbf{k}^e$, $\mathbf{f}^e$, $\mathbf{T}^e$ can be assembled using the global numbering scheme to obtain the global potential energy, Π_p:

$$\Pi_p = \frac{1}{2}\{\mathbf{D}\}^T[\mathbf{K}]\{\mathbf{D}\} - \{\mathbf{D}\}^T\{\mathbf{F}\}, \tag{4.17}$$

where [**K**] is the global stiffness matrix assembled from all the elemental stiffness matrices, and $\{\mathbf{D}\}$ is the global displacement vector. $\{\mathbf{F}\}$ is the global force vector obtained by combining and assembling the elemental body force terms, traction terms, and applying the point forces at the proper location of the force vector.

4.1.2 Finite Element Periodic Boundary Conditions

Periodic boundary conditions are enforced within the global force term, $\{\mathbf{F}\}$. The displacement field for the periodic structure can be written as [139]:

$$\mathbf{D} = \bar{\boldsymbol{\epsilon}}\mathbf{x} + \mathbf{D}^*, \tag{4.18}$$

where $\bar{\boldsymbol{\epsilon}}$ is the global strain tensor of the periodic structure, and so $\bar{\boldsymbol{\epsilon}}\mathbf{x}$ is a displacement field. As usual, $\mathbf{D}$ is nodal displacements, and $\mathbf{D}^*$ is a periodic function between repeated units cells. Using this, the displacement of any boundary nodes on two opposite sides of a repeated cell can be written as:

$$\mathbf{D}_j^+ = \bar{\boldsymbol{\epsilon}}\mathbf{x}_j^+ + \mathbf{D}_j^* \tag{4.19}$$

$$\mathbf{D}_j^- = \bar{\boldsymbol{\epsilon}}\mathbf{x}_j^- + \mathbf{D}_j^*, \tag{4.20}$$

where the subscript j indicates a matching pair of boundary nodes. The difference between the two equations yields the periodic boundary condition, where j will be iterated over of all pairs of matching nodes along a boundary:

$$\mathbf{D}_j^+ - \mathbf{D}_j^- = \bar{\boldsymbol{\epsilon}}(\mathbf{x}_j^+ - \mathbf{x}_j^-). \tag{4.21}$$

In order to enforce this condition, a number of methods are commonly used such as the elimination method, Lagrange multiplier method, and penalty method [139–141]. The elimination method was used here, which reduces the number of unknowns in the system, and works by replicating the nodal displacements on one boundary to the corresponding opposite boundary:

$$\mathbf{D}_j^+ = \mathbf{D}_j^- + \bar{\boldsymbol{\epsilon}}(\mathbf{x}_j^+ - \mathbf{x}_j^-). \tag{4.22}$$

The condition in Eq. 4.22 is to be enforced on the boundary nodes, and this is done by first breaking the displacement vector into parts for the internal nodes and boundary nodes:

$$\mathbf{D} = \begin{bmatrix} \mathbf{D}_n \\ \mathbf{D}_+^b \\ \mathbf{D}_-^b \end{bmatrix}, \tag{4.23}$$

where the subscript n designates internal displacements not subjected to these boundary conditions. The superscript b designates a boundary node, while the subscripts $+$ and $-$ are used to specify a positive or negative node displacement. This can be used to break up

Eq. 4.17 into:

$$\Pi_p = \begin{bmatrix} \mathbf{D}_n & \mathbf{D}_+^b & \mathbf{D}_-^b \end{bmatrix} \begin{bmatrix} \mathbf{K}_{nn} & \mathbf{K}_{n+} & \mathbf{K}_{n-} \\ \mathbf{K}_{+n} & \mathbf{K}_{++} & \mathbf{K}_{+-} \\ \mathbf{K}_{-n} & \mathbf{K}_{-+} & \mathbf{K}_{--} \end{bmatrix} \begin{bmatrix} \mathbf{D}_n \\ \mathbf{D}_+^b \\ \mathbf{D}_-^b \end{bmatrix} - \begin{bmatrix} \mathbf{D}_{int} & \mathbf{D}_i^+ & \mathbf{D}_i^+ \end{bmatrix} \begin{bmatrix} \mathbf{F}_n \\ \mathbf{F}_+^b \\ \mathbf{F}_-^b \end{bmatrix}. \tag{4.24}$$

Next, applying Eq. 4.6 for equilibrium, and substituting Eq. 4.22 to enforce the boundary condition, given in the current labeling system as $\mathbf{D}_+^b = \mathbf{D}_-^b + \bar{\boldsymbol{\epsilon}}(\mathbf{x}_+^b - \mathbf{x}_-^b)$:

$$\begin{bmatrix} \mathbf{K}_{nn} & \mathbf{K}_{n+} + \mathbf{K}_{n-} \\ \mathbf{K}_{+n} + \mathbf{K}_{-n} & \mathbf{K}_{++} + \mathbf{K}_{+-} + \mathbf{K}_{-+} + \mathbf{K}_{--} \end{bmatrix} \begin{bmatrix} \mathbf{D}_n \\ \mathbf{D}_-^b \end{bmatrix} - \begin{bmatrix} \mathbf{F}_n - \mathbf{K}_{n+} \left(\mathbf{D}_-^b + \bar{\boldsymbol{\epsilon}} \left(\mathbf{x}_+^b - \mathbf{x}_-^b \right) \right) \\ \mathbf{F}_+^b + \mathbf{F}_-^b - (\mathbf{K}_{++} + \mathbf{K}_{-+}) \left(\mathbf{D}_-^b + \bar{\boldsymbol{\epsilon}} \left(\mathbf{x}_+^b - \mathbf{x}_-^b \right) \right) \end{bmatrix} = 0. \tag{4.25}$$

Clearly, the reduction method gets its name from the fact it reduces the number of unknowns to be solved in the system. This can be written in a more shorthand notation as:

$$[\mathbf{K}^*]\{\mathbf{Q}^*\} = \{\mathbf{F}^*\}, \tag{4.26}$$

where $[\mathbf{K}^*]$, $\{\mathbf{Q}^*\}$, $\{\mathbf{F}^*\}$ are the modified stiffness matrix, displacement vector and force vector, respectively. The modified stiffness matrix is non-singular. For all of the boundary nodes, the nodal displacements are substituted from the negative boundary to the positive boundary. This reduces the size of the stiffness matrix, displacement vector, and force vector; where the force vector includes the terms to enforce the boundary condition.

4.1.3 Minimization

The conjugate gradient method was used to minimize Eq. 4.17 [136, 142]. Conjugate gradient is used solve [**A**] $\{x\}$ =$\{\mathrm{b}\}$, and can be used to minimize an equation of the form of Eq. 4.17:

$$f(x) = \frac{1}{2}\{\mathbf{x}\}^T[\mathbf{A}]\{\mathbf{x}\} - \{\mathbf{x}\}^T\{\mathbf{b}\}, \tag{4.27}$$

where as $f(x)$ gets smaller, the value of x that will minimize the equation is approached. The gradient of Eq. 4.27 is:

$$\{\mathbf{g}\} = [\mathbf{A}]\{\mathbf{x}\} - \{\mathbf{b}\} \tag{4.28}$$

So, the residual, $\{\mathbf{r}\}$, is equal to the negative of the gradient and represents the direction of steepest descent for a given value of $\{\mathbf{x}\}$. Search directions, $\{\mathbf{p}\}$, that are conjugate to one another and close to directions of steepest descent are used. The constraint of conjugate search directions means that $\{\mathbf{p}\}_m^T[\mathbf{A}]\{\mathbf{p}\}_n = 0$ when $m \neq n$. The next position, x_{i+1}, will be given based on the current position, x_i, as:

$$\{\mathbf{x}\}_{i+1} = \{\mathbf{x}\}_i + \alpha_i\{\mathbf{p}\}_i \text{ where } \alpha_i = \frac{\{\mathbf{r}\}_i^T\{\mathbf{r}\}_i}{\{\mathbf{p}\}_i^T[\mathbf{A}]\{\mathbf{p}\}_i}. \tag{4.29}$$

The iteration stops when $\{\mathbf{x}\}$ is close enough to the actual value such that there is no significant further relaxation of stresses within an element.

4.1.4 Multiscale Model

We use the Finite Element method in conjunction with Molecular Dynamics to create a multiscale model. One of the primary benefits of this method is that it allows the vol% or wt% of the SWNTs to be controlled, and generate much more realistic cases than were possible with Molecular Dynamics alone. This was done by assigning a desired percentage of elements with the mechanical properties of neat epoxy, which is isotropic and therefore has no orientation effects. The molecular-scale data from Chapter 2 was input to individual elements and then FE analysis was carried out. The microstructures for the SWNT-epoxy nanocomposite yielded the full elastic stiffness matrix for the multiple configurations tested including short and infinite, functionalized and pristine SWNTs. For a random oriented composite, every element was assigned the stiffness matrix corresponding to a random nanotube orientation. This can be illustrated in Fig. 4.2. The left part of the image shows a 2D example with 8x8 elements, and so 81 total nodes. The right image shows that each of the elements being assigned the elastic properties of the MD lattice, represented by the green boxes, at a random nanotube orientation. The orientation of the nanotubes being assigned can be controlled, and as such the effects of nanotube alignment can be studied.

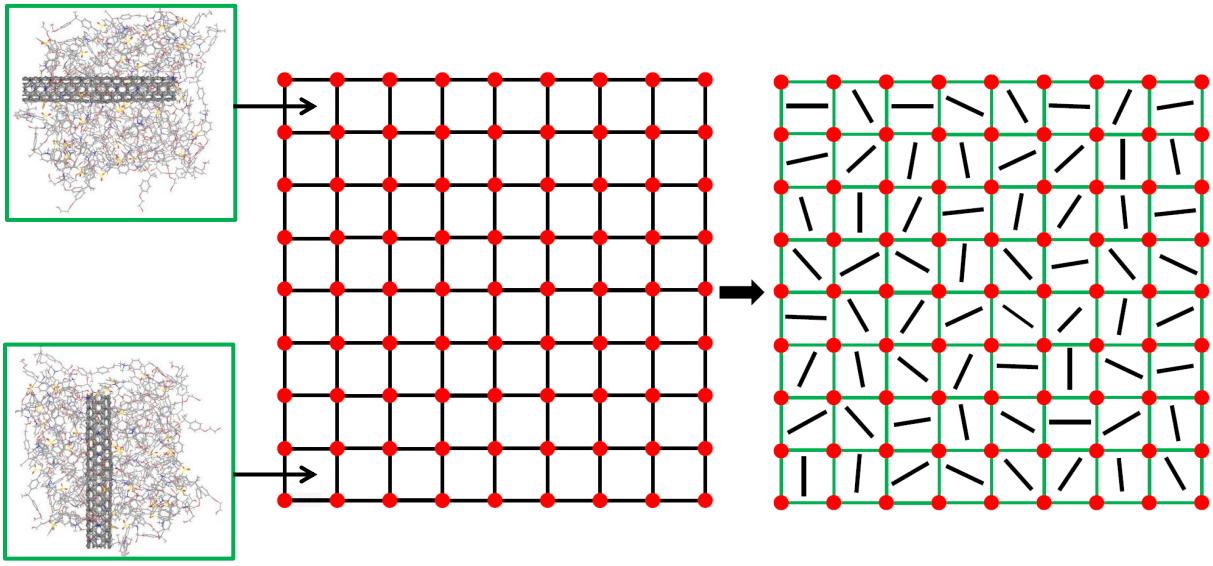

Figure 4.2: Left: 8x8 2D finite elements with 81 total nodes. Right: Each element is randomly assigned the elastic properties of a SWNT-epoxy lattice orientation.

For all configurations, every element was assigned a transversely isotopic C-matrix, which exhibits hexagonal symmetry. This was done probabilistically according to the desired nanotube distribution. The complete orientation space was represented by discretizing Rodrigues space, accounting for HCP symmetries, which will be described in detail in Section 4.2.2. Due to the symmetry, 50 of the 111 nodes in Rodrigues space shown in Fig. 4.3a are independent, as indicated by the red nodes in Fig. 4.3b. These nodes are assigned weights based on the symmetry and sampling volume in orientation space, shown in Fig. 4.4. In Fig. 4.5, the colors indicate the nodes that are equivalent. Center nodes '2' and '94' are equivalent, along with '47' and '111', '36' and '110, ect. The exact weight per node depends on how many equivalent nodes exist, and the volume weightage, q, of the node in the normalization constraint.

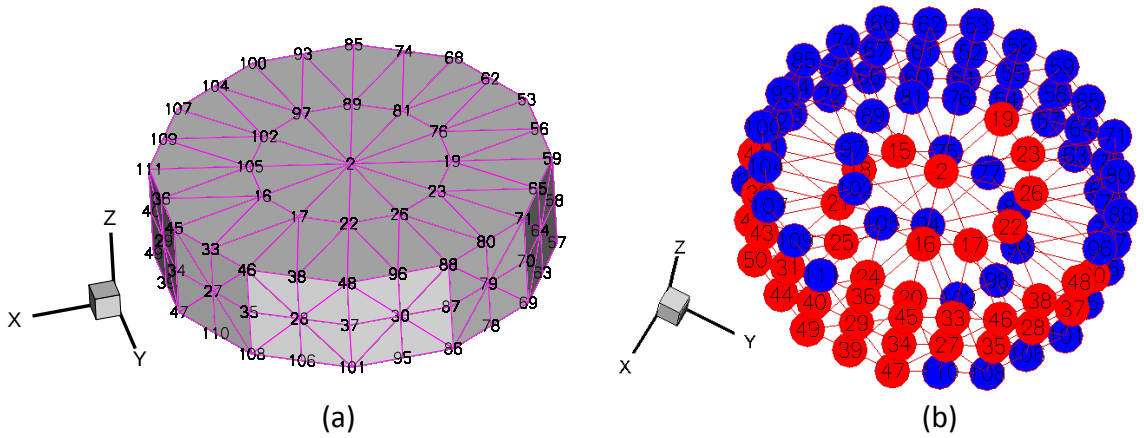

Figure 4.3: a. Discretized hexagonal region used to span all of orientation space. b. Independent nodes in Rodrigues space are marked in red.

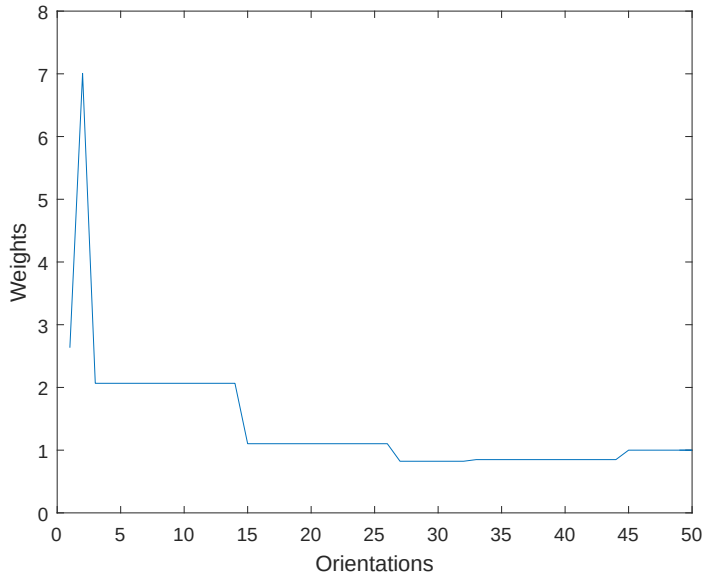

Figure 4.4: Weights for the 50 independent nodes for hexagonal symmetry in Rodrigues space.

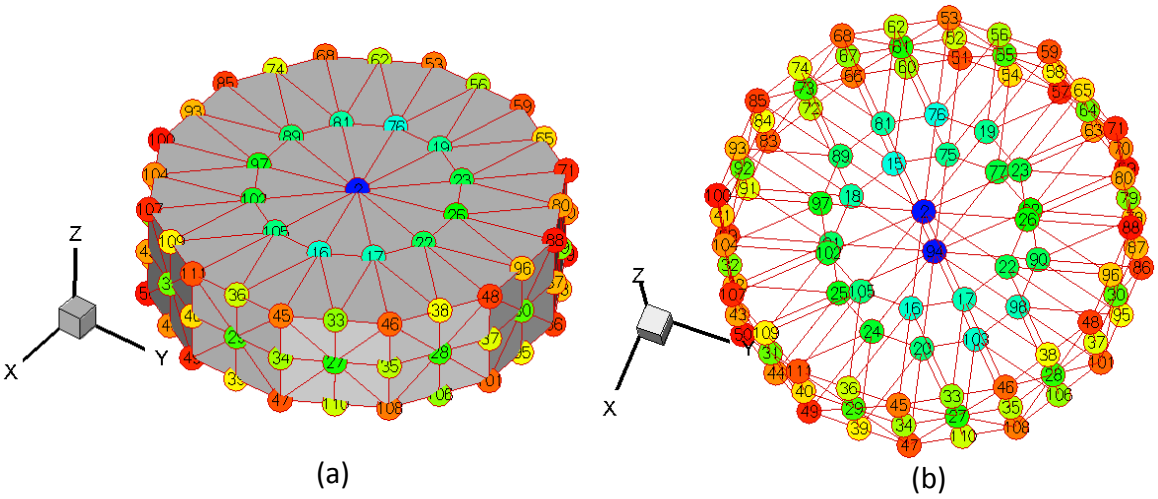

Figure 4.5: Equivalent nodes are represented by matching colors.

The probability of any orientation in a random composite occurring is given by normalizing Fig. 4.4 by the total value of the weights. This yields the probability distribution that will be used to assign elements their orientation. For a truly random distribution, the frequency that each of the 50 independent orientations, corresponding to Fig. 4.3b, will occur according to this probability distribution. When extra epoxy elements are added, the SWNT-epoxy elements follow the same probability distribution, but scaled accordingly. For example, if 50% neat epoxy are used, a given node has a 50% chance of being assigned a neat epoxy node, and the probability of being assigned any given orientation is $\frac{1}{2}$ of the probabilities resulting from normalizing the weights shown in Fig. 4.4. This method can be used to study the effects of nanotube alignment, and this will be done in Chapter 5.

4.2 ODF Multiscale Method

The orientation distribution function (ODF) was used to represent the alignment of SWNTs in SWNT-epoxy composites. The ODF for SWNT-epoxy composites was represented over the Rodrigues space discretely by implementing a Finite Element technique. ODFs representing random nanotube orientation are considered in this Chapter. ODFs representing fully aligned orientation are considered in Chapter 5 in order to study the effects of SWNT alignment. The SWNT-epoxy lattice obtained from molecular dynamics was used in conjunction with the ODF to generate an effective macroscopic stiffness matrix. The SWNT-epoxy lattice is transversely isotropic, and therefore contains hexagonal symmetry, and so the fundamental region of the hexagonal crystal system was used when sampling over orientation space.

4.2.1 ODF for SWNT-Epoxy Nanocomposites

Alignment of the nanotubes was represented using the ODF, which describes local densities of SWNTs over orientation space. The ODFs are defined by parametrizations for lattice rotations; here the hexagonal closed packed crystal geometry was used for the transversely isotropic composites. Commonly used representations include Euler-angles [143], and angle-axis representations, of which the most frequently used is the Rodrigues parametrization [144]. Discrization techniques are needed in order to convert the continuous orientation space into a finite degrees of freedom to optimize the material properties. The popular discritization techniques can be broken up into two major categories: global basis based representations and Finite Element based. The majority of schemes use global basis based representations via spherical harmonics [143, 145–147]. Finite Element based approaches represent the ODF by discritizing Rodrigues space via polynomial shape functions that are defined locally over an element [148, 149]. This technique allows any ODF to be represented by the nodal values of the Finite Element grid. This means that the dimensionality of the space is equal to the total independent nodes in the ODF discretization. The relationship between texture and properties is through linear homogenization relationships for both Fourier and Finite Element spaces. The Finite Element representations are accurate when sharp gradients are present, where as global basis functions lack local support and therefore would require a large number of terms to accurately capture sharp textures. Finite Element quadrature based integration techniques allow for volume averaged properties to be easily computed.

4.2.2 Modeling in Rodrigues Space

The complete orientation space of a nanotube-epoxy system can be reduced to a smaller subset; the fundamental region. The fundamental region a subset of orientation space such that all orientations are uniquely represented accounting for symmetries. The fundamental region for the hexagonal symmetry group used results in a structure shown in Fig. 4.6. The 12 lateral faces forming the prismatic volume are given by symmetries about the $\langle 0001 \rangle$ (c–axis) axis and the $\langle 1000 \rangle$ family of axes. The surface of the fundamental region is formed by bounding planes that can be grouped into pairs, where the planes of each pair are equivalent due to symmetry, as shown in Fig. 4.6 [151]. Every orientation is uniquely represented within the fundamental region by a coordinate, $\boldsymbol{g}$, which is the parametrization for the rotation (eg. Euler angles, Rodrigues vector, etc.). The local density of SWNT alignment over the fundamental region is given by the ODF, $\mathcal{A}(\boldsymbol{g})$. The ODF at an orientation $\boldsymbol{g}$, assuming that the ODF is a continuous function in the fundamental region, is defined as:

$$\mathcal{A}(\boldsymbol{g}) = \lim_{\delta \to 0} \frac{v_f(R_\delta)}{\int_{R_\delta} d\boldsymbol{g}}, \tag{4.30}$$

where $v_f(R_\delta)$ is the volume fraction of nanotubes that have orientations that occur within volume R_δ.

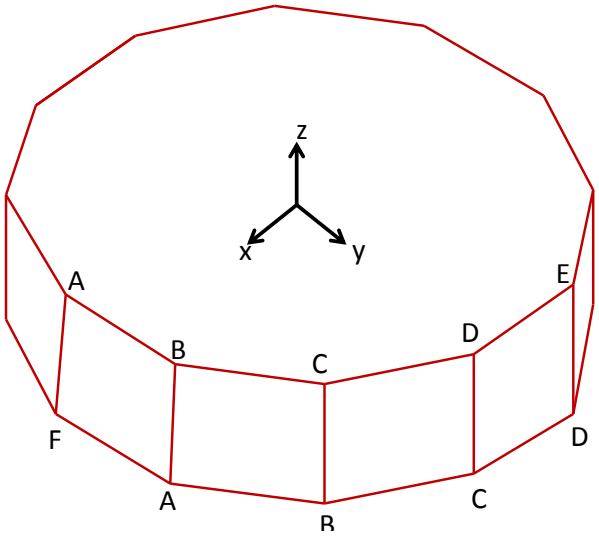

Figure 4.6: Fundamental region for HCP crystals using Rodrigues parameterization.

The Finite Element ODF representation uses parameterizations for the SWNT-epoxy lattice rotation, which together with the HCP crystal symmetry define the problem domain. While the most common method of representing textures is through the use of Euler angles, here the axis-angle characterization of the orientation space proposed by Rodrigues was used [143, 148, 150]. The axis-angle characterization is based on the unique association of an orientation with an axis of rotation, **n**, and a rotation angle, θ, about the axis. The Rodrigues' parametrization, **r**, is scaled as $\mathbf{r} = \mathbf{n}tan(\frac{\theta}{2})$. A proper rotation, **R**, relates the lattice orientation to a reference orientation. The rotation can given in terms of the Rodrigues paramrization as:

$$\mathbf{R} = \frac{1}{1 + \mathbf{r}.\mathbf{r}}\big((\mathbf{I}(1 - \mathbf{r}.\mathbf{r}) + 2(\mathbf{r} \otimes \mathbf{r} + \mathbf{I} \times \mathbf{r})\big) \tag{4.31}$$

The ODF, $\mathcal{A}$, contains the local density of nanotubes over the fundamental region. If a section of the fundamental region is designated as $\Re^*$, then the volume fraction of nanotubes in that section is given as $v_f(\Re^*) = \int_{\Re^*} \mathcal{A} dv$. The ODF is normalized to unity over the fundamental region. The volume element is given as $dv = \sqrt{det\boldsymbol{g}} r_1 dr_2 dr_3$, and is scaled by $\sqrt{det\boldsymbol{g}} = cos^4(\theta/2)$, since the orientation space is non-Euclidean, where $\boldsymbol{g}$ is the

metric for the space. Given the orientation-dependent property for a single nanocomposite, $\chi(\boldsymbol{r}, t)$, any equivalent macroscropic property can be expressed as a value or expectation value by:

$$< \chi >= \int_{\mathcal{R}} \chi(\boldsymbol{r}, t)\mathcal{A}(\boldsymbol{r}, t)dv \tag{4.32}$$

4.2.3 Property Representation and Optimization in Rodrigues Space

Matrix representation of several properties of the ODF are possible due to the Finite Element discretization of the orientation space, and the Finite Element integration schemes via Gauss quadrature. The ODF is discretized into N independent nodes with N_{elem} finite elements and N_{int} integration points per element. As mentioned earlier, the ODF is normalized to unity over the fundamental region, and this can be written as a constraint:

$$\int_{\mathcal{R}} \mathcal{A}dv = \sum_{n=1}^{N_{elem}} \sum_{m=1}^{N_{int}} A(\boldsymbol{r}_m) w_m |J_n| \frac{1}{(1 + \boldsymbol{r}_m \cdot \boldsymbol{r}_m)^2} = 1, \tag{4.33}$$

where $A(\boldsymbol{r}_m)$ is the value of the ODF at the n^{th} integration point possessing global coordinate $\boldsymbol{r}_m$ of the n^{th} element, w_m is the integration weight of the m^{th} integration point, and $|J_n|$ is the Jacobian determinant of the n^{th} element. This can be written as a linear constraint:

$$\boldsymbol{q}^{int^T} \boldsymbol{A}^{int} = 1, \tag{4.34}$$

where $q_i^{int} = w_i |J_i| \frac{1}{(1+r_i \cdot r_i)^2}$, and $A_i^{int} = A(\boldsymbol{r}_i)$. Each i corresponds to a combination of (n, m), $i = 1, \ldots, N_{int} \times N_{elem}$. A system with multiple nanotube-epoxy lattices can be expressed in a linear form if the orientation-dependent property for a single lattice, $\chi, (\boldsymbol{r})$ is known:

$$< \chi >= \int_{\mathcal{R}} \chi(\boldsymbol{r})\mathcal{A}(\boldsymbol{r})dv = \sum_{n=1}^{nel} \sum_{m=1}^{nint} \chi(\boldsymbol{r}_m) A(\boldsymbol{r}_m) w_m |J_n| \frac{1}{(1 + \boldsymbol{r}_m \cdot \boldsymbol{r}_m)^2}. \tag{4.35}$$

Similar to Eq 4.33, this can be written to as an equivalent linear equation in the ODF:

$$< \chi >= \boldsymbol{p}^{int^T} \boldsymbol{A}^{int}, \tag{4.36}$$

where $p_i^{int} = \chi(\boldsymbol{r}_i) w_i |J_i| \frac{1}{(1+r_i \cdot r_i)^2}$ and $A_i^{int} = A(\boldsymbol{r}_i)$, $i = 1, \ldots, N_{int} \times N_{elem}$.

The symmetry of the ODF is an additional constraint that must be considered. Orientations on each pair of planes in the fundamental region are equivalent under the symmetries.

The HCP fundamental region was shown in Fig. 4.6, and symmetries exist about the $\langle 0001 \rangle$ (c–axis) axis and the $\langle 1000 \rangle$ family of axes [151]. This symmetry is not represented by the space of ODF values at the integration points of the FE mesh. To enforce the symmetry conditions, a reduced set of nodes; independent nodal points, are used rather than the integration points. Independent nodal points are obtained by accounting for the symmetry conditions at the boundary of the ODF. To convert the independent nodal values, $\boldsymbol{A}^{node}$, to the integration point values, $\boldsymbol{A}^{int}$, a matrix of the shape functions, $\boldsymbol{H}$, is used:

$$\boldsymbol{A}^{int} = \boldsymbol{H}\boldsymbol{A}^{node} \tag{4.37}$$

Due to symmetry in fundamental region, $\boldsymbol{A}^{node}$ is sufficient to describe the ODF. The linear ODF constraint from Eq. 4.34 can now be written in terms of a modified $\boldsymbol{q}^{node^T} = \boldsymbol{q}^{int^T}\boldsymbol{H}$ as:

$$\boldsymbol{q}^{node^T}\boldsymbol{A}^{node} = 1, \boldsymbol{A}^{node} \geq 0. \tag{4.38}$$

Eq. 4.38 means that the complete set of all possible ODFs is a hyperplane in the space of independent nodal values, called the 'material plane'. Likewise, Eq. 4.36 can now be written in terms of a modified $\boldsymbol{p}^T \equiv \boldsymbol{p}^{int^T}\boldsymbol{H}$ to specify properties:

$$< \chi >= \boldsymbol{p}^T\boldsymbol{A}. \tag{4.39}$$

When more than one property is being calculated, $\boldsymbol{p}$ will be a matrix. The ODF must be positive, and this constrains the nodal values of the ODF to being positive as well, $\boldsymbol{A} \geq 0$. In summary, the space of all possible ODFs is subjected to three constraints: normalization, positiveness and symmetry.

4.2.4 ODF for Randomly Oriented Nanotubes

ODFs can be constructed to represent a fully random composite, fully aligned composite, and various percentages of aligned nanotubes with the rest being random. In this Section, randomly oriented nanotubes are considered, and alignment will be considered in Chapter 5. The ODF indicates the probability of finding a given SWNT orientation within a macroscopic sample. This is an alternative method to using the Finite Element multiscale method described in Section 4.1.4, and is less computationally expensive. The direction of preferable nanotube alignment was chosen to be the z-direction, or the $< 001 >$ direction. So, for increasing amounts of nanotube alignment, there will be more SWNT aligned in the z-direction. To visually represent the nanotube orientation, pole figures were used. Pole

figures are a stereographic projections representing the orientation distribution function. Only the z-axis, or $< 001 >$ axis is plotted, so with increasing alignment it is expected the $< 001 >$ pole figure will show a higher intensity of nanotubes aligned in that direction. Likewise, the $< 100 >$ and $< 010 >$ pole figures will show an increasing intensity for SWNTs perpendicular to those directions. In this Section, a random orientation is desired, so none of the pole figures should indicate any orientation being preferential. The $< 001 >$ $< 100 >$ and $< 010 >$ pole figures are shown in Figs. 4.7a, 4.8a, and 4.8b, respectively. They all show that there is no orientation preference and and that all orientations are equally represented. The scale of the legend is determined by the case of maximum alignment. The cross section of the ODF is shown in Fig. 4.7b, and again shows that the desired random ODF has been achieved.

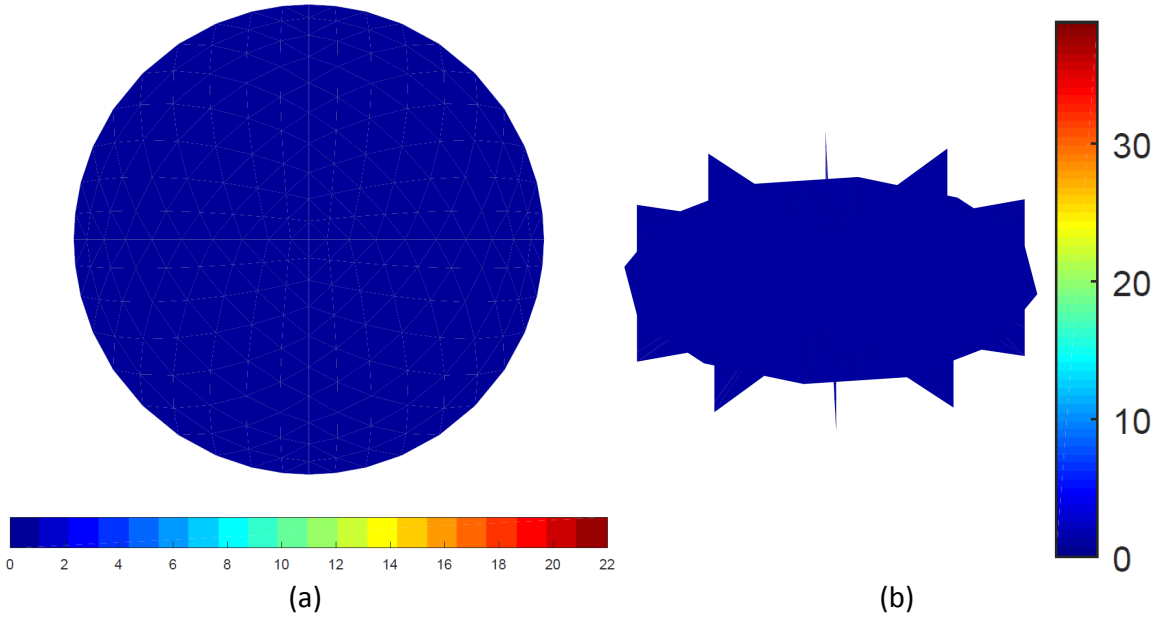

Figure 4.7: a. $< 001 >$ pole figure and b. cross-section of the ODF for 0% SWNT alignment.

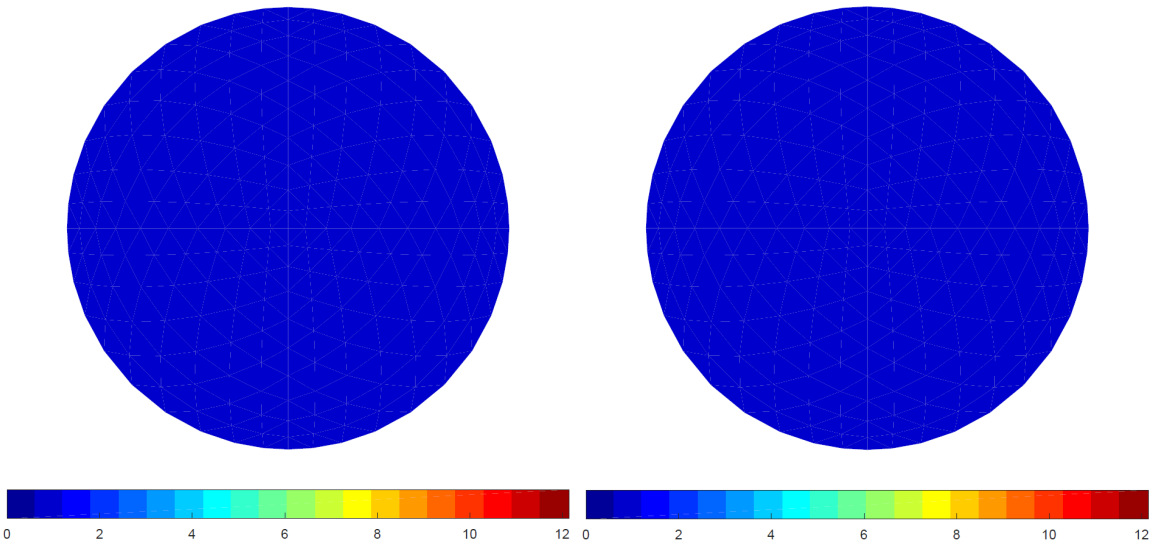

Figure 4.8: a. $< 100 >$ and b. $< 010 >$ pole figures for 0% SWNT alignment.

4.2.5 Varying Volume Fraction of SWNT

One limitation of the ODF method compared to the Finite Element multiscale method is that this approach does not allow for direct control over the volume fraction of the SWNT. The orientation-dependent property obtained from Eq. 4.39 will have the same volume fraction as the representative SWNT-epoxy lattice, which is the microscopic basis for the ODF. In order to vary the volume fraction, bounding methods using the parallel and series rule of mixtures models were used to find the upper and lower bounds on the composite elastic properties based on energy methods [152, 153]. The parallel, or Voigt, model where uniform strain in both phases is considered gives the composite stiffness matrix, $C^{\bar{\epsilon}}$:

$$C^{\bar{\epsilon}} = C_1 V_1 + C_2 V_2, \tag{4.40}$$

where C_1 and C_2 are the stiffness matrices of materials 1 and 2 respectively. V_1 and V_2 are the volume fractions of material 1 and 2, and so a constraint is that $V_1 + V_2 = 1$. If instead, uniform stress in both phases is considered, this will yield the composite compliance matrix, $S^{\bar{\sigma}}$, for the series or Reuss model:

$$S^{\bar{\sigma}} = S_1 V_1 + S_2 V_2. \tag{4.41}$$

The compliance matrix is the inverse of the stiffness matrix, and so in terms of the stiffness matrix, Eq. 4.41 can be written as:

$$C^{\bar{\sigma}} = \left(C_1^{-1} V_1 + C_2^{-1} V_2 \right)^{-1}. \tag{4.42}$$

Eqs. 4.40 and 4.42 can be shown to be upper and lower bounds though the theorem of minimum potential energy and theorem of complementary energy, respectively. The strain energy stored in a material over volume is given as:

$$U = \frac{1}{2} \int_V \sigma_i \epsilon_i dV. \tag{4.43}$$

In the elastic region, where the stress and strain states are assumed to be macroscopically uniform, stress can be written in terms of strain by the stiffness matrix, C_{ij}: $\sigma_i = C_{ij}\epsilon_j$. Similarly, strain can be written in terms of stress via the compliance matrix, S_{ij}, $\epsilon_i = S_{ij}\sigma_j$. This allows Eq. 4.43 to be written in terms of just strain or stress:

$$U = \frac{1}{2} \int_V (C_{ij}\epsilon_j)\epsilon_i dV = \frac{1}{2} \int_V \sigma_i (S_{ij}\sigma_j) dV \tag{4.44}$$

For the upper bound uniform strain is assumed, $\bar{\epsilon}$, in both of the materials. If the applied strain is required to only satisfy compatibility and the displacement boundary conditions, thus allowing the stress to be discontinuous, the actual energy (U) is less than or equal to the elastic strain energy ($U^{\bar{\epsilon}}$):

$$U \leq U^{\bar{\epsilon}}. \tag{4.45}$$

Using Eq. 4.48 in terms of strain, Eq. 4.45 can be expanded as such:

$$\frac{1}{2} \int_V (C_{ij}^{eff} \epsilon_j)\epsilon_i dV \leq \frac{1}{2} \int_V (C_{ij}^{\bar{\epsilon}} \epsilon_j)\epsilon_i dV, \tag{4.46}$$

where $C_{ij}^{\bar{\epsilon}}$ is the stiffness from the assumed strain state, and C_{ij}^{eff} is the actual stiffness of the composite. This gives that the actual stiffness is less than the stiffness of the assumed strain state.

$$C_{ij}^{eff} \leq C_{ij}^{\bar{\epsilon}} \tag{4.47}$$

For the lower bound, uniform stress $\bar{\sigma}$, is assumed in both of the materials. If an applied stress is required to only satisfy equilibrium and the traction boundary conditions, thus allowing the strain to be discontinuous, the actual energy (U) is less than or equal to the elastic strain energy ($U^{\bar{\sigma}}$)

$$U \leq U^{\bar{\sigma}}. \tag{4.48}$$

Using Eq. 4.48 in terms of strain, Eq. 4.48 can be expanded to obtain:

$$\frac{1}{2}\int_V \sigma_i(S_{ij}^{eff}\sigma_j)dV \leq \frac{1}{2}\int_V \sigma_i(S_{ij}^{\bar{\sigma}}\sigma_j)dV, \tag{4.49}$$

where $S_{ij}^{\bar{\sigma}}$ is the compliance from our assumed stress states, and S_{ij}^{eff} is the actual stiffness of the composite. This yields the relation that the actual compliance is less than the compliance of the assumed stress state, giving an upper bound on compliance:

$$S_{ij}^{eff} \leq S_{ij}^{\bar{\sigma}}. \tag{4.50}$$

In terms of stiffness, this yields the lower bound:

$$C_{ij}^{eff} \geq C_{ij}^{\bar{\sigma}}. \tag{4.51}$$

Putting this all together in terms of Eqs. 4.40 and 4.42, the effective composite stiffness matrix, C^{eff}, lies between the uniform strain state of the parallel model and uniform stress state of the series model:

$$\left(C_1^{-1}V_1 + C_2^{-1}V_2\right)^{-1} \leq C^{eff} \leq C_1V_1 + C_2V_2. \tag{4.52}$$

4.2.6 Multiscale Modeling

In calculating the effective macroscopic properties, homogeneity for the stress and strain tensors was assumed. So, the ensemble averages for stress, $< \sigma_{ij} >$, and strain, $< \epsilon_{ij} >$, from all the microscopic lattices are related by an effective macroscopic stiffness or compliance matrix:

$$< \sigma_{ij} >= C_{ijkl}^{eff} < \epsilon_{ij} > \tag{4.53}$$

$$< \epsilon_{ij} >= S_{ijkl}^{eff} < \sigma_{ij} > . \tag{4.54}$$

The ODF methods allows the macroscopic properties to be calculated from a single microscopic lattice for random nanocomposites, and nanocomposites with preferred orientations. Two methods are used to find the upper bound and the lower bounds for the effective macroscopic stiffness matrices. The upper bound method, known as the Voigt approximation [154, 155], assumes that all the strain to be constant in all of the lattices, or equal to the ensemble average. Therefore, the strain is required to satisfy compatibility and the displacement boundary conditions, but the stress is not required to satisfy equilibrium or trac-

tion boundary conditions. Using the ODF, the elastic constants are calculated via weighted integration over all orientations, where the weighting function is the ODF describing the nanotube orientations. From Eq. 4.32 and Eq. 4.53, a value for C_{ijkl}^{eff} can be found. The orientation dependent property here is the stiffness matrix for a single lattice, $C_{ijkl}(\boldsymbol{r})$ where the Rodrigues parametrization is $\boldsymbol{r}$, and the ODF for the desired nanotube orientation is given by $\mathcal{A}$:

$$< C_{ijkl} >= \int_{\mathcal{R}} C_{ijkl}(\boldsymbol{r})\mathcal{A}(\boldsymbol{r})dv. \tag{4.55}$$

This expectation value is the upper bound, or Voigt approximation:

$$C_{ijkl}^{V} = \int_{\mathcal{R}} C_{ijkl}(\boldsymbol{r})\mathcal{A}(\boldsymbol{r})dv \;\text{ for }\; \epsilon_{ij} = constant. \tag{4.56}$$

This is the same as the parallel model for stiffness shown in Eq. 4.40, where the 50 independent orientations from Fig. 4.3b are averaged over in Rodrigues space.

Similarly, the lower bound method, known as the Reuss approximation [154, 155], assumes that all the stress to be constant in all of the lattices, or equal to the ensemble average. Therefore, the stress is required to satisfy equilibrium and the traction boundary conditions, but the strain is not required to satisfy compatibility or displacement boundary conditions. As before, from Eq. 4.32 and Eq. 4.54, S_{ijkl}^{eff} can be obtained. The orientation dependent property here is the compliance matrix for a single lattice, $S_{ijkl}(\boldsymbol{r})$:

$$< S_{ijkl} >= \int_{\mathcal{R}} S_{ijkl}(\boldsymbol{r})\mathcal{A}(\boldsymbol{r})dv. \tag{4.57}$$

This expectation value is the Reuss approximation, which is an upper bound for compliance:

$$S_{ijkl}^{R} = \int_{\mathcal{R}} S_{ijkl}(\boldsymbol{r})\mathcal{A}(\boldsymbol{r})dv \;\text{ for }\; \sigma_{ij} = constant \tag{4.58}$$

This is the same as the series model for stiffness shown in Eq. 4.42, except the 50 independent orientations were averaged over in Rodrigues space from Fig. 4.3b. By inverting the compliance to obtain the stiffness matrix, the Reuss approximation gives a lower bound for stiffness:

$$C_{ijkl}^{R} = (S_{ijkl}^{R})^{-1}. \tag{4.59}$$

4.3 Results

For randomly oriented nanotubes, two multiscale approaches were used to obtain the elastic properties of the nanocomposites. The Finite Element approach, described in Section 4.1 was the first method used. Depending on the percentage of neat epoxy units, elements were probabilistically assigned with the elastic properties of a SWNT-epoxy nanocomposite from Chapter 2 at a random orientation, or with the elastic properties of neat epoxy. The second approach was described in Section 4.2. An ODF for randomly oriented composites was generated, and using the results of Chapter 2, the stiffness matrix was calculated. The Voigt and Reuss models were used to find the upper and lower bounds of the stiffness matrix for the randomly oriented composite at the volume fraction of the MD cell using Eqs 4.56 and 4.59, respectively. The volume fraction of the Molecular Dynamics cells can be found in table 4.2. The volume of all the cells was around 52,000 $Å^3$, and the effective radius of the SWNT was taken as the midpoint between the equilibrium edge of the edge of the SWNT, and the edge of the epoxy, as shown in Fig. 4.9. In order to vary the volume fraction of SWNT, a rule of mixtures approach described Section 4.2.5 was implemented. The parallel rule of mixtures was used in conjunction with the upper bound of the randomly oriented nanocomposite and neat epoxy to find the upper bound value at various volume fractions of nanotubes using Eq. 4.40. Similarly, the series rule of mixtures was used with the lower bound of the randomly oriented nanocomposite and neat epoxy to find the lower bound value at various volume fractions of nanotubes using Eq. 4.41.

Repeat Units	Nanotube Length (Å)	Volume of SWNT ($Å^3$)	Volume Fraction of SWNT
11	27.05	1623	3.1%
13	31.97	1918	3.7%
15	36.89	2213	4.3%

Table 4.2: Volume fraction of SWNT in MD nanocomposite cells.

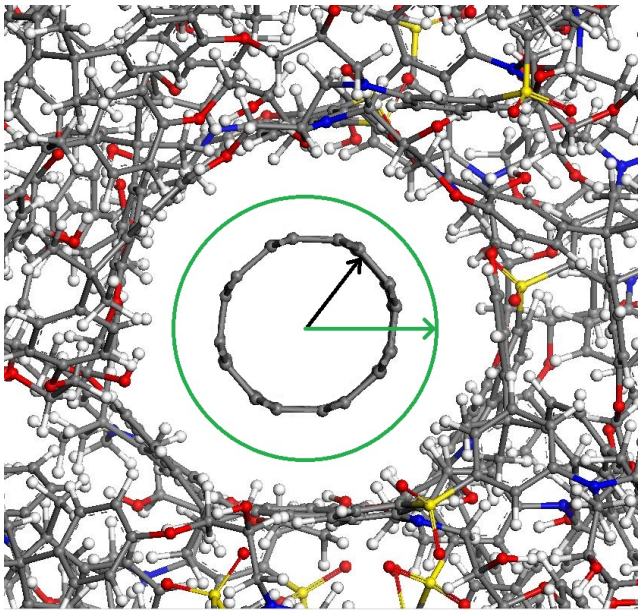

Figure 4.9: Effective radius of the SWNT in volume fraction calculations is shown in green.

The results in this Section were plotted as a function of neat epoxy units out of convenience due to the nature of the formulation. While the volume fraction of SWNT is truly the quantity of interest, this method is equivalent. The exact volume fraction of SWNTs can be calculated as:

$$\Phi_{SWNT} = (1 - \Phi_{neatepoxy}) * \Phi_{MDlattice}, \tag{4.60}$$

where $\Phi_{neatepoxy}$ represents the volume fraction of neat epoxy units, and $\Phi_{MDlattice}$ was given in Table 4.2; and will be equal to 0.031 for nanocomposites with 11 repeat unit SWNTs, 0.037 for nanocomposites with 13 repeat unit SWNTs, and 0.043 for systems with 15 repeat unit (infinite) SWNTs.

4.3.1 Multiscale Results for Various SWNT-Epoxy Nanocomposites

4.3.1.1 Pristine SWNT-Epoxy (11 Repeat Units)

The multiscale results for the Young's modulus and shear modulus of the isotropic, randomly oriented, discontinuous, pristine SWNT-epoxy system with 11 repeat units are reported in this section. The Finite Element results, ODF upper bound, and the ODF lower bound for the Young's modulus vs. percentage of neat epoxy units at various temperatures are seen in Figs. 4.10a, 4.11a, and 4.12a, respectively. The results superimposed for the various methods are plotted in Fig. 4.13a. The Finite Element results shows a near linear

decrease as the percent of epoxy units increases, and the ODF upper bound results in a linear decrease due to the parallel model. The ODF lower bound shows a non-linear but similar trend due to the use of the series model. As expected, the modulus decreases with increasing temperature. The slopes essentially result from MD results for a single lattice of pure epoxy (the result at 100% of neat epoxy) and the equivalent isotropic result of a single lattice of the nanocomposite at the given temperature, and so some minor inconsistencies for various temperatures is to be expected. For the shear modulus, the Finite Element results, ODF upper bound, and the ODF lower bound are seen in Figs. 4.10b, 4.11b, and 4.12b, respectively. The superimposed results are plotted in Fig. 4.13b. The same trends are seen for the shear modulus as for the Young's modulus for the isotropic system. For both the Young's modulus and shear modulus, the Finite Element results are in between the upper bound and lower bound ODF results, and closer to the upper-bound results. For the randomly oriented, pristine, SWNT-epoxy system with 11 repeat units; the Finite Element results, ODF upper bound, and the ODF lower bound all give very similar results in the temperature range of 1 K - 350 K investigated.

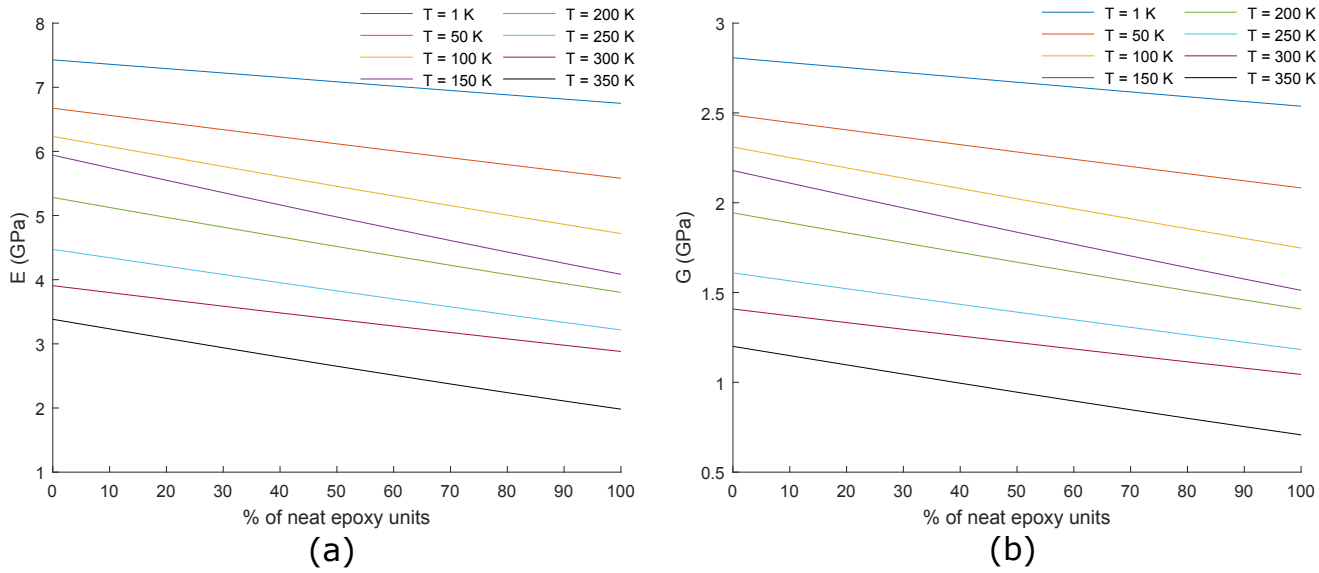

Figure 4.10: Finite Element results for the a. Young's modulus and b. shear modulus vs. % of neat epoxy for the pristine nanocomposite (11 repeat units) at various temperatures.

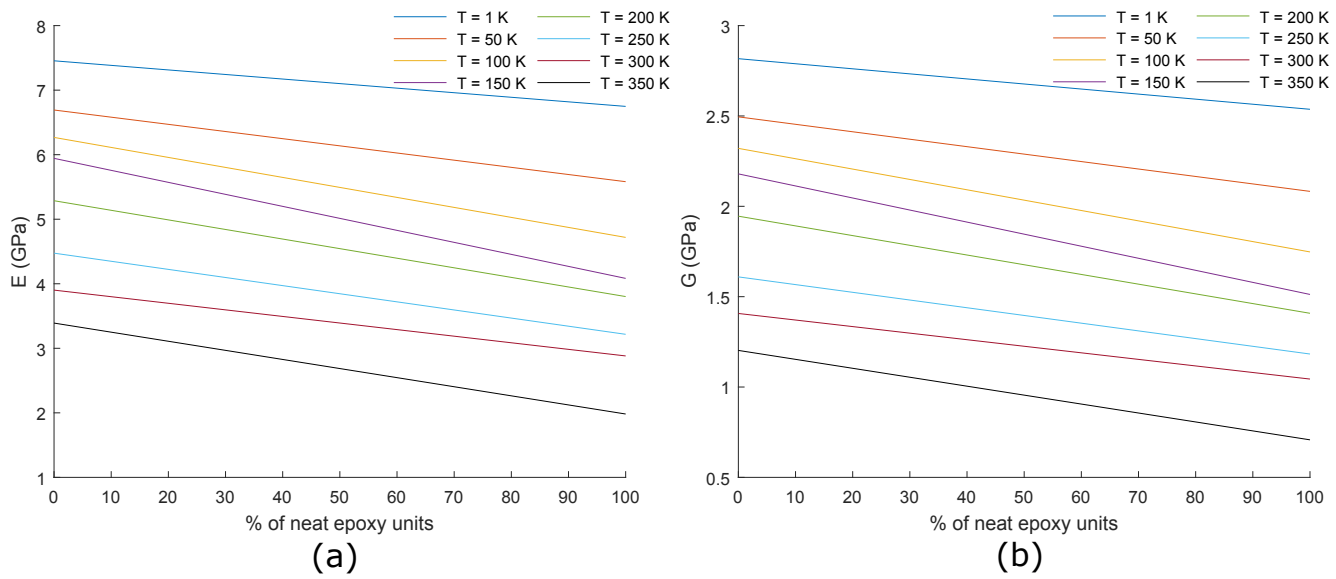

Figure 4.11: ODF upper bound for the a. Young's modulus and b. shear modulus vs. % of neat epoxy for the pristine nanocomposite (11 repeat units) at various temperatures.

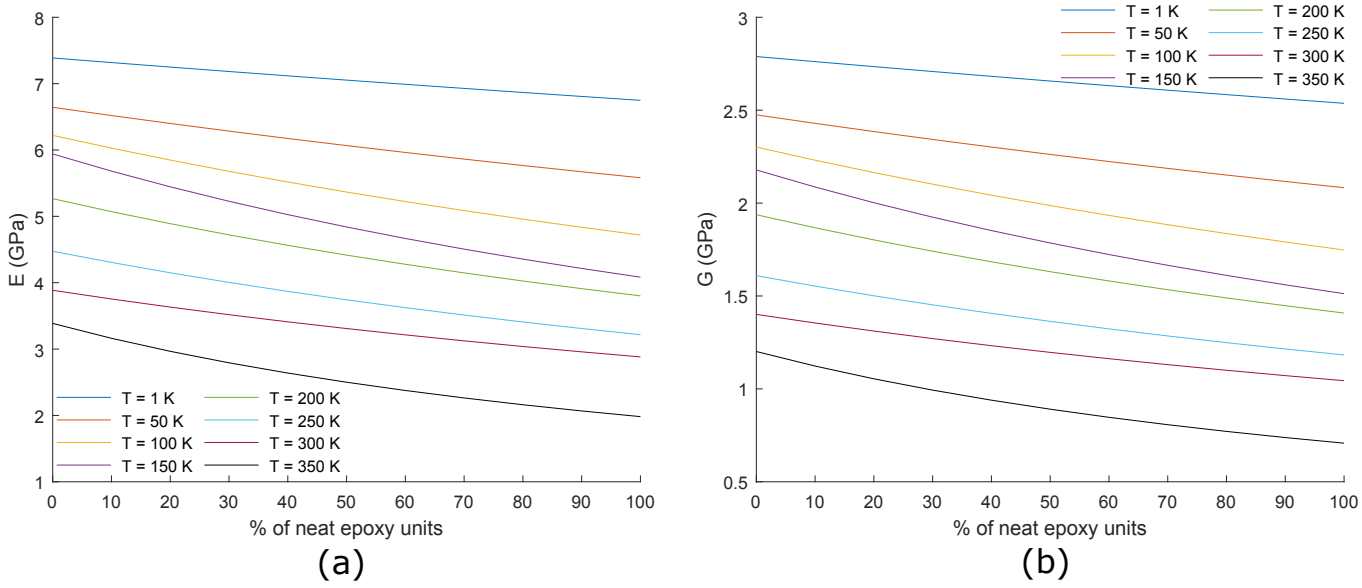

Figure 4.12: ODF lower bound for the a. Young's modulus and b. shear modulus vs. % of neat epoxy for the pristine nanocomposite (11 repeat units) at various temperatures.

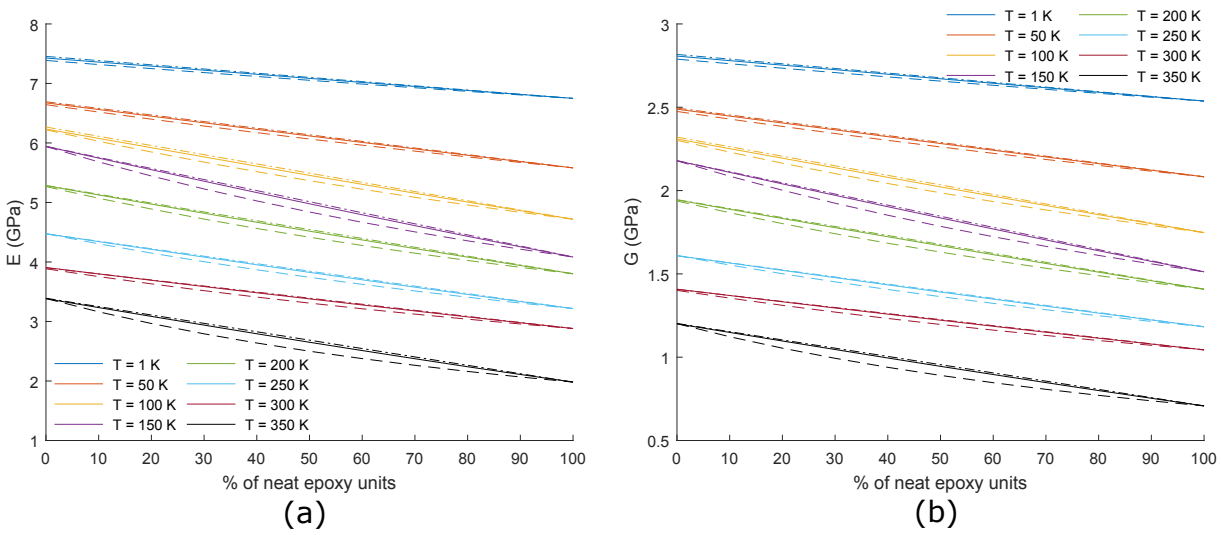

Figure 4.13: Comparison of the ODF upper bound, lower bound and Finite Element results for the a. Young's modulus and b. shear modulus vs. % of neat epoxy units seen in Figs. 4.10, 4.11 and 4.12.

4.3.1.2 Functionalized SWNT-Epoxy (11 Repeat Units)

The multiscale results for the Young's modulus and shear modulus of the isotropic, randomly oriented, discontinuous, functionalized SWNT-epoxy system with 11 repeat units are reported in this section. The Finite Element results, ODF upper bound, and the ODF lower bound for the Young's modulus vs. percentage of neat epoxy units at various temperatures are seen in Figs 4.14a, 4.15a, and 4.16a, respectively. The results superimposed for the various methods are plotted in Fig. 4.17a. Much like the pristine system, the Finite Element results shows a near linear decreases as the percent of epoxy units increases, and the ODF upper bound results shows a linear decrease. The ODF lower bound shows a non-linear but similar trend due to the use of the series model. As expected, the modulus decreases with increasing temperature. For the shear modulus, the Finite Element results, ODF upper bound, and the ODF lower bound are seen in Figs. 4.14b, 4.15b, and 4.16b, respectively. The superimposed results are plotted in Fig. 4.17b. The same trends are seen for the shear modulus as for the Young's modulus in the equivalent isotropic system. For both the Young's modulus and shear modulus, the Finite Element results are in between the upper bound and lower bound ODF results, and closer to the upper-bound results. For the randomly oriented, functionalized, SWNT-epoxy system with 11 repeat units; the Finite Element results, ODF upper bound, and the ODF lower bound all give very similar results in the temperature range of 1 K - 350 K investigated.

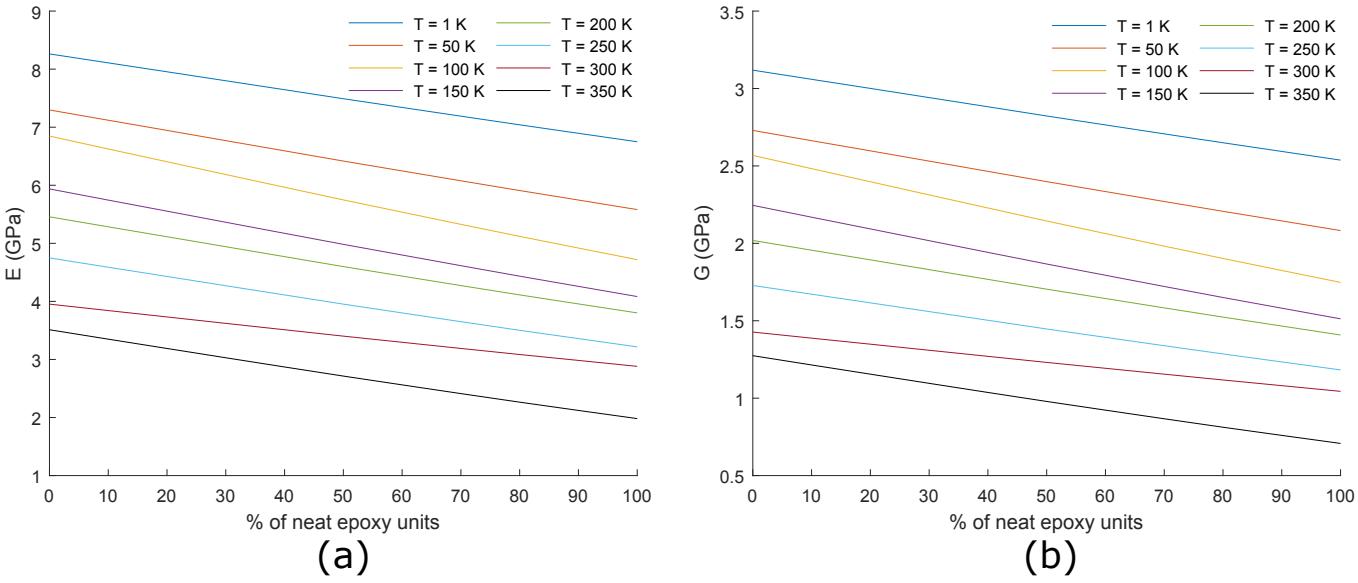

Figure 4.14: Finite Element results for the a. Young's modulus and b. shear modulus vs. % of neat epoxy for the functionalized nanocomposite (11 repeat units) at various temperatures.

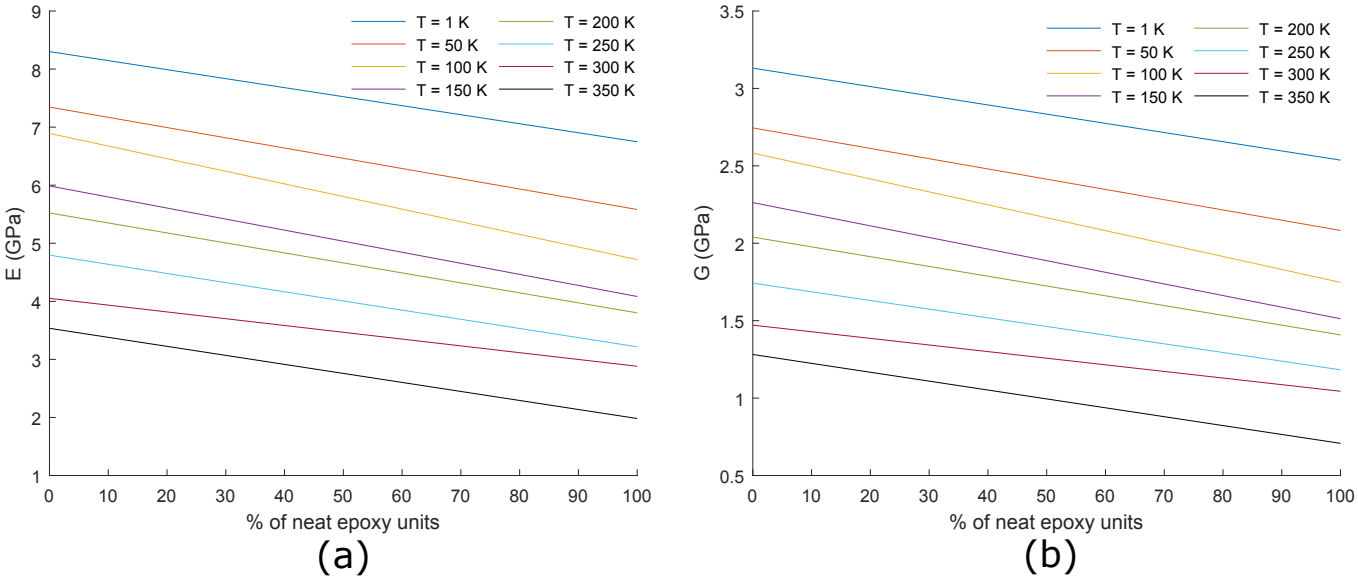

Figure 4.15: ODF upper bound for the a. Young's modulus and b. shear modulus vs. % of neat epoxy for the functionalized nanocomposite (11 repeat units) at various temperatures.

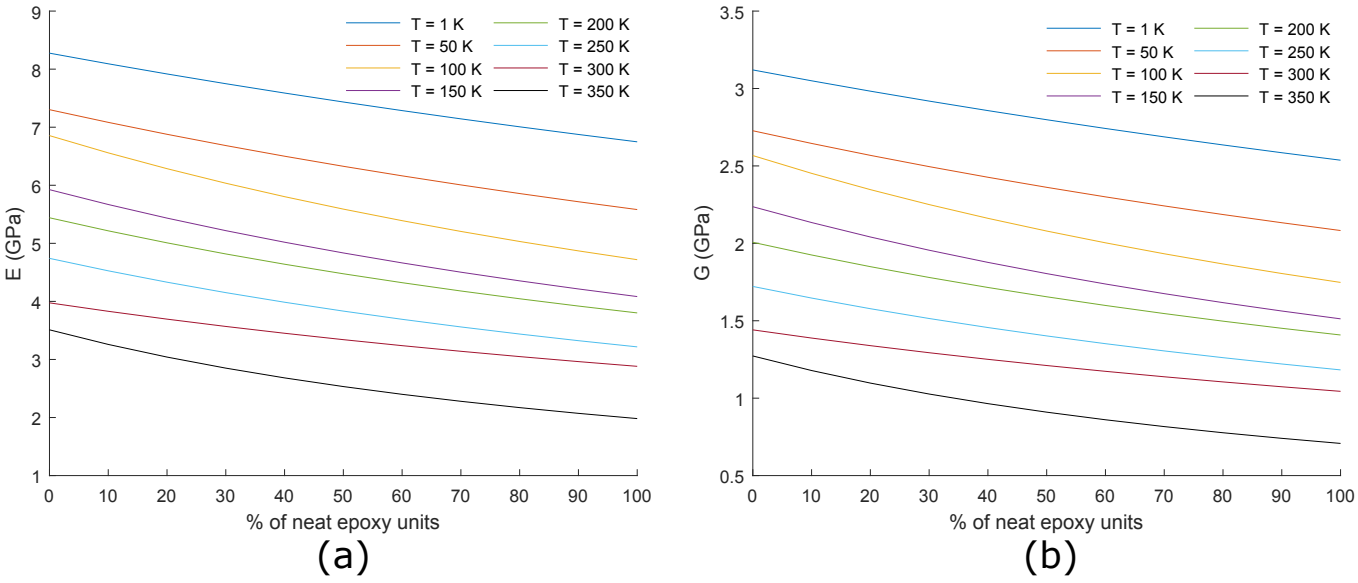

Figure 4.16: ODF lower bound for the a. Young's modulus and b. shear modulus vs. % of neat epoxy for the functionalized nanocomposite (11 repeat units) at various temperatures.

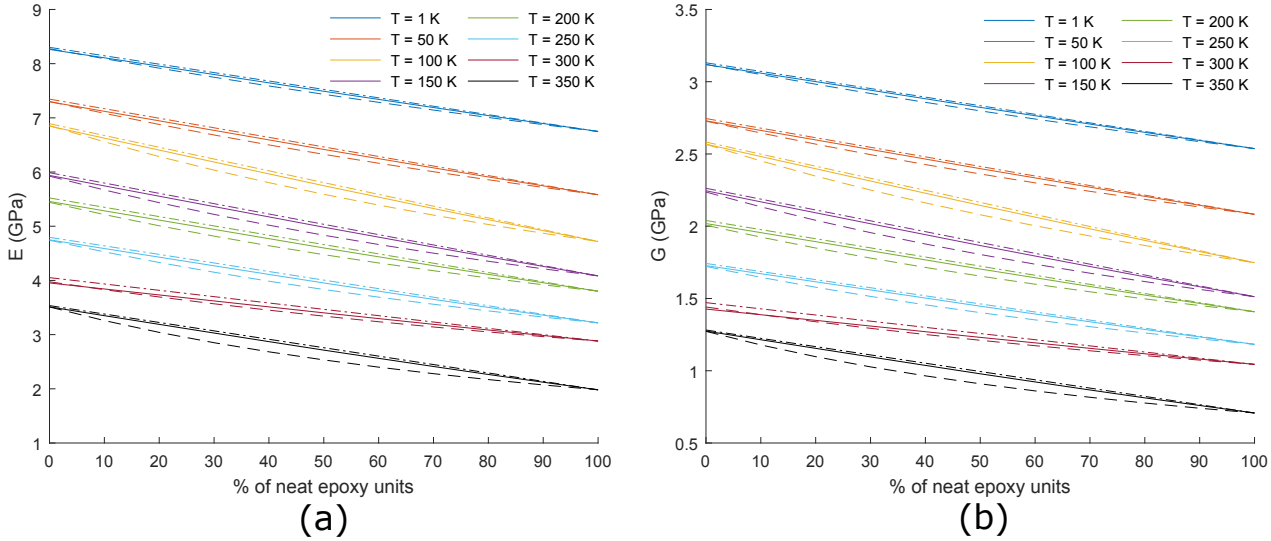

Figure 4.17: Comparison of the ODF upper bound, lower bound and Finite Element results for the a. Young's modulus and b. shear modulus vs. % of neat epoxy units seen in Figs. 4.14, 4.15 and 4.16.

4.3.1.3 Pristine SWNT-Epoxy (13 Repeat Units)

The multiscale results for the Young's modulus and shear modulus of the isotropic, randomly oriented, discontinuous, pristine SWNT-epoxy system with 13 repeat units are reported in this section. The Finite Element results, ODF upper bound, and the ODF lower bound for the Young's modulus vs. percentage of neat epoxy units at various temperatures are seen in Figs. 4.18a, 4.19a, and 4.20a, respectively. The results superimposed for the various methods are plotted in Fig. 4.21a. For the shear modulus, the Finite Element results, ODF upper bound, and the ODF lower bound are seen in Figs. 4.18b, 4.19b, and 4.20b respectively. The superimposed results are plotted in Fig. 4.21b. The Young's modulus and shear modulus show similar trends to the system with 11 repeat units, with the Finite Element results lying in between the upper and lower ODF bounds. For the randomly oriented, pristine, SWNT-epoxy system with 13 repeat units; the Finite Element results, ODF upper bound, and the ODF lower bound all give very similar results in the temperature range of 1 K - 350 K investigated.

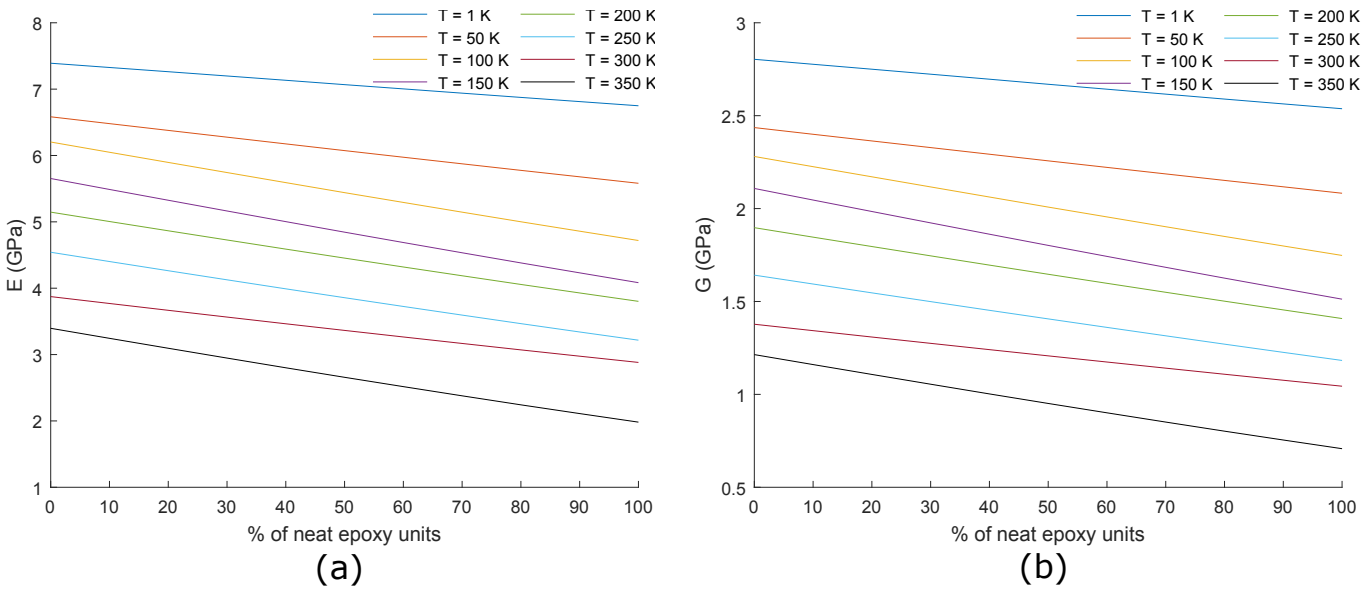

Figure 4.18: Finite Element results for the a. Young's modulus and b. shear modulus vs. % of neat epoxy for the pristine nanocomposite (13 repeat units) at various temperatures.

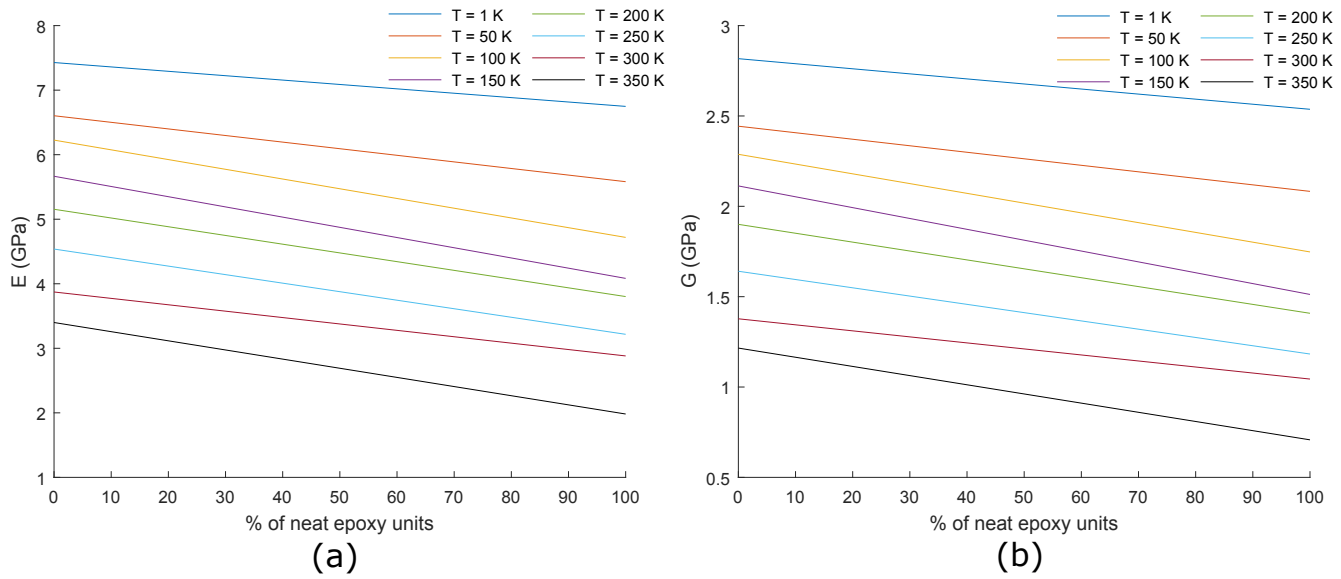

Figure 4.19: ODF upper bound for the a. Young's modulus and b. shear modulus vs. % of neat epoxy for the pristine nanocomposite (13 repeat units) at various temperatures.

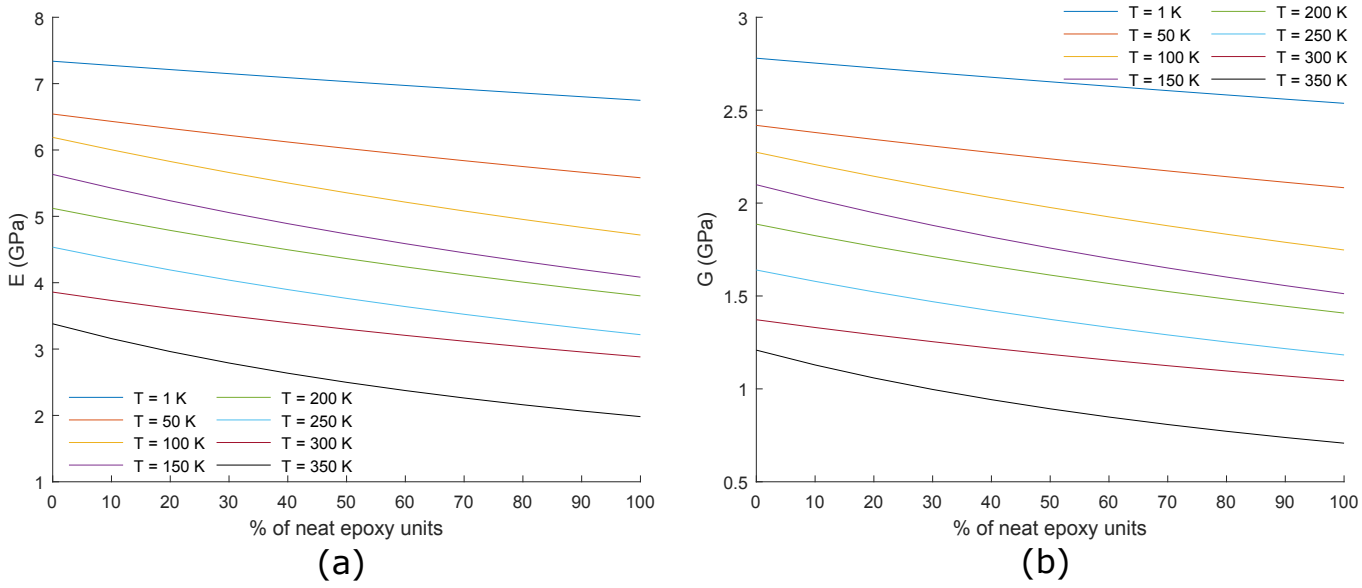

Figure 4.20: ODF lower bound for the a. Young's modulus and b. shear modulus vs. % of neat epoxy for the pristine nanocomposite (13 repeat units) at various temperatures.

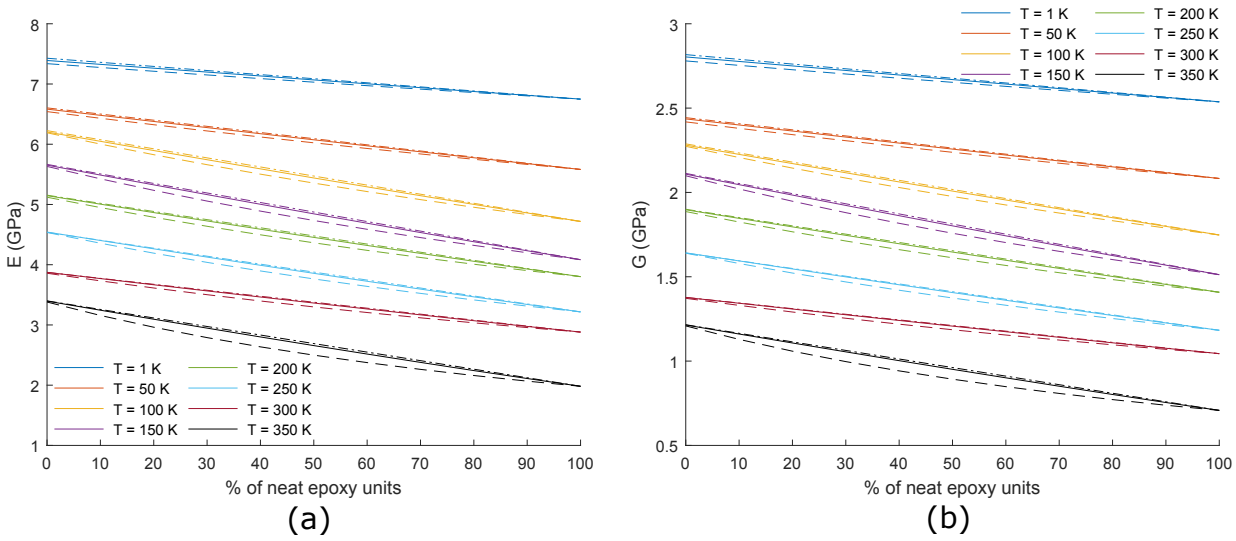

Figure 4.21: Comparison of the ODF upper bound, lower bound and Finite Element results for the a. Young's modulus and b. shear modulus vs. % of neat epoxy units seen in Figs. 4.18, 4.19 and 4.20.

4.3.1.4 Functionalized SWNT-Epoxy (13 Repeat Units)

The multiscale results for the Young's modulus and shear modulus of the isotropic, randomly oriented, discontinuous, functionalized SWNT-epoxy system with 13 repeat units are reported in this section. The Finite Element results, ODF upper bound, and the ODF lower bound for the Young's modulus vs. percentage of neat epoxy units at various temperatures are seen in Figs. 4.22a, 4.23a, and 4.24a, respectively. The results superimposed for the various methods are plotted in Fig. 4.25a. For the shear modulus, the Finite Element results, ODF upper bound, and the ODF lower bound are seen in Figs. 4.22b, 4.23b, and 4.24b respectively. The superimposed results are plotted in Fig. 4.25b. The Young's modulus and shear modulus show similar trends to the system with 11 repeat units, with the Finite Element results lying in between the upper and lower ODF bounds. For the randomly oriented, functionalized, SWNT-epoxy system with 13 repeat units; the Finite Element results, ODF upper bound, and the ODF lower bound all give very similar results in the temperature range of 1 K - 350 K investigated.

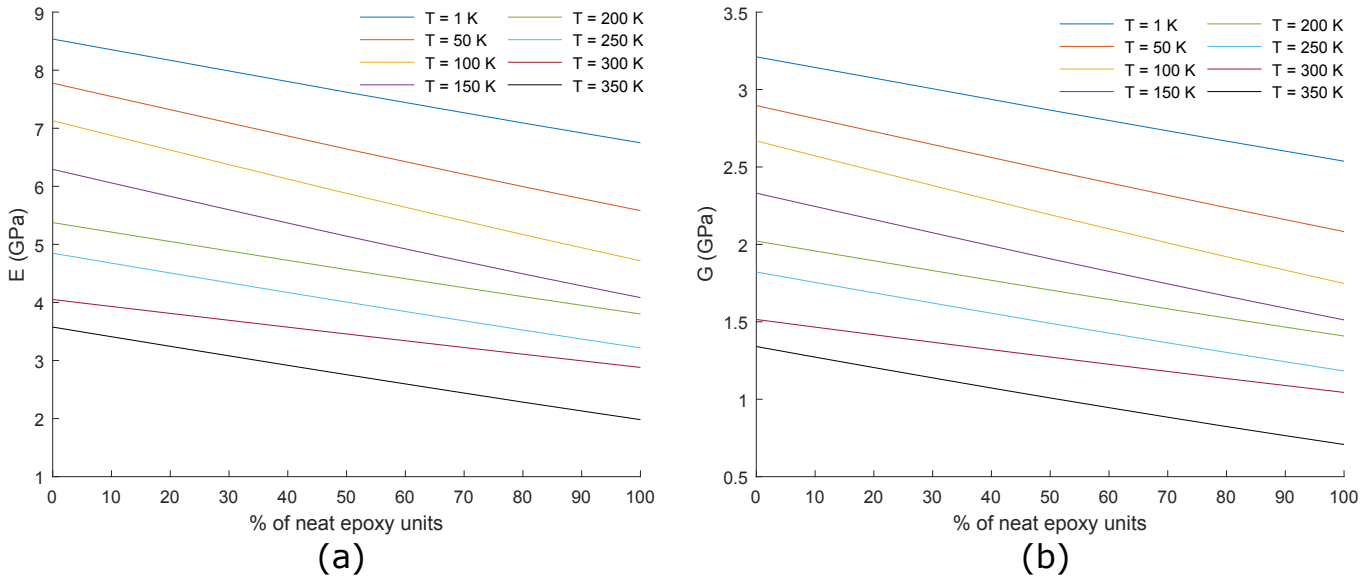

Figure 4.22: Finite Element results for the a. Young's modulus and b. shear modulus vs. % of neat epoxy for the functionalized nanocomposite (13 repeat units) at various temperatures.

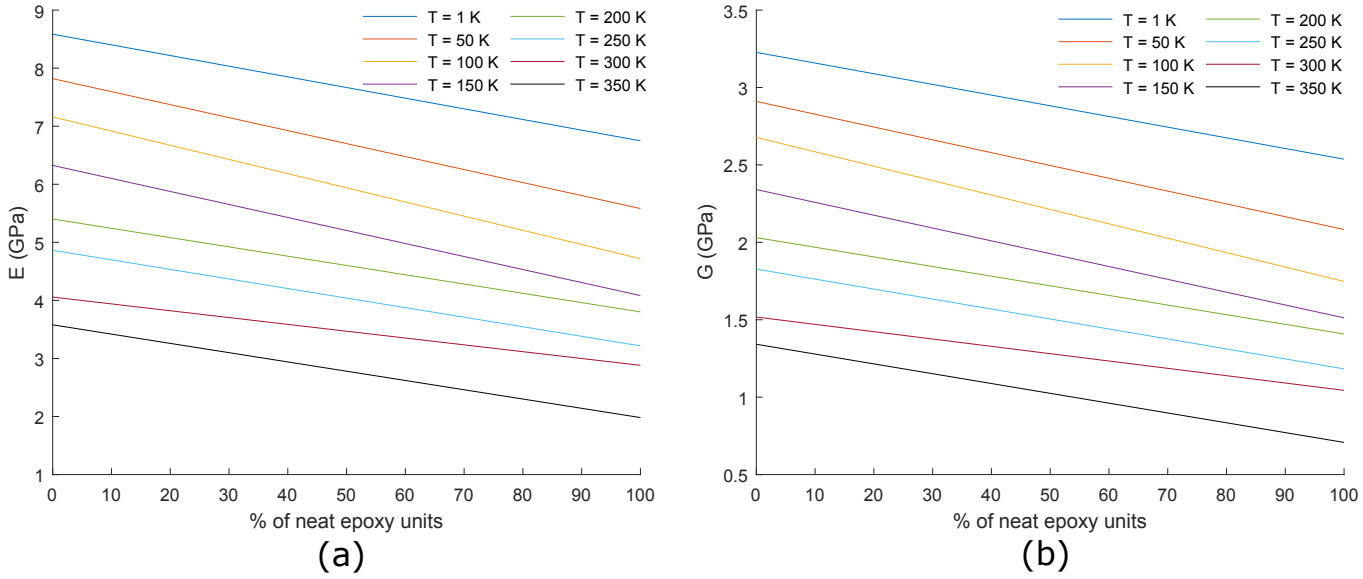

Figure 4.23: ODF upper bound for the a. Young's modulus and b. shear modulus vs. % of neat epoxy for the functionalized nanocomposite (13 repeat units) at various temperatures.

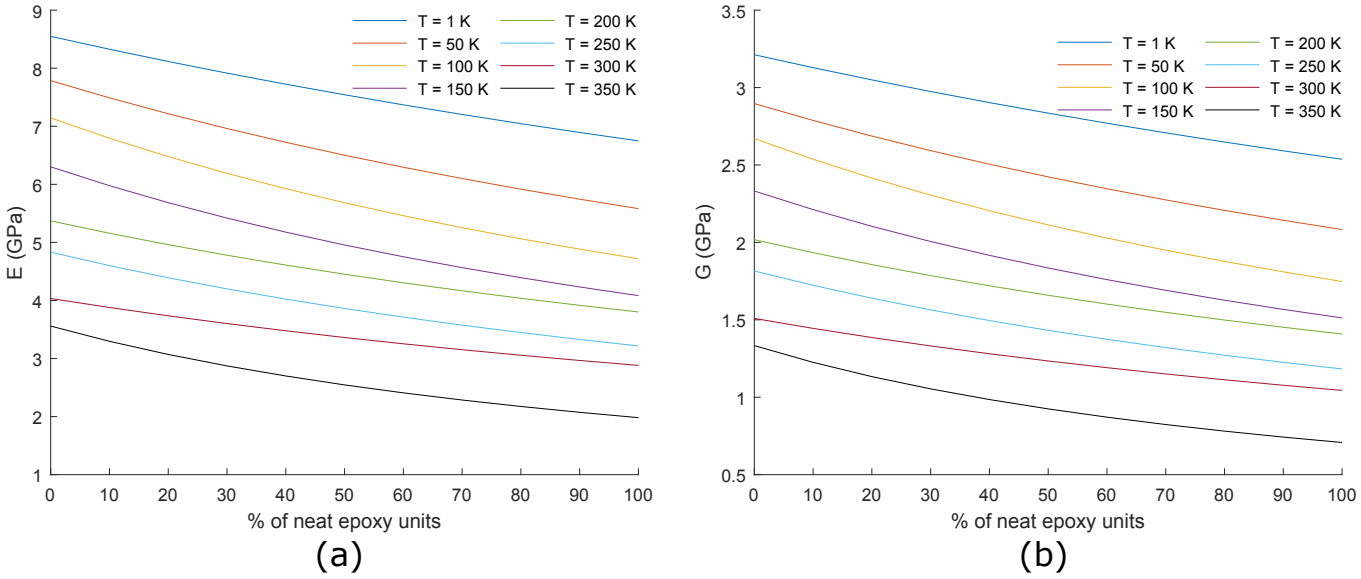

Figure 4.24: ODF upper bound for the a. Young's modulus and b. shear modulus vs. % of neat epoxy for the functionalized nanocomposite (13 repeat units) at various temperatures.

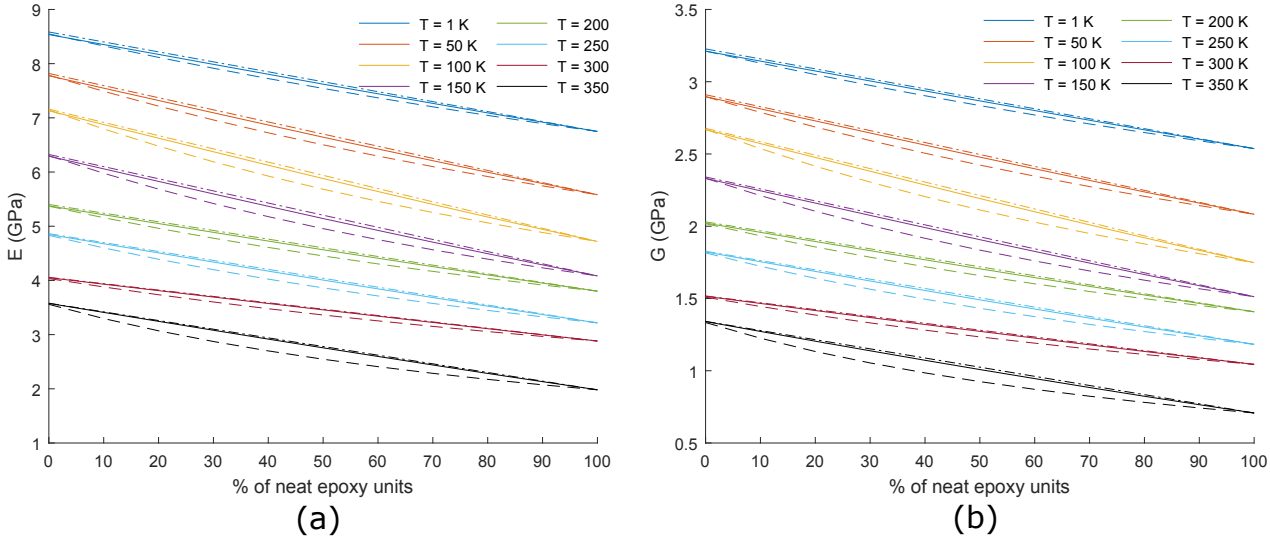

Figure 4.25: Comparison of the ODF upper bound, lower bound and Finite Element results for the a. Young's modulus and b. shear modulus vs. % of neat epoxy units seen in Figs. 4.22, 4.23 and 4.24.

4.3.1.5 Pristine SWNT-Epoxy (Infinite)

The multiscale results for the Young's modulus and shear modulus of the isotropic, randomly oriented, continuous, pristine SWNT-epoxy system are reported in this section. The Finite Element results, ODF upper bound, and the ODF lower bound for the Young's modulus vs. percentage of neat epoxy units at various temperatures are seen in Figs. 4.26a, 4.27a, and 4.28a, respectively. The results superimposed for the various methods for T = 1 K, T = 200 K and T = 350 K are plotted in Fig. 4.29a. Unlike the discontinuous systems, the Finite Element results for the continuous system do not show a near linear relation for the Young's modulus with varying percentages of neat epoxy units. Here, the modulus decreases more rapidly with increasing amounts of epoxy when compared to the discontinuous systems. Due to the nature of the parallel model, the ODF upper bound continues to show a linear response. Likewise, the lower bound shows a non-linear response similar to the discontinuous systems due to the series model. For the shear modulus, the Finite Element results, ODF upper bound, and the ODF lower bound are seen in Figs. 4.26b, 4.27b, and 4.28b respectively. The superimposed results for the various methods at T = 1 K, T = 200 K and T = 350 K are plotted in Fig. 4.29b. Both the Young's modulus and shear modulus decrease with increasing temperature, and all temperatures show similar trends. The Finite Element results lie in the middle of the ODF upper bound and lower bound, which have a significantly wider range than the discontinuous systems. This is due to the extremely high stiffness in the nanotube direction leading to a large variation when averaging the stiffness matrix over all orientations for the equivalent isotropic systems calculated via the Voigt and Reuss models. The limits of the ODF models in conjunction with a rule of mixtures approach are seen here, as they give a very large range of possible values, especially at higher percentages of SWNTs. The average of the two results, however, would line up well the Finite Element model. For higher temperatures, the Finite Element result is closer with the lower bound result, where as at higher temperatures it is very close to the average between the two bounds.

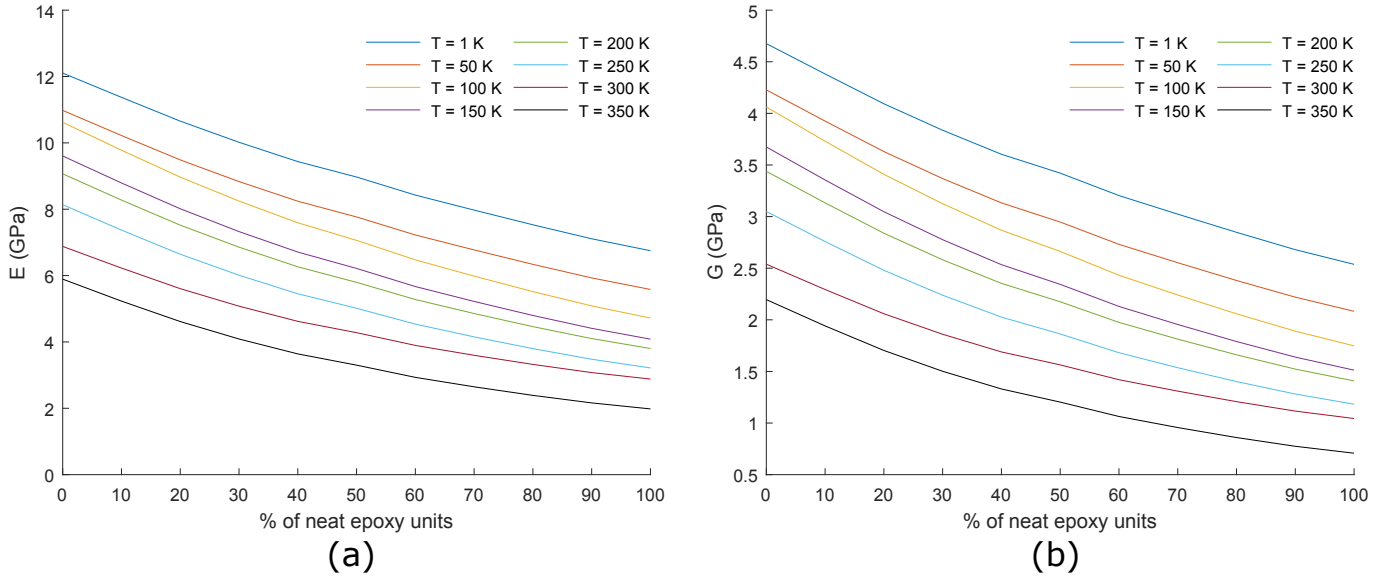

Figure 4.26: Finite Element results for the a. Young's modulus and b. shear modulus vs. % of neat epoxy for the pristine nanocomposite (infinite) at various temperatures.

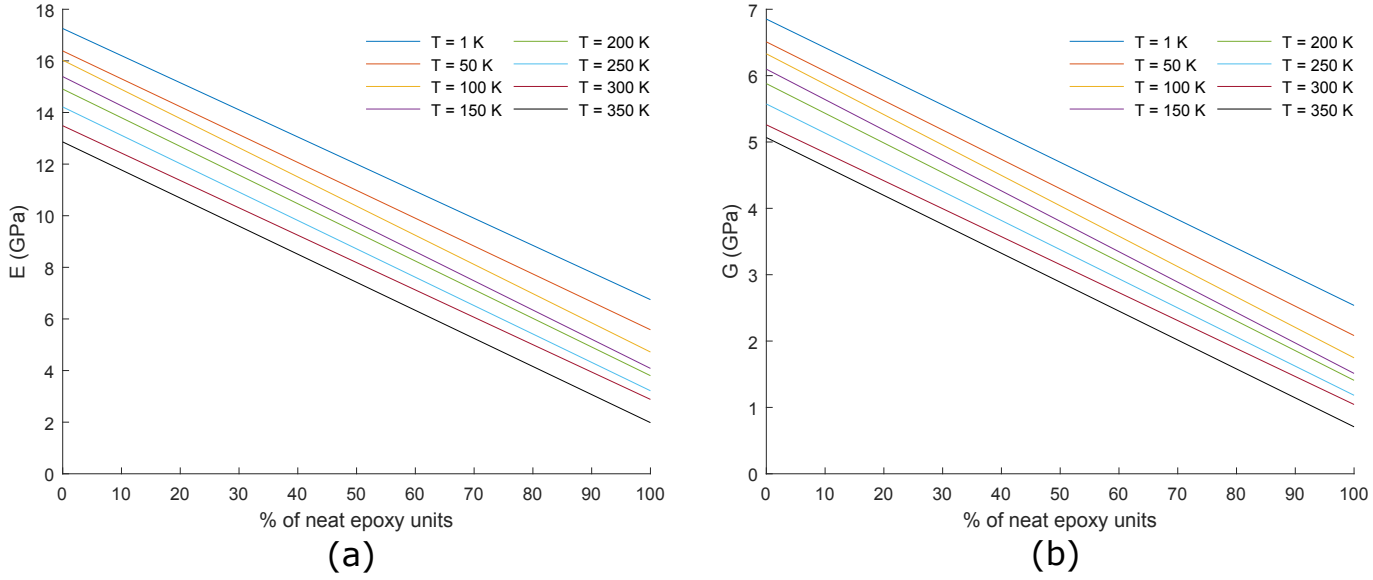

Figure 4.27: ODF upper bound for the a. Young's modulus and b. shear modulus vs. % of neat epoxy for the pristine nanocomposite (infinite) at various temperatures.

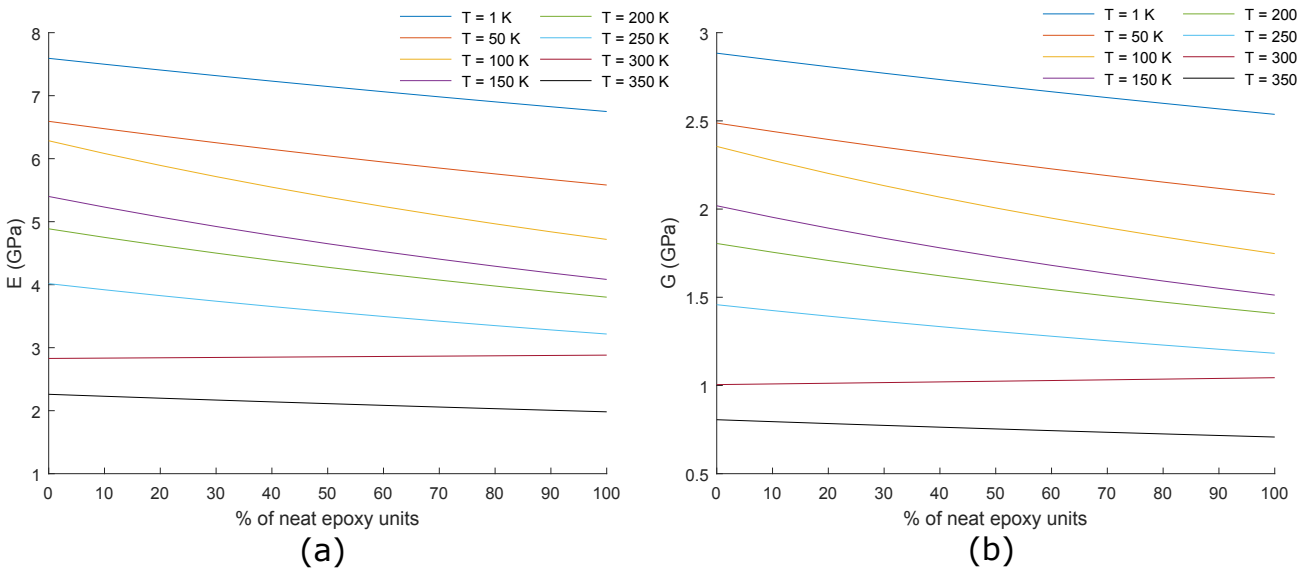

Figure 4.28: ODF lower bound for the a. Young's modulus and b. shear modulus vs. % of neat epoxy for the pristine nanocomposite (infinite) at various temperatures.

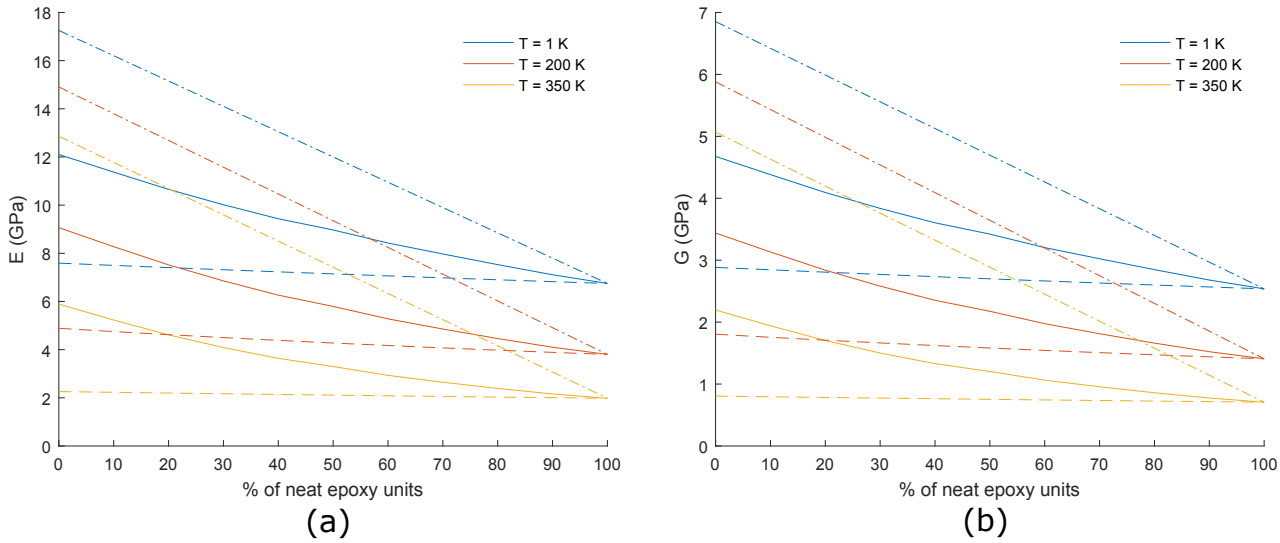

Figure 4.29: Comparison of the ODF upper bound, lower bound and Finite Element results for the a. Young's modulus and b. shear modulus vs. % of neat epoxy units seen in Figs. 4.26, 4.27 and 4.28.

4.3.1.6 Functionalized SWNT-Epoxy (Infinite)

The multiscale results for the Young's modulus and shear modulus of the isotropic, randomly oriented, continuous, functionalized SWNT-epoxy system are reported in this sec-

tion. The Finite Element results, ODF upper bound, and the ODF lower bound for the Young's modulus vs. percentage of neat epoxy units at various temperatures are seen in Figs. 4.30a, 4.31a, and 4.32a, respectively. The results superimposed for the various methods for T = 1 K, T = 200 K and T = 350 K are plotted in Fig. 4.33a. Similar to the infinite, pristine system, the Finite Element results for the functionalized system show a non-linear relationship for the Young's modulus with varying percentages of neat epoxy units. Due to the nature of the parallel and series models, the ODF upper bound continues to show a linear response, and the lower bound shows a non-linear response, similar to the discontinuous systems. For the shear modulus, the Finite Element results, ODF upper bound, and the ODF lower bound are seen in Figs. 4.30b, 4.31b, and 4.32b respectively. The superimposed results for the various methods at T = 1 K, T = 200 K and T = 350 K are plotted in Fig. 4.33b. Both the Young's modulus and shear modulus decrease with increasing temperature, and all temperatures show similar trends. The Finite Element results lie in the middle of the ODF upper bound and lower bound, which have a wide range due to the high stiffness in the nanotube direction, causing a large variation in the equivalent isotropic stiffness matrix calculated by the Voigt and Reusss models. This results in large bounds from the ODF models in conjunction with a rule of mixtures approach, especially at higher percentages of SWNTs. The average of the two results, however, would line up well the Finite Element model. For higher temperatures, the Finite Element result is closer with the lower bound result, where as at higher temperatures it is very close to the average between the two bounds.

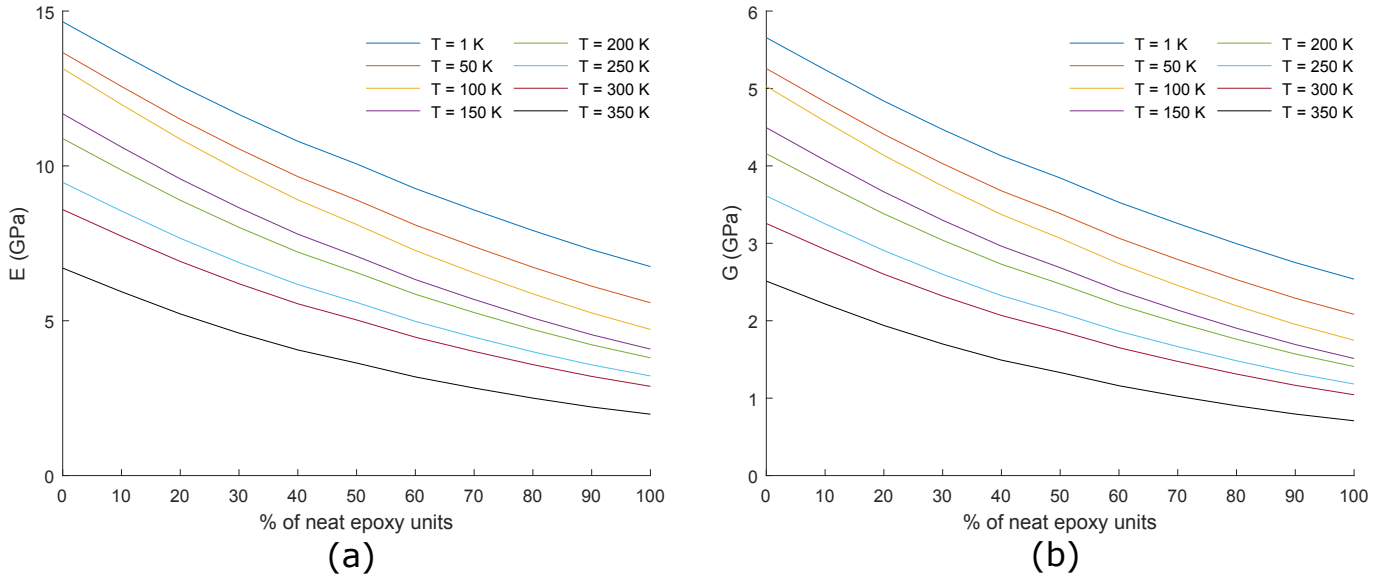

Figure 4.30: Finite Element results for the a. Young's modulus and b. shear modulus vs. % of neat epoxy for the functionalized nanocomposite (infinite) at various temperatures.

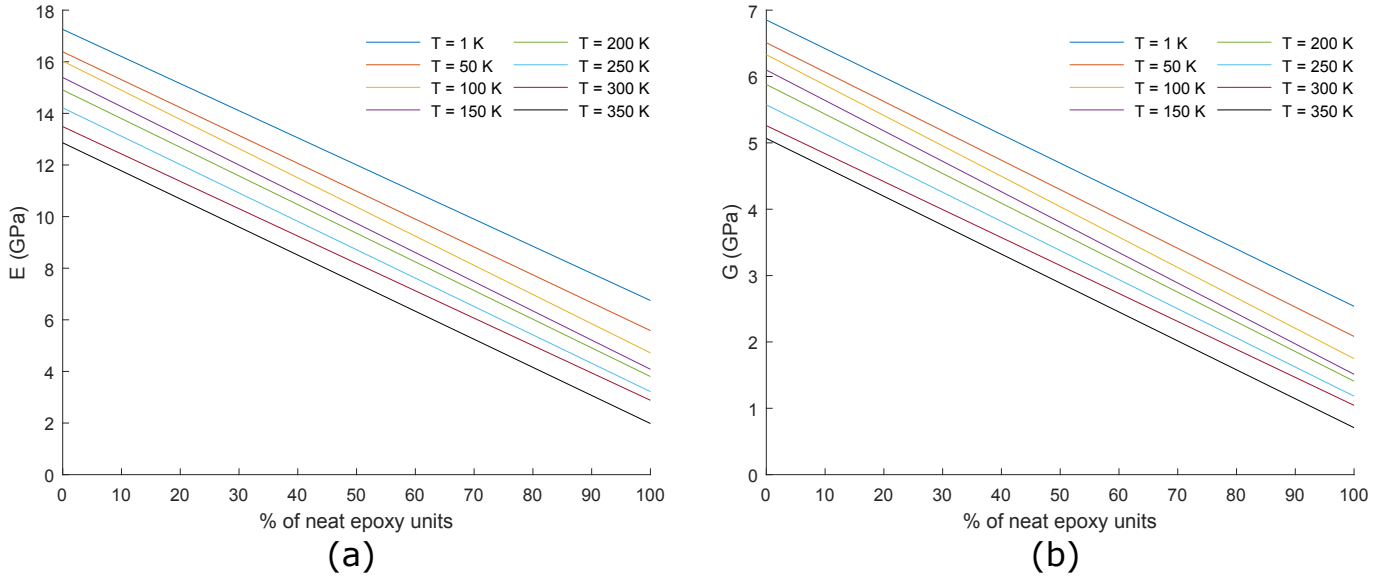

Figure 4.31: ODF upper bound for the a. Young's modulus and b. shear modulus vs. % of neat epoxy for the functionalized nanocomposite (infinite) at various temperatures.

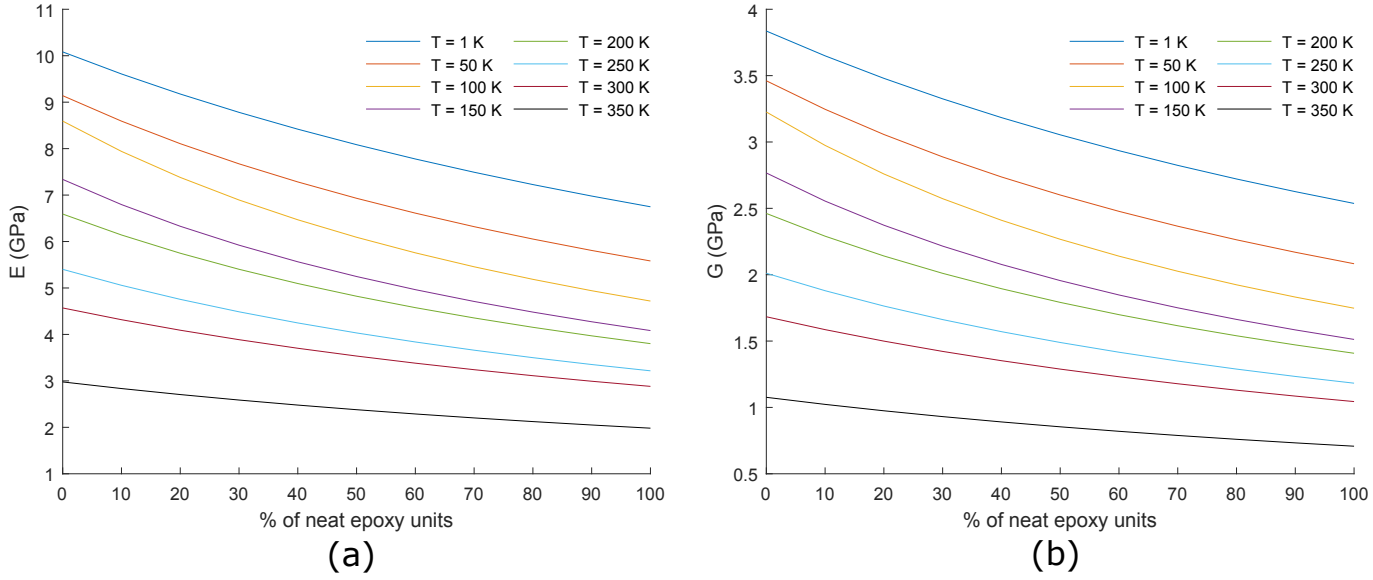

Figure 4.32: ODF lower bound for the a. Young's modulus and b. shear modulus vs. % of neat epoxy for the functionalized nanocomposite (infinite) at various temperatures.

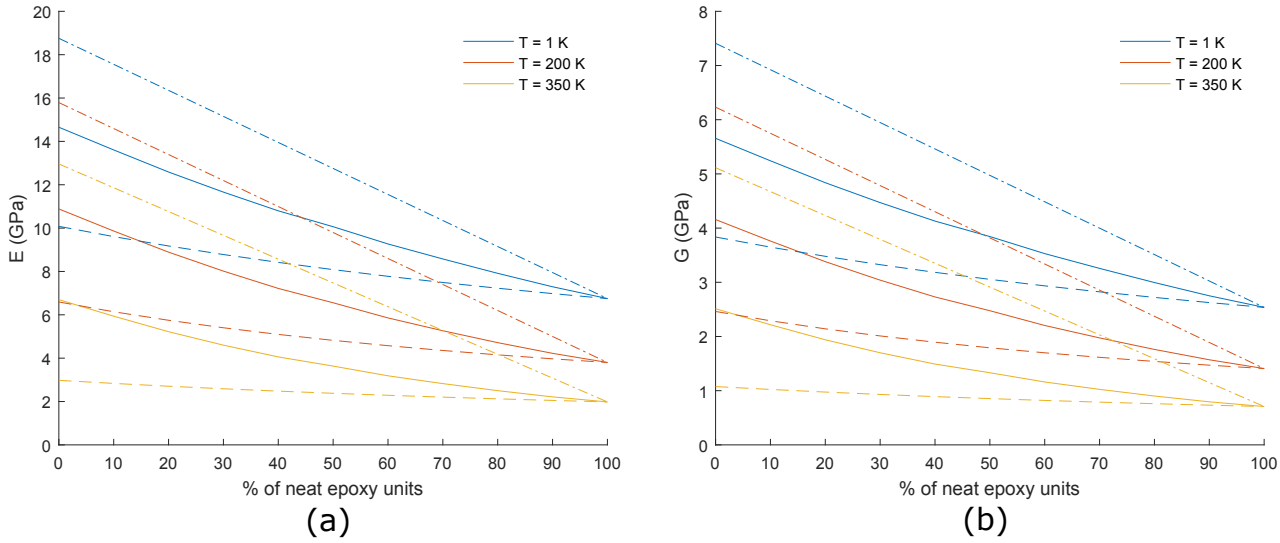

Figure 4.33: Comparison of the ODF upper bound, lower bound and Finite Element results for the a. Young's modulus and b. shear modulus vs. % of neat epoxy units seen in Figs. 4.30, 4.31 and 4.32.

4.3.2 Compare Systems

In this section, the Finite Element results for various randomly oriented nanocomposite systems are compared with one another. Two different plotting techniques are used to visualize the results: elastic properties vs. temperature at a fixed volume fraction of SWNTs, and elastic properties vs. volume fraction at fixed temperature. In section 4.3.2.1, the plots show results for the Young's modulus and Poisson's ratio vs. temperature for constant volume fractions of 0, 0.3, 0.6, and 0.9 of neat epoxy units. In section 4.3.2.2, results for the Young's modulus and Poisson's ratio vs. volume fraction for constant temperatures of 1 K, 100 K, 200 K and 300 K are shown.

4.3.2.1 Fixed Volume Fraction

Here, the volume fractions are held fixed for a given plot, and property vs. temperature are plotted for a given volume fraction of neat epoxy units, with the remaining units being a randomly oriented SWNT-epoxy lattice. A volume fraction of 0 of neat epoxy units means that the volume fraction of SWNT is the same as the MD lattice used for the various systems. A volume fraction of 1 neat epoxy units would represent neat epoxy, which the mechanical properties over a range of temperatures can be found in Fig. 3.13. Here, volume fractions of 0, 0.3, 0.6 and 0.9 of neat epoxy units are considered for the various nanocomposite systems. The exact volume fraction of SWNT can be calculated using Eq.

4.60.

For all volume fractions of neat epoxy units, the systems where the nanotube spans the MD cell demonstrate the highest stiffness and least amount of lateral contraction throughout the entire temperature range. The functionalized SWNT case shows higher stiffness than the pristine SWNT, and shows a lesser or equal lateral contraction compared to the pristine system over the entire temperature range. For the systems where the nanotube does not span the entire MD cell, the functionalized systems show higher stiffness than the pristine systems. Additionally, systems with the longer nanotube demonstrate higher stiffness for the functionalized system. For the pristine, discontinuous systems the change in length makes no appreciable difference. The improvement due to functionalization for the discontinuous systems is less appreciable at higher temperatures, and around 200 K the systems begin to converge. All the composite systems demonstrate improved stiffness at all volume fractions relative to neta eopxy over the temperate range considered. However, as expected, as the percentage of neat epoxy units increases, the various systems begin to converge and move closer the to neat epoxy values. The lateral contraction of the discontinuous systems is approximately equal to that of neat epoxy, though the small range of values makes the data appear somewhat noisy.

0% Neat Epoxy Units

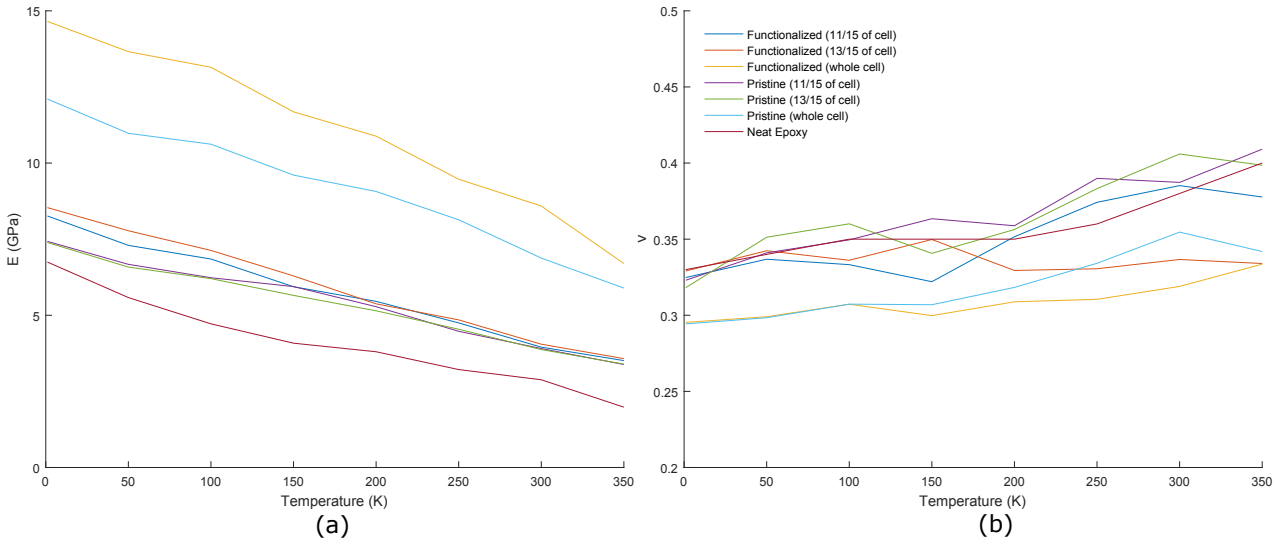

Figure 4.34: Finite Element results for the a. Young's modulus and b. Poisson's ratio vs. temperature for the various randomly oriented nanocomposite systems studied.

30% Neat Epoxy Units

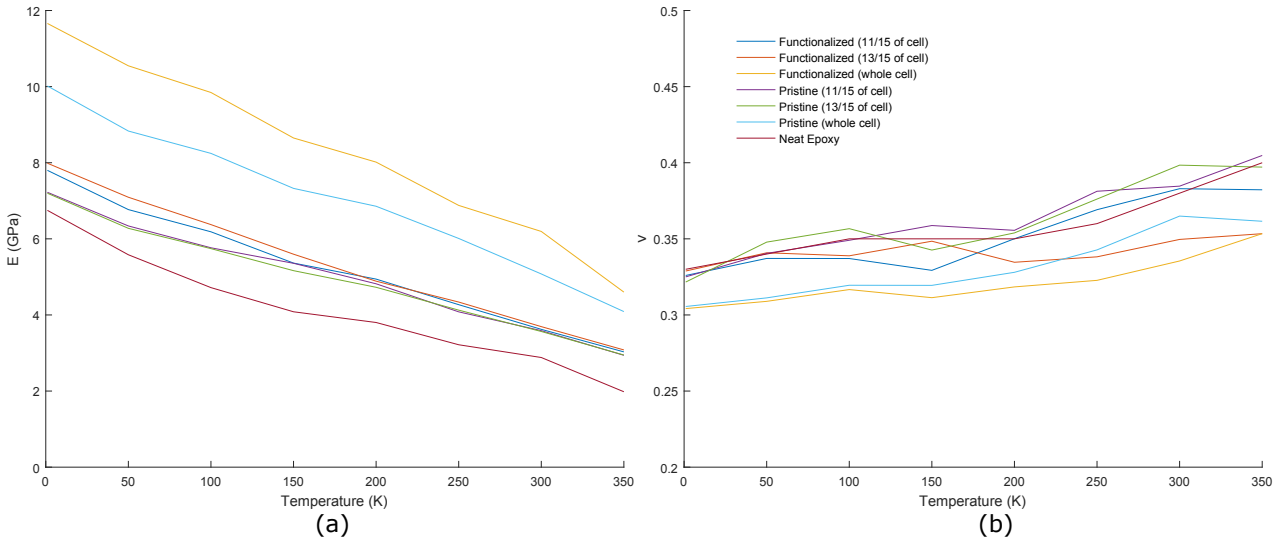

Figure 4.35: Finite Element results for the a. Young's modulus and b. Poisson's ratio vs. temperature for the various randomly oriented nanocomposite systems studied.

60% Neat Epoxy Units

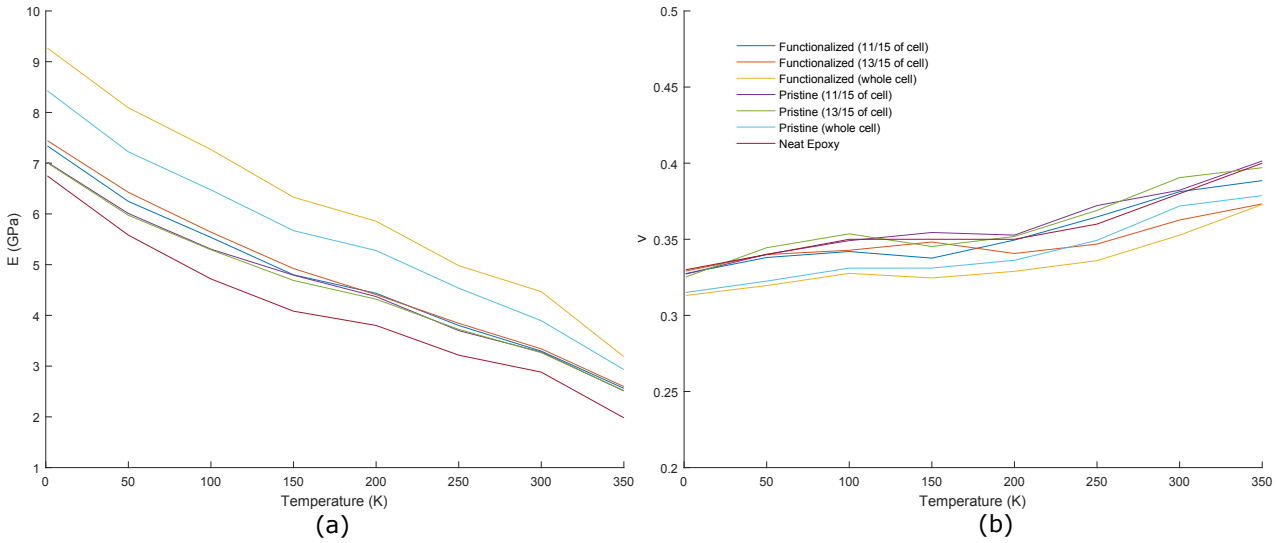

Figure 4.36: Finite Element results for the a. Young's modulus and b. Poisson's ratio vs. temperature for the various randomly oriented nanocomposite systems studied.

90% Neat Epoxy Units

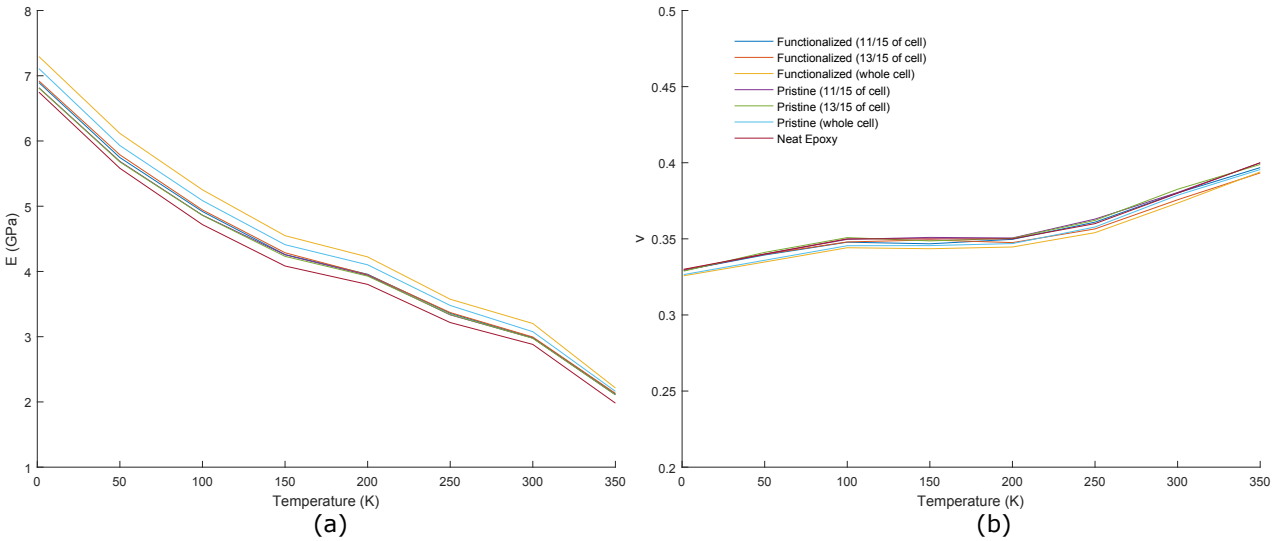

Figure 4.37: Finite Element results for the a. Young's modulus and b. Poisson's ratio vs. temperature for the various randomly oriented nanocomposite systems studied.

4.3.2.2 Fixed Temperature

Here, the temperatures are held fixed for a given plot, and an elastic property vs. volume fraction of neat epoxy units are plotted for a given fixed temperature. One subtracted by the volume fraction of neat epoxy gives volume fraction of units of the randomly oriented SWNT-epoxy lattice. The temperatures considered are 1 K, 100 K, 200 K, and 300 K, and the volume fraction of neat epoxy units is varied from 0 to 1. The Young's modulus and Poisson's ratio are plotted.

For all temperatures, the systems where the nanotube spans the MD cell demonstrate the highest stiffness and least amount of lateral contraction for the entire volume fraction range until unity. The functionalized, infinite SWNT system displays higher stiffness than the pristine, infinite SWNT systems. The functionalized and pristine infinite systems show a very similar trend for lateral contraction at low temperatures, but continue to diverge at higher temperatures, with the functionalized result consistently being lower. For the systems where the nanotube does not span the entire MD cell, the functionalized systems shows higher stiffness than the pristine systems. Additionally, systems with the longer nanotube demonstrate higher stiffness for the functionalized system. For the pristine, discontinuous system, the change in length makes no appreciable difference. As the temperature increases, the discontinuous systems begin to collapse on one another. All the composite systems demonstrate improved stiffness at all volume fractions of SWNT

relative to neat epoxy, and so a volume fraction of unity gives the lowest stiffness over all temperatures. The Poisson's ratio plots demonstrate at low temperatures the continuous nanotubes display the least lateral expansion, followed by the functionalized, discontinuous systems. The pristine discontinuous systems show the most lateral contraction. At 100 K, the discontinuous, pristine system with a SWNT spanning 13/15 of the cell length has a larger Poisson's ratio than neat epoxy. At 200 K and 300 K, both the pristine, discontinuous systems have a larger Poisson's ratio than neat epoxy, and the functionalized system with the nanotube that spans 11/15 is approximately equal to that of neat epoxy. At 300 K, the functionalized system that spans 13/15 of the cell has a smaller Poisson's ratio than the infinite, pristine system. The infinite, functionalized system continues to show the most resistance to lateral contraction.

1 K

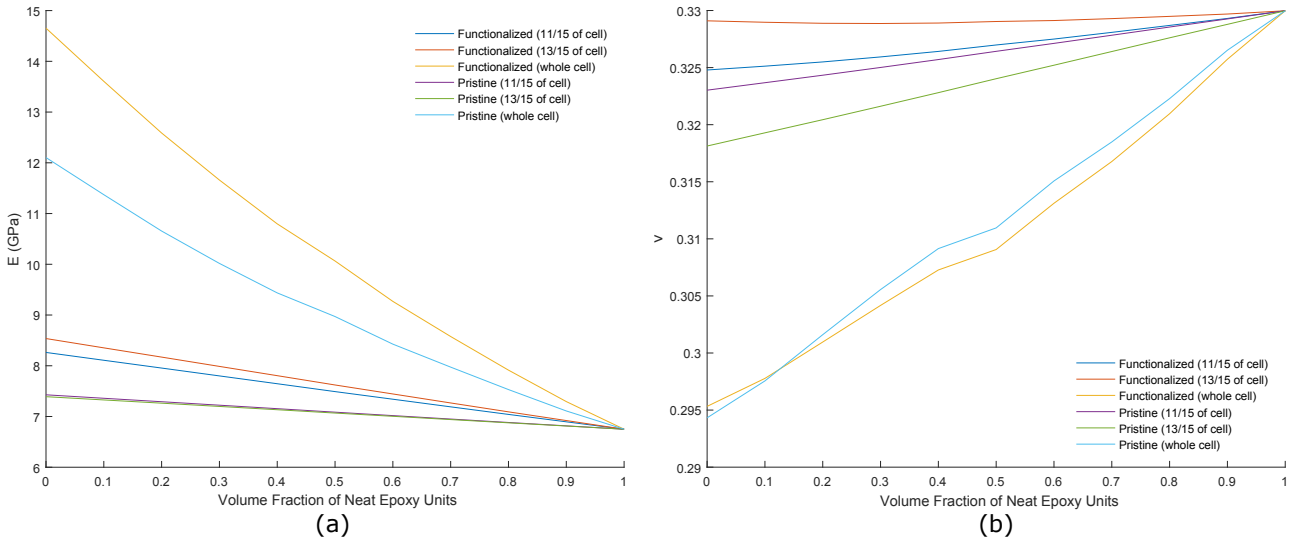

Figure 4.38: Finite Element results for the a. Young's modulus and b. Poisson's ratio vs. volume fraction for the various randomly oriented nanocomposite systems studied.

100 K

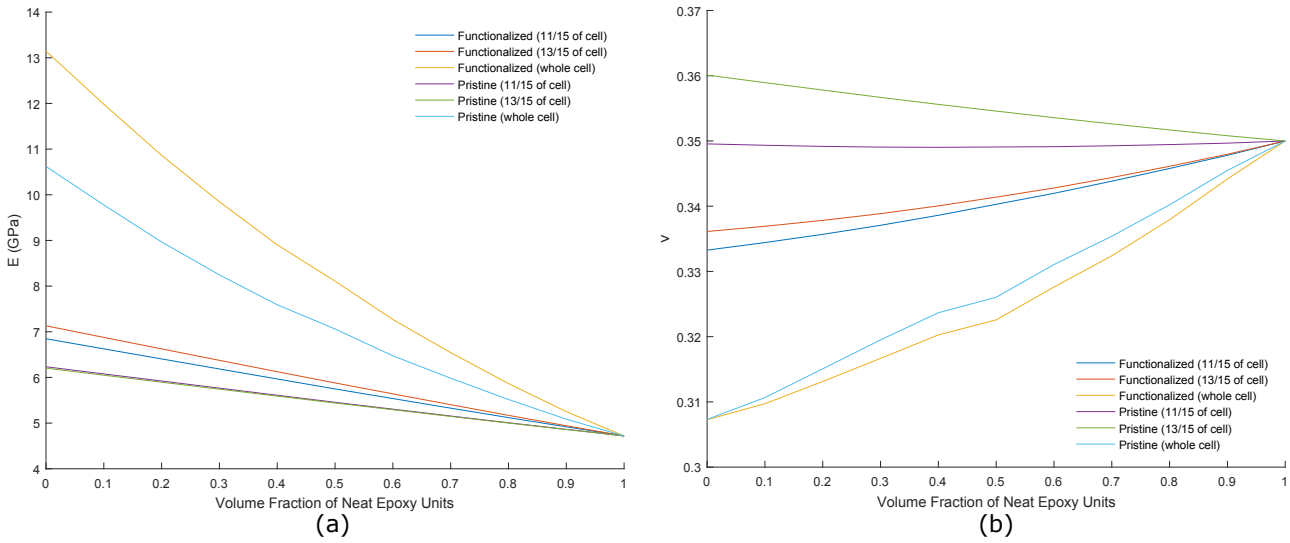

Figure 4.39: Finite Element results for the a. Young's modulus and b. Poisson's ratio vs. volume fraction for the various randomly oriented nanocomposite systems studied.

200 K

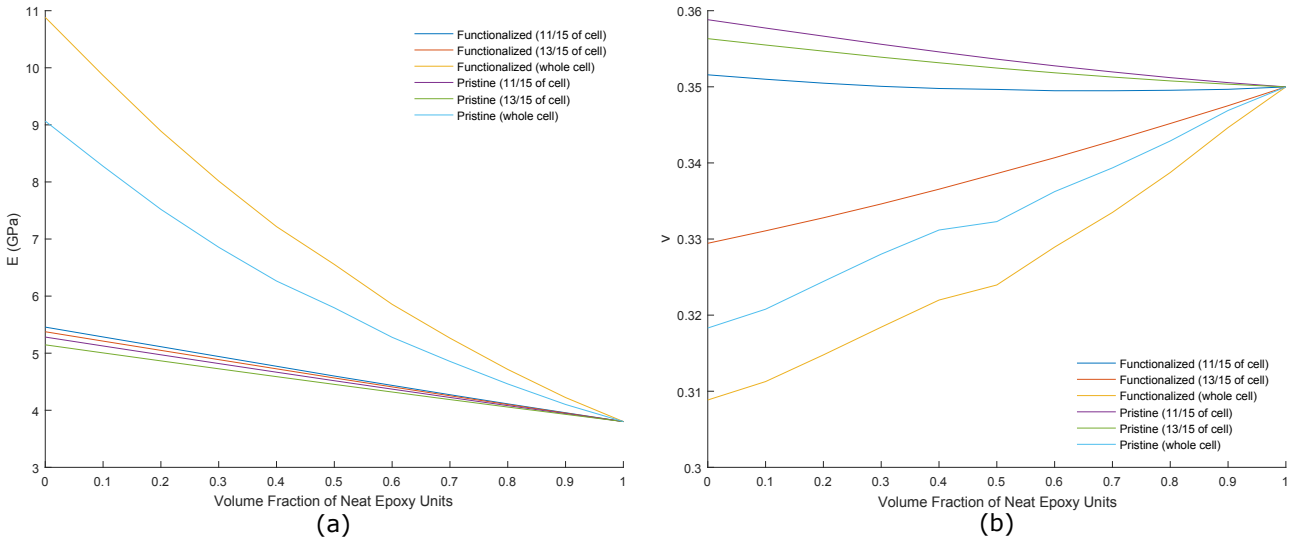

Figure 4.40: Finite Element results for the a. Young's modulus and b. Poisson's ratio vs. volume fraction for the various randomly oriented nanocomposite systems studied.

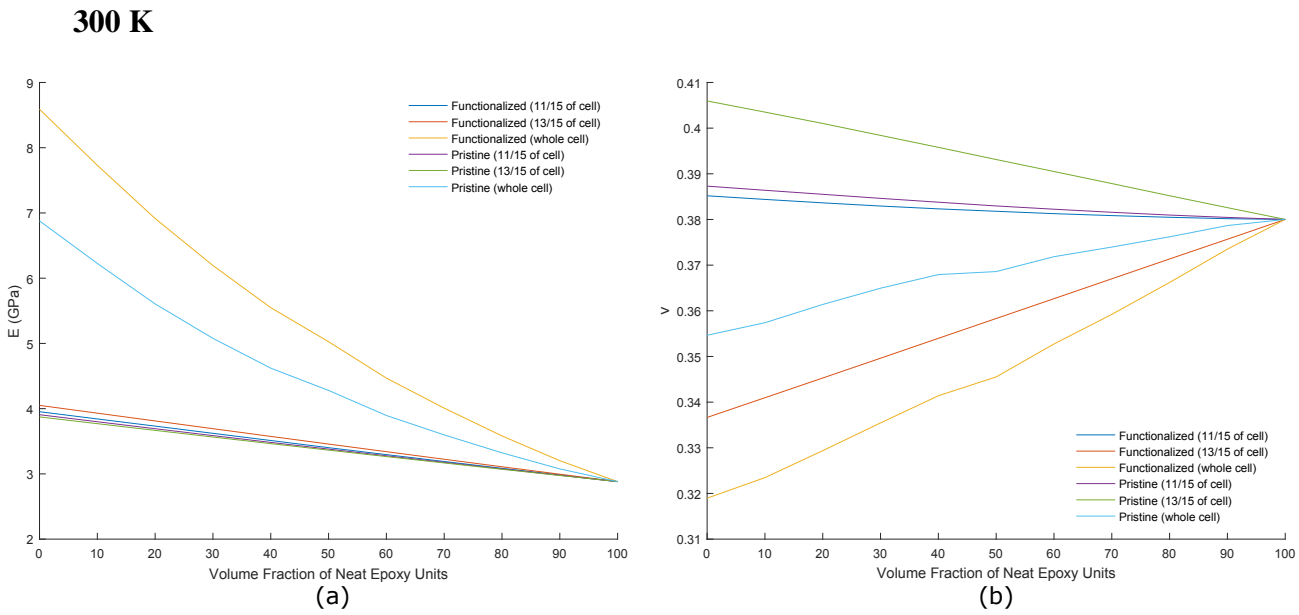

Figure 4.41: Finite Element results for the a. Young's modulus and b. Poisson's ratio vs. volume fraction for the various randomly oriented nanocomposite systems studied.

4.4 Conclusions

In this Chapter, the multiscale methods used to calculate the elastic properties of SWNT-epoxy nanocomposites were reviewed. The Finite Element approach, described in Section 4.1 was the first method used. Depending on the percentage of neat epoxy units, elements were probabilistically assigned with the elastic properties of a SWNT-epoxy nanocomposite from Chapter 2 at a random orientation, or with the elastic properties of neat epoxy. The second approach, an ODF based model, was described in Section 4.2. An ODF for randomly oriented composites was generated, and using the results of Chapter 2 the stiffness matrix was calculated. The Voigt and Reuss models were used to find the upper and lower bounds of the stiffness matrix for the randomly oriented composite at the volume fraction of the MD cell using Eqs 4.56 and 4.59, respectively. In order to vary the volume fraction of SWNT, a rule of mixtures approach described Section 4.2.5 was implemented. The parallel rule of mixtures was used in conjunction with the upper bound of the randomly oriented nanocomposite and neat epoxy to find the upper bound value at various volume fractions of nanotubes. Likewise, the series rule of mixtures is used with the lower bound of the randomly oriented nanocomposite and neat epoxy to find the lower bound value at various volume fractions.

Results for randomly oriented, equivalently isotropic, composites were shown in this

Chapter. For all of the various nanocomposite systems studied, the Finite Element results, ODF upper bound, and ODF lower bound were calculated and compared as a function of volume fraction of neat epoxy for various temperatures in Section 4.3.1. In Section 4.3.2, the Finite Element results for the various, randomly oriented nanocomposite systems were compared with one another. Two different plotting techniques were used to visualize the results, elastic properties vs. temperature at a fixed volume fraction of SWNTs, and elastic properties vs. volume fraction at a fixed temperature. In Section 4.3.2.1, the results for the Young's modulus and Poisson's ratio vs. temperature for constant volume fractions of 0, 0.3, 0.6, and 0.9 neat epoxy units were plotted. In Section 4.3.2.2, results for the Young's modulus and Poisson's ratio vs. volume fraction for constant temperatures of 1 K, 100 K, 200 K and 300 K were plotted.

CHAPTER 5

Modeling Aligned Nanocomposites

In this Chapter, the effects of nanotube alignment are considered. The results shown were obtained using two different multiscale methods; the Finite Element and ODF based methods described in Chapter 4, using the MD lattice results for a single SWNT-epoxy unit from Chapter 2. The application of these methods leads to five different multiscale results, though only three turn out to be independent. The Finite Element model described in Section 5.1, directly leads to a solution where the percentage of alignment and volume fraction of SWNT can be controlled, since the elemental stiffness matrices can be assigned the properties of one of the MD SWNT-epoxy nanocomposite lattices at any orientation, or that of neat epoxy. In Section 5.2, the ODF method is used to generate macroscopic upper and lower bound results for systems with fully aligned SWNTs, fully random SWNTs, and systems where a desired percentage of nanotubes are aligned and the rest are random. These systems all contain the same volume fraction of SWNT as the MD SWNT-epoxy lattice, and to vary the volume fraction, rule of mixtures approaches were employed. This ultimately leads to four different results for each SWNT-epoxy system: upper and lower bounds via two-phase and three-phase approaches. In the two-phase model, the upper bound and lower bound stiffness matrices were obtained from the ODF for a desired amount of alignment, and were used in conjunction with the parallel and series rule of mixtures approaches to obtain upper and lower bound stiffness matrices for various amounts of alignment, and volume fractions of SWNTs. In the three-phase model, the calculation of new stiffness matrices for a given amount of alignment was unnecessary, and rule of mixture approaches were applied to the fully aligned and fully random nanocomposites via the ODF model, along with neat epoxy. This leads to upper and lower bound macroscopic stiffness results for various amounts of alignment and volume fraction of nanotubes, where the only required inputs are the stiffness matrices for the fully random nanocomposite, fully aligned nanocomposite, and neat epoxy. The percentage of alignment and nanotube volume fraction are controlled by the rule of mixtures. It was shown in Section 5.2.1.3 that for only one preferential alignment, the 2-phase and 3-phase results give nearly identical

results, and so only the less computationally expensive 3-phase ODF model results were plotted.

5.1 Finite Element Multiscale Method for Aligned SWNTs

The Finite Element multiscale method used here is essentially the same as the one described earlier in Chapter 4.1. It is done by by inputting molecular-scale data to individual elements and then carrying out the FEM analysis. The elastic stiffness matrices obtained from the MD lattice of the epoxy and the SWNT-epoxy nanocomposites systems were assigned to Finite Element elements based on the desired distribution and loading of SWNTs. In Section 4.1.4, the desired distribution of SWNT was randomly oriented, and so using evenly spaced points over Rodrigues space, all orientations were given an equal probability of being assigned when accounting for symmetry. For the case of aligned nanotubes, the probability is broken up into three portions: the neat epoxy units, the aligned nanotubes, and the random nanotubes. First, the percentage of neat epoxy elements is considered; the probability of an element being assigned neat epoxy is just the percentage desired divided by 100. Next, the alignment is considered, and a given orientation is picked and elements are assigned a probability based on the percentage of alignment desired. This done by first subtracting the probability of a neat epoxy node, and then multiplying the remaining probability by the percentage of alignment desired:

$$P_{aligned} = (1 - P_{neat\ epoxy}) * \frac{\%\ \text{alignment}}{100} \tag{5.1}$$

Finally, the probability of a node being assigned a non-aligned orientation is based on the remaining probability left to achieve unity after subtracting out the neat epoxy and aligned probabilities. The non-aligned nanotubes are considered to be random, and therefore will continue to be assigned following the same distribution as shown earlier in Fig. 4.4. Since the orientation chosen as the "aligned" direction still appears in the "random" nanotube probability, there will be more than just the assigned alignment percentage in that direction. This is done to keep the random portion truly "random", since leaving out the orientation used for the alignment direction would cause a bias in the "random" portion. This means an additional percentage of nanotubes in a given direction exist over what was explicitly assigned. As an example, if a composite has 50% neat epoxy units and then 30% nanotube alignment, the probability of a node being assigned as neat epoxy is $P_{neat\ epoxy} = 0.5$. Then to achieve the 30% alignment, using Eq. 5.1 we find $P_{aligned} = 0.15$. So, then the probability of a nanotube being assigned a random orientation is $P_{random} = 0.35$.

Therefore probability of being assigned a given orientation within the "random" portion is P_{random} multiplied by the probability of that orientation occurring according to distribution shown previously in Fig. 4.4. So, if "Orientation 1" is picked as the alignment direction, we expect 15% of tubes to be aligned in that direction from $P_{aligned}$, plus an additional $P_{random} * P_{weights}(Orientation\ 1)$, which gives an additional 1.5% of nanotubes aligned in "Orientation 1" from the "random" portion.

5.2 ODF Method for Aligned SWNTs

In Chapter 4.2, ODFs were constructed to represent a fully random composite. Here, the effects of nanotube alignment was considered by generating ODFs for fully aligned composites, and various percentages of nanotube alignment with the remainder being random. The ODF indicates the probability of finding a given SWNT orientation within a macroscopic sample. The direction of preferential nanotube alignment was chosen to be the z-direction, or the $< 001 >$ direction. So, for increasing amounts of nanotube alignment there will be more SWNTs aligned in the z-direction. To visualize this, pole figures are shown for various orientations as well as a cross-section of the ODF. The pole figures for the $< 001 >$ direction and a cross section of the ODF for random composites, and pole figures for the $< 100 >$, $< 010 >$ directions are seen in Figs. 5.1 and 5.2 for 0% alignment, Figs. 5.3 and 5.4 for 30% alignment, Figs. 5.5 and 5.6 for 60% alignment, and Figs. 5.7 and 5.8 for 100% alignment. Since the nanotubes alignment direction is the $< 001 >$ direction, the pole figures for the $< 100 >$ and $< 010 >$ directions are the same, save for a shift of 90°. Only the pole for the z-direction, $< 001 >$ is plotted, so intensity of poles (SWNTs) aligned for the $< 001 >$ pole figures increases with increasing percentage of desired nanotube alignment. Likewise, the intensity of poles (SWNTs) perpendicular to the $< 100 >$ and $< 010 >$ increases with increasing amounts of desired nanotube alignment for the $< 100 >$ and $< 010 >$ pole figures. The ODF images show the same trend, where all orientations start out equally represented. As the desired alignment increases; a specific orientation, in this case alignment in the z-direction, become increasingly represented until it is the only orientation present for full alignment.

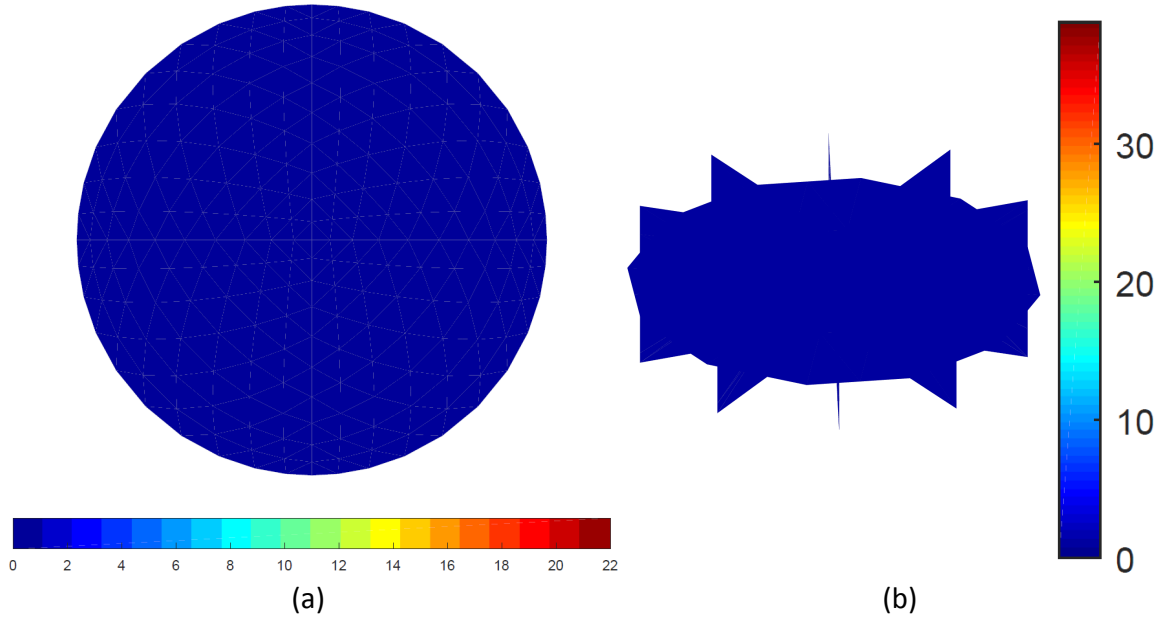

Figure 5.1: a. $< 001 >$ pole figure and b. cross section of the ODF for 0% SWNT alignment.

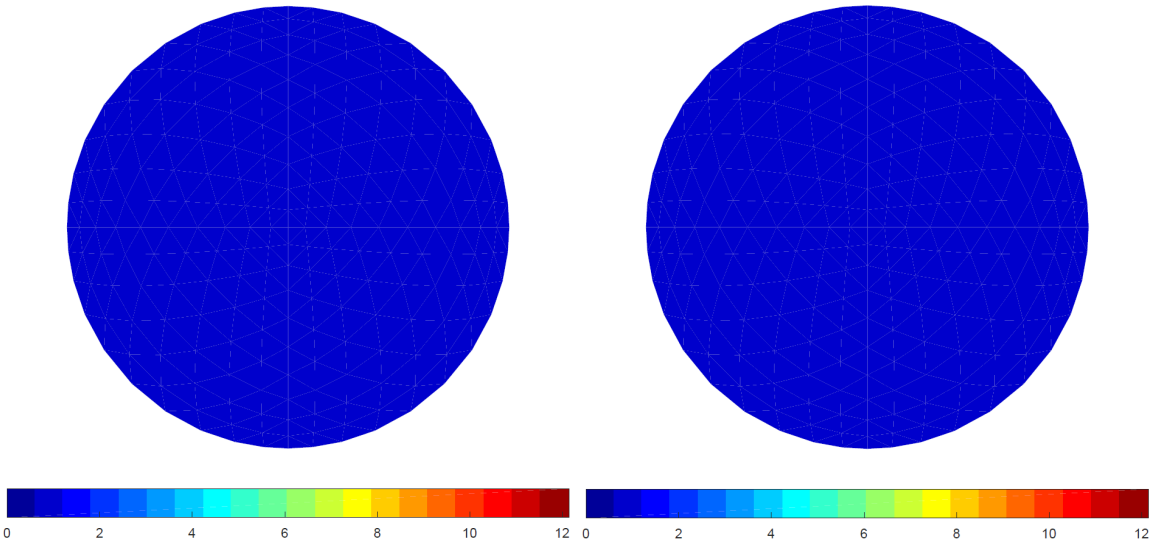

Figure 5.2: a. $< 100 >$ and b. $< 010 >$ pole figures for 0% SWNT alignment.

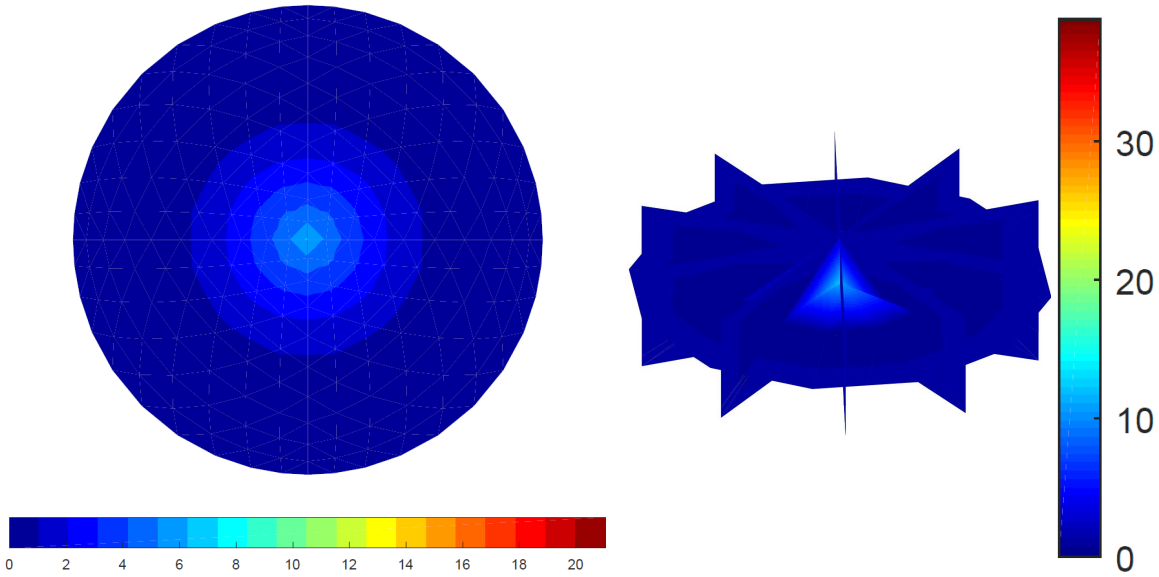

Figure 5.3: a. $< 001 >$ pole figure and b. cross section of the ODF for 30% SWNT alignment.

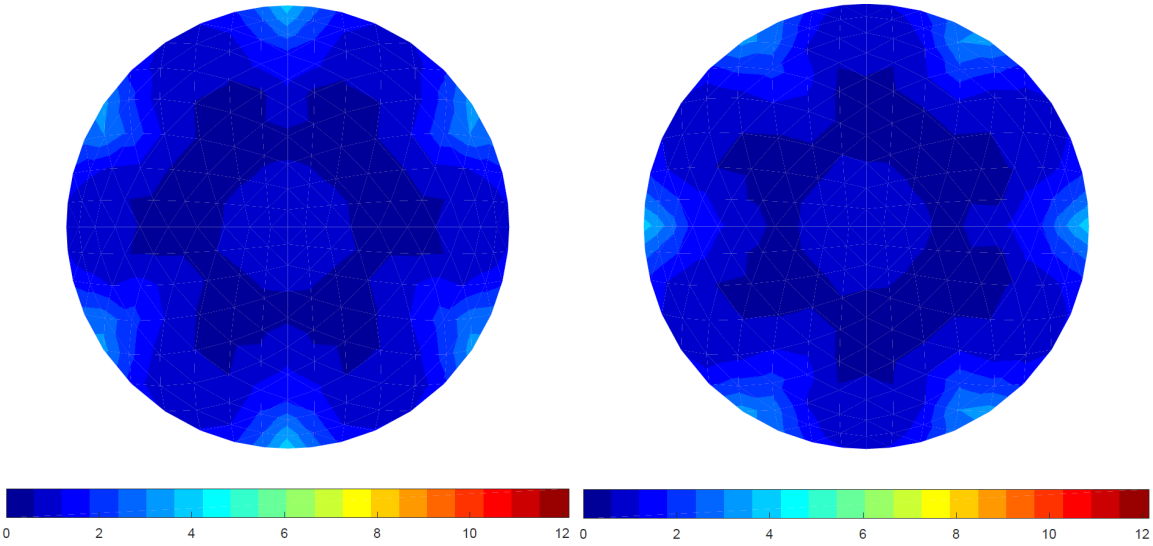

Figure 5.4: a. $< 100 >$ and b. $< 010 >$ pole figures for 30% SWNT alignment.

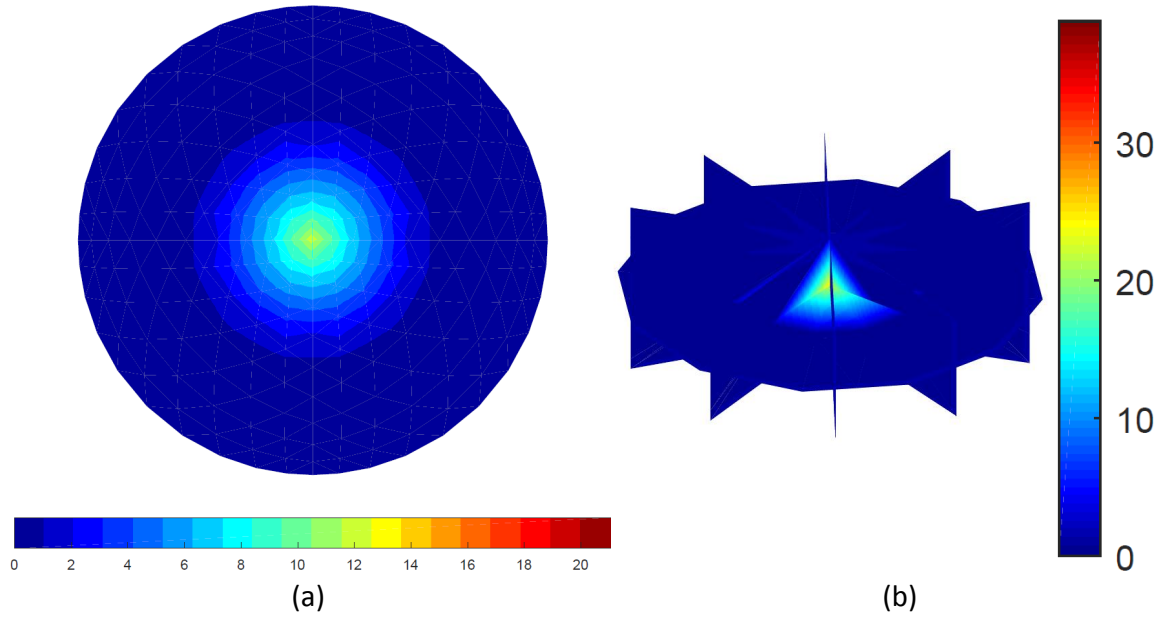

Figure 5.5: a. $< 001 >$ pole figure and b. cross section of the ODF for 60% SWNT alignment.

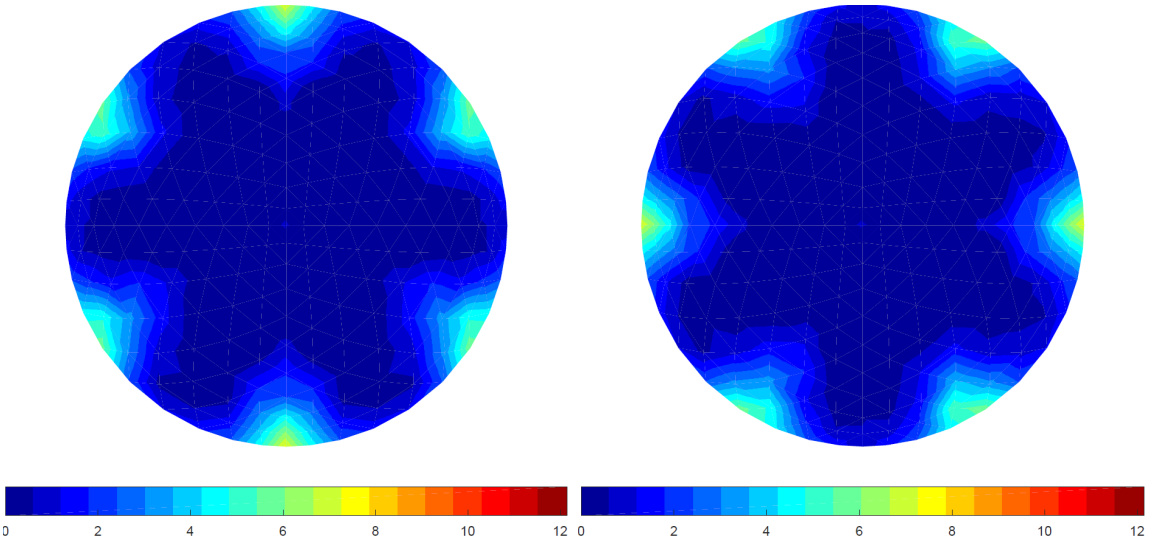

Figure 5.6: a. $< 100 >$ and b. $< 010 >$ pole figures for 60% SWNT alignment.

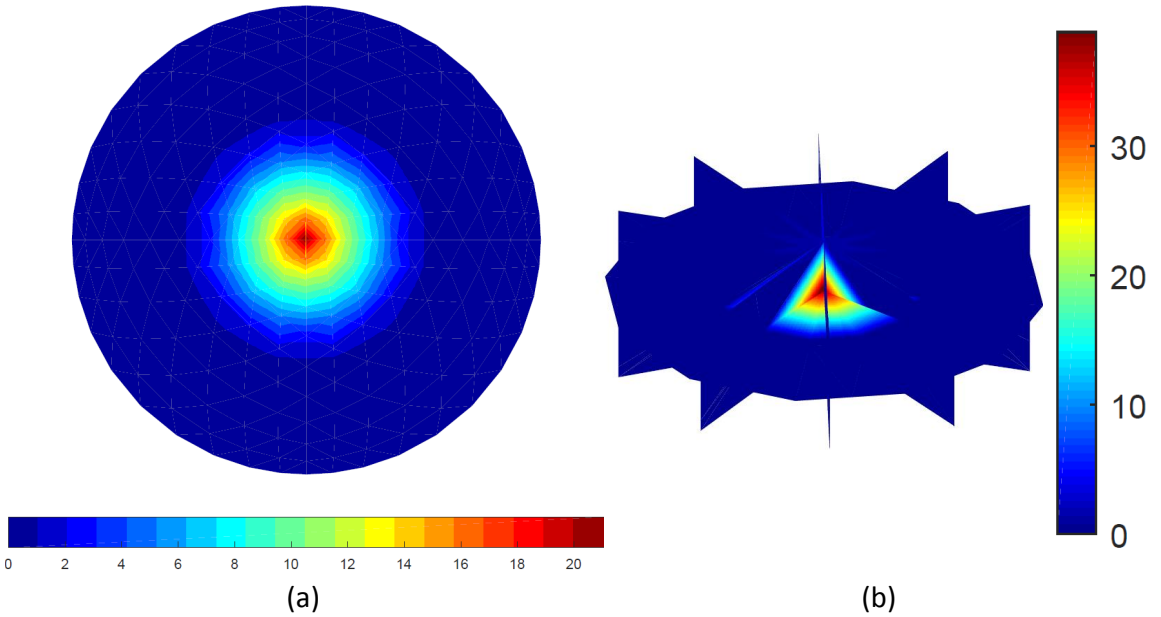

Figure 5.7: a. $< 001 >$ pole figure and b. cross section of the ODF for 100% SWNT alignment.

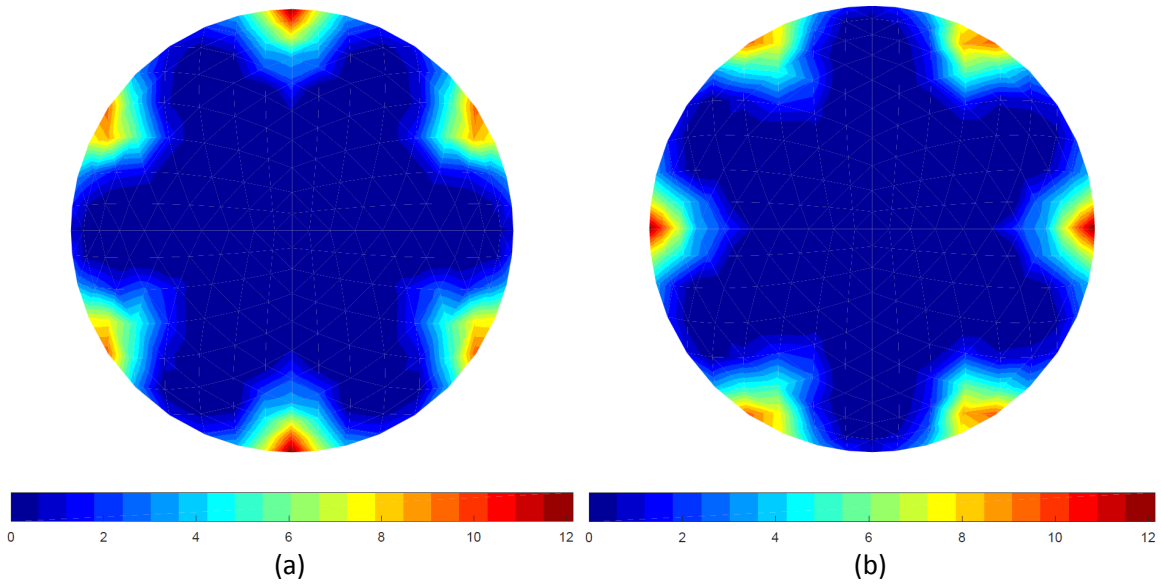

Figure 5.8: a. $< 100 >$ and b. $< 010 >$ pole figures for 100% SWNT alignment.

5.2.1 Aligned Muliscale Model

5.2.1.1 2-phase model

The macroscopic stiffness properties for the aligned nanocomposites via the ODF method are calculated in two different ways. For the first method, which is called the 2-phase method, an ODF is generated where a desired percentage of nanotubes are aligned and the rest are randomly oriented. The ODFs were plotted for various percentages of alignment in the pole figures in Section 5.2. The macroscopic C-matrix was calculated using the Voigt and Reuss formulations for the maximum and minimum values, respectively. In order to control the volume fraction of SWNT, the rule of mixtures approaches outline in Section 4.2.5 were applied. The series and parallel models were used in conjunction with the Reuss and Voigt model, respectively, to yield the minimum and maximum stiffness matrix for nanocomposite with a controllable amount of alignment and volume fraction of SWNTs. The two phases in the rule of mixtures calculations were the SWNT-epoxy nanocomposites for a given percentage of alignment, and neat epoxy. This method is more flexible in terms of specific alignment distribuitions, and will allow for various orientational preferences to be studied, such as the case of nanotube bundles. This method can also be used to find optimal configurations of SWNTs.

5.2.1.2 3-phase model

The second method does not require the calculation of a new ODF for specific percentages of alignment, and therefore runs faster. Instead, the ODF for fully random nanocomposites, or 0% alignment, used in Chapter 4 and seen in Figs. 5.1 and 5.2, is used in conjunction with the fully aligned case, or 100% alignment, seen in Figs. 5.7 and 5.8. The maximum and minimum macroscopic stiffness matrices have been previously calculated via the Voigt and Reuss models, and they are used in conjunction with the parallel and series rule of mixtures models to obtain the maximum and minimum macroscopic stiffness matrix, where the volume fraction of SWNTs and nanotube alignment can be controlled. The rule of mixture equations for the maximum and minimum macroscopic stiffness mixtures can be seen in Eqs 5.2 and 5.3, respectively:

$$C^{max}_{3_{phase}} = V_{epoxy}C_{epoxy} + V_{aligned}C^{V}_{aligned} + (1 - V_{ep} - V_{aligned})C^{V}_{random} \tag{5.2}$$

$$C^{min}_{3phase} = \frac{1}{V_{ep}/C_{ep} + V_{aligned}/C^R_{aligned} + (1 - V_{epoxy} - V_{aligned})/C^R_{random}}, \tag{5.3}$$

where the superscripts V and R indicate if the stiffness matrix was calculated via the Voigt or Reuss formulation. The three phases in the rule of mixtures calculations are: the SWNT-epoxy nanocomposites for a fully aligned composite, the SWNT-epoxy nanocomposites for a fully random composite, and neat epoxy. This method is limited to the case where there is only one orientation preferably orientated, and the 2-phase should be used if there are multiple.

5.2.1.3 Comparison of 2-phase and 3-phase Models

For the case explored here of one preferential orientation, it is expected the 2 and 3-phase models should theoretically give the same results. This is because because the calculation of the upper and lower bound stiffness and compliance matrices via Eqs. 4.56 and 4.59 is the same principle as the parallel and series mixtures approaches from Eqs. 4.40 and 4.42. In practice, there are a few differences that can occur from the way the problems were expressed. The 3-phase model was formulated like the Finite Element method, described in 5.1, where the probability was broken up into three parts: the neat epoxy units, the aligned nanotubes, and the random nanotubes. The random portion was taken to still follow the weights from Fig. 4.4, as to not have any orientational preference. This means the orientation chosen as the "aligned" direction still appears in the "random" nanotube probability, so there will be more than just the assigned alignment percentage in that direction. For this reason, an additional percentage of nanotubes in a given direction exist over what was explicitly assigned. When the 2-part cases were run, the percentage aligned is exactly the assigned amount of nanotubes aligned in that direction, and the other phase (neat epoxy) does not contain any of that orientation. These, therefore, will only be the same if the additional alignment due to the "random" portion in the FE and 3-part models was input as the desired alignment for the 2-part method. The other possible limitation is due to the Finite Element discretization of the orientation space for the 2-part method. A mesh with 111 nodes, 50 of which were independent was considered, and some error could be caused by interpolation of the ODF. This error could be minimized by further refining the mesh. A comparison of the 2-part and 3-part for the pristine SWNT-epoxy system with 11 repeat units is shown in Fig. 5.9 for the calculation of E_{xx}. It is seen here that the results are virtually identical. For this reason, for the rest of the dissertation the ODF results presented will be from the 3-part method since it is more computationally efficient. It is also more

suitable for a direct comparison to the FE method since the percentages of alignment are calculated in the same way.

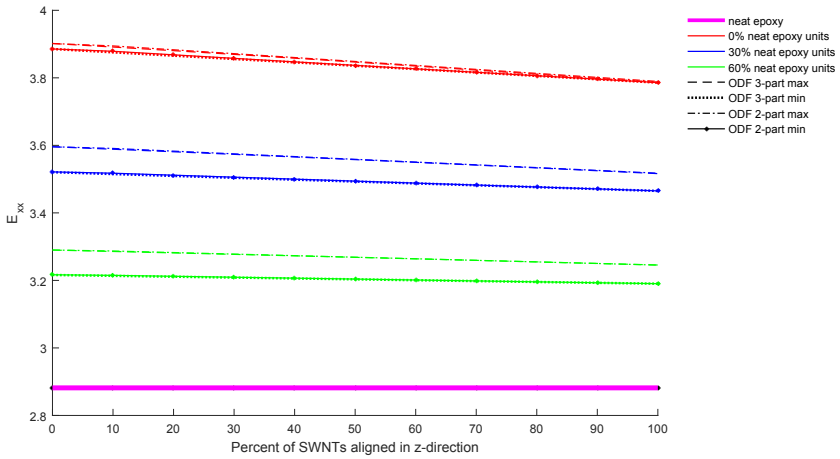

Figure 5.9: Comparison of E_{xx} calculated for the 2-part and 3-part ODF methods vs. % of SWNT alignment at various % of neat epoxy units and 300 K.

5.3 Aligned Results for the Various Multiscale Methods

For the results in this Section, one of the transversely isotropic properties was plotted against the percentage of alignment of SWNTs for a fixed amount of neat epoxy units. Results are calculated for each of the MD lattice configurations: the discontinuous systems; pristine SWNT-epoxy with 11 and 13 repeat units, functionalized SWNT-epoxy with 11 and 13 repeat units, and the funtionalized and pristine systems where nanotube the nanotube spans the entire lattice and was effectively infinite. This was done for fixed percentages of neat epoxy units from 0% to 100% in 10% intervals. For each system, E_{xx}, E_{zz}, G_{xz}, ν_{xy}, ν_{xz} are plotted for each of methods outlined: the Finite Element method, and the ODF upper and lower bounds. The results of the various multiscale methods are compared for each nanocompsite system. Finally, the Finite Element results of the various nanocomposite systems are compared with varying alignment for fixed amounts of neat epoxy units.

5.3.1 Pristine SWNT-Epoxy (11 Repeat Units)

For the pristine SWNT-epoxy system with 11 repeat units, the results of the Finite Element multiscale model are shown in Section 5.3.1.1, the 3-phase ODF upper bound in Section

5.3.1.2, and the 3-phase ODF lower bound in Section 5.3.1.3. All of the multiscale methods at 0%, 30%, 60% neat epoxy units are compared with neat epoxy (100% epoxy units) in Section 5.3.1.4. As expected, all of the methods show a decreasing value of E_{xx} when the percentage of alignment of SWNT in the z-direction increases. From the comparison figure, Fig. 5.19, it is clear the three multiscale models give very similar results, with larger differences occurring when there is more epoxy units and therefore a smaller volume fraction of SWNTs. The Finite Element results lie in the middle of the ODF bounds, but much closer to the upper bound. The value of E_{zz} increases with increasing alignment of nanotubes in the z-direction. For all percentages of neat epoxy units, the Finite Element results lie between the ODF upper and lower bound values, best seen in Fig. 5.20a, and closer to the upper bound value. For G_{xz}, which results from applying stress in the z-direction which acts on a plane normal to the equivalent x or y-directions, the models are essentially constant for varying alignment of nanotubes, and demonstrate decreasing values when the volume fraction of SWNTs was reduced. The Finite Element results fall between the upper bound and lower bounds of the ODF model, seen in 5.20b. At all percentages of alignment, ν_{xy} was increased in the plane of isotropy relative to neat epoxy, meaning there will be more contraction in the y-direction when the system is pulled in the x-direction, or vice versa since the x and y-directions are equivalent. For the various percentages of neat epoxy, the Finite Element model results lies within the upper and lower ODF bounds, shown in Fig. 5.21a. Lastly, for the out of plane Poisson's ratio, ν_{zx}, the nanocomposite starts out with a higher value relative to neat epoxy, and then reduces below neat epoxy around 10% alignment for all models. This value represents the amount of contraction that will occur along the z-direction when there is a tensile load in the plane of isotropy (x-y). The ODF upper and lower bounds are flipped, with the lower bound being higher than the upper bound for both the ODF models. The ODF models bounds the Finite Element model at lower percentages of neat epoxy units. At higher percentages, the Finite Element result lies a bit below the ODF upper bound, though they generally agree very closely, best shown in Fig. 5.21b.

5.3.1.1 Finite Element

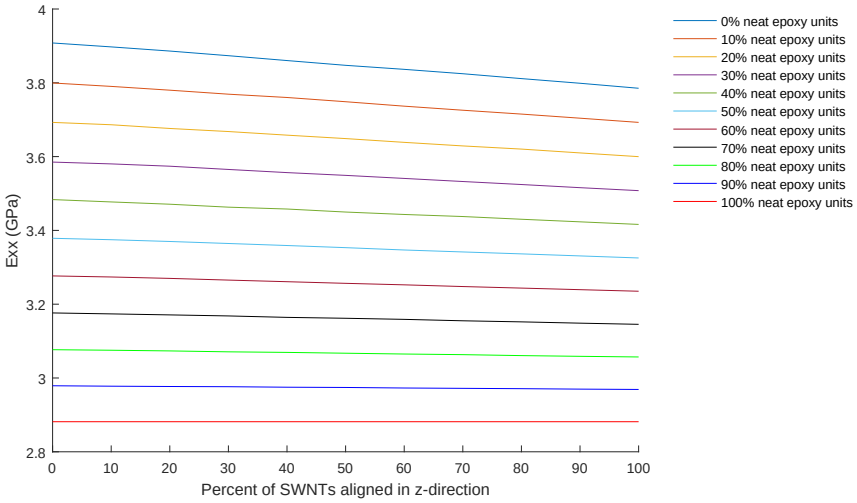

Figure 5.10: Finite Element results for the variation of E_{xx} with respect to % SWNT alignment at various % of neat epoxy units and 300 K.

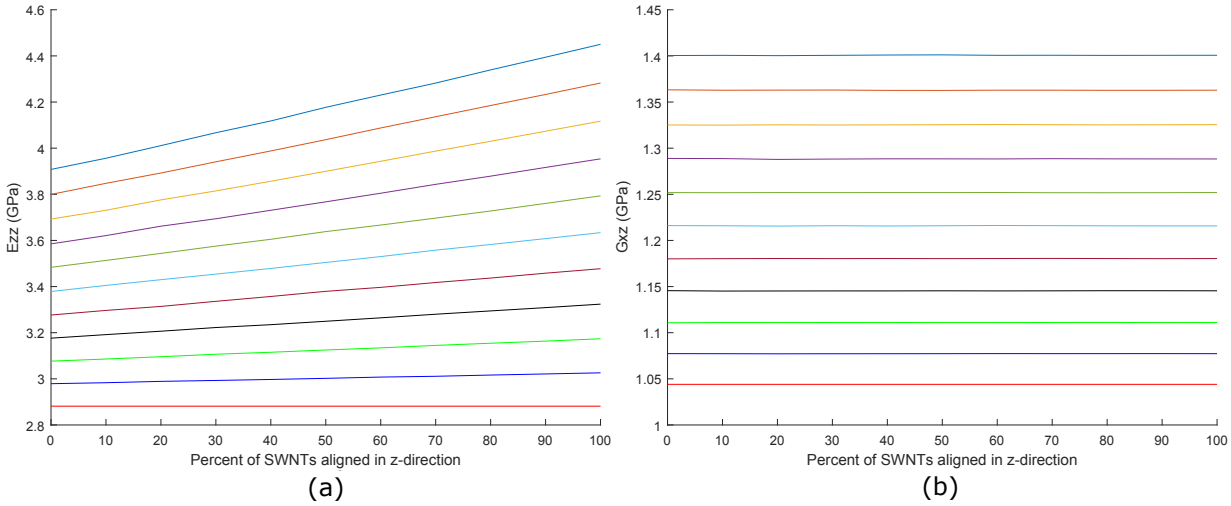

Figure 5.11: Finite Element results for the variation of a. E_{zz} and b. G_{xz} with respect to % SWNT alignment at various % of neat epoxy units and 300 K.

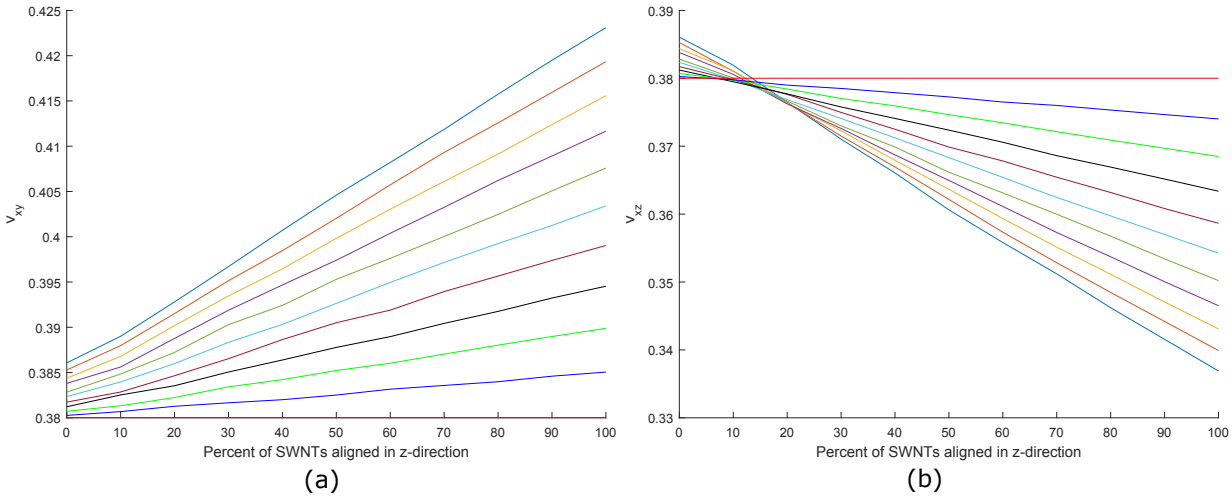

Figure 5.12: Finite Element results for the variation of a. ν_{xy} and b. ν_{xz} with respect to % SWNT alignment at various % of neat epoxy units and 300 K.

5.3.1.2 ODF Upper Bound

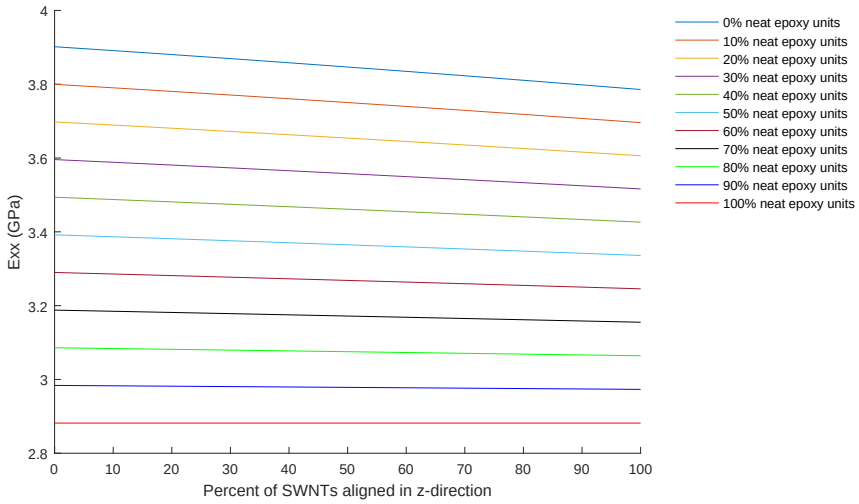

Figure 5.13: ODF upper bound results for the variation of E_{xx} with respect to % SWNT alignment at various % of neat epoxy units and 300 K.

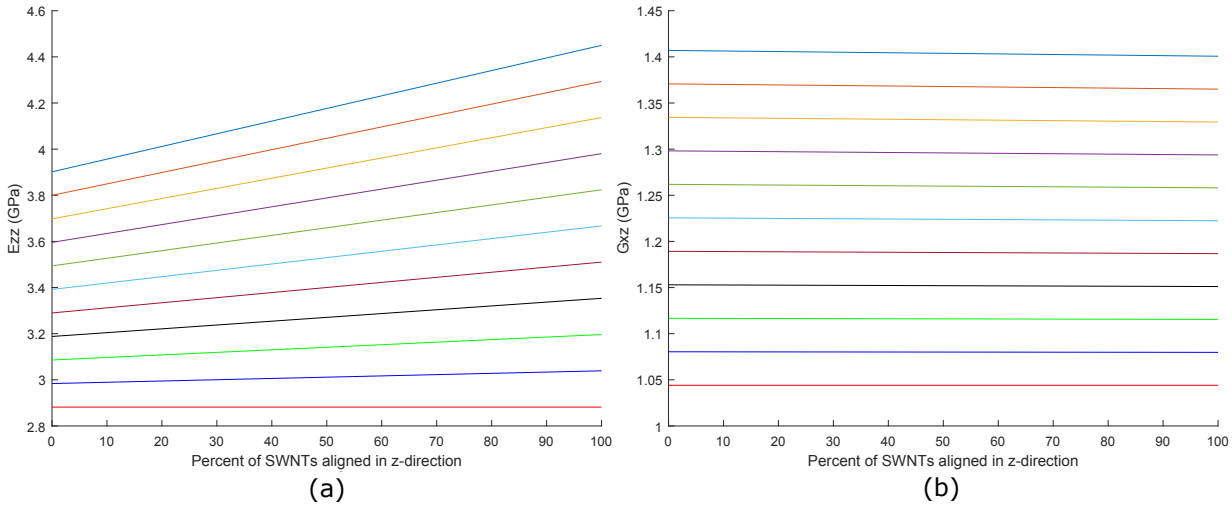

Figure 5.14: ODF upper bound results for the variation of a. E_{zz} and b. G_{xz} with respect to % SWNT alignment at various % of neat epoxy units and 300 K.

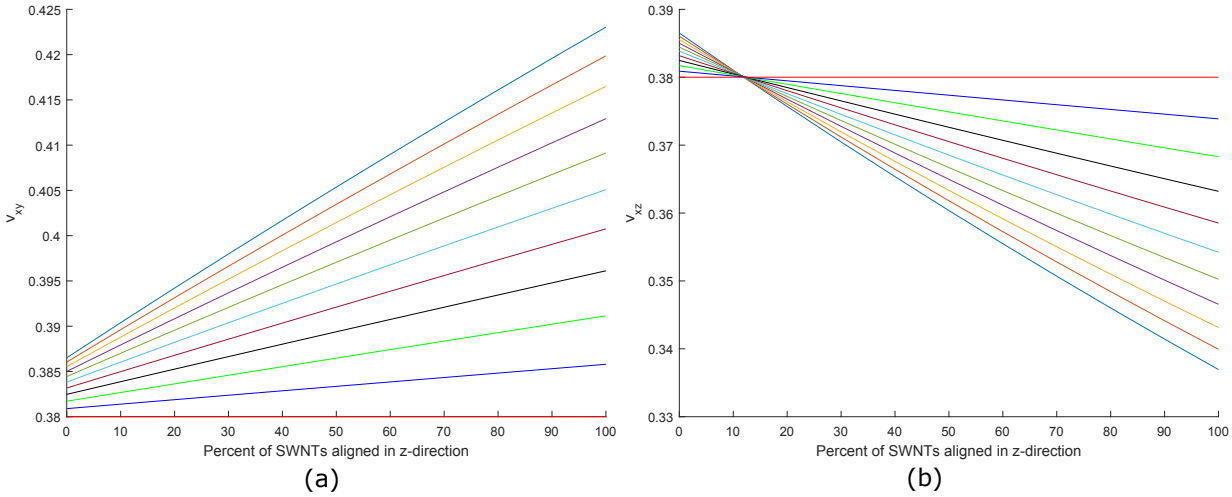

Figure 5.15: ODF upper bound results for the variation of a. ν_{xy} and b. ν_{xz} with respect to % SWNT alignment at various % of neat epoxy units and 300 K.

5.3.1.3 ODF Lower Bound

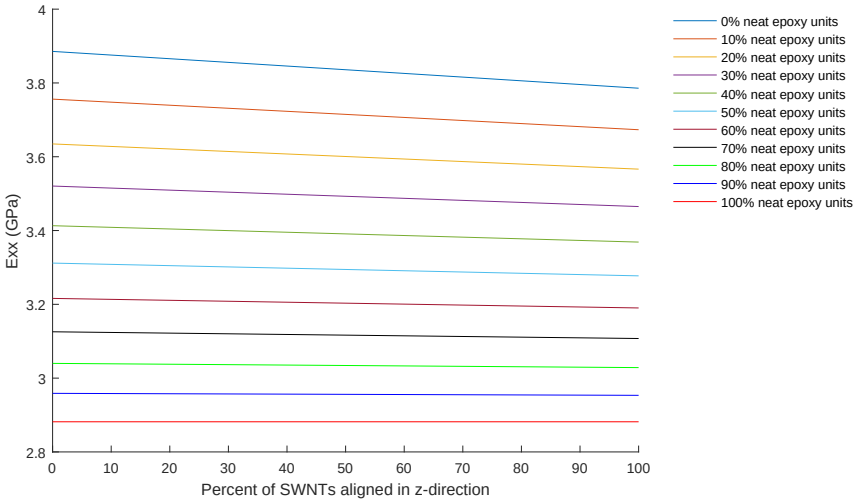

Figure 5.16: ODF lower bound results for the variation of E_{xx} with respect to % SWNT alignment at various % of neat epoxy units and 300 K.

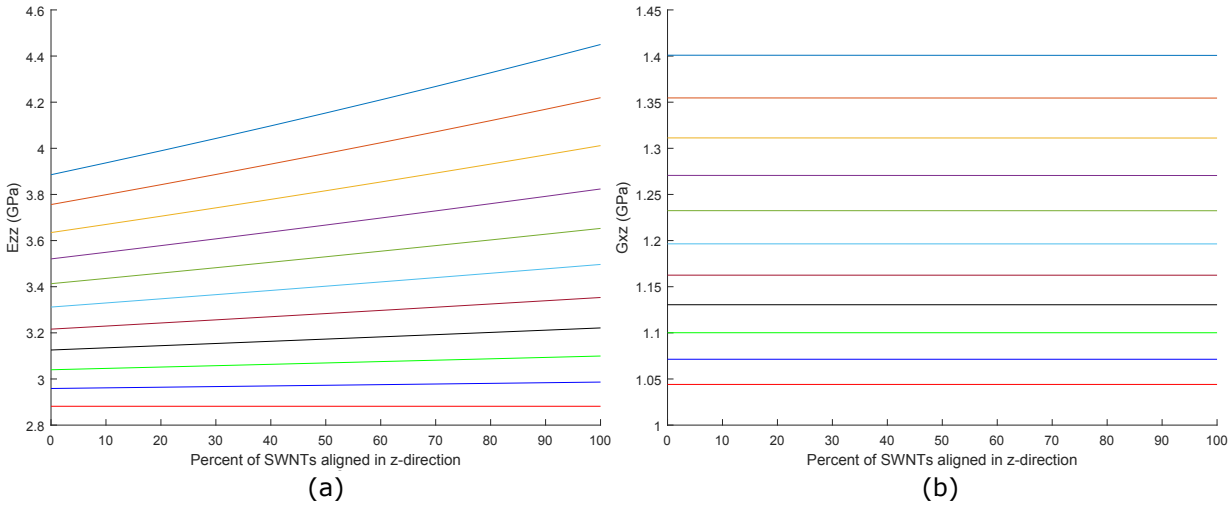

Figure 5.17: ODF lower bound results for the variation of a. E_{zz} and b. G_{xz} with respect to % SWNT alignment at various % of neat epoxy units and 300 K.

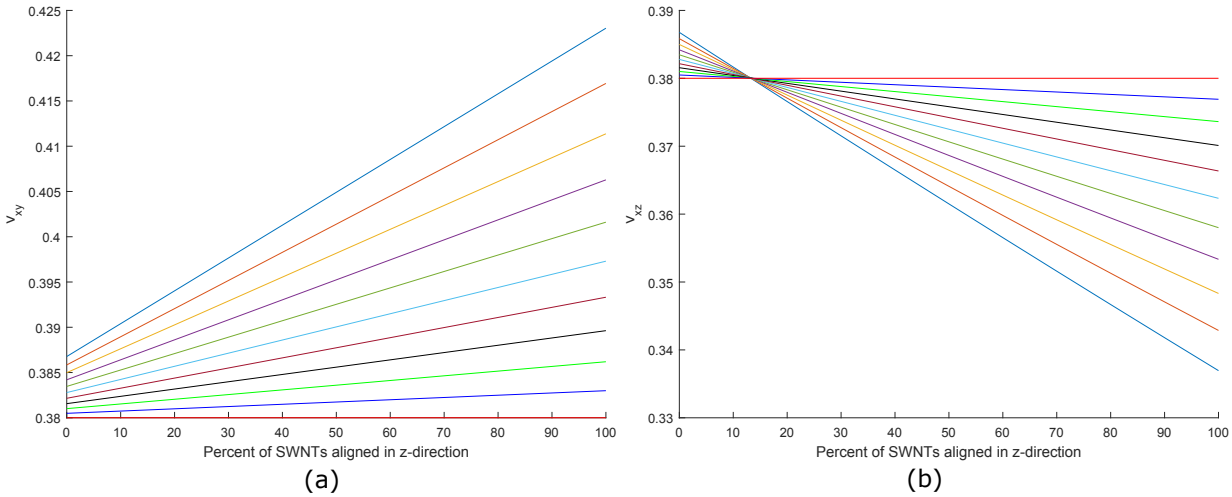

Figure 5.18: ODF lower bound results for the variation of a. ν_{xy} and b. ν_{xz} with respect to % SWNT alignment at various % of neat epoxy units and 300 K.

5.3.1.4 Compare Methods

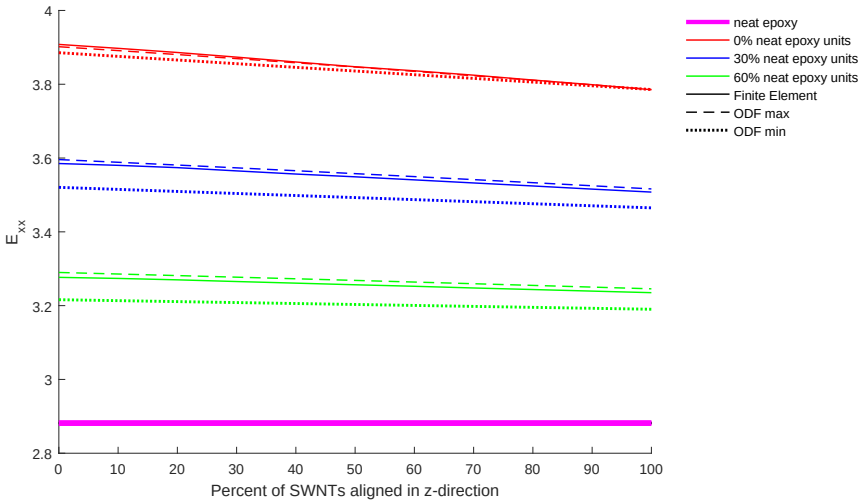

Figure 5.19: Comparison of the methods used to calculate the variation of E_{xx} with respect to % SWNT alignment for various % of neat epoxy units at 300 K.

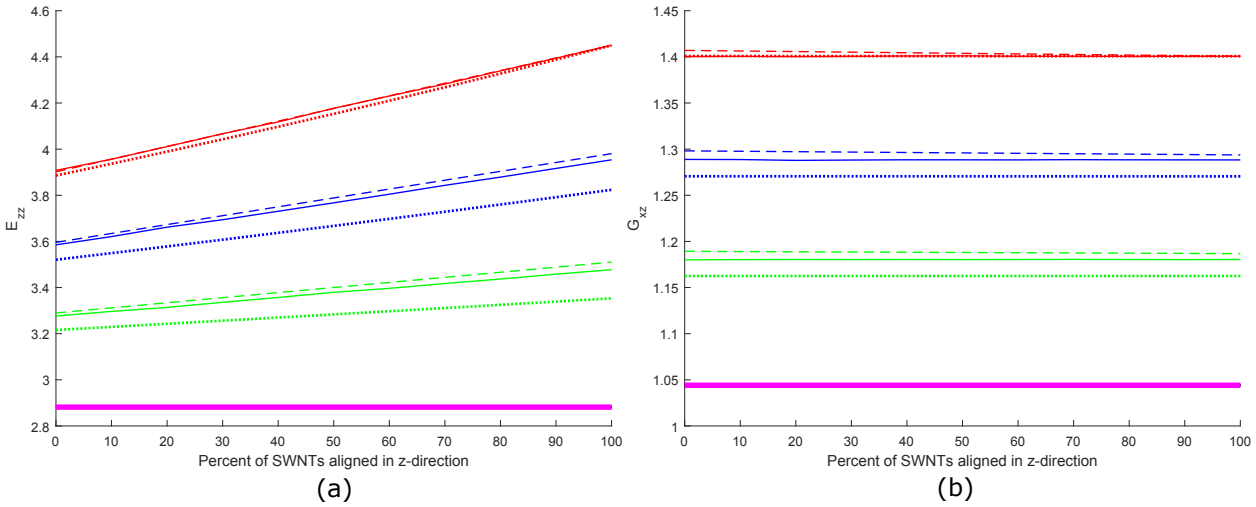

Figure 5.20: Comparison of the methods used to calculate the variation of a. E_{zz} and b. G_{xz} with respect to % SWNT alignment for various % of neat epoxy units at 300 K.

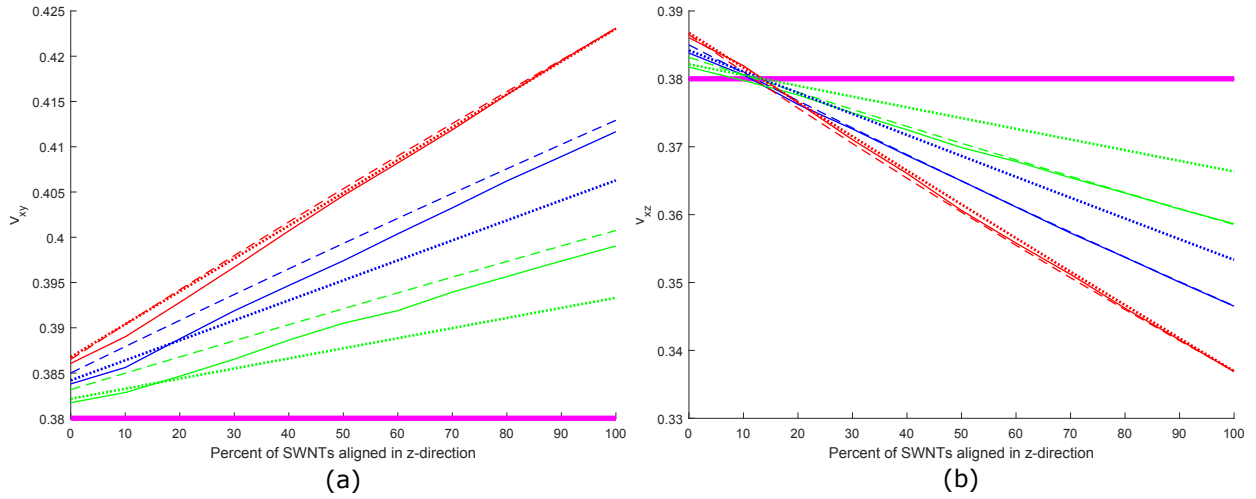

Figure 5.21: Comparison of the methods used to calculate the variation of a. ν_{xy} and b. ν_{xz} with respect to % SWNT alignment for various % of neat epoxy units at 300 K.

5.3.2 Functionalized SWNT-Epoxy (11 Repeat Units)

For the functionalized SWNT-epoxy system with 11 repeat units, the results of the Finite Element multiscale model are shown in Section 5.3.2.1, the 3-phase ODF upper bound in Section 5.3.2.2, and the 3-phase ODF lower bound in Section 5.3.2.3. All of the multiscale methods at 0%, 30%, 60% neat epoxy units are compared with neat epoxy (100% epoxy units) in Section 5.3.2.4. All of the methods give a decreasing value of E_{xx} when the percentage of alignment of SWNT in the z-direction increases, and when the percentage of

epoxy units increases. From the comparison figure, Fig. 5.31, the Finite Element results lie within the bounds of the ODF method. For E_{zz}, the models show a decreasing value of E_{zz} for increased number of nanotubes aligned in the z-direction, which is an unexpected result. The Finite Element results for varying alignment are bounded by the ODF model and follow the same trend. To explain this: the first thing to point out is that, as seen from comparing Figs. 5.22 to 5.23a, 5.25 to 5.26a, and 5.28 to 5.29a, the values of E_{xx} and E_{zz} are comparable, with E_{xx} actually being higher. This is due to the boost in E_{xx} due to functionalization, and the corresponding degradation in E_{zz}. The fact that both E_{xx} and E_{zz} decrease with increasing alignment seems to be an artifact of the effective averaging of the stiffness matrix, where the values of $C(1,1)$ and $C(3,3)$ increase for random composites at the expense of the shear and off-diagonal terms. The initial transversely isotropic stiffness matrix given by MD is:

$$C_{MD} = \begin{bmatrix} 7.60 & 4.94 & 4.80 & 0 & 0 & 0 \\ 4.94 & 7.60 & 4.80 & 0 & 0 & 0 \\ 4.80 & 4.80 & 7.37 & 0 & 0 & 0 \\ 0 & 0 & 0 & 1.59 & 0 & 0 \\ 0 & 0 & 0 & 0 & 1.59 & 0 \\ 0 & 0 & 0 & 0 & 0 & 1.33 \end{bmatrix}.$$

For the fully random case with no alignment, rotation via the Voigt model yields: $C^V(1,1) = C^V(2,2) = C^V(3,3) = 7.65$ and $C^V(4,4) = C^V(5,5) = C^V(6,6) = 1.43$. The lower bound via the the Reuss method leads to: $C^R(1,1) = C^R(2,2) = C^R(3,3) = 7.63$ and $C^R(4,4) = C^R(5,5) = C^R(6,6) = 1.42$. So, from this trend it is expected G_{xz} will increase relatively rapidly with increased alignment to compensate for the decreased E_{xx} and E_{zz} at full alignment, and this is the case for the Finite Element model (Fig. 5.23b), ODF upper bound (Fig. 5.26b), and ODF lower bound (Fig. 5.29b) A comparison of the three methods was plotted in Figs. 5.32a and 5.32b for E_{zz} and G_{xz}, respectively.

For the in-plane Poisson's ratio ν_{xy}, all of the models show the composites have a reduced value relative to neat epoxy for fully random SWNTs, and then at a certain alignment percentage cross neat epoxy, and so there will be more contraction in the y-direction when the system is pulled in the x-direction, or vice versa since the x and y directions are equivalent relative to neat epoxy. The Finite Element model, Fig. 5.24a, shows a linearly increasing ν_{xy} response with increasing alignment, with all percentages of neat epoxy units crossing the epoxy value by 10% alignment. The ODF models show ν_{xy} increasing linearly, and crossing the value of neat epoxy at 10% for the upper bound, and 5% for the

lower bound. A comparison for all the methods is shown in Fig. 5.32a. The out of plane Poisson's ratio, ν_{zx}, gives the amount of contraction that will occur along the nanotube direction when there is a tensile load in the plane of isotropy (x-y). The ODF models show ν_{zx} to be below the neat epoxy value, and linearly decreasing with increasing alignment. For the Finite Element model in Fig. 5.24b, all amounts of epoxy and alignment are above the neat epoxy value, though the magnitude of increase is small, with a 2% maximum from 100% to 0% neat epoxy units. This result, while somewhat surprising, does make sense since the FE model predicts stiffness in the plane of isotropy to be higher than that of the nanotube direction. A comparison for all the methods for ν_{zx} is shown in Fig. 5.32b.

5.3.2.1 Finite Element

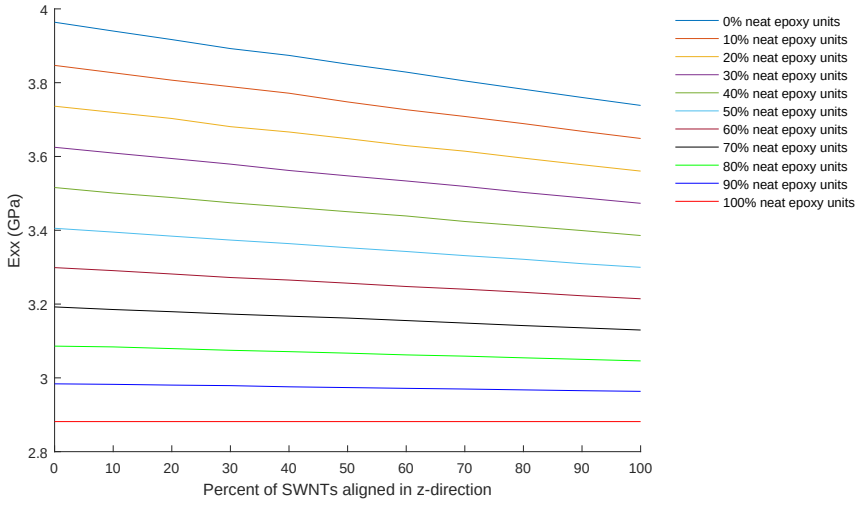

Figure 5.22: Finite Element results for the variation of E_{xx} with respect to % SWNT alignment at various % of neat epoxy units and 300 K.

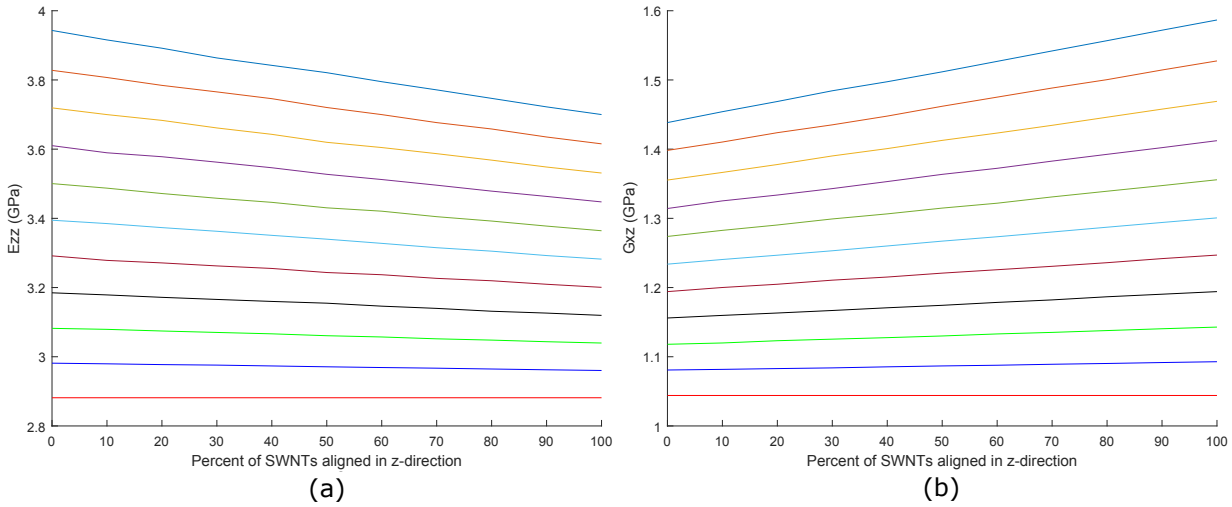

Figure 5.23: Finite Element results for the variation of a. E_{zz} and b. G_{xz} with respect to % SWNT alignment at various % of neat epoxy units and 300 K.

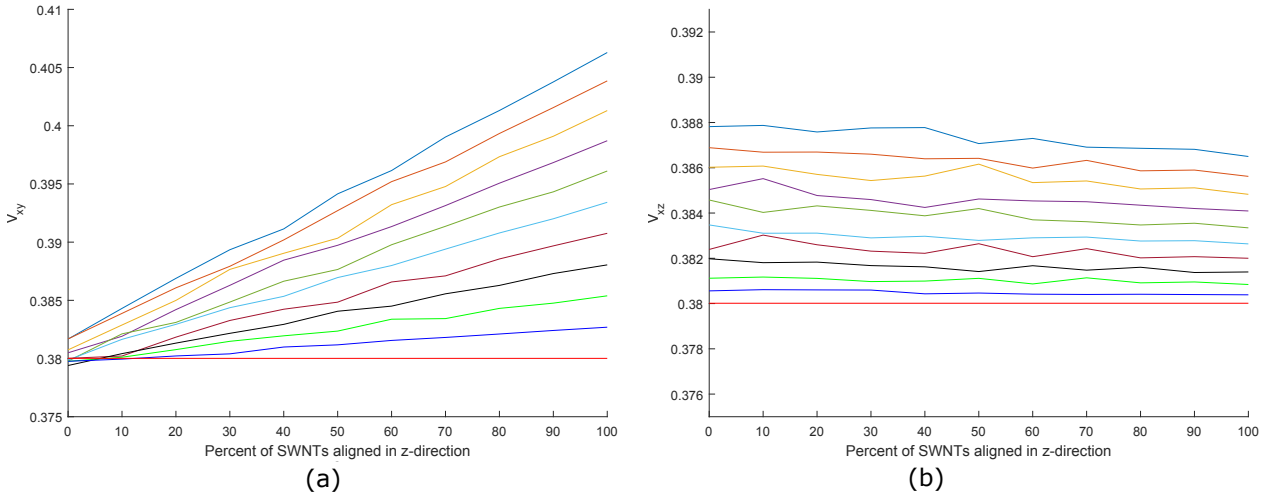

Figure 5.24: Finite Element results for the variation of a. ν_{xy} and b. ν_{xz} with respect to % SWNT alignment at various % of neat epoxy units and 300 K.

5.3.2.2 ODF Upper Bound

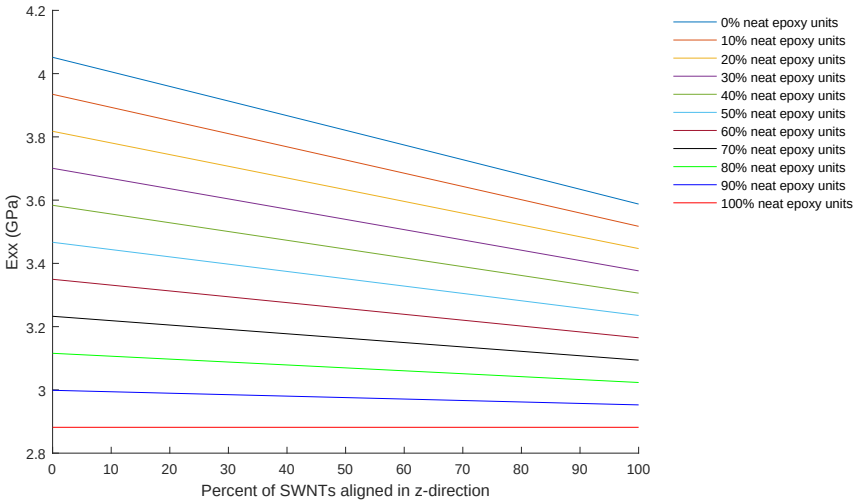

Figure 5.25: ODF upper bound results for the variation of E_{xx} with respect to % SWNT alignment at various % of neat epoxy units and 300 K.

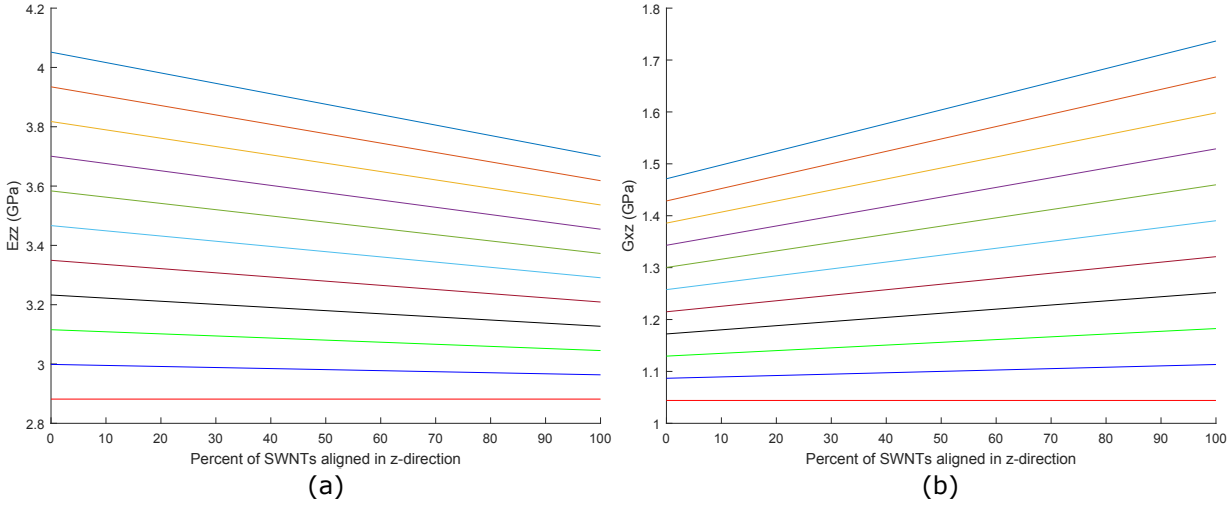

Figure 5.26: ODF upper bound results for the variation of a. E_{zz} and b. G_{xz} with respect to % SWNT alignment at various % of neat epoxy units and 300 K.

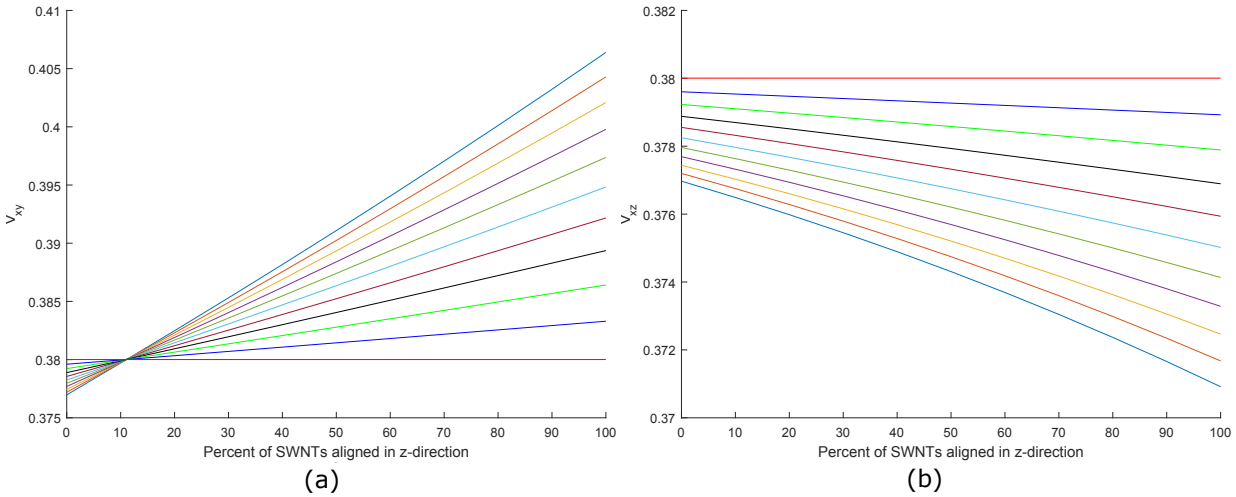

Figure 5.27: ODF upper bound results for the variation of a. ν_{xy} and b. ν_{xz} with respect to % SWNT alignment at various % of neat epoxy units and 300 K.

5.3.2.3 ODF Lower Bound

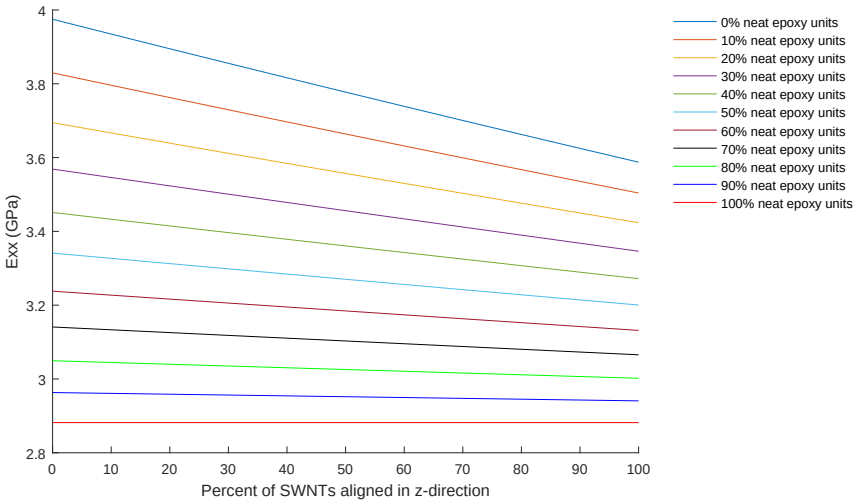

Figure 5.28: ODF lower bound results for the variation of E_{xx} with respect to % SWNT alignment at various % of neat epoxy units and 300 K.

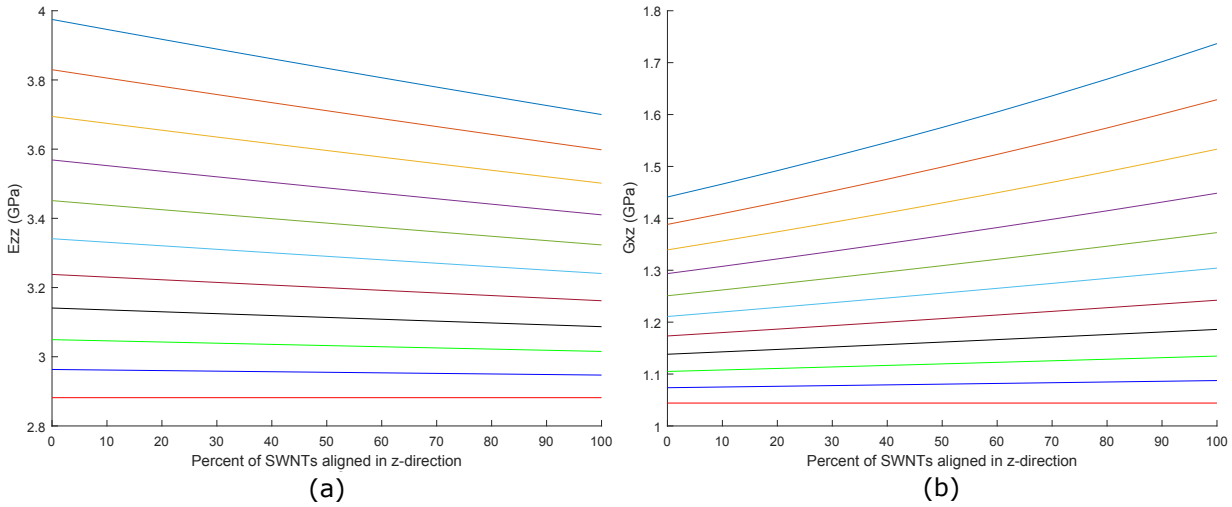

Figure 5.29: ODF lower bound results for the variation of a. E_{zz} and b. G_{xz} with respect to % SWNT alignment at various % of neat epoxy units and 300 K.

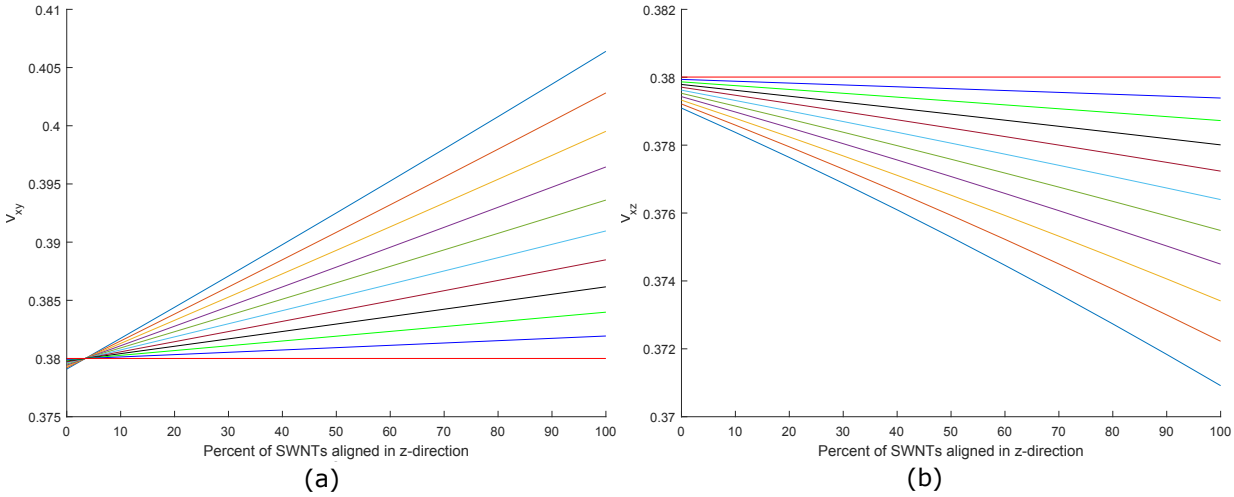

Figure 5.30: ODF lower bound for the variation of a. ν_{xy} and b. ν_{xz} with respect to % SWNT alignment at various % of neat epoxy units and 300 K.

5.3.2.4 Compare Methods

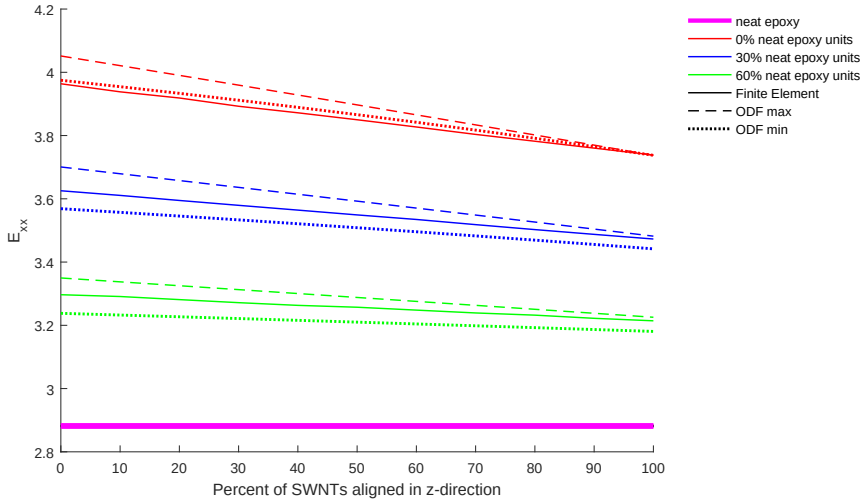

Figure 5.31: Comparison of the methods used to calculate the variation of E_{xx} with respect to % SWNT alignment for various % of neat epoxy units at 300 K.

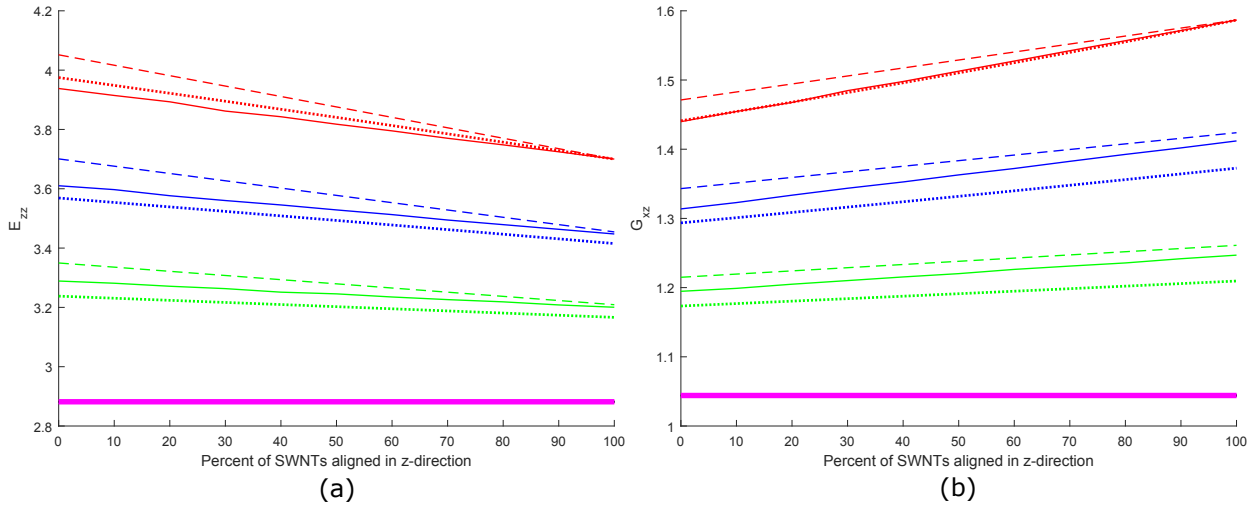

Figure 5.32: Comparison of the methods used to calculate the variation of a. E_{zz} and b. G_{xz} with respect to % SWNT alignment for various % of neat epoxy units at 300 K.

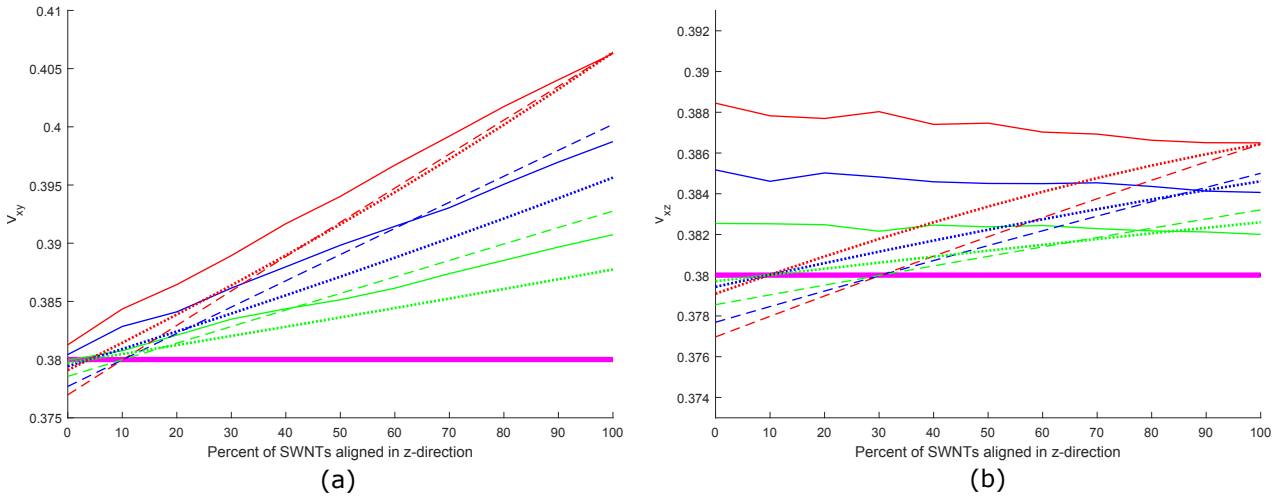

Figure 5.33: Comparison of the methods used to calculate the variation of a. ν_{xy} and b. ν_{xz} with respect to % SWNT alignment for various % of neat epoxy units at 300 K.

5.3.3 Pristine SWNT-Epoxy (13 Repeat Units)

For the pristine SWNT-epoxy system with 13 repeat units, the results of the Finite Element multiscale model are shown in Section 5.3.3.1, the ODF upper bound in Section 5.3.3.2, and the ODF lower bound in Section 5.3.3.3. All of the multiscale methods at 0%, 30%, 60% neat epoxy units are compared with neat epoxy (100% epoxy units) in Section 5.3.3.4. For E_{xx} and E_{zz}, a similar trends to the pristine SWNT-epoxy system with 11 repeat units was seen for the three models. E_{xx} decreases with increasing alignment, and all the models give very close results, with the ODF models being very close to one another and tightly bounding the Finite Element result, seen in Fig. 5.43. E_{zz} and G_{xz} increase with increasing alignment, and the Finite Element model is bounded by the ODF model, shown in 5.44a and 5.44b, respectively. At all percentages of alignment, there is an increased ν_{xy} in the plane of isotropy relative to neat epoxy, meaning there will be more contraction in the y-direction when the system is pulled in the x-direction, or vice versa since the x and y directions are equivalent. Once again, the ODF model bounds the Finite Element model at all percentages of neat epoxy, shown in 5.45a. All the models initially show an increased ν_{zx} when compared to neat epoxy, before eventually being equal at somewhere between 40-70% alignment for the various models, shown in Fig. 5.45b, where systems with more epoxy units reach the neat epoxy value with less percentage alignment. The transition occurs between 40-50% for the Finite Element model, and around 50-70% for the ODF upper and lower bounds. The upper and lower bounds have flipped roles for the ODF results. The Finite Element model generally shows the least amount of contraction along

the nanotube direction when a tensile load is applied in the plane of isotropy (x-y), and crosses the neat epoxy value at the lowest percentage of alignment.

5.3.3.1 Finite Element

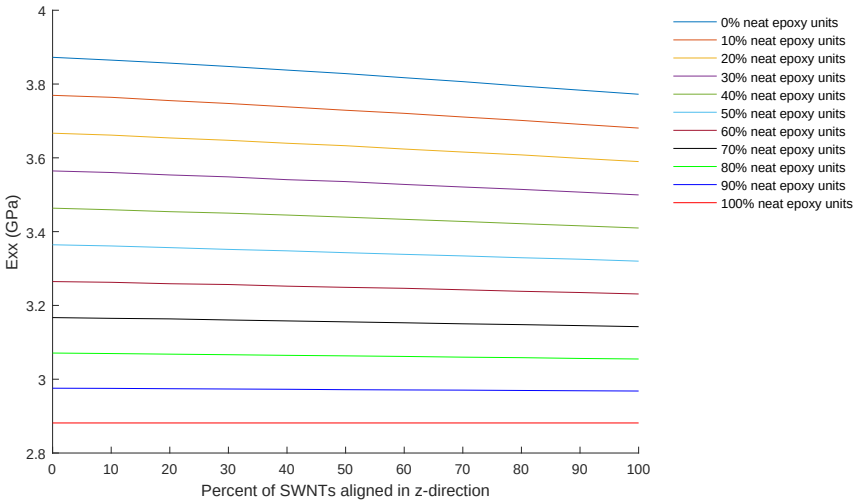

Figure 5.34: Finite Element results for the variation of E_{xx} with respect to % SWNT alignment at various % of neat epoxy units and 300 K.

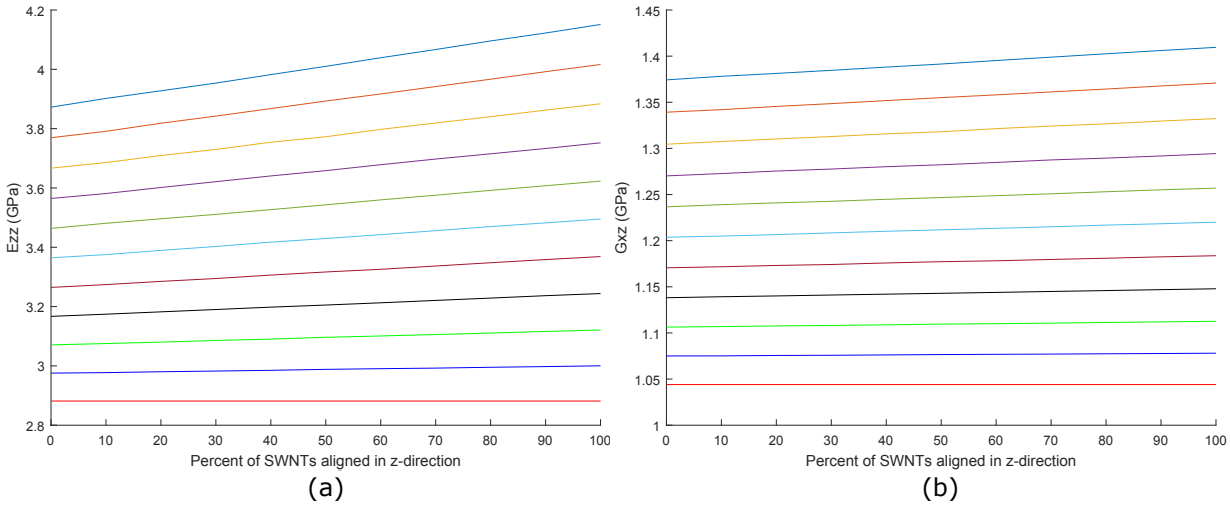

Figure 5.35: Finite Element results for the variation of a. E_{zz} and b. G_{xz} with respect to % SWNT alignment at various % of neat epoxy units and 300 K.

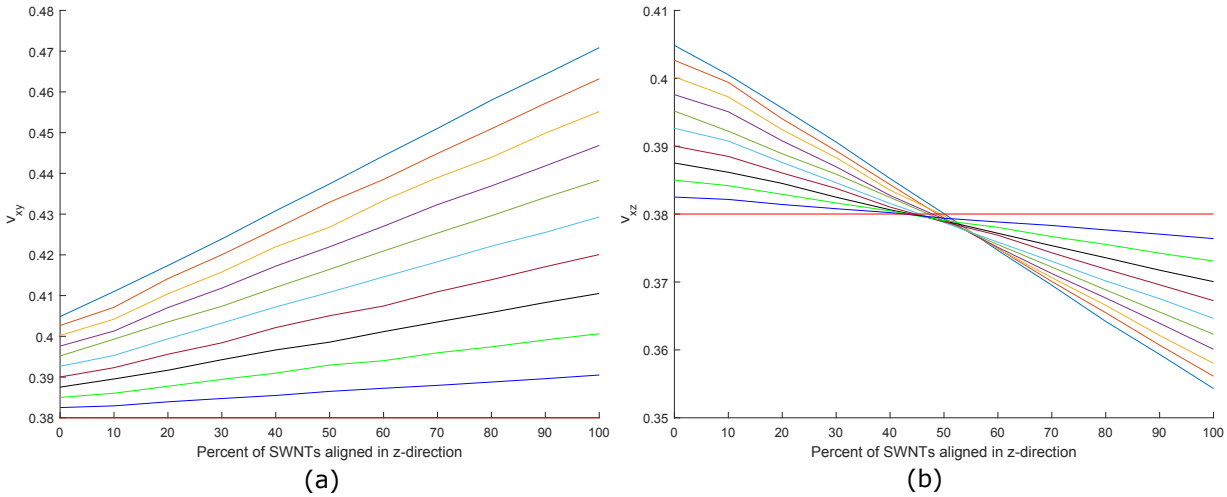

Figure 5.36: Finite Element results for the variation of a. ν_{xy} and b. ν_{xz} with respect to % SWNT alignment at various % of neat epoxy units and 300 K.

5.3.3.2 ODF Upper Bound

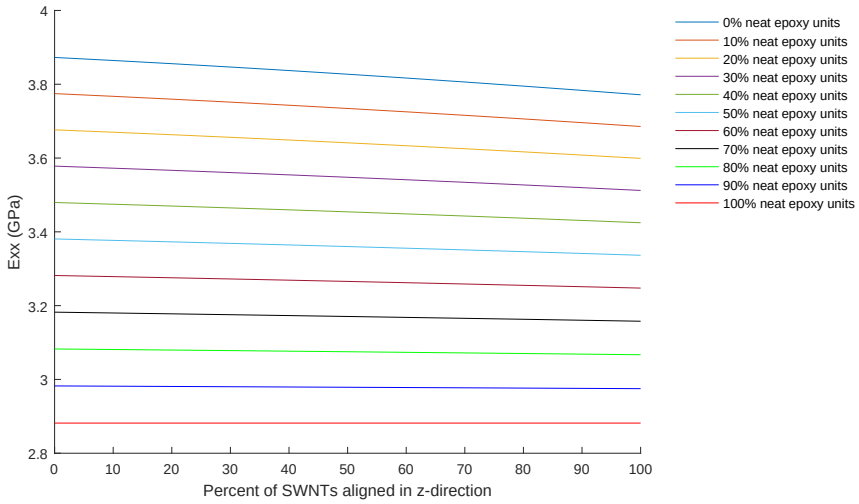

Figure 5.37: ODF upper bound results for the variation of E_{xx} with respect to % SWNT alignment at various % of neat epoxy units and 300 K.

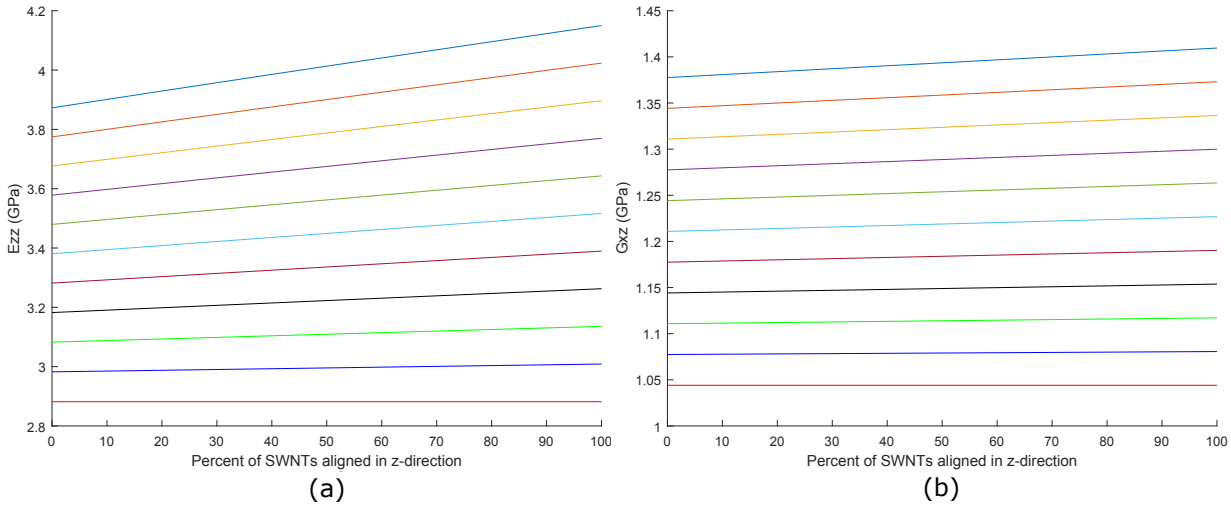

Figure 5.38: ODF upper bound results for the variation of a. E_{zz} and b. G_{xz} with respect to % SWNT alignment at various % of neat epoxy units and 300 K.

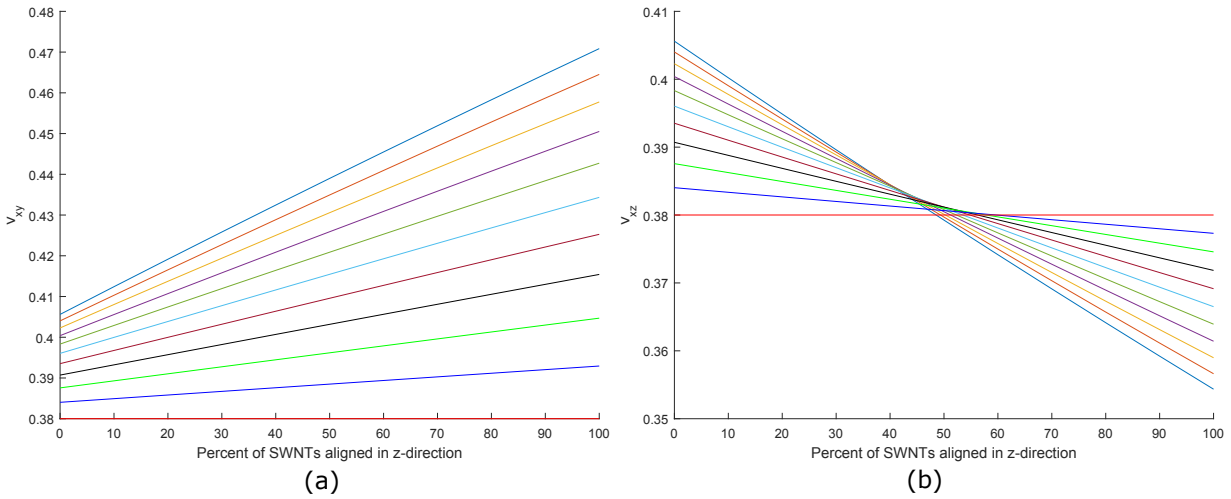

Figure 5.39: ODF upper bound results for the variation of a. ν_{xy} and b. ν_{xz} with respect to % SWNT alignment at various % of neat epoxy units and 300 K.

5.3.3.3 ODF Lower Bound

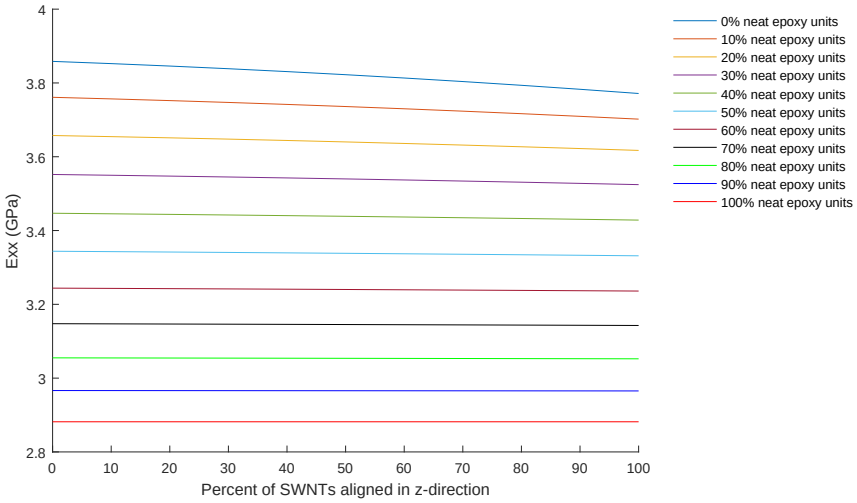

Figure 5.40: ODF lower bound results for the variation of E_{xx} with respect to % SWNT alignment at various % of neat epoxy units and 300 K.

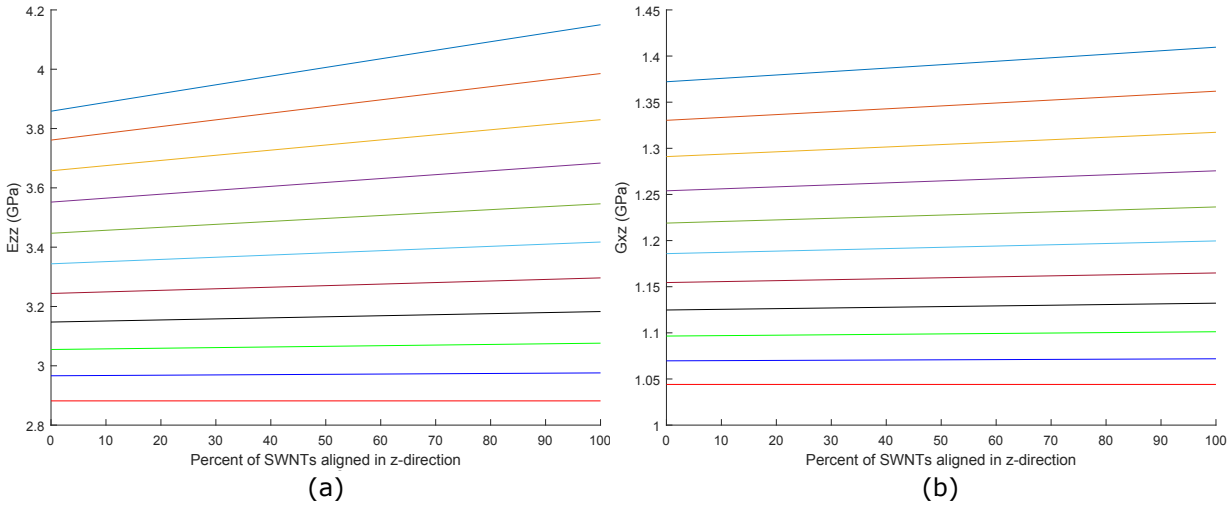

Figure 5.41: ODF lower bound results for the variation of a. E_{zz} and b. G_{xz} with respect to % SWNT alignment at various % of neat epoxy units and 300 K.

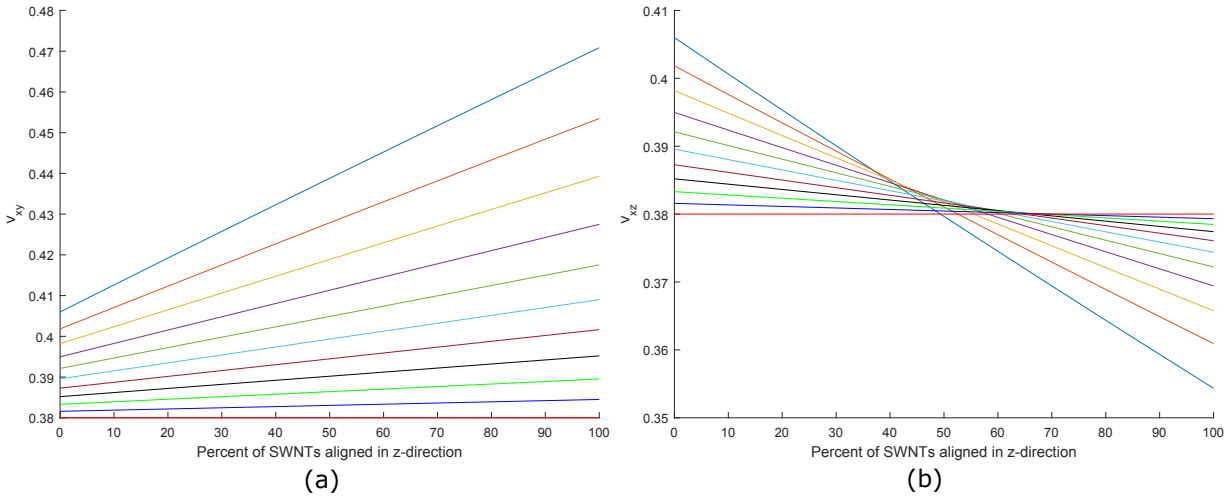

Figure 5.42: ODF lower bound results for the variation of a. ν_{xy} and b. ν_{xz} with respect to % SWNT alignment at various % of neat epoxy units and 300 K.

5.3.3.4 Compare Methods

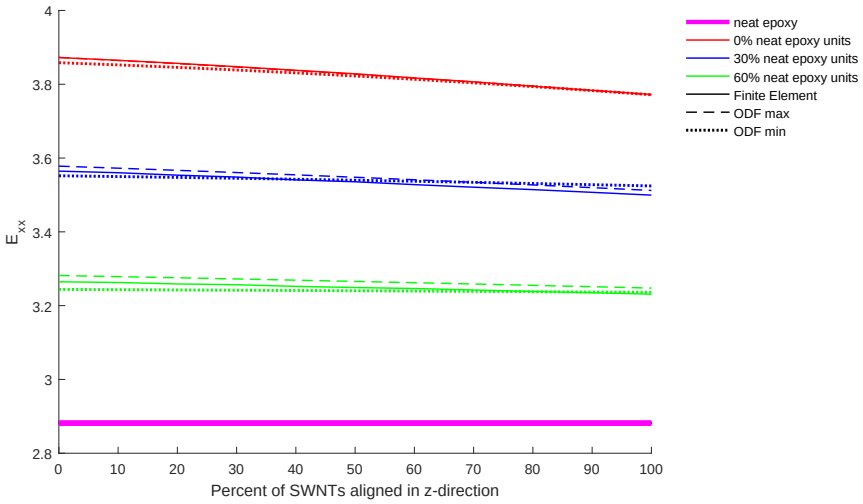

Figure 5.43: Comparison of the methods used to calculate the variation of E_{xx} with respect to % SWNT alignment for various % of neat epoxy units at 300 K.

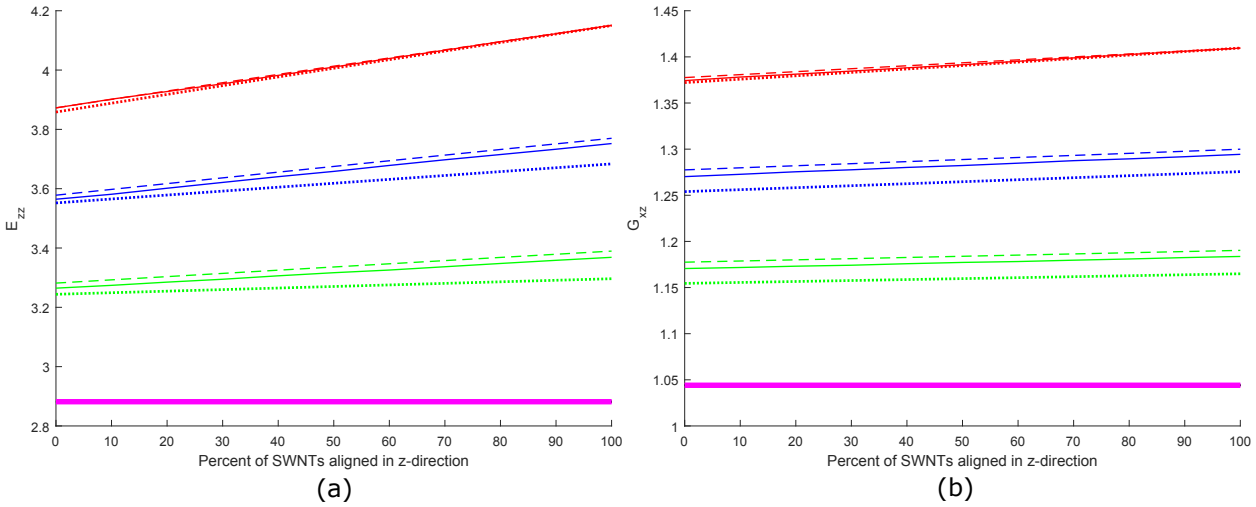

Figure 5.44: Comparison of the methods used to calculate the variation of a. E_{zz} and b. G_{xz} with respect to % SWNT alignment for various % of neat epoxy units at 300 K.

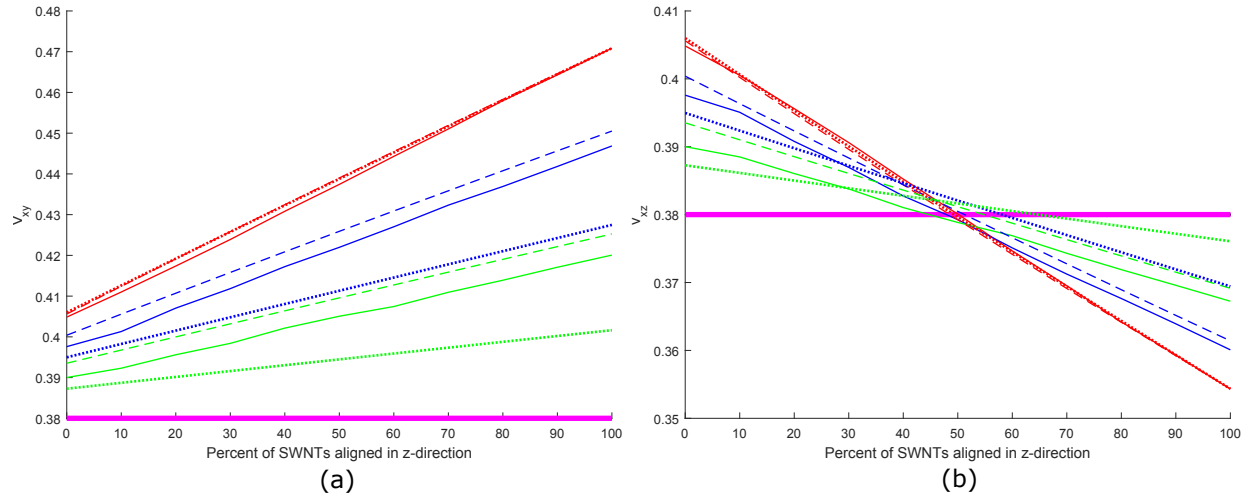

Figure 5.45: Comparison of the methods used to calculate the variation of a. ν_{xy} and b. ν_{xz} with respect to % SWNT alignment for various % of neat epoxy units at 300 K.

5.3.4 Functionalized SWNT-Epoxy (13 Repeat Units)

For the functionalized SWNT-epoxy system with 13 repeat units, the results of the Finite Element multiscale model are shown in Section 5.3.4.1, the ODF upper bound in Section 5.3.4.2, and the lower bound in Section 5.3.4.3. Comparisons between the three models at 0%, 30%, 60% and 100% neat epoxy units are given in Section 5.3.4.4. This system shows the most prominent effects of the nanotubes among the discontinuous systems, with the in-plane, ν_{xy}, and out-of-plane, ν_{xz}, Poisson's ratios being smaller than the neat epoxy value

for all volume fractions and alignment of SWNT. The various methods all give a decreasing value of E_{xx} when the percentage of alignment of SWNT in the z-direction increases, and when the percentage of epoxy units increases. The Finite Element model lies within the narrow bonds of the ODF model, shown in Fig. 5.55. Unlike the functionalized system with 11 repeat units, all of the models show an increasing value of E_{zz} with increasing alignment. Similar to E_{xx}, the Finite Element result is tightly bounded by the ODF results, except at lower amounts of alignment seen in 5.56a. All the models show increasing G_{xz} with increasing alignment, and the three models display the similar trends they did relative to one another for E_{zz}, shown in Fig. 5.56b. As mentioned earlier, all of the models have a reduced ν_{xy} value relative to neat epoxy at all volume fractions of SWNT and all alignments, with lower values for less alignment and higher amounts of SWNTs. The Finite Element model shows an initially small increase in ν_{xy} before the slope increases at higher alignments. Due to this non-linear relationship between ν_{xy} and alignment, the Finite Element model is not bounded well by the ODF method, seen in Fig. 5.57a. The ODF model shows increasingly widening bounds at higher percentages of neat epoxy units. The magnitude of ν_{xz} is reduced with increasing alignment for all the models. In Fig. 5.57b, the Finite Element is in good agreement with the ODF model. For the functionalized nanocomposite with SWNTs with 13 repeat units, the amount contraction transverse to the tension direction is reduced for all loading directions.

5.3.4.1 Finite Element

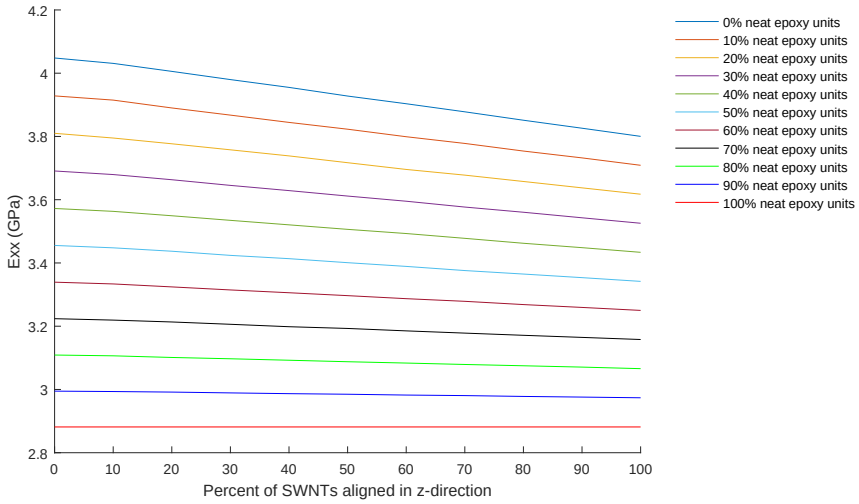

Figure 5.46: Finite Element results for the variation of E_{xx} with respect to % SWNT alignment at various % of neat epoxy units and 300 K.

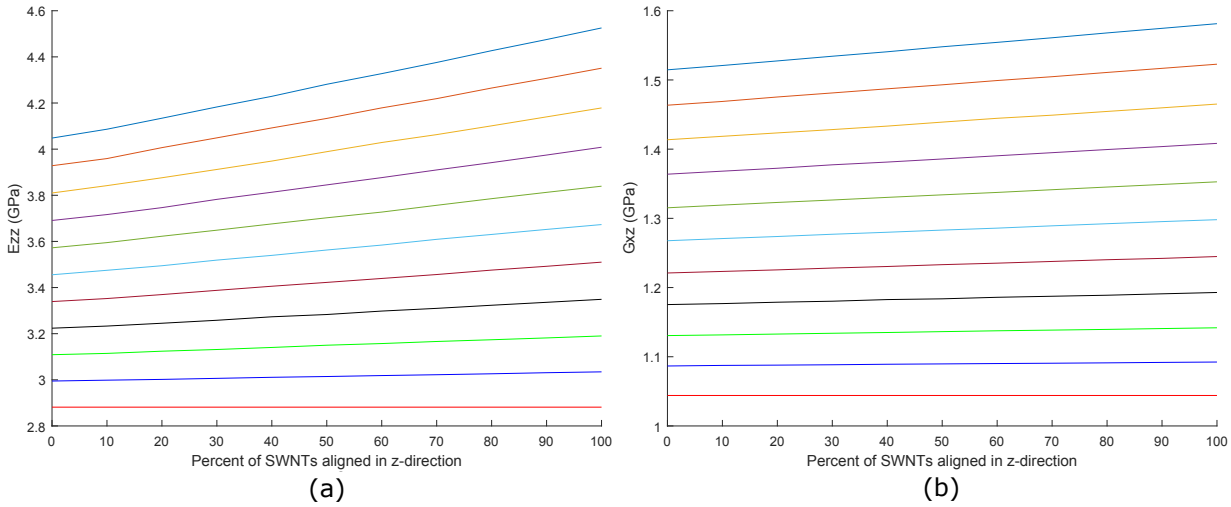

Figure 5.47: Finite Element results for the variation of a. E_{zz} and b. G_{xz} with respect to % SWNT alignment at various % of neat epoxy units and 300 K.

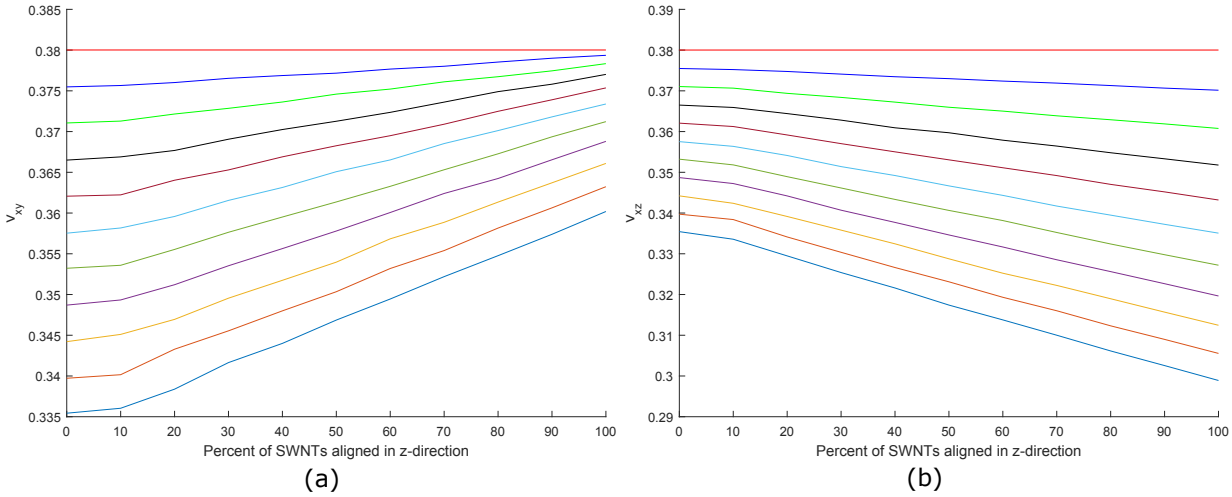

Figure 5.48: Finite Element results for the variation of a. ν_{xy} and b. ν_{xz} with respect to % SWNT alignment at various % of neat epoxy units and 300 K.

5.3.4.2 ODF Upper Bound

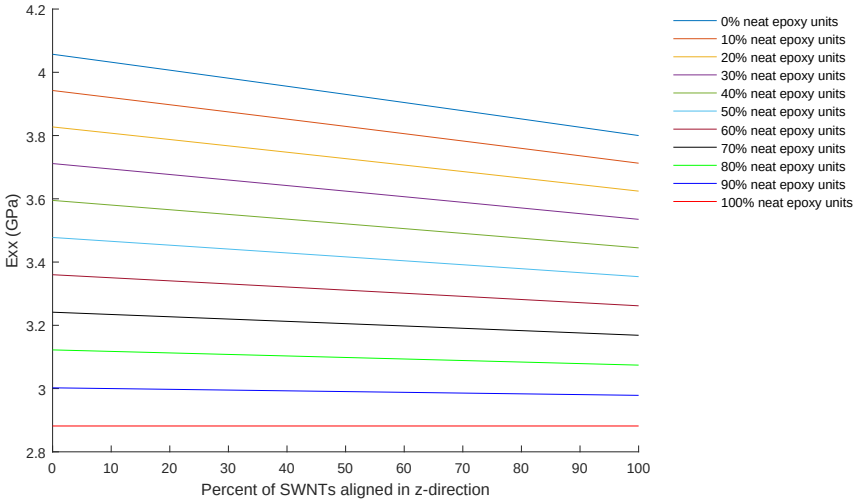

Figure 5.49: ODF upper bound results for the variation of E_{xx} with respect to % SWNT alignment at various % of neat epoxy units and 300 K.

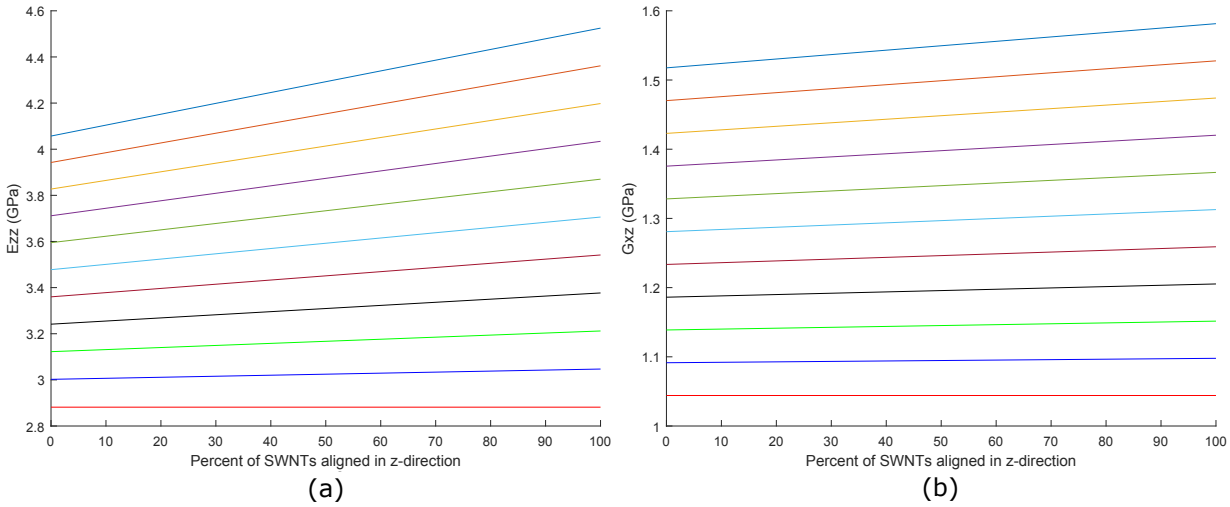

Figure 5.50: ODF upper bound results for the variation of a. E_{zz} and b. G_{xz} with respect to % SWNT alignment at various % of neat epoxy units and 300 K.

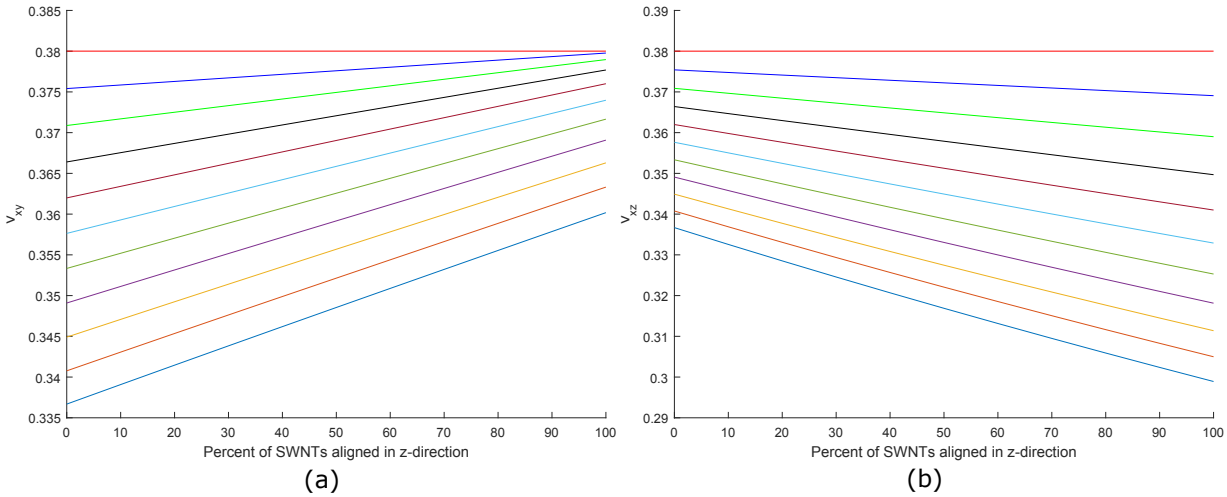

Figure 5.51: ODF upper bound results for the variation of a. ν_{xy} and b. ν_{xz} with respect to % SWNT alignment at various % of neat epoxy units and 300 K.

5.3.4.3 ODF Lower Bound

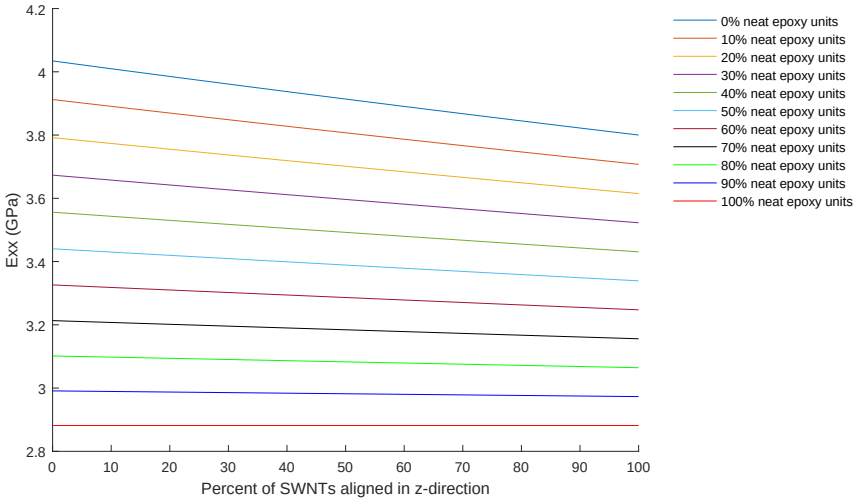

Figure 5.52: ODF lower bound results for the variation of E_{xx} with respect to % SWNT alignment at various % of neat epoxy units and 300 K.

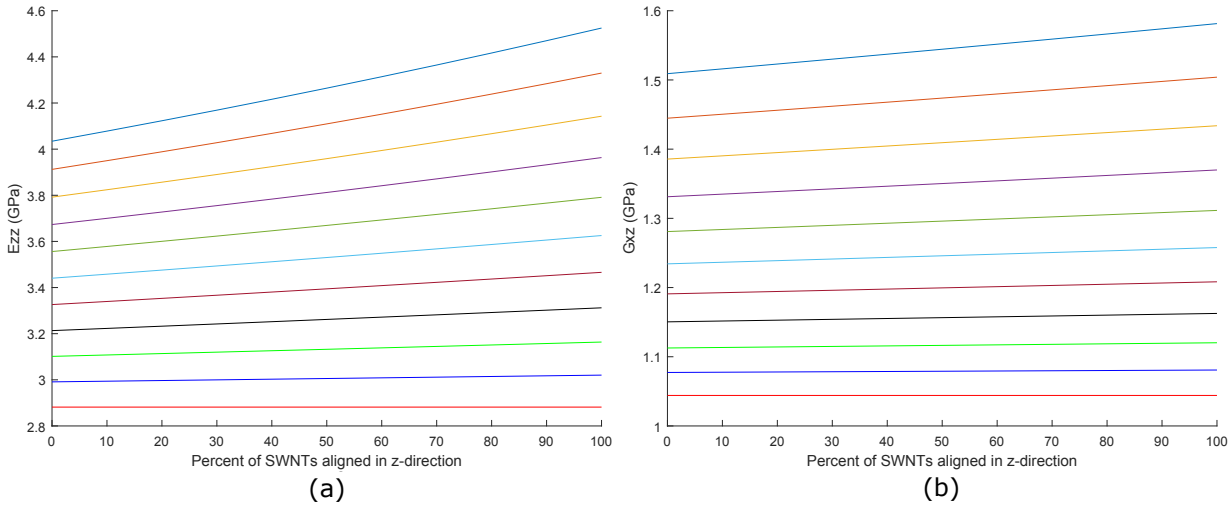

Figure 5.53: ODF lower bound results for the variation of a. E_{zz} and b. G_{xz} with respect to % SWNT alignment at various % of neat epoxy units and 300 K.

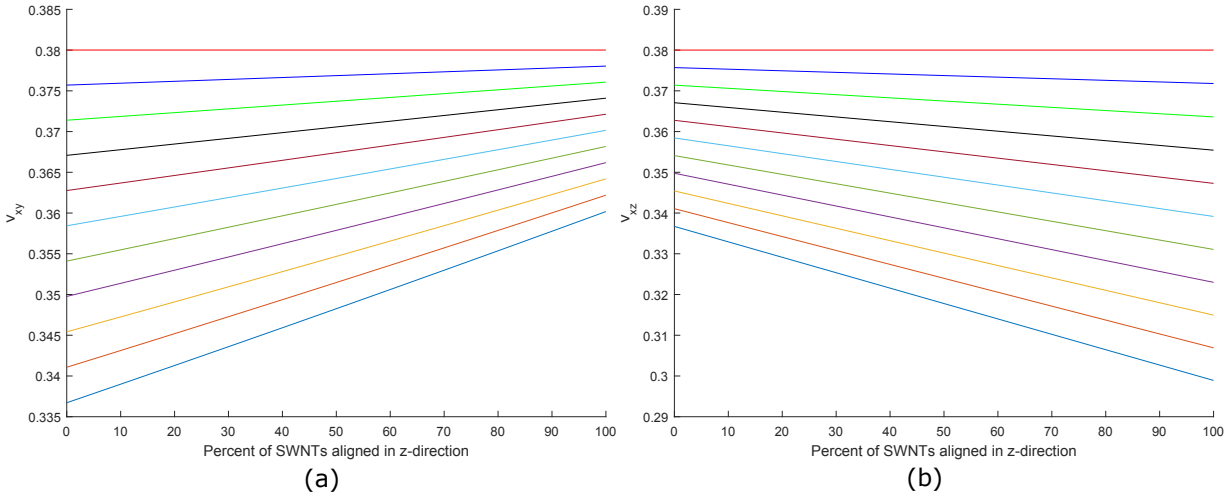

Figure 5.54: ODF lower bound results for the variation of a. ν_{xy} and b. ν_{xz} with respect to % SWNT alignment at various % of neat epoxy units and 300 K.

5.3.4.4 Compare Methods

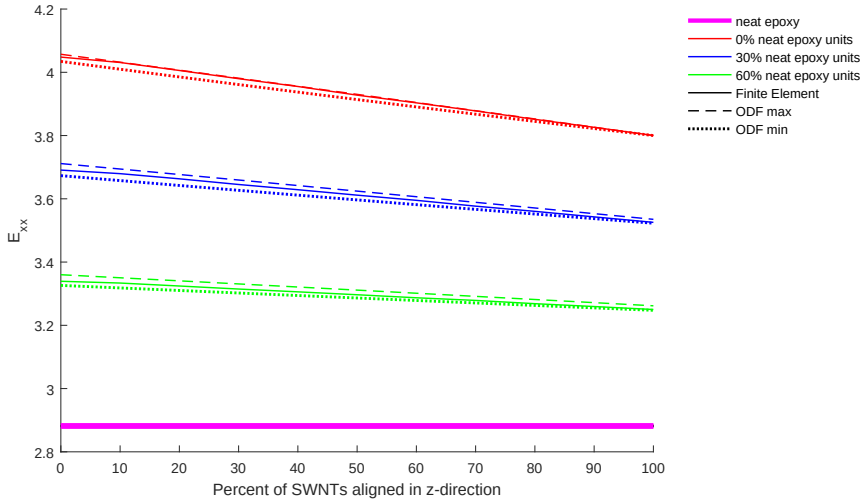

Figure 5.55: Comparison of the methods used to calculate the variation of E_{xx} with respect to % SWNT alignment for various % of neat epoxy units at 300 K.

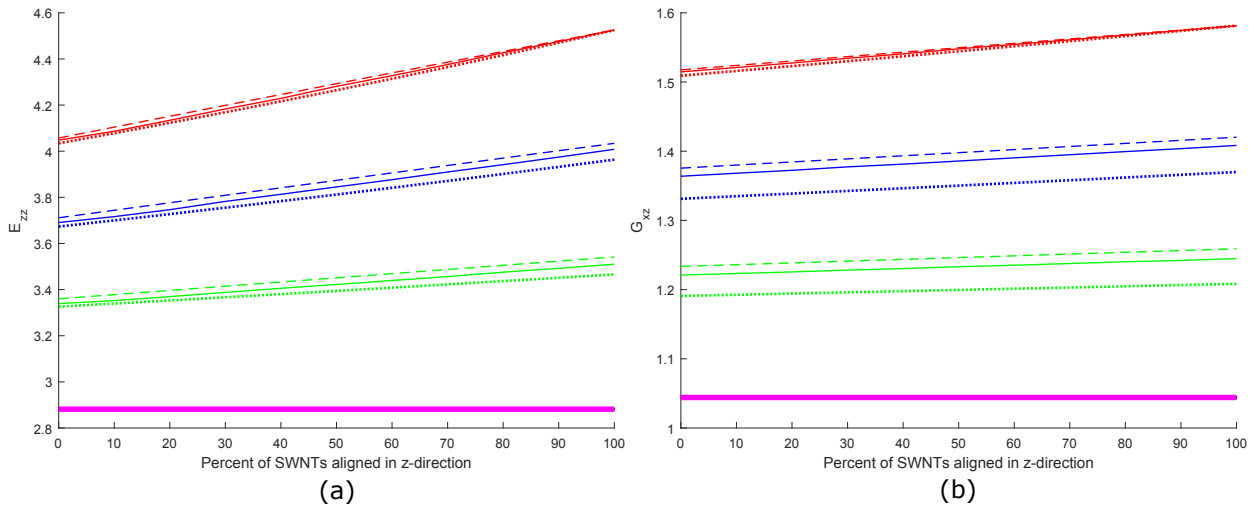

Figure 5.56: Comparison of the methods used to calculate the variation of a. E_{zz} and b. G_{xz} with respect to % SWNT alignment for various % of neat epoxy units at 300 K.

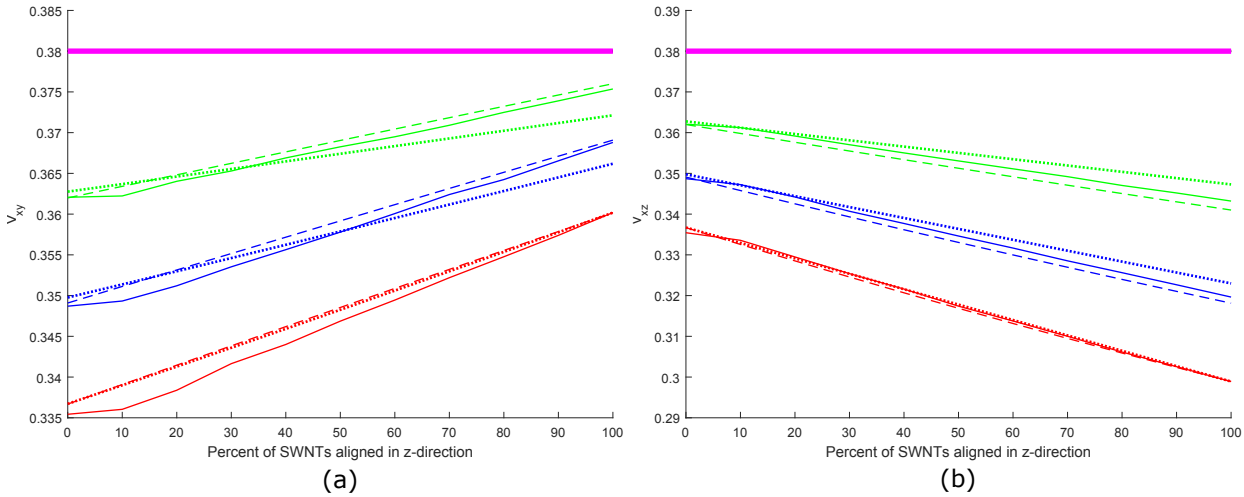

Figure 5.57: Comparison of the methods used to calculate the variation of a. ν_{xy} and b. ν_{xz} with respect to % SWNT alignment for various % of neat epoxy units at 300 K.

5.3.5 Pristine SWNT-Epoxy (Infinite)

For the pristine SWNT-epoxy system with nanotubes that span the entire lattice, becoming effectively infinite with periodic boundary conditions applied, the results of the Finite Element multiscale model are shown in Section 5.3.5.1, the ODF upper bound in Section 5.3.5.2, and the ODF lower bound in Section 5.3.5.3. Comparisons between the three models at 0%, 30%, 60% and 100% neat epoxy units are given in Section 5.3.5.4. The massive differences in stiffness between the nanotube direction and the plane of isotropy leads to very large bounds for the ODF models.

For E_{xx}, as expected, all the models show a decreasing value for increasing amounts of alignment. The Finite Element model decreases close to linear with increasing alignment, in Fig. 5.58, and at full alignment is close to the Young's modulus of neat epoxy (100% epoxy units). With all of the nanotubes aligned in the z-direction, it logical the x and y directions would not see any increase in stiffness. The ODF upper bound, in Fig. 5.61, shows a greater than linear decrease in stiffness in the x and y-directions with increasing alignment. All of the systems converge towards the neat epoxy value at 100% alignment. For the ODF lower bound, shown in Fig. 5.64, with 50% or less neat epoxy units, E_{xx} initially increases with increasing alignment, and then begins to decrease sharply. This decrease happens earlier and more steeply at low percentages of neat epoxy units, though only the systems with 0% and 10% neat epoxy units ever go below the value of neat epoxy. For systems with 50% or less neat epoxy units, the stiffness increases with increasing amounts of epoxy units, and the opposite is true for systems with greater than 50% neat epoxy units.

The systems with greater than 50% neat epoxy units show a linearly increasing response with the amount of alignment.

The three models show an increasing E_{zz} as more nanotubes are aligned in the z-direction, which is to be expected. As was the case with E_{xx}, the large differential in stiffness in the plane of isotropy and the nanotube direction lead to very large bounds. The Finite Element model, Fig. 5.59a, and the ODF upper bound, 5.62a, show a linear response for E_{xx} vs. alignment. The ODF lower bound, Fig. 5.65a initially shows a close to linear response with increasing alignment, before showing a faster increase in stiffness. From the comparison figure, Fig. 5.68a, it is clear ODF method bounds the Finite Element method, though with a very wide margin.

For G_{xz}, all of the models show a close to linear response with increasing amount of alignment. The Finite Element model, Fig. 5.59b, and ODF models, 5.62b and 5.65b, show a decreasing magnitude with the amount of alignment. A comparison figure for G_{xz} is shown for 0%, 30%, 60% neat epoxy units in 5.68b. The models all show an increasing magnitude of ν_{xy} with increasing alignment, and the contraction in the plane of isotropy from loading within the plane becomes greater than that of neat epoxy between 0 and 25% alignment, seen in Fig. 5.69a. For ν_{xz}, or the contraction in the z-direction due to a tensile load in the plane of isotropy, the presence of the SWNTs in the z-direction cause this value to decrease with increasing alignment, which can be seen in Fig. 5.69b. The magnitude of ν_{xz} is below neat epoxy's Possion's ratio for all amounts of alignment and SWNT volume fraction for the Finite Element model, the ODF upper bounds, and all of the ODF lower bound except for less than 10% alignment.

5.3.5.1 Finite Element

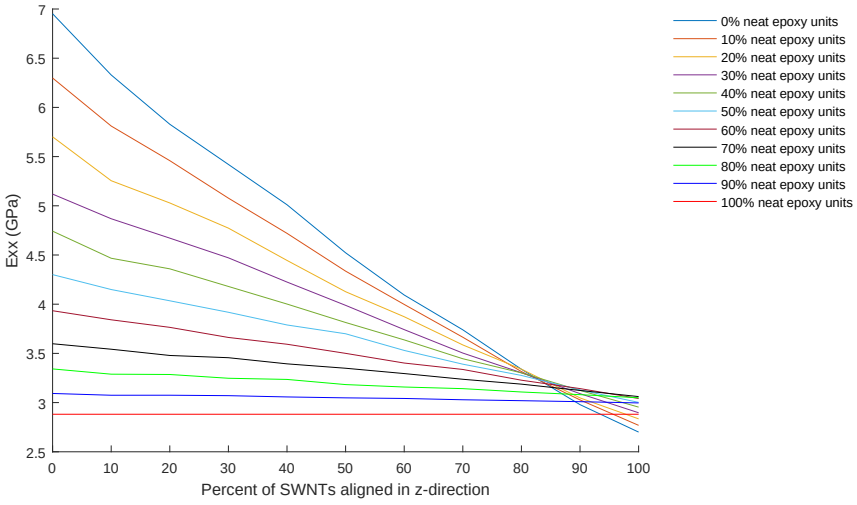

Figure 5.58: Finite Element results for the variation of E_{xx} with respect to % SWNT alignment at various % of neat epoxy units and 300 K.

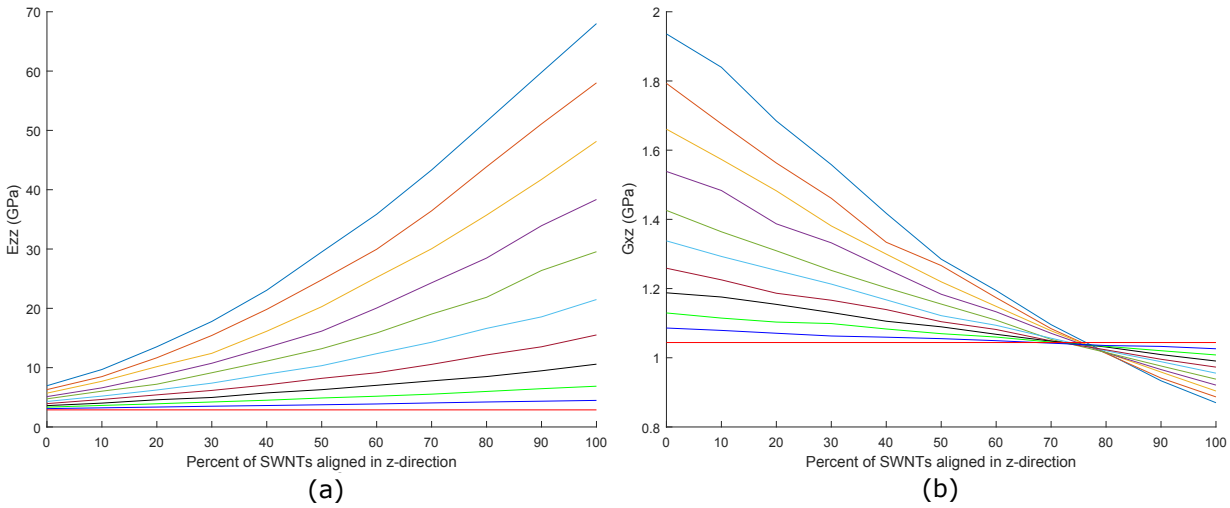

Figure 5.59: Finite Element results for the variation of a. E_{zz} and b. G_{xz} with respect to % SWNT alignment at various % of neat epoxy units and 300 K.

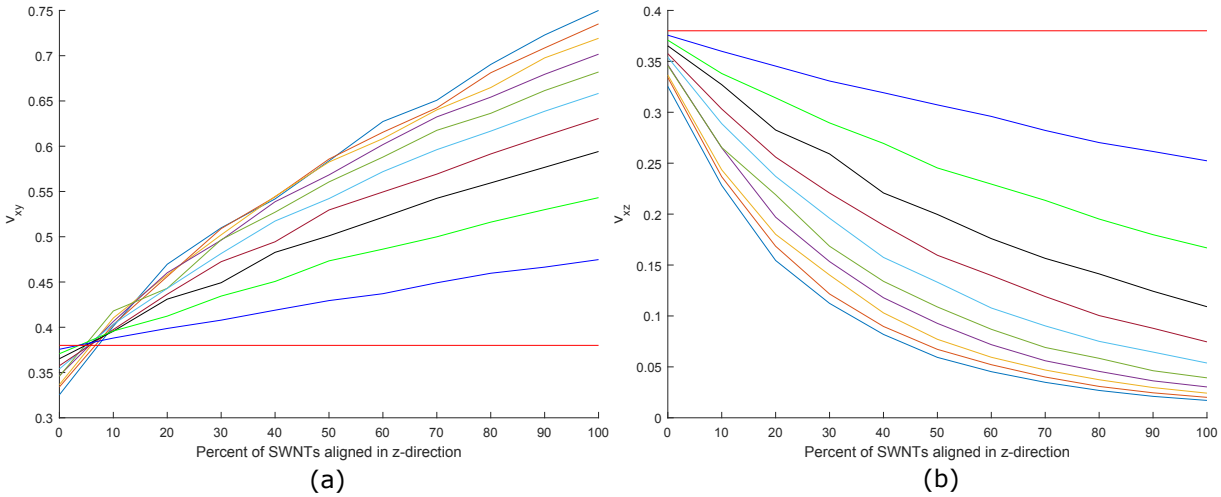

Figure 5.60: Finite Element results for the variation of a. ν_{xy} and b. ν_{xz} with respect to % SWNT alignment at various % of neat epoxy units and 300 K.

5.3.5.2 ODF Upper Bound

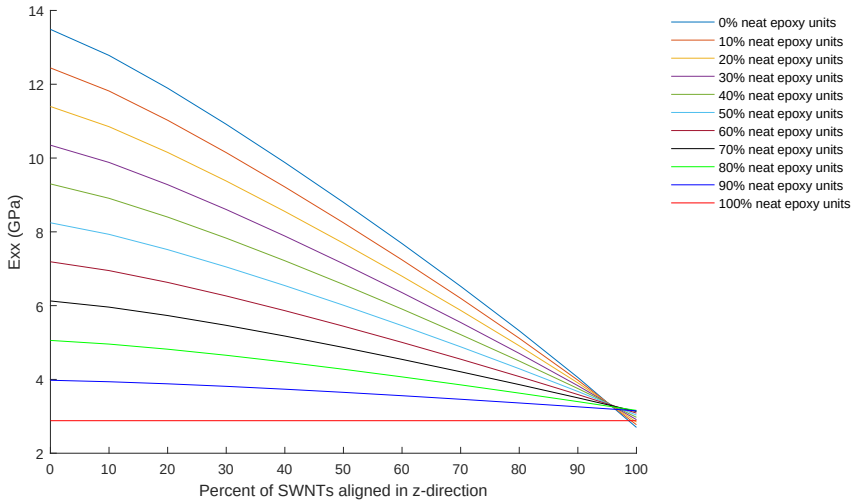

Figure 5.61: ODF upper bound results for the variation of E_{xx} with respect to % SWNT alignment at various % of neat epoxy units and 300 K.

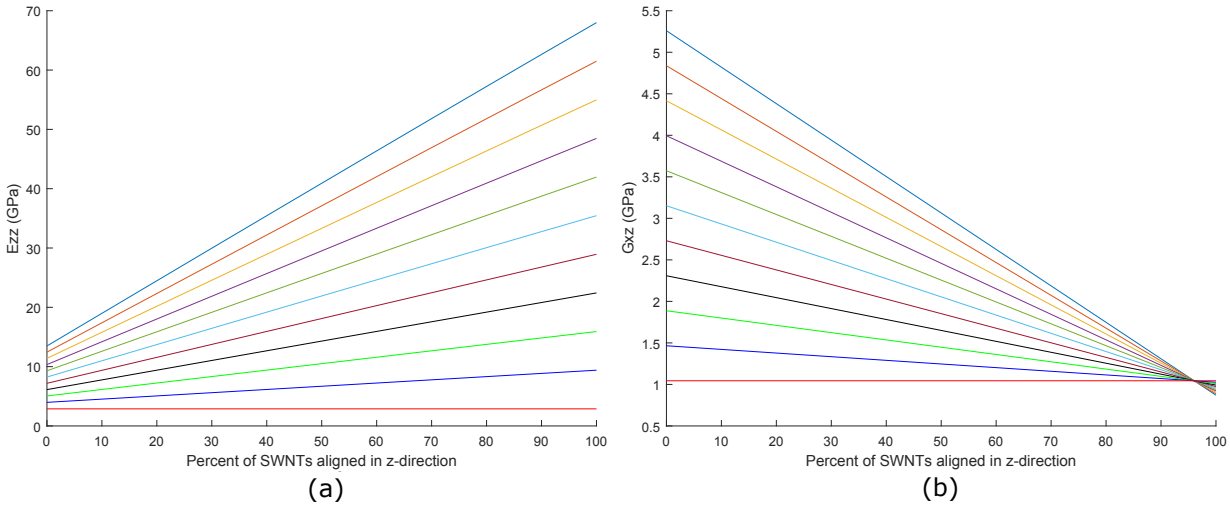

Figure 5.62: ODF upper bound results for the variation of a. E_{zz} and b. G_{xz} with respect to % SWNT alignment at various % of neat epoxy units and 300 K.

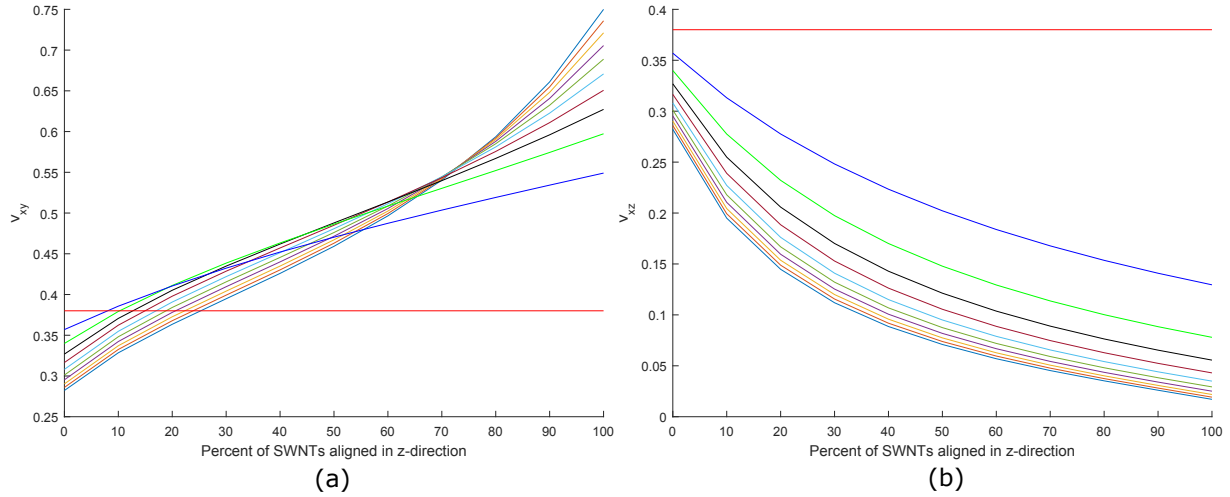

Figure 5.63: ODF upper bound results for the variation of a. ν_{xy} and b. ν_{xz} with respect to % SWNT alignment at various % of neat epoxy units and 300 K.

5.3.5.3 ODF Lower Bound

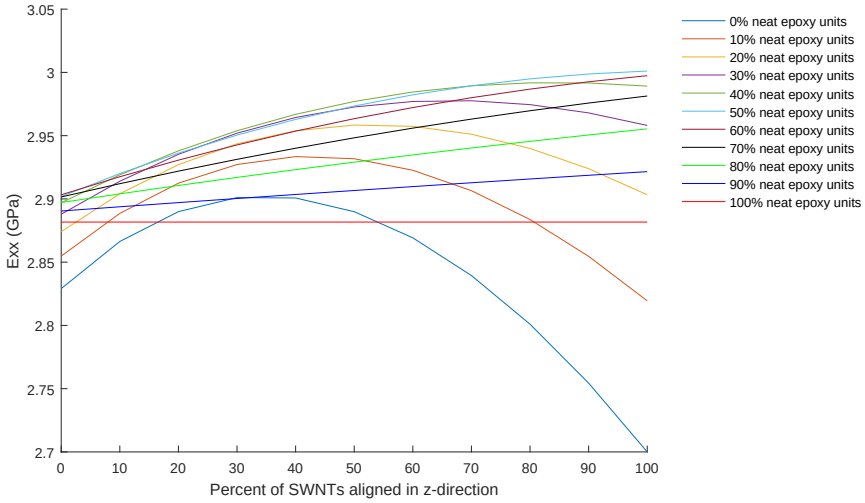

Figure 5.64: ODF lower bound results for the variation of E_{xx} with respect to % SWNT alignment at various % of neat epoxy units and 300 K.

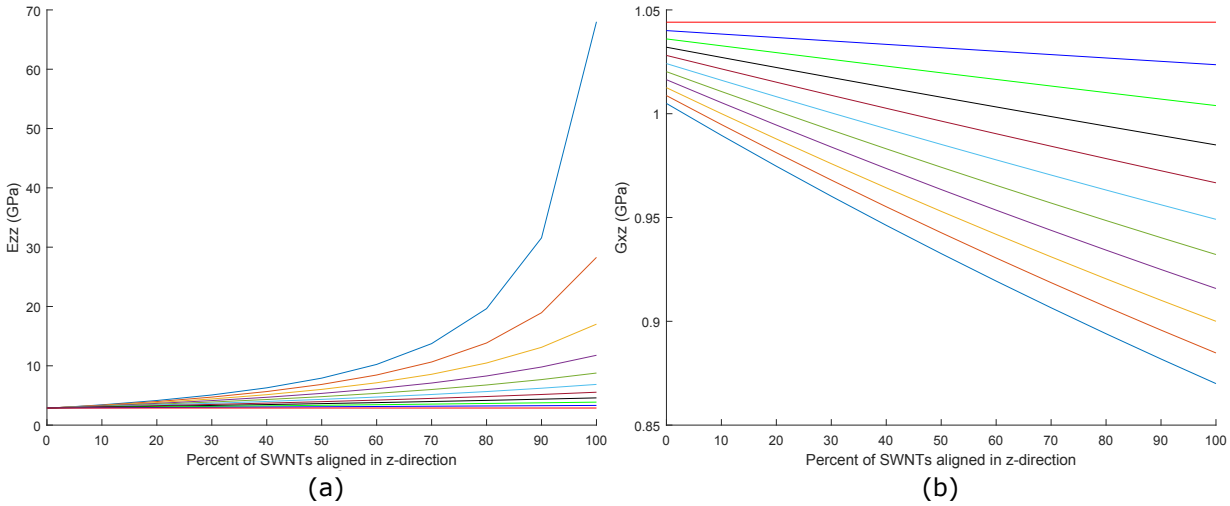

Figure 5.65: ODF lower bound results for the variation of a. E_{zz} and b. G_{xz} with respect to % SWNT alignment at various % of neat epoxy units and 300 K.

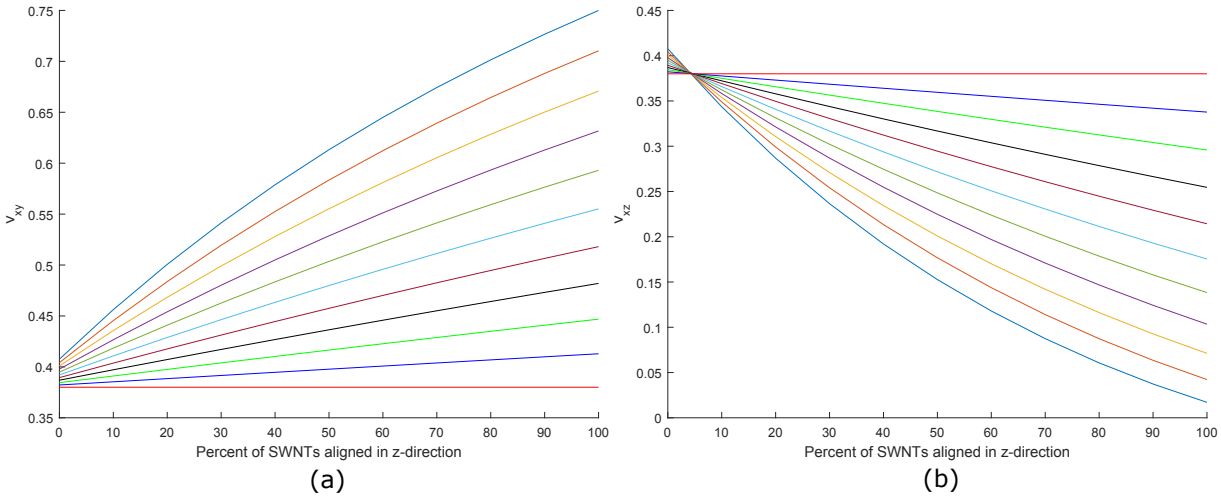

Figure 5.66: ODF lower bound results for the variation of a. ν_{xy} and b. ν_{xz} with respect to % SWNT alignment at various % of neat epoxy units and 300 K.

5.3.5.4 Compare Methods

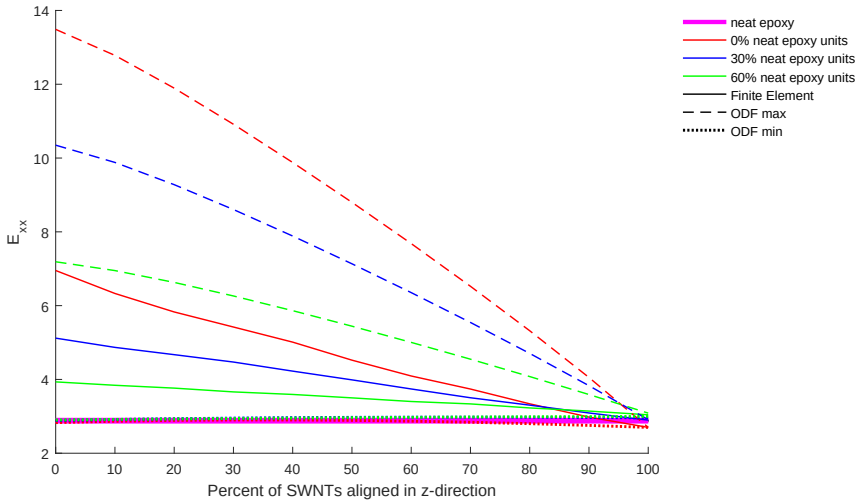

Figure 5.67: Comparison of the methods used to calculate the variation of E_{xx} with respect to % SWNT alignment for various % of neat epoxy units at 300 K.

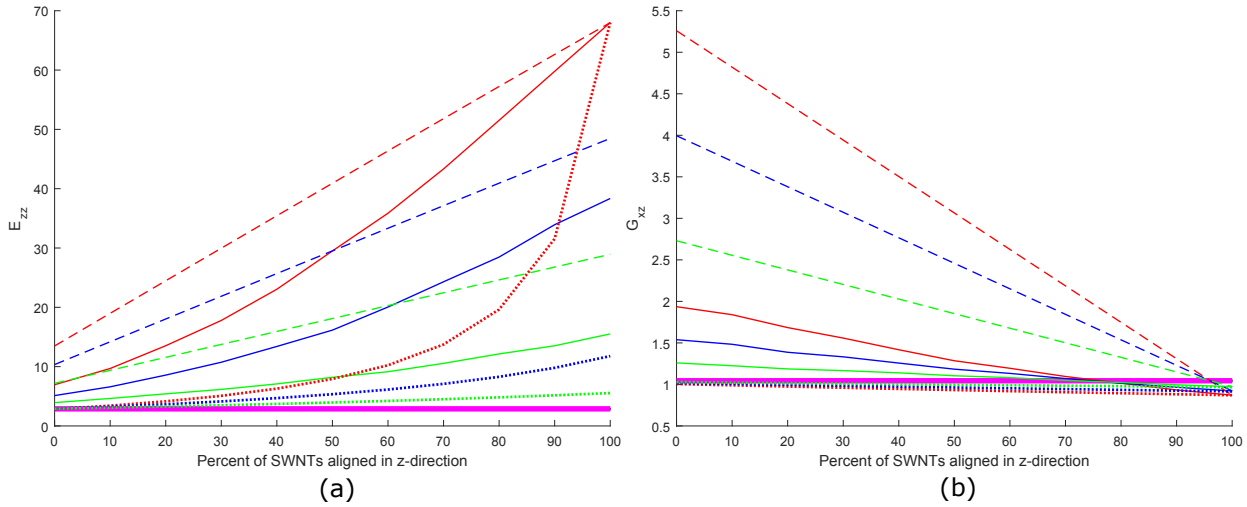

Figure 5.68: Comparison of the methods used to calculate the variation of a. E_{zz} and b. G_{xz} with respect to % SWNT alignment for various % of neat epoxy units at 300 K.

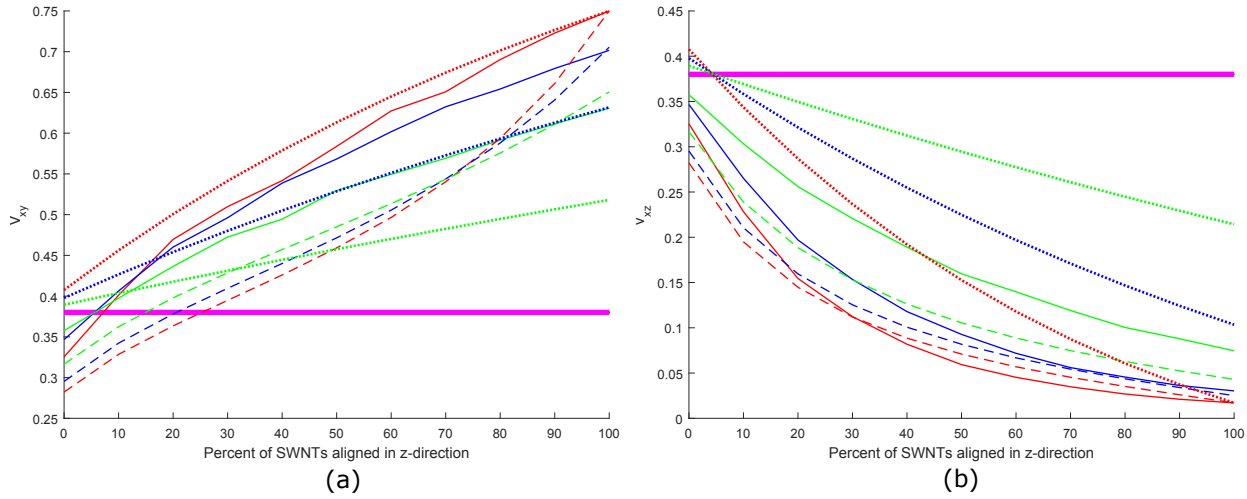

Figure 5.69: Comparison of the methods used to calculate the variation of a. ν_{xy} and b. ν_{xz} with respect to % SWNT alignment for various % of neat epoxy units at 300 K.

5.3.6 Functionalized SWNT-Epoxy (Infinite)

For the functionalized SWNT-epoxy system with nanotubes that span the entire lattice, therefore becoming effectively infinite with periodic boundary conditions applied, the results of the Finite Element multiscale model are shown in Section 5.3.6.1, the ODF upper bound in Section 5.3.6.2, and the lower bound in Section 5.3.6.3. Comparisons between the three models at 0%, 30%, 60% and 100% neat epoxy units are given in Section 5.3.6.4. While the difference in stiffness between the nanotube direction and plane of isotopy is not

quite as large as the pristine, infinite system, due to improvements in stiffness in the direction transverse to the SWNT and degradation to the SWNT, there is still a large difference, leading to large bounds for the ODF method.

For E_{xx}, very similar trends are seen here as for the pristine/infinite system. As expected, all of the models show higher values compared to the pristine system at equal alignment and volume fractions due to the nanotube functionalization. A decreasing value for increasing amounts of alignment is observed, and unlike the pristine system, the value of E_{xx} never goes below the Young's modulus of neat epoxy for any volume fraction or percentage alignment in any of the models due to the nanotube functionalization, seen in Fig. 5.79. The Finite Element results lie roughly in the middle of the ODF bounds. The models show an increasing E_{zz} as more nanotubes are aligned in the z-direction, which is to be expected. Again, the functionalized, infinite system shows very similar trends as the pristine, infinite system described earlier. The Finite Element model, and ODF lower bound show greater than linear gains in E_{zz} with increasing SWNT alignment. The ODF upper bound, Fig. 5.74a gives a linear response for E_{xx} vs. alignment, and shows the largest prediction for stiffness with alignment. From the comparison figure, Fig. 5.80a, it is clear the ODF method bounds the Finite Element method, though with a very wide margin.

For G_{xz}, all of the models show a close to linear response with increasing amount of alignment. Much like the pristine system, the Finite Element model, and ODF models show a decreasing magnitude with increasing amounts of alignment. A comparison figure for G_{xz} is shown for 0%, 30%, 60% neat epoxy units in Fig. 5.80b. The models display an increasing magnitude of ν_{xy} with increasing alignment, and contraction in the plane of isotropy with from load within the plane becomes greater than that of the Poisson's ratio of neat epoxy between 5% and 40% alignment, seen in Fig. 5.81a. For ν_{xz}, or the contraction in the z-direction due to a tensile load in the plane of isotropy, the presence of the SWNTs in the z-direction causes this value to decrease with increasing alignment, which can be seen in Fig. 5.81b. The magnitude of ν_{xz} is below neat epoxy's Possion's ratio for all amounts of alignment and SWNT volume fraction for all three models, unlike the pristine, infinite system.

5.3.6.1 Finite Element

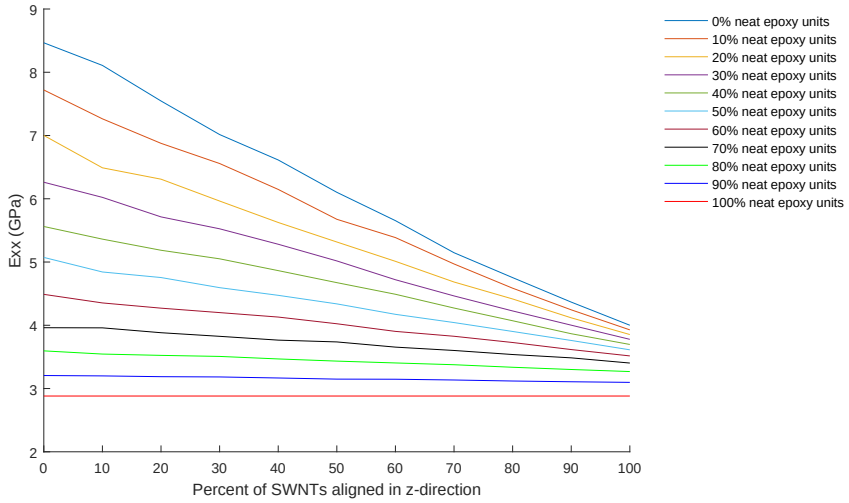

Figure 5.70: Finite Element results for the variation of E_{xx} with respect to % SWNT alignment at various % of neat epoxy units and 300 K.

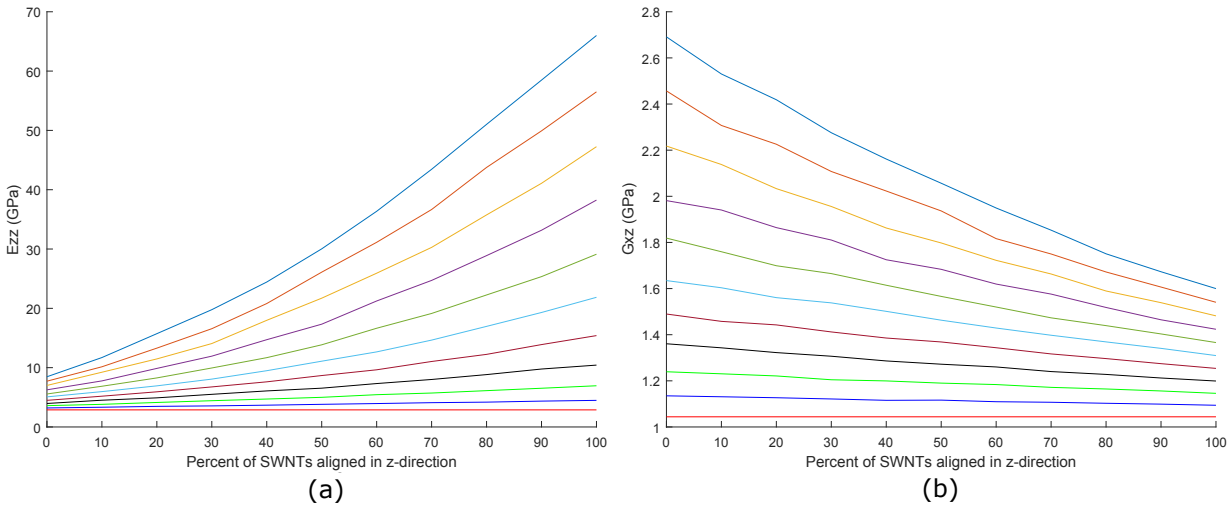

Figure 5.71: Finite Element results for the variation of a. E_{zz} and b. G_{xz} with respect to % SWNT alignment at various % of neat epoxy units and 300 K.

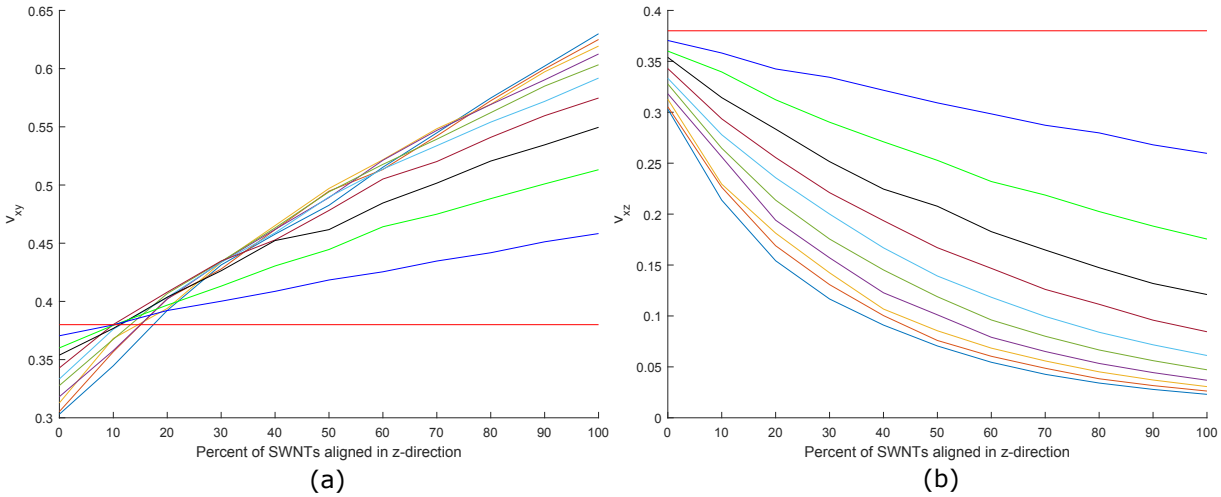

Figure 5.72: Finite Element results for the variation of a. ν_{xy} and b. ν_{xz} with respect to % SWNT alignment at various % of neat epoxy units and 300 K.

5.3.6.2 ODF Upper Bound

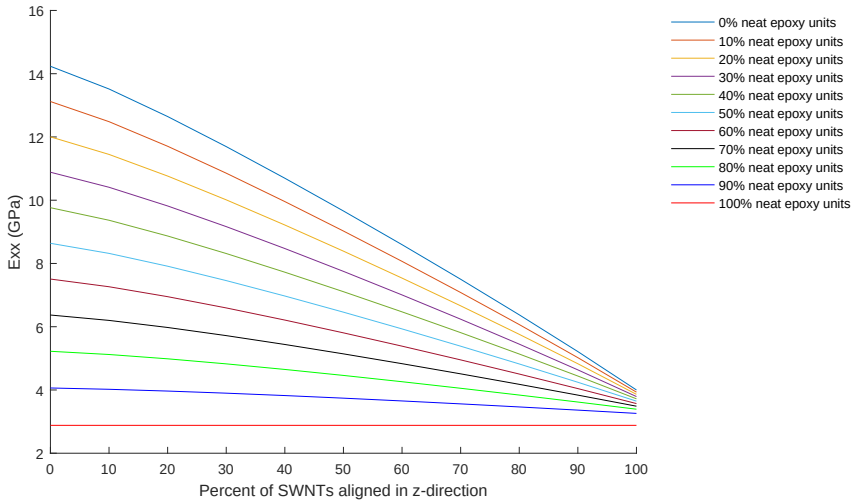

Figure 5.73: ODF upper bound results for the variation of E_{xx} with respect to % SWNT alignment at various % of neat epoxy units and 300 K.

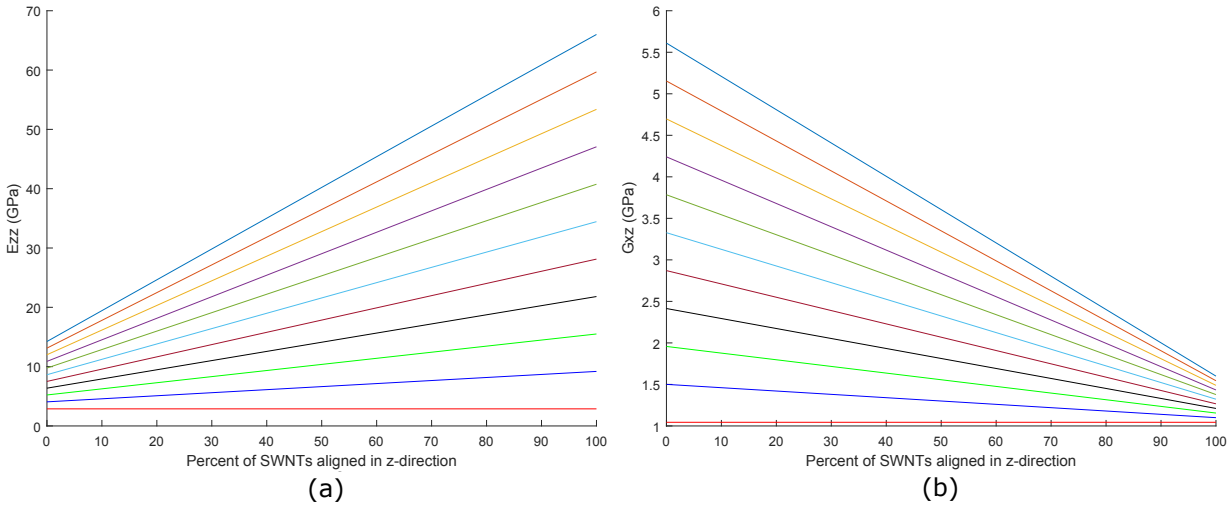

Figure 5.74: ODF upper bound results for the variation of a. E_{zz} and b. G_{xz} with respect to % SWNT alignment at various % of neat epoxy units and 300 K.

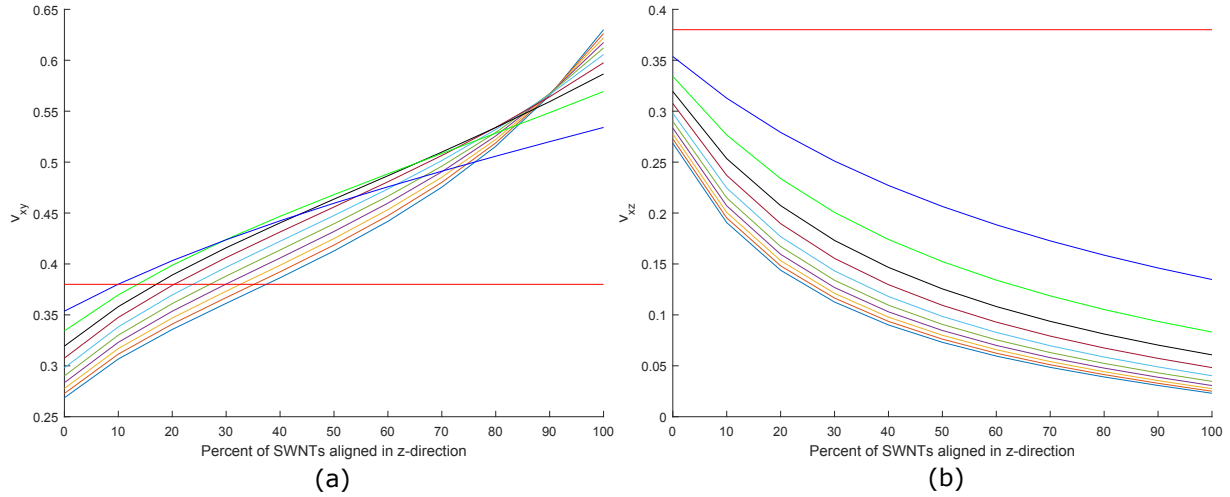

Figure 5.75: ODF upper bound results for the variation of a. ν_{xy} and b. ν_{xz} with respect to % SWNT alignment at various % of neat epoxy units and 300 K.

5.3.6.3 ODF Lower Bound

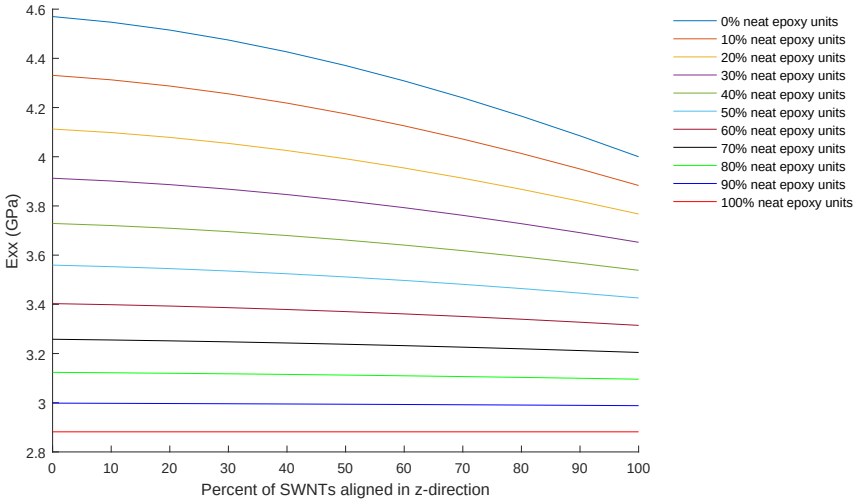

Figure 5.76: ODF lower bound results for the variation of E_{xx} with respect to % SWNT alignment at various % of neat epoxy units and 300 K.

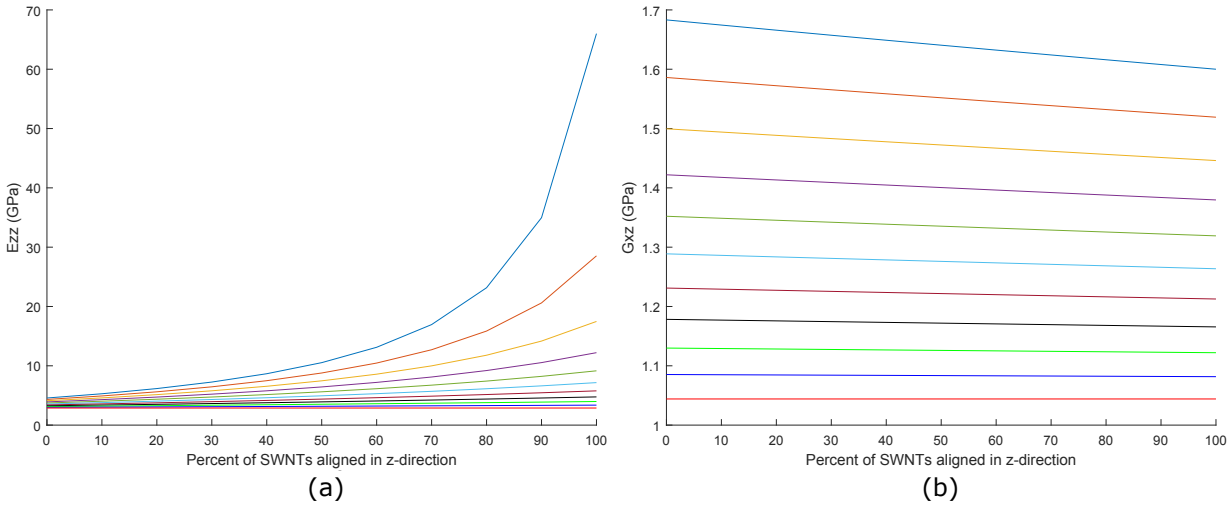

Figure 5.77: ODF lower bound results for the variation of a. E_{zz} and b. G_{xz} with respect to % SWNT alignment at various % of neat epoxy units and 300 K.

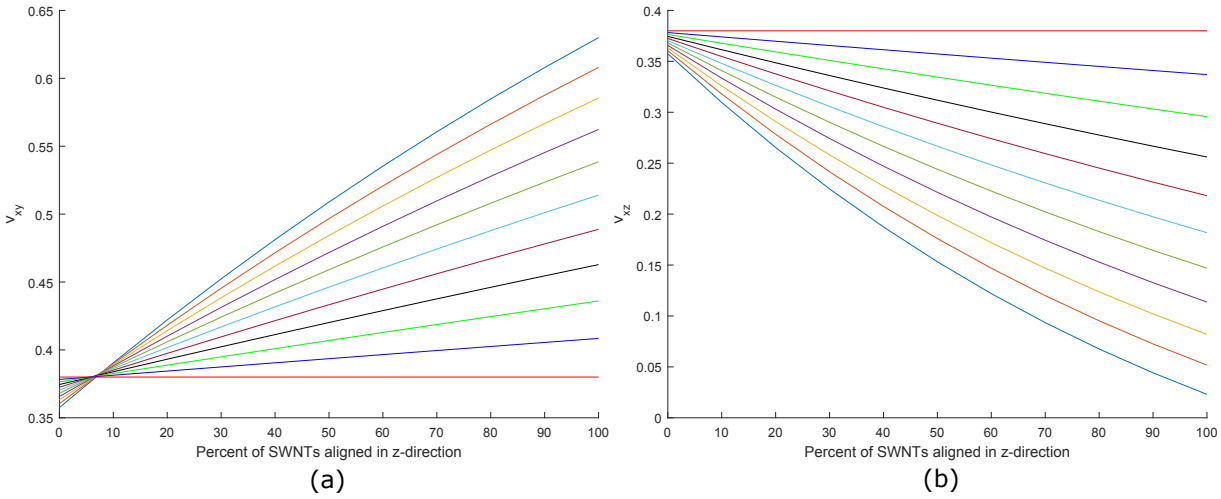

Figure 5.78: ODF lower bound results for the variation of a. ν_{xy} and b. ν_{xz} with respect to % SWNT alignment at various % of neat epoxy units and 300 K.

5.3.6.4 Compare Methods

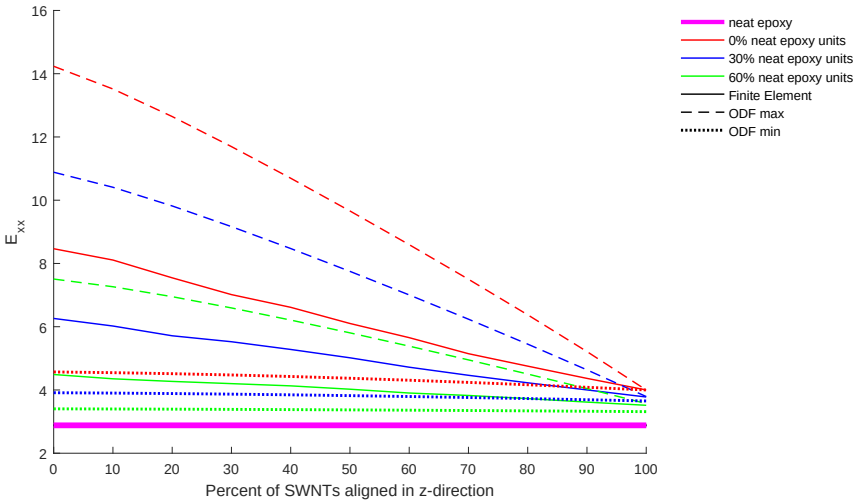

Figure 5.79: Comparison of the methods used to calculate the variation of E_{xx} with respect to % SWNT alignment for various % of neat epoxy units at 300 K.

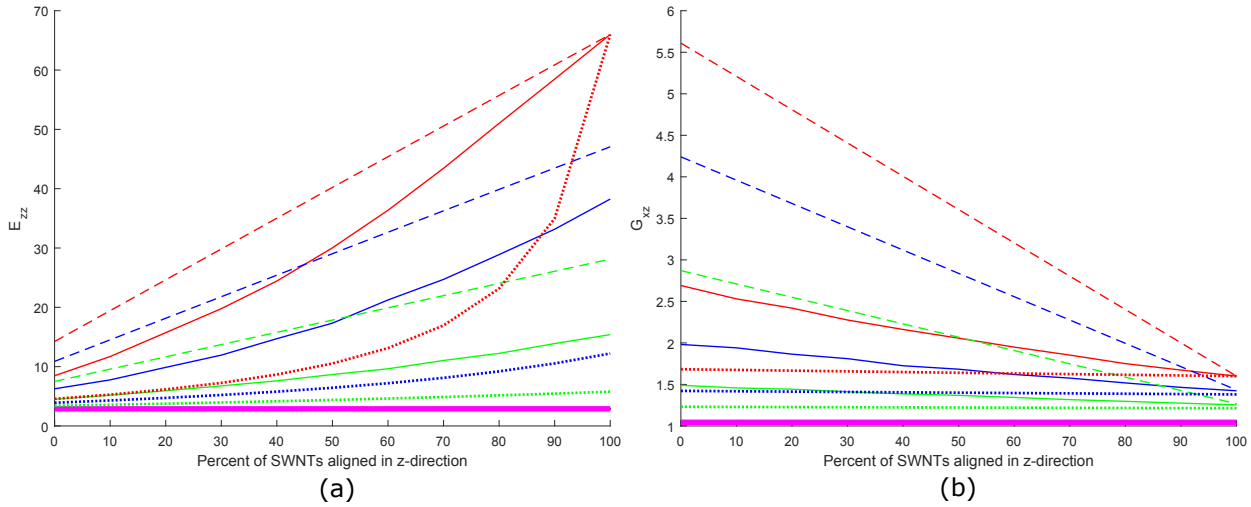

Figure 5.80: Comparison of the methods used to calculate the variation of a. E_{zz} and b. G_{xz} with respect to % SWNT alignment for various % of neat epoxy units at 300 K.

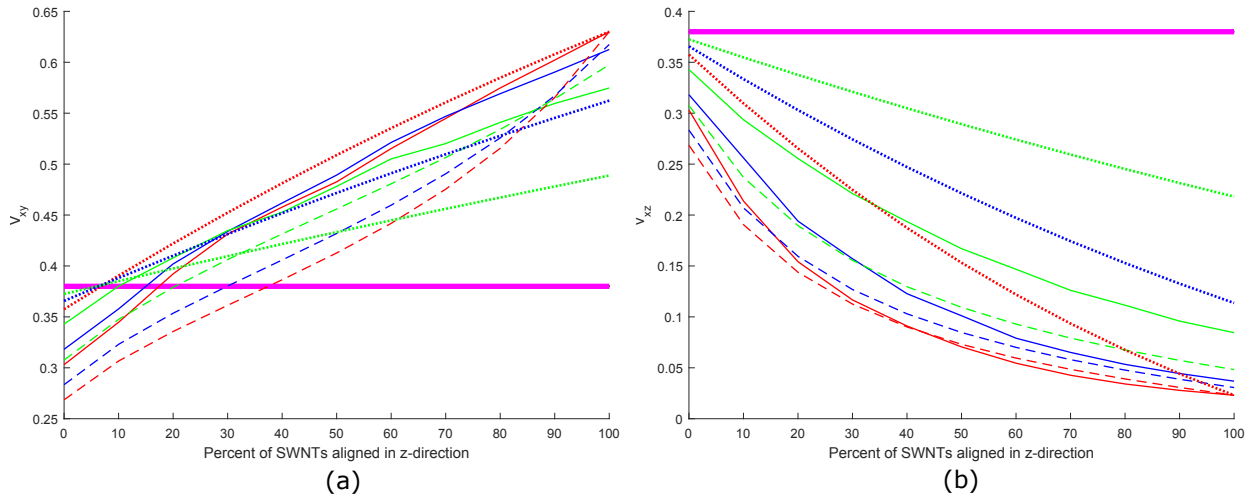

Figure 5.81: Comparison of the methods used to calculate the variation of a. ν_{xy} and b. ν_{xz} with respect to % SWNT alignment for various % of neat epoxy units at 300 K.

5.4 Compare Systems

In this section, the various nanocomposite system's elastic properties are compared with one another. Here, the effects of the discontinuous nanotubes and functionalization the macroscopic stiffness properties can be seen. For the sake of brevity, only the Finite Element model results were plotted in this section. This model was chosen because it almost always lied within the bounds of the ODF model. All of the nanocomposite systems are

plotted together for a given property, and then just the discontinuous systems are plotted since the systems with the continuous (infinite) nanotubes often give results an order of magnitude larger. An elastic property is plotted vs. percent of SWNTs aligned in the z-direction for various amounts of epoxy units: 0% in Section 5.4.1, 30% in Section 5.4.2, 60% in Section 5.4.3, and 90% in Section 5.4.4, corresponding to volume fractions that can be calculated via Eq. 4.60, repeated here:

$$\Phi_{SWNT} = (1 - \Phi_{neatepoxy}) * \Phi_{MDlattice}, \tag{5.4}$$

where $\Phi_{neatepoxy}$ represents the volume fraction of neat epoxy units, and $\Phi_{MDlattice}$ was given in Table 4.2, and will be equal to 0.031 for nanocomposites with 11 repeat unit SWNTs, 0.037 for nanocomposites with 13 repeat unit SWNTs, and 0.043 for systems with 15 repeat unit (infinite) SWNTs. The tests in this section were all run at 300 K. All of the results for varying amounts of epoxy units show similar trends, and it is logical that the results would scale since these are calculated by assigning more elements with the elastic properties of neat epoxy.

For E_{xx}, the systems with continuous (infinite) SWNTs show the greatest improvement for low amounts of alignment. The functionalized, infinite system has the greatest value of E_{xx} at all alignments, where the pristine, infinite system goes below the discontinuous systems around 70% alignment in the z-direction, and converges to the neat epoxy value around 95% alignment. This results make intuitive sense; when there are long, infinite nanotubes still aligned in the plane of isotropy (x-y), or even have a component of their stiffness in that direction, this will lead to large improvements in stiffness. For the functionalized system, even in the case with full alignment, there is still some effect of the nanotube due to the covalent bonding. For the pristine system, the nanotubes clearly have no effect in the stiffness in the plane of isotropy when they are not aligned in that direction. For the discontinuous systems, the functionalized system with 13 repeat units shows the largest improvements in E_{xx}, where the functionalized system with 11 repeat units shows the second highest value at low amounts of alignment, but it drops off the most with increasing alignment. The two discontinuous, pristine nanotube results show very similar trends with decreasing E_{xx} values for increasing alignment.

The systems with the continuous nanotubes show substantially greater improvements for E_{zz} than the discontinuous systems, and this is not surprising with there being no interaction between the epoxy and SWNT at the end of the nanotube. The pristine, infinite system shows slightly higher E_{zz} at very high amounts alignment due to some deterioration of the SWNT due to the covalent bonding to the nanotube. However, for up to 50% alignment for the 0% neat epoxy units, and up to 70% alignment for the 30%, 60% and 90% neat

epoxy units, the functionalized system shows a higher E_{zz} value, as the improvements due to functionalization of the non-aligned tubes outweighs the deterioration of the nanotube properties for the aligned nanotubes. Compared to the continuous systems, the discontinuous systems show modest improvements over the elastic modulus of neat epoxy due to their small aspect ratios. At all percentages of neat epoxy units, the pristine systems give the best improvements for E_{zz}. The functionalized system with 13 repeat units increases with a slightly lesser slope as the pristine, discontinuous systems, and starts out at a lower value. The functionalized system with 11 repeat units shows a decreasing trend for E_{zz} with alignment, and this was addressed in Section 5.3.2. These somewhat odd trends can be attributed to the high value of G_{xz} and relatively low values of E_{zz} at 300 K compared to the other discontinuous systems, as show in Tables 2.4-2.7. The averaging of the stiffness matrix therefore leads to an improvement in E_{zz} for a random system. This does tell that functionalization on a very short nanotube can have very negative effects on the SWNT's stiffness and contribution to the composite, and indeed the direction perpendicular to the nanotube sees greater stiffness improvements due to its covalent bonds to the SWNT than the direction the nanotube is actually aligned.

The continuous (infinite) systems show a decreasing G_{xz} with increasing alignment. G_{xz} represents stress in the z-direction acting on a plane normal to the equivalent x or y-directions. For the infinite nanotubes, The direction the SWNT is aligned is very stiff, and so it makes intuitive sense that increasing alignment in the z-direction would cause a decreasing shear modulus G_{xz}. For the pristine, infinite system it becomes equal with neat epoxy's shear modulus around 70-80% alignment for all of percentages of neat epoxy units, and then goes below the neat epoxy value. For the functionalized, infinite system, even at 100% alignment, there is an increase in G_{xz} due to the covalent bonding, which decreases with increasing amount of neat epoxy units. At 90% neat epoxy units; a 5% for G_{xz} was seen, and at 0% neat epoxy units, an improvement of 56% was seen. The discontinuous, functionalized systems all show slight increases of G_{xz} with increasing alignment, while the pristine systems stay fairly close to constant. The functionalized system with 11 repeat units showed the largest slope with increasing alignment of all the systems, and that correlated to an improvement of 40% over neat epoxy at 0% alignment and 55% at 100% alignment for 0% neat epoxy units. The improvement becomes lesser at higher amounts of neat epoxy units. So, this make it clear that there is not a substantial effect of alignment on G_{xz} for the discontinuous nanotubes, and this is because there is a much less dramatic difference in the nanotube direction and the directions perpendicular to the nanotube, as evidenced in Tables 2.4-2.7.

All of the systems show increasing in-plane Poisson's ratio, ν_{xy} with increasing align-

ment, with the magnitudes decreasing for increasing amounts of neat epoxy units. The continuous (infinite) SWNT composites showed a greater than linear increase, with the pristine system being greater than that of the functionalized system. The discontinuous systems showed a near linear increase in ν_{xy} with increasing alignment. Like the continuous SWNTs, the discontinuous, pristine systems displayed a higher magnitude of ν_{xy} than the discontinuous, functionalized systems. This value represents the amount of contraction in the y-direction when the system is pulled in the x-direction, or vice versa since the x and y directions are equivalent. Therefore, it makes intuitive sense that less nanotubes laying, or containing a component, in the plane of isotropy due to increased alignment would lead to more contraction. Likewise, the results agree with the expectation that for a given alignment, the functionalized system would show less contraction because there is still some effect of the nanotubes aligned in the z-direction within the plane of isotropy due to the covalent bonds.

The systems generally show decreasing ν_{xz} for increasing amounts of alignment, with the exception being the discontinuous, functionalized system with 11 repeat units, which is essentially constant. The continuous (infinite) systems show a very large dependence on alignment. For lower amounts of neat epoxy units, these systems have a substantially smaller ν_{xz} than the Poisson's ratio of neat epoxy for all values of alignment. Even at 90% neat epoxy units, ν_{xz} goes below the neat epoxy value at around 15% alignment. This value represents the amount of contraction that will occur along the z-direction when there is a tensile load in the plane of isotropy (x-y). So, as expected, more nanotubes aligned in the z-direction will cause the composite to contract less due to a tensile load in the plane of isotopy. The same logic applies to the discontinuous systems, except there is much smaller difference in stiffness between the nanotube direction and the directions perpendicular to the nanotube, so the effects are substantially lesser. This is most evident for the funtionalized system with 11 repeat units, where the degradation of stiffness along the nanotube direction, and improvement in the direction perpendicular to the nanotube lead to comparable values for each direction, and so ν_{xz} stays constant.

5.4.1 0% Epoxy Units

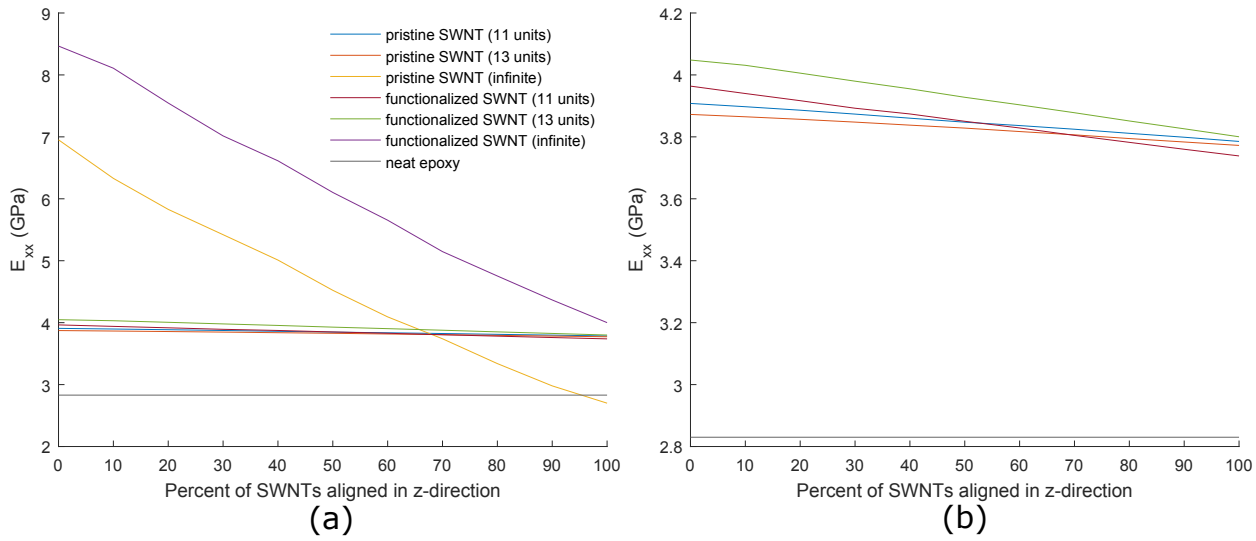

Figure 5.82: Variation of E_{xx} with respect to % of SWNT alignment in the z-direction for a. all and b. discontinuous nanocomposite systems studied for 0% epoxy units at 300 K.

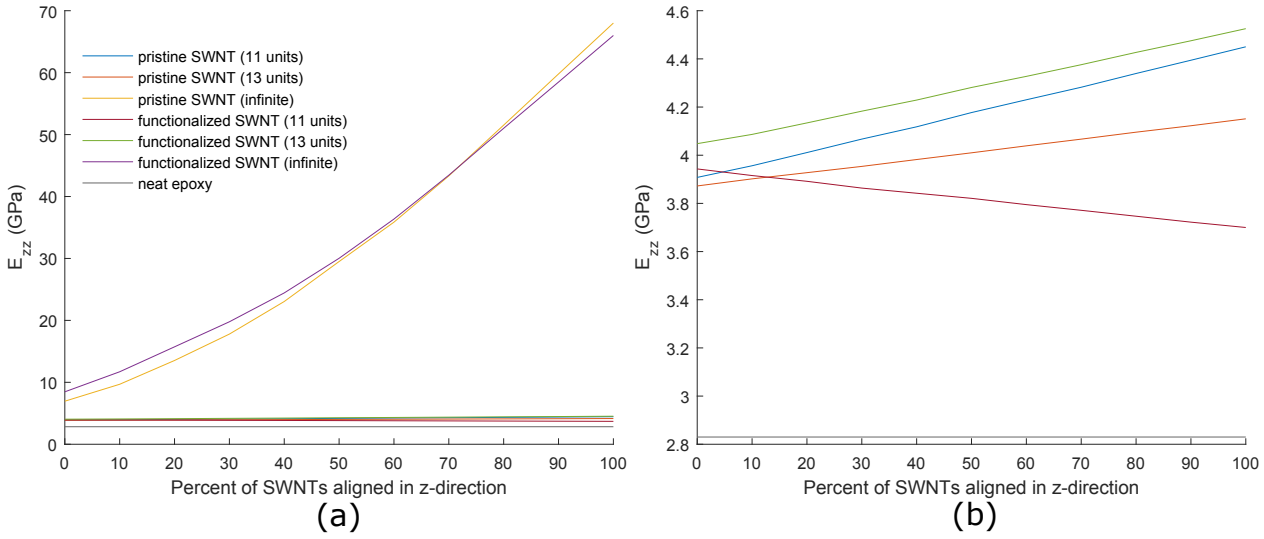

Figure 5.83: Variation of E_{zz} with respect to % of SWNT alignment in the z-direction for a. all and b. discontinuous nanocomposite systems studied for 0% epoxy units at 300 K.

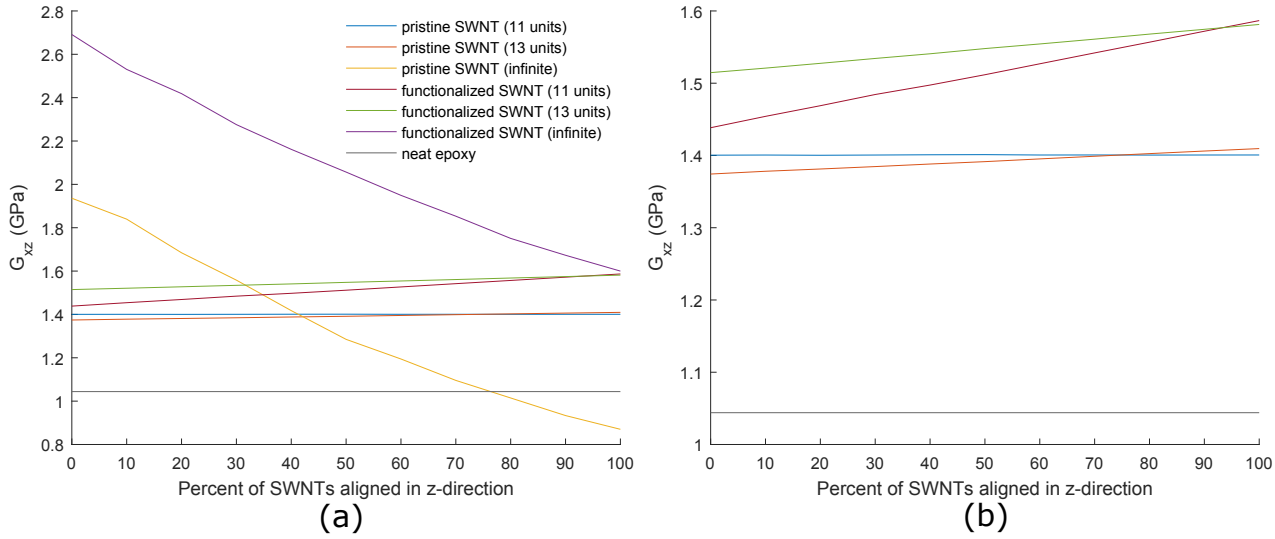

Figure 5.84: Variation of G_{xz} with respect to % of SWNT alignment in the z-direction for a. all and b. discontinuous nanocomposite systems studied for 0% epoxy units at 300 K.

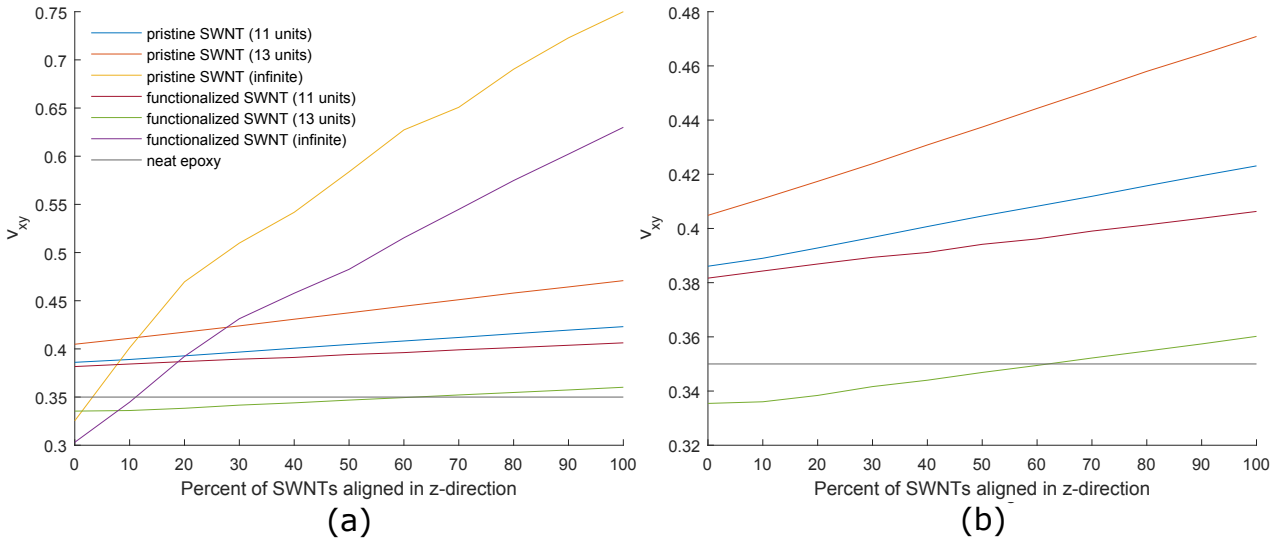

Figure 5.85: Variation of ν_{xy} with respect to % of SWNT alignment in the z-direction for a. all and b. discontinuous nanocomposite systems studied for 0% epoxy units at 300 K.

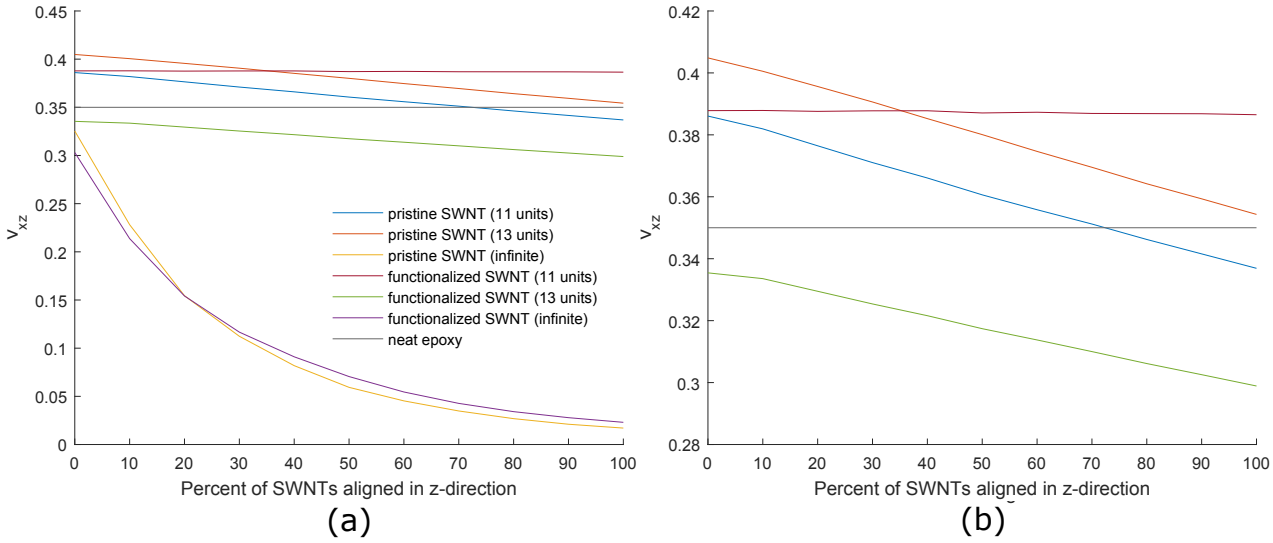

Figure 5.86: Variation of ν_{xz} with respect to % of SWNT alignment in the z-direction for a. all and b. discontinuous nanocomposite systems studied for 0% epoxy units at 300 K.

5.4.2 30% Epoxy Units

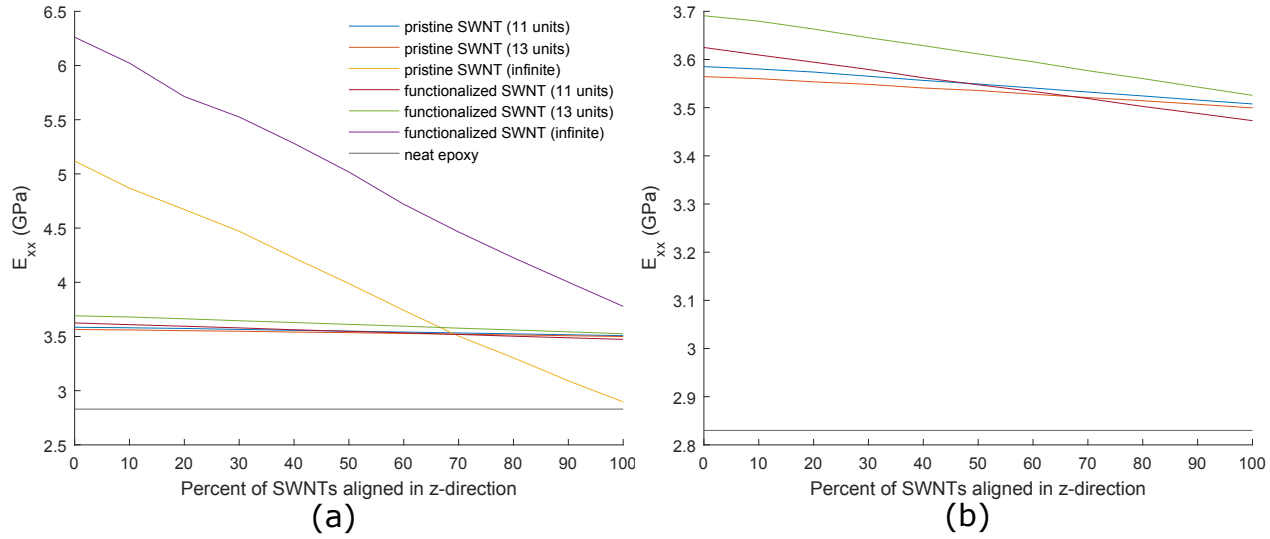

Figure 5.87: Variation of E_{xx} with respect to % of SWNT alignment in the z-direction for a. all and b. discontinuous nanocomposite systems studied for 30% epoxy units at 300 K.

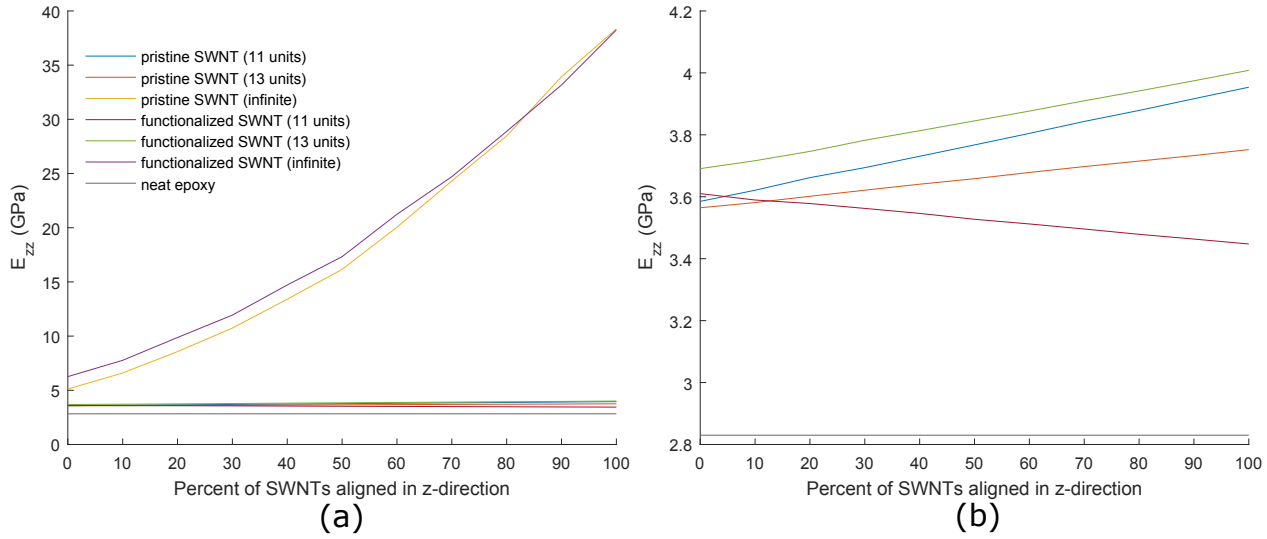

Figure 5.88: Variation of E_{zz} with respect to % of SWNT alignment in the z-direction for a. all and b. discontinuous nanocomposite systems studied for 30% epoxy units at 300 K.

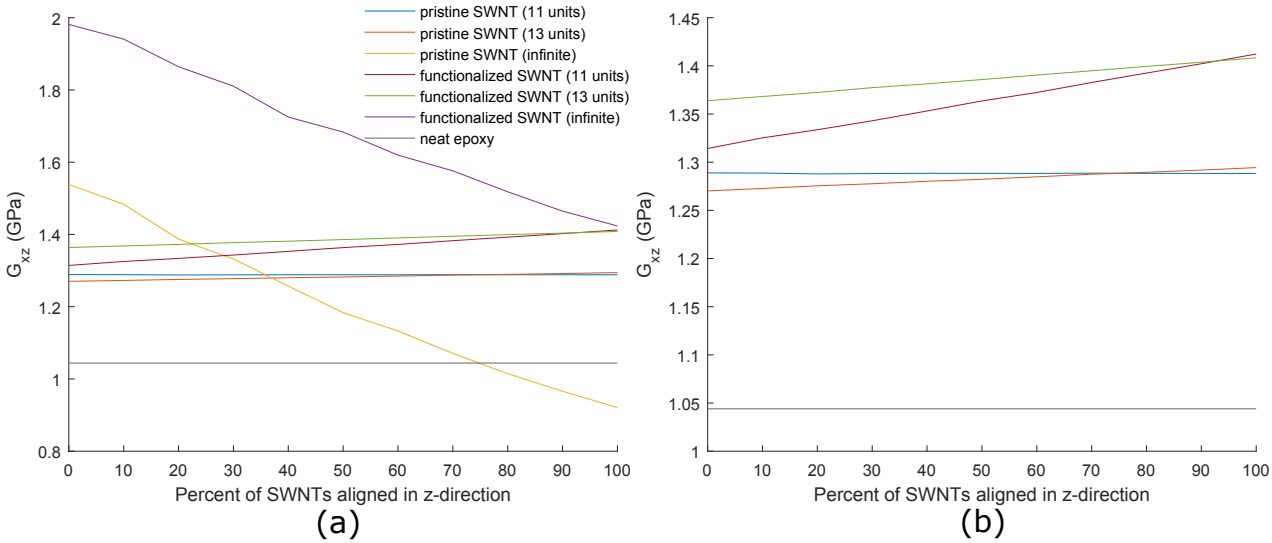

Figure 5.89: Variation of G_{xz} with respect to % of SWNT alignment in the z-direction for a. all and b. discontinuous nanocomposite systems studied for 30% epoxy units at 300 K.

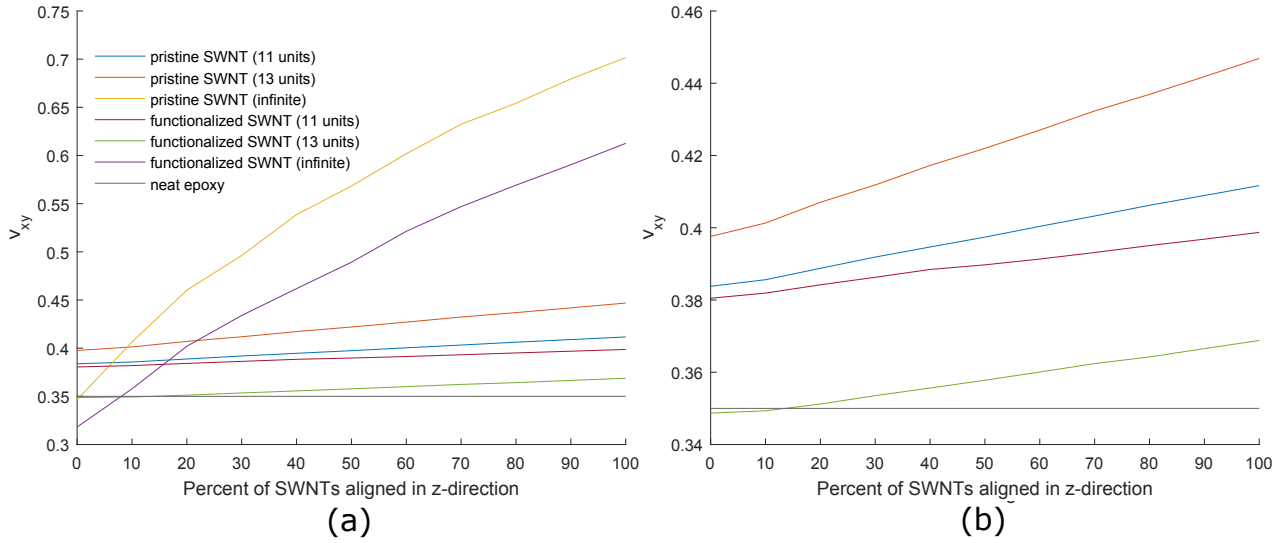

Figure 5.90: Variation of ν_{xy} with respect to % of SWNT alignment in the z-direction for a. all and b. discontinuous nanocomposite systems studied for 30% epoxy units at 300 K.

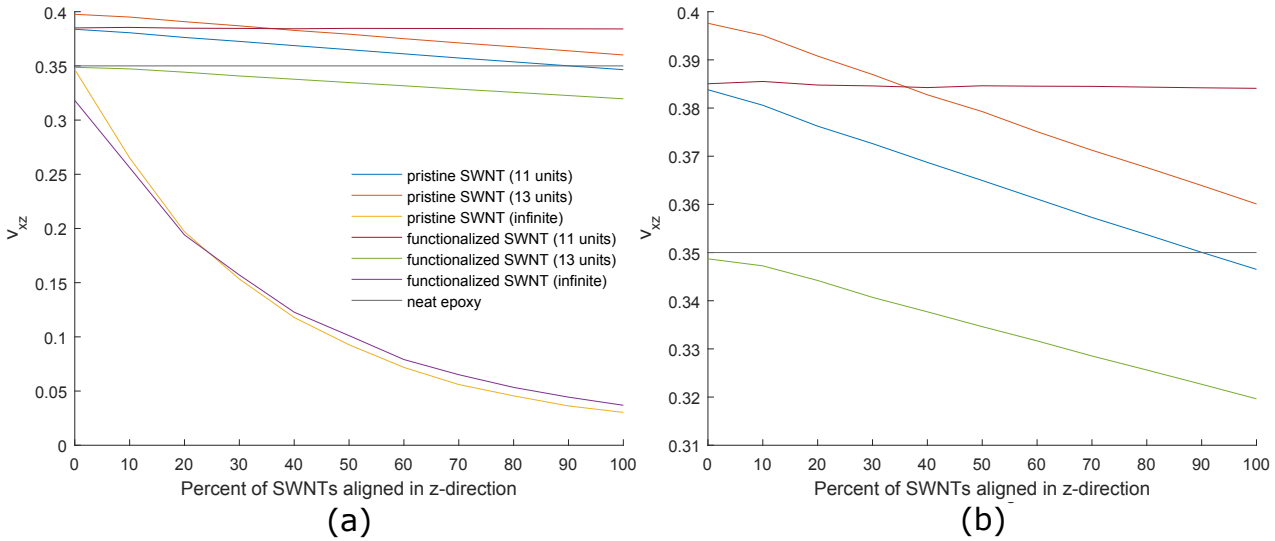

Figure 5.91: Variation of ν_{xz} with respect to % of SWNT alignment in the z-direction for a. all and b. discontinuous nanocomposite systems studied for 30% epoxy units at 300 K.

5.4.3 60% Epoxy Units

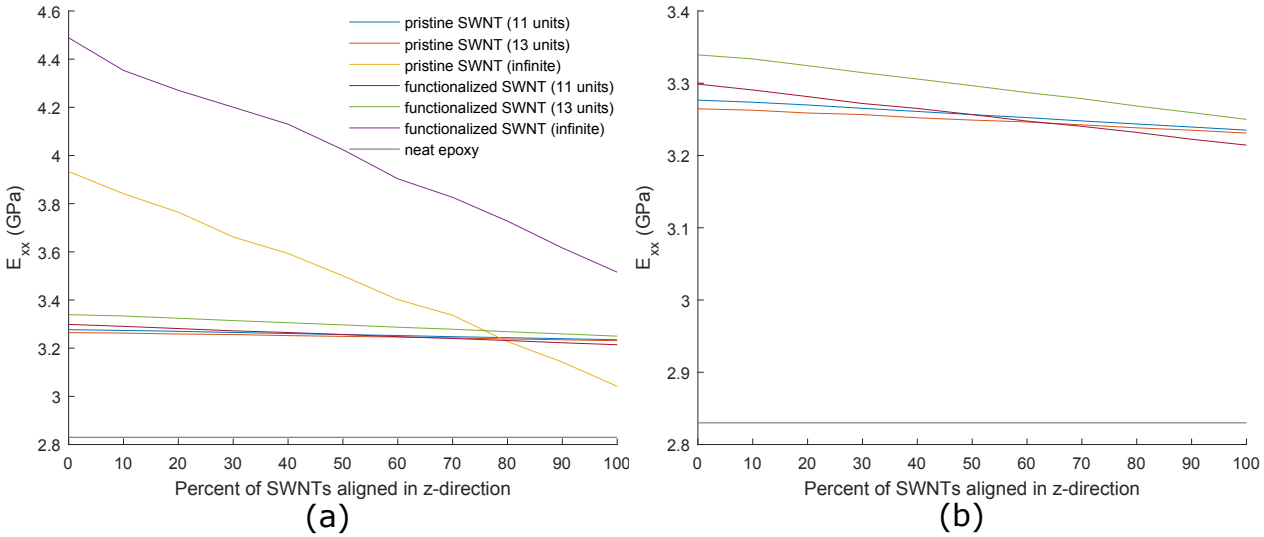

Figure 5.92: Variation of E_{xx} with respect to % of SWNT alignment in the z-direction for a. all and b. discontinuous nanocomposite systems studied for 60% epoxy units at 300 K.

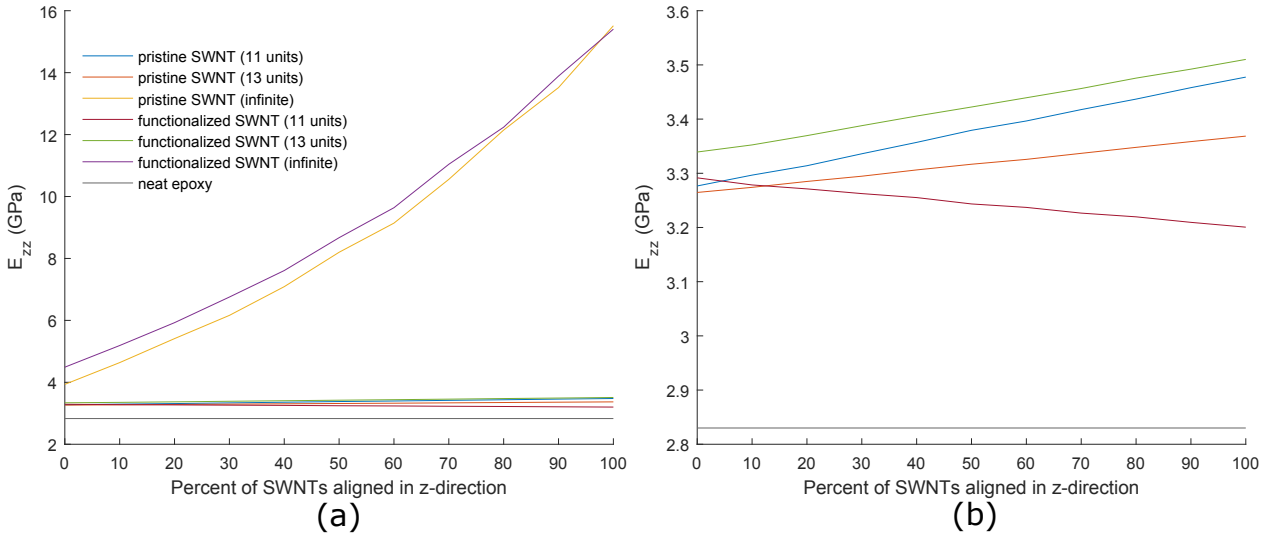

Figure 5.93: Variation of E_{zz} with respect to % of SWNT alignment in the z-direction for a. all and b. discontinuous nanocomposite systems studied for 60% epoxy units at 300 K.

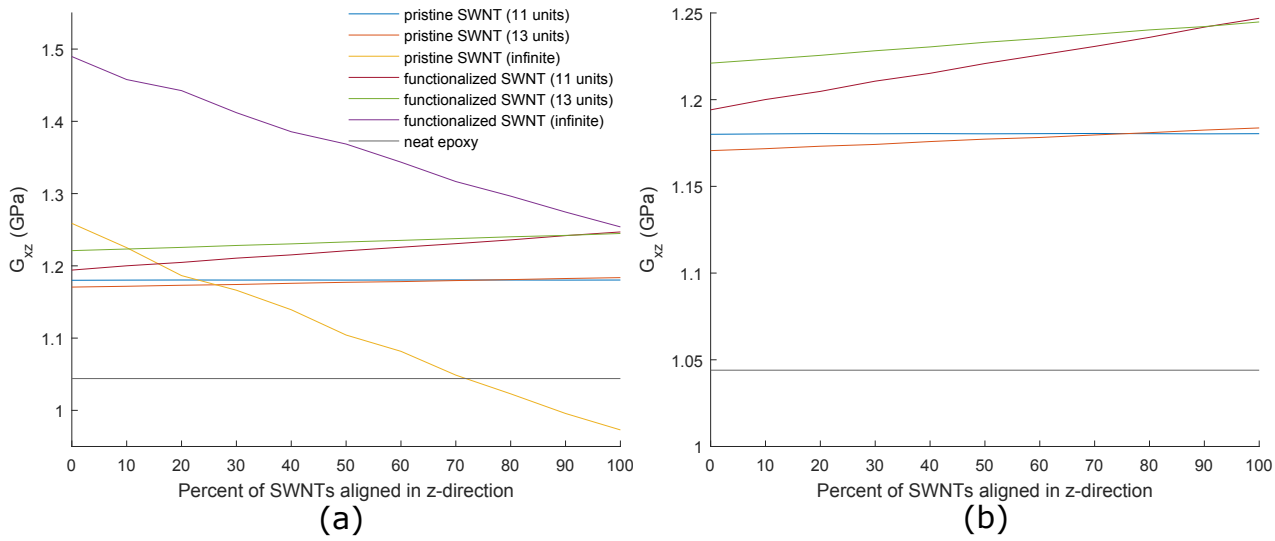

Figure 5.94: Variation of G_{xz} with respect to % of SWNT alignment in the z-direction for a. all and b. discontinuous nanocomposite systems studied for 60% epoxy units at 300 K.

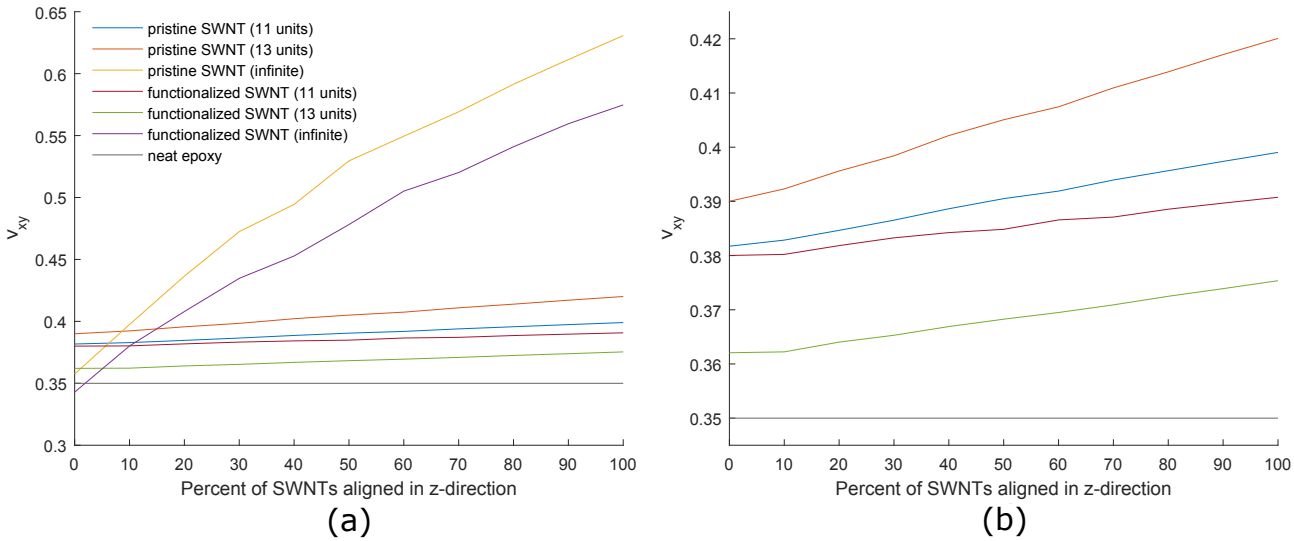

Figure 5.95: Variation of ν_{xy} with respect to % of SWNT alignment in the z-direction for a. all and b. discontinuous nanocomposite systems studied for 60% epoxy units at 300 K.

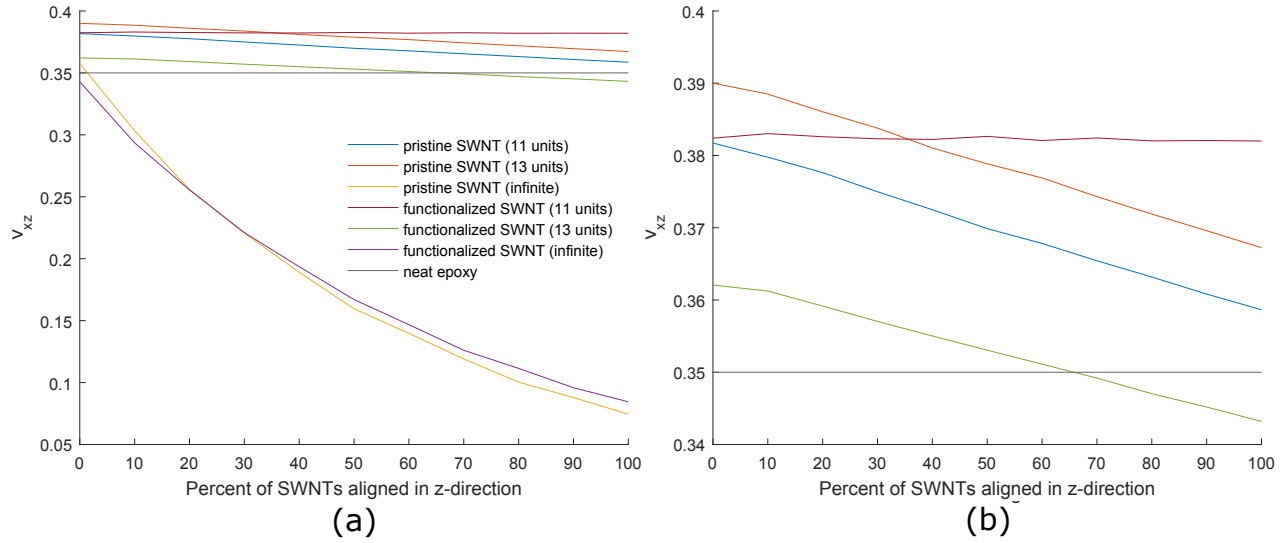

Figure 5.96: Variation of ν_{xz} with respect to % of SWNT alignment in the z-direction for a. all and b. discontinuous nanocomposite systems studied for 60% epoxy units at 300 K.

5.4.4 90% Epoxy Units

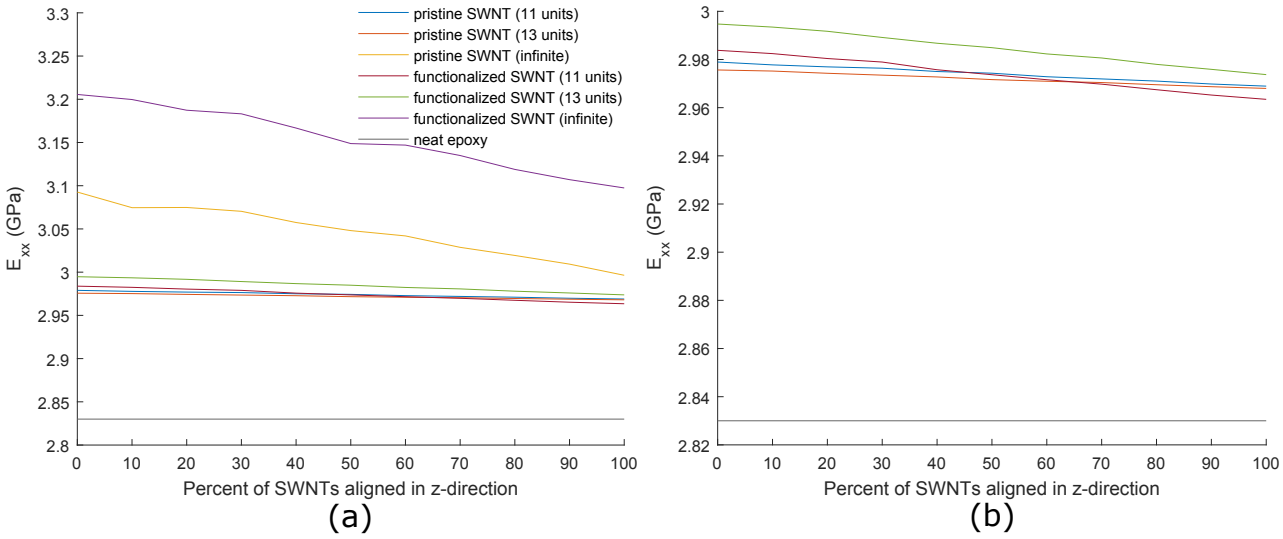

Figure 5.97: Variation of E_{xx} with respect to % of SWNT alignment in the z-direction for a. all and b. discontinuous nanocomposite systems studied for 90% epoxy units at 300 K.

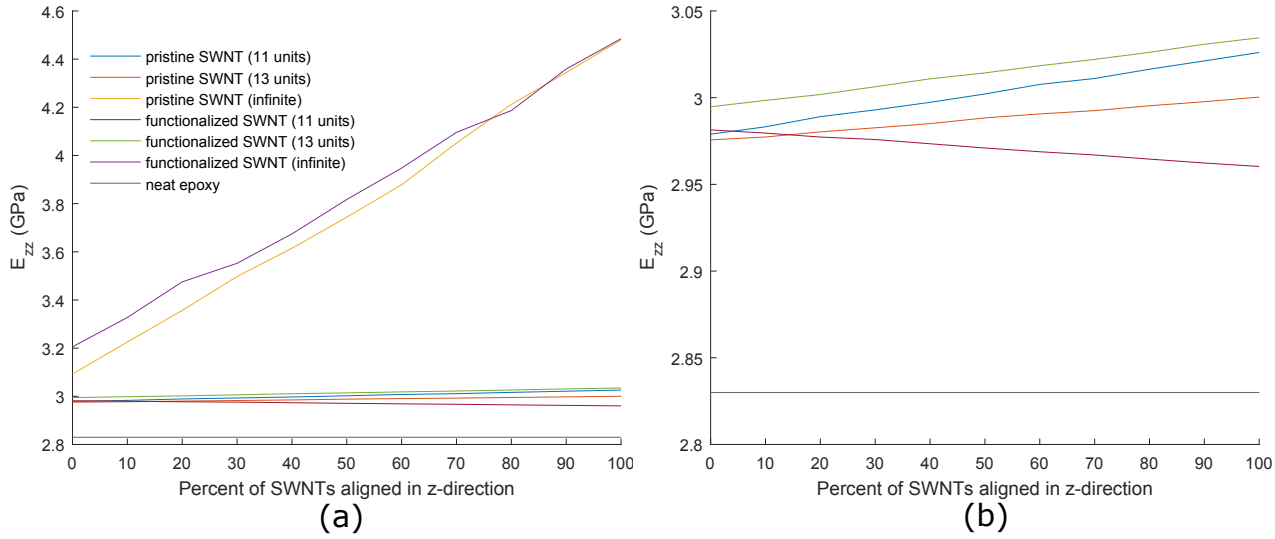

Figure 5.98: Variation of E_{zz} with respect to % of SWNT alignment in the z-direction for a. all and b. discontinuous nanocomposite systems studied for 90% epoxy units at 300 K.

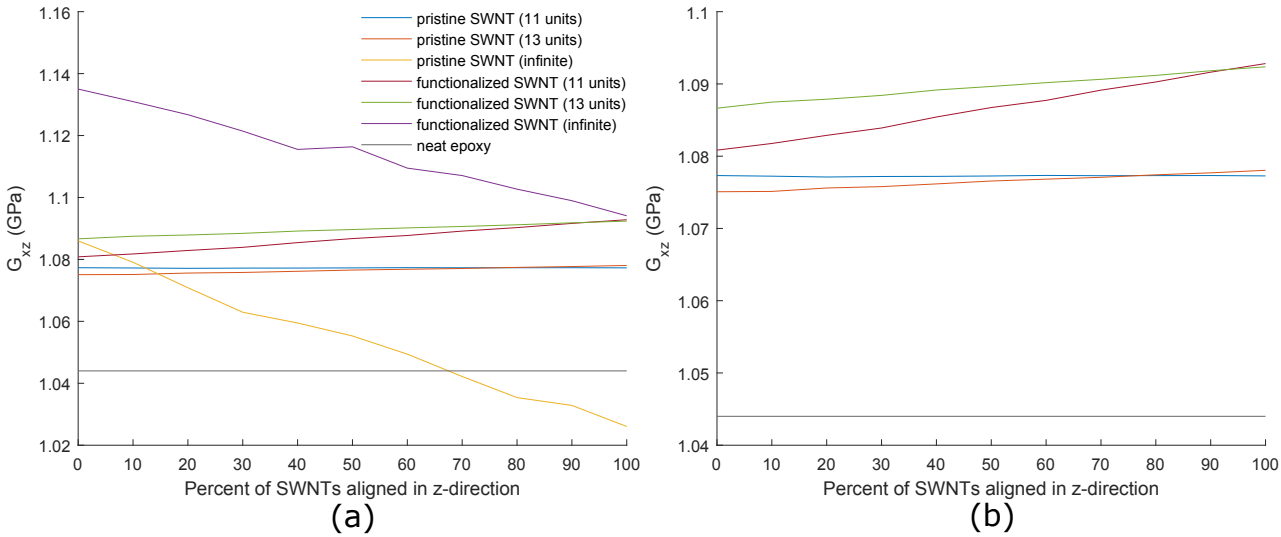

Figure 5.99: Variation of G_{xz} with respect to % of SWNT alignment in the z-direction for a. all and b. discontinuous nanocomposite systems studied for 90% epoxy units at 300 K.

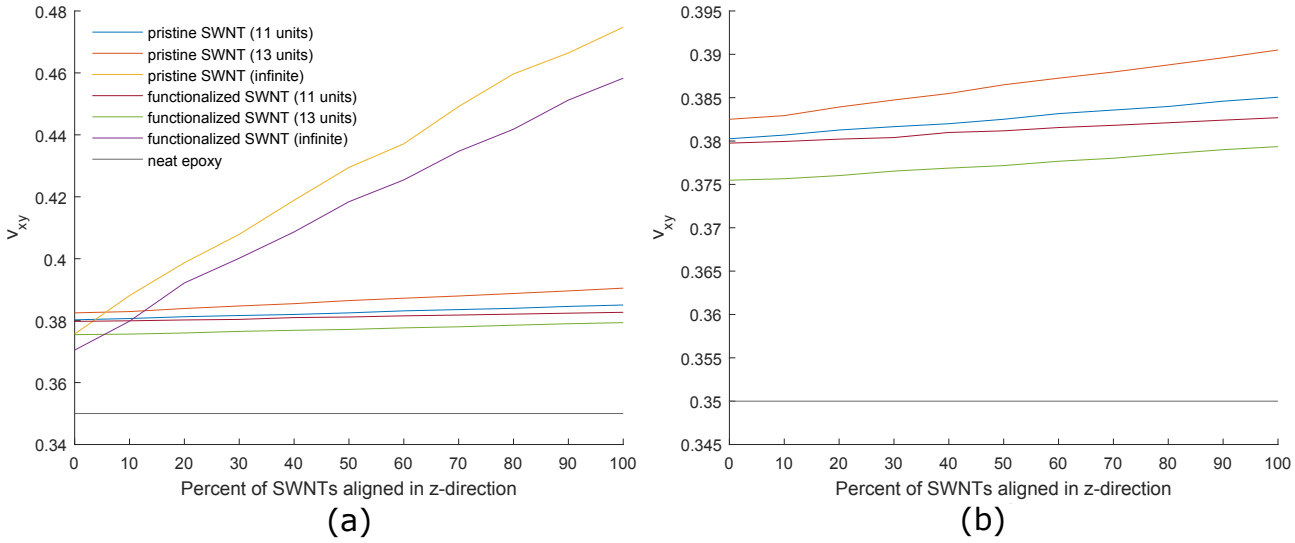

Figure 5.100: Variation of ν_{xy} with respect to % of SWNT alignment in the z-direction for a. all and b. discontinuous nanocomposite systems studied for 90% epoxy units at 300 K.

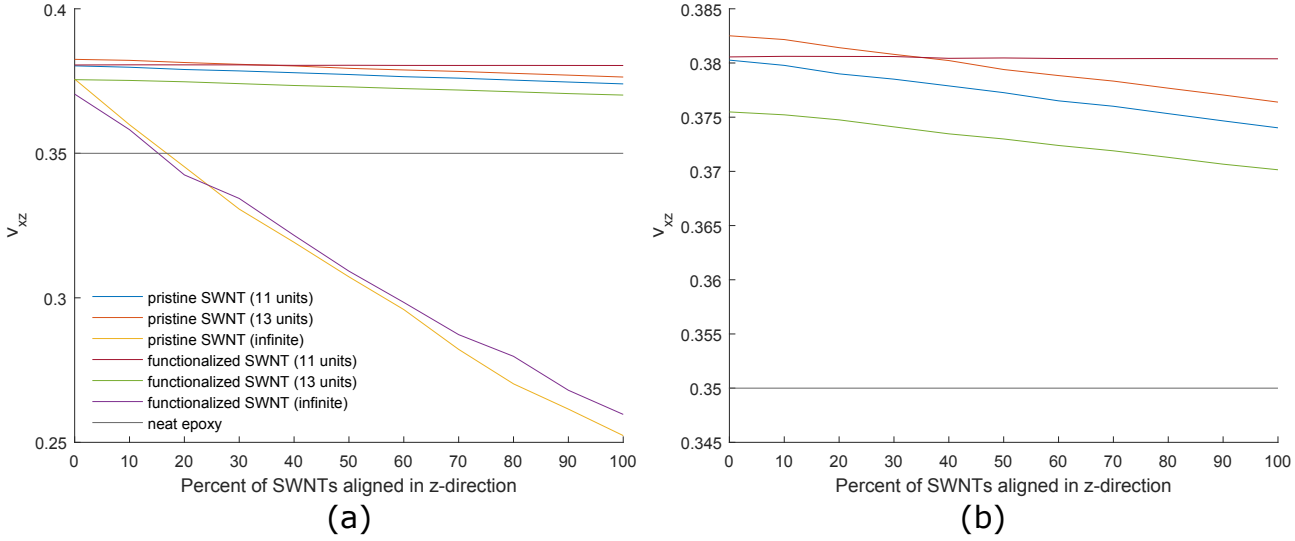

Figure 5.101: Variation of ν_{xz} with respect to % of SWNT alignment in the z-direction for a. all and b. discontinuous nanocomposite systems studied for 90% epoxy units at 300 K.

5.5 Conclusions

In this Chapter, aligned nanotube results were considered for the various nanocomposite systems at variable amounts of neat epoxy units. The Finite Element and ODF-based multiscale methods were used to generate the results. The Finite Element model was performed by assigning the elemental stiffness matrices elastic properties from MD SWNT-

epoxy nanocomposite lattices at a desired orientation, or of neat epoxy. This directly led to solutions where the percentage of alignment and volume fraction of SWNT could be controlled. The ODF method was used to generate macroscopic upper and lower bound results via the Voigt and Reuss models for systems with fully aligned SWNTs, fully random SWNTs, and systems where a desired percentage of nanotubes are aligned and the rest are random. These systems all contain the same volume fraction of SWNT as the MD SWNT-epoxy lattice, and to vary the volume fraction rules of mixtures approaches were employed. In the two-phase model, the upper bound and lower bound stiffness matrices calculated via the ODF for a desired amount of alignment are used in conjunction with the parallel and series rule of mixtures approaches to obtain upper and lower bound stiffness matrices for various amounts of alignment and various volume fractions of SWNTs. In the three-phase model, the calculation of new stiffness matrices for a given amount of alignment was unnecessary, and rule of mixture approaches were applied to the fully aligned and fully random nanocomposites via the ODF model, along with neat epoxy. This leads to five total model results, though it was shown the 2-phase and 3-phase are essentially equivalent for the special case of only one preferential orientation.

Section 5.3 outlined how the various multiscale models compare for the different nanocomposite systems. In general, the Finite Element model was well bounded by the ODF model. Section 5.4 showed how the results for the various nanocomposite systems compare for a given method, where the Finite Element model was selected. This model was chosen because it almost always lied within the bounds of the ODF model. The elastic properties were compared at various amounts of epoxy units at 300 K and 1 atm. Functionalization led to larger improvements relative to neat epoxy for E_{xx} at a given SWNT length due to the fact that even for high amounts of SWNT alignment in the z-direction, the nanotube still effects the direction transverse to it due to covalent bonding. For E_{zz}, despite deterioration in inherent SWNT stiffness due to functionalization, the functionalized, infinite system showed greater values than the pristine system except at very high percentages of alignment. This shows that the improvements due to functionalization of the non-aligned tubes often outweigh the deterioration of the nanotube properties. For the discontinuous systems: the pristine systems gave higher values of E_{zz}. The discontinuous, functionalized system with 11 repeat units displayed a decreasing E_{zz} with increasing alignment, telling that functionalization on a very short nanotube can have negative effects on the SWNT's stiffness and contribution to the composite; and indeed the direction perpendicular to the nanotube saw greater stiffness improvements due to its covalent bonds to the SWNT than the direction the nanotube was actually aligned.

For the infinite systems, increasing amounts of alignment in the z-direction will cause

a decreased shear modulus G_{xz}. Covalent bonding led to improvements in G_{xz}, where even in a fully aligned case all directions showed improved stiffness compared to neat epoxy. There were only minor change in G_{xz} for various alignments for the discontinuous systems, because there is a much less dramatic difference in the stiffness between the nanotube direction and the directions perpendicular to the nanotube. All of the systems show increasing ν_{xy}, and decreasing ν_{xz} with increasing alignment. Less nanotubes in the plane of isotropy, leads to more contraction in the plane of isotropy when loaded in that direction, and less contraction in the z-direction. The pristine systems show higher magnitude of ν_{xy} than the functionalized systems, since the functionalization allowed stiffness of the nanotube to be imparted in the plane of isotropy even with increasing alignment. The discontinuous systems showed a much lesser effect of ν_{xz} than the infinite systems, since the stiffness increase along the SWNT direction was significantly lesser.

CHAPTER 6

Conclusions

6.1 Summary

This dissertation showed results for multiscale modeling techniques of epoxy-SWNT composite. In Chapter 1, the problem was outlined and the relevant computational and experimental literature was reviewed. The main body of the thesis was divided into four sections: atomistic modeling for thermomechanical properties, atomistic modeling for thermal conductivity, multiscale modeling for elastic properties of random SWNT-epoxy nanocomposites, and multiscale modeling for elastic properties of aligned SWNT-epoxy nanocomposites.

Chapters 2 and 3 focus on Molecular Dynamics modeling of epoxy-based nanocomposites with continuous and discontinuous nanotubes. Continuous nanotubes span the entire MD lattice and therefore become infinite with the application of periodic boundary conditions. The epoxy model was built using a 'dendrimeric' approach that was verified by matching the experimental density, glass transition temperature, and thermal expansion. In Chapter 2, MD was used to analyze the thermomechanical properties of pristine and functionalized SWNT-epoxy nanocomposites. In Chapter 3, thermal conductivity of functionalized and pristine SWNT-epoxy nanocomposites was investigated using MD via the Green-Kubo integral of the heat current auto correlation function. In epoxies, there are long range interatomic interactions due to electrostatic forces, and this was modeled via a k-space approach. The discontinuous nanotube systems allowed the end effects to be investigated.

Chapters 4 and 5 focused on multiscale modeling for the elastic properties of the SWNT-epoxy nanocomposites. Two multiscale approaches were implemented: a Finite Element based approach, and an orientation distribution function based approach. The Finite Element approach probabilistically assigned elements with the elastic properties of a SWNT-epoxy nanocomposite from Chapter 2 at a given orientation, or the elastic proper-

ties of neat epoxy, depending on the desired volume fraction and alignment of the SWNTs. For the ODF-based method, ODFs for randomly oriented through fully aligned composites were generated, accounting for symmetry. Using results of Chapter 2 in conjunction with stiffness and compliance based approaches, upper bounds and lower bounds for the macroscopic stiffness matrices were obtained. In order to vary the volume fraction of SWNT, rule of mixtures approaches were implemented. Nanocomposites with randomly oriented nanotubes, creating an equivalent isotropic system, were investigated in Chapter 4. Chapter 5 focuses on the effects of SWNT alignment on the mechanical properties.

6.2 Concluding Remarks

From the MD results, the addition of SWNTs to epoxy led to large improvements in stiffness for the continuous nanotube systems, up to 200% for randomly oriented nanotubes, and more moderate improvements for the discontinuous systems. Large reductions in thermal expansion were seen, up to 32%, that were able to be experimentally verified. For the short nanotubes investigated, functionalization provided greater improvement in overall composite thermal conductivity than pristine nanotubes. For the long nanotubes investigated, the massive increase in the thermal conductivity along the tube boosted composite conductivity much greater than the added improvements in the plane perpendicular to the nanotube due to functionalization when considering deterioration of the inherent tube conductivity. The simulations demonstrated there is a SWNT length threshold where the best improvement for a composite system with randomly oriented nanotubes would transition from functionalized SWNTs to pristine SWNTs.

From the multiscale modeling results for equivalently isotropic systems; for all volume fractions of neat epoxy units, the systems where the nanotube spans the MD cell demonstrated the highest stiffness and least amount of lateral contraction from 1-350 K. For both the continuous and discontinuous systems, functionalized SWNTs showed higher stiffness than the pristine SWNTs, suggesting that functionalization of SWNTs improves the elastic properties regardless of nanotube length. From the aligned nanotube results yielding transversely isotropic results; despite deterioration in inherent SWNT stiffness due to functionalization, the functionalized, infinite system displayed greater values for E_{zz} than the pristine system except at very high percentages of alignment. This demonstrated that the improvements due to functionalization of the non-aligned tubes often outweigh the deterioration of the intrinsic nanotube stiffness. The discontinuous, functionalized system with 11 repeat units gave a decreasing E_{zz}, telling that functionalization on a very short nanotube can have negative effects on the SWNT's stiffness and its contribution to the composite;

and indeed the direction perpendicular to the nanotube saw greater stiffness improvements due to its covalent bonds to the SWNT than the direction the nanotube was actually aligned.

6.3 Future Work

The modeling techniques used are physics based, and therefore several future directions exist to extend the work to a number of systems of interest:

- **Cure Conversion**: The degree of curing has been shown to have large effects on the thermal, tensile, and fracture properties of epoxies [156,157]. CNTs, especially those that have undergone surface modification, have been shown to alter curing behavior [158]. Therefore, it is important to model these effects for increased accuracy and improved generality for CNT-epoxy nanocomposites.

- **Degree of Functionalization and Bond Distribution**: Experimentally, techniques have been developed to increase the degree of functionalization to overcome the insolubility of CNTs [159]. It has been shown in this thesis that functionalization has counteracting effects on the macroscopic thermomechanical properties by degrading the inherent tube stiffness and conductivity, but increasing that of the surrounding polymer. Expanding the current models to study the effects of the degree of functionalization and the covalent bond distribution will allow the optimum values to be found.

- **Effects of Varying the Diameter, Chirality, Number of Walls, and Ends of the CNTs**: CNTs come in many different forms, and each can have vastly different thermomechanical properties. Parameters that can be changed include: the number of walls of the CNT, the diameter of the tube, the chirality, or the chiral angle between hexagons and the tube axis, and the geometry of the ends (i.e nanotubes with and without capped ends). For example, chirality has a massive effect on the band-gap SWNTs, even with identical diameters [160]. The SWNT length was shown in this thesis to have large effects on the thermomechanical properties. To improve the generality of the model and optimize for a variety of different applications, a larger variety of CNTs should be considered.

- **Inclusion of Various Nanofillers**: There have been numerous studies on other types of nanofillers to improve mechanical, electrical and thermal properties; such as buckyballs, graphene, metal nanopaticles, clay nanoplatelets, ect. [161]. Some of these fillers may lead to more desirable results than CNTs for certain applications.

- **Effects of CNT bundling**: SWNTs form bundles during their production, and it can be hard to achieve uniform dispersion of nanotubes since they are attracted to each other by weak van der Waals forces [162]. Using the ODF model, bundles CNTs can be considered by dictating multiple preferential CNT orientations representing bundles.

Applying the experimentally verified techniques used in this dissertation to various nanocomposite systems can allow materials to be designed and tailored to specific applications without having to run physical experiments.

BIBLIOGRAPHY

[1] M. J. Treacy, T. Ebbesen, and J. Gibson, "Exceptionally high young's modulus observed for individual carbon nanotubes," 1996.

[2] B. I. Yakobson and P. Avouris, "Mechanical properties of carbon nanotubes," in *Carbon nanotubes*, pp. 287–327, Springer, 2001.

[3] D. Walters, L. Ericson, M. Casavant, J. Liu, D. Colbert, K. Smith, and R. Smalley, "Elastic strain of freely suspended single-wall carbon nanotube ropes," *Applied Physics Letters*, vol. 74, no. 25, pp. 3803–3805, 1999.

[4] A. Thess, R. Lee, P. Nikolaev, and H. Dai, "Crystalline ropes of metallic carbon nanotubes," *Science*, vol. 273, no. 5274, p. 483, 1996.

[5] J. W. Wilder, L. C. Venema, A. G. Rinzler, R. E. Smalley, and C. Dekker, "Electronic structure of atomically resolved carbon nanotubes," *Nature*, vol. 391, no. 6662, pp. 59–62, 1998.

[6] T. W. Odom, J.-L. Huang, P. Kim, and C. M. Lieber, "Atomic structure and electronic properties of single-walled carbon nanotubes," *Nature*, vol. 391, no. 6662, pp. 62–64, 1998.

[7] M. Dresselhaus and P. Eklund, "Phonons in carbon nanotubes," *Advances in Physics*, vol. 49, no. 6, pp. 705–814, 2000.

[8] J. Hone, "Phonons and thermal properties of carbon nanotubes," in *Carbon Nanotubes*, pp. 273–286, Springer, 2001.

[9] M.-F. Yu, B. S. Files, S. Arepalli, and R. S. Ruoff, "Tensile loading of ropes of single wall carbon nanotubes and their mechanical properties," *Physical review letters*, vol. 84, no. 24, p. 5552, 2000.

[10] F. F. T. Araujo and H. M. Rosenberg, "The thermal conductivity of epoxy-resin/metal-powder composite materials from 1.7 to 300k," *Journal of Physics D: Applied Physics*, vol. 9, no. 4, p. 665, 1976.

[11] E. Pop, D. Mann, Q. Wang, K. Goodson, and H. Dai, "Thermal conductance of an individual single-wall carbon nanotube above room temperature," *Nano letters*, vol. 6, no. 1, pp. 96–100, 2006.

[12] L. Sun, G. Warren, J. Oreilly, W. Everett, S. Lee, D. Davis, D. Lagoudas, and H.-J. Sue, "Mechanical properties of surface-functionalized swcnt/epoxy composites," *Carbon*, vol. 46, no. 2, pp. 320–328, 2008.

[13] J. Zhu, H. Peng, F. Rodriguez-Macias, J. L. Margrave, V. N. Khabashesku, A. M. Imam, K. Lozano, and E. V. Barrera, "Reinforcing epoxy polymer composites through covalent integration of functionalized nanotubes," *Advanced Functional Materials*, vol. 14, no. 7, pp. 643–648, 2004.

[14] S. Wang, Z. Liang, T. Liu, B. Wang, and C. Zhang, "Effective amino-functionalization of carbon nanotubes for reinforcing epoxy polymer composites," *Nanotechnology*, vol. 17, no. 6, p. 1551, 2006.

[15] S. Wang and J. Qiu, "Modification of epoxy resins via m-chloroperbenzoic acid-epoxidized carbon nanotubes," *Journal of applied polymer science*, vol. 112, no. 6, pp. 3322–3326, 2009.

[16] S. Wang, R. Liang, B. Wang, and C. Zhang, "Reinforcing polymer composites with epoxide-grafted carbon nanotubes," *Nanotechnology*, vol. 19, no. 8, p. 085710, 2008.

[17] J. Zhu, J. Kim, H. Peng, J. L. Margrave, V. N. Khabashesku, and E. V. Barrera, "Improving the dispersion and integration of single-walled carbon nanotubes in epoxy composites through functionalization," *Nano letters*, vol. 3, no. 8, pp. 1107–1113, 2003.

[18] L. Valentini, D. Puglia, F. Carniato, E. Boccaleri, L. Marchese, and J. M. Kenny, "Use of plasma fluorinated single-walled carbon nanotubes for the preparation of nanocomposites with epoxy matrix," *Composites Science and Technology*, vol. 68, no. 3, pp. 1008–1014, 2008.

[19] L. Liu, A. H. Barber, S. Nuriel, and H. D. Wagner, "Mechanical properties of functionalized single-walled carbon-nanotube/poly (vinyl alcohol) nanocomposites," *Advanced Functional Materials*, vol. 15, no. 6, pp. 975–980, 2005.

[20] M. Paiva, B. Zhou, K. Fernando, Y. Lin, J. Kennedy, and Y.-P. Sun, "Mechanical and morphological characterization of polymer–carbon nanocomposites from functionalized carbon nanotubes," *Carbon*, vol. 42, no. 14, pp. 2849–2854, 2004.

[21] H. Geng, R. Rosen, B. Zheng, H. Shimoda, L. Fleming, J. Liu, and O. Zhou, "Fabrication and properties of composites of poly (ethylene oxide) and functionalized carbon nanotubes," tech. rep., DTIC Document, 2006.

[22] T. V. Sreekumar, T. Liu, B. G. Min, H. Guo, S. Kumar, R. H. Hauge, and R. E. Smalley, "Polyacrylonitrile single-walled carbon nanotube composite fibers," *Advanced Materials*, vol. 16, no. 1, pp. 58–61, 2004.

[23] K. Şahin, N. A. Fasanella, I. Chasiotis, K. M. Lyons, B. A. Newcomb, M. G. Kamath, H. G. Chae, and S. Kumar, "High strength micron size carbon fibers from polyacrylonitrile–carbon nanotube precursors," *Carbon*, vol. 77, pp. 442–453, 2014.

[24] H. Guo, T. Sreekumar, T. Liu, M. Minus, and S. Kumar, "Structure and properties of polyacrylonitrile/single wall carbon nanotube composite films," *Polymer*, vol. 46, no. 9, pp. 3001–3005, 2005.

[25] M. L. Shofner, V. N. Khabashesku, and E. V. Barrera, "Processing and mechanical properties of fluorinated single-wall carbon nanotube-polyethylene composites," *Chemistry of Materials*, vol. 18, no. 4, pp. 906–913, 2006.

[26] A. R. Bhattacharyya, T. Sreekumar, T. Liu, S. Kumar, L. M. Ericson, R. H. Hauge, and R. E. Smalley, "Crystallization and orientation studies in polypropylene/single wall carbon nanotube composite," *Polymer*, vol. 44, no. 8, pp. 2373–2377, 2003.

[27] M. L. Manchado, L. Valentini, J. Biagiotti, and J. Kenny, "Thermal and mechanical properties of single-walled carbon nanotubes–polypropylene composites prepared by melt processing," *Carbon*, vol. 43, no. 7, pp. 1499–1505, 2005.

[28] R. Haggenmueller, H. Gommans, A. Rinzler, J. E. Fischer, and K. Winey, "Aligned single-wall carbon nanotubes in composites by melt processing methods," *Chemical physics letters*, vol. 330, no. 3, pp. 219–225, 2000.

[29] C. A. Cooper, D. Ravich, D. Lips, J. Mayer, and H. D. Wagner, "Distribution and alignment of carbon nanotubes and nanofibrils in a polymer matrix," *Composites science and technology*, vol. 62, no. 7, pp. 1105–1112, 2002.

[30] F. Du, J. E. Fischer, and K. I. Winey, "Coagulation method for preparing single-walled carbon nanotube/poly (methyl methacrylate) composites and their modulus, electrical conductivity, and thermal stability," *Journal of Polymer Science Part B: Polymer Physics*, vol. 41, no. 24, pp. 3333–3338, 2003.

[31] V. Skakalova, U. Dettlaff-Weglikowska, and S. Roth, "Electrical and mechanical properties of nanocomposites of single wall carbon nanotubes with pmma," *Synthetic Metals*, vol. 152, no. 1-3, pp. 349–352, 2005.

[32] Y. Xu, G. Ray, and B. Abdel-Magid, "Thermal behavior of single-walled carbon nanotube polymer–matrix composites," *Composites Part A: Applied Science and Manufacturing*, vol. 37, no. 1, pp. 114–121, 2006.

[33] X. Gong, J. Liu, S. Baskaran, R. D. Voise, and J. S. Young, "Surfactant-assisted processing of carbon nanotube/polymer composites," *Chemistry of materials*, vol. 12, no. 4, pp. 1049–1052, 2000.

[34] R. G. de Villoria, A. Miravete, J. Cuartero, A. Chiminelli, and N. Tolosana, "Mechanical properties of swnt/epoxy composites using two different curing cycles," *Composites Part B: Engineering*, vol. 37, no. 4, pp. 273–277, 2006.

[35] S. Wang, Z. Liang, P. Gonnet, Y.-H. Liao, B. Wang, and C. Zhang, "Effect of nanotube functionalization on the coefficient of thermal expansion of nanocomposites," *Advanced functional materials*, vol. 17, no. 1, pp. 87–92, 2007.

[36] Q. Wang, J. Dai, W. Li, Z. Wei, and J. Jiang, "The effects of cnt alignment on electrical conductivity and mechanical properties of swnt/epoxy nanocomposites," *Composites science and technology*, vol. 68, no. 7, pp. 1644–1648, 2008.

[37] C. Pizzutto, J. Suave, J. Bertholdi, S. Pezzin, L. Coelho, and S. Amico, "Mechanical and dilatometric properties of carboxylated swcnt/epoxy composites: effects of the dispersion in the resin and in the hardener," *Journal of Reinforced Plastics and Composites*, 2009.

[38] Q.-P. Feng, X.-J. Shen, J.-P. Yang, S.-Y. Fu, Y.-W. Mai, and K. Friedrich, "Synthesis of epoxy composites with high carbon nanotube loading and effects of tubular and wavy morphology on composite strength and modulus," *Polymer*, vol. 52, no. 26, pp. 6037–6045, 2011.

[39] C. Wei, D. Srivastava, and K. Cho, "Thermal expansion and diffusion coefficients of carbon nanotube-polymer composites," *Nano Letters*, vol. 2, no. 6, pp. 647–650, 2002.

[40] Z. Zhang, D. Ward, Y. Xue, H. Zhang, and M. Horstemeyer, "Interfacial characteristics of carbon nanotube-polyethylene composites using molecular dynamics simulations," *ISRN Materials Science*, vol. 2011, 2011.

[41] S. Frankland, V. Harik, G. Odegard, D. Brenner, and T. Gates, "The stress–strain behavior of polymer–nanotube composites from molecular dynamics simulation," *Composites Science and Technology*, vol. 63, no. 11, pp. 1655–1661, 2003.

[42] M. Griebel and J. Hamaekers, "Molecular dynamics simulations of the elastic moduli of polymer–carbon nanotube composites," *Computer methods in applied mechanics and engineering*, vol. 193, no. 17, pp. 1773–1788, 2004.

[43] Y. Han and J. Elliott, "Molecular dynamics simulations of the elastic properties of polymer/carbon nanotube composites," *Computational Materials Science*, vol. 39, no. 2, pp. 315–323, 2007.

[44] S. Rouhi, Y. Alizadeh, and R. Ansari, "Molecular dynamics simulations of the single-walled carbon nanotubes/poly (phenylacetylene) nanocomposites," *Superlattices and Microstructures*, vol. 72, pp. 204–218, 2014.

[45] S. Frankland and V. Harik, "Simulation of carbon nanotube pull-outwhen bonded to a polymer matrix," in *MRS Proceedings*, vol. 740, pp. I12–1, Cambridge Univ Press, 2002.

[46] G. M. Odegard, S.-J. V. Frankland, and T. S. Gates, "Effect of nanotube functionalization on the elastic properties of polyethylene nanotube composites," *AIAA journal*, vol. 43, no. 8, pp. 1828–1835, 2005.

[47] Z. Liang, J. J. Gou, C. Zhang, B. Wang, and L. Kramer, "Investigation of molecular interactions between (10, 10) single-walled nanotube and epon 862 resin/detda

curing agent molecules," *Materials Science and Engineering: A*, vol. 365, no. 1, pp. 228–234, 2004.

[48] J. Gou, B. Fan, G. Song, and A. Khan, "Study of affinities between single-walled nanotube and epoxy resin using molecular dynamics simulation," *International Journal of Nanoscience*, vol. 5, no. 1, pp. 131–144, 2006.

[49] J. Gou, B. Minaie, B. Wang, Z. Liang, and C. Zhang, "Computational and experimental study of interfacial bonding of single-walled nanotube reinforced composites," *Computational Materials Science*, vol. 31, no. 3, pp. 225–236, 2004.

[50] R. Zhu, E. Pan, and A. Roy, "Molecular dynamics study of the stress–strain behavior of carbon-nanotube reinforced epon 862 composites," *Materials Science and Engineering: A*, vol. 447, no. 1, pp. 51–57, 2007.

[51] R. Mohan, E. Fefey, and A. Kelkar, "Predictive mechanical properties of epon 862 (dgebf) cross-linked with curing agent w (detda) and swcnt using md simulationseffect of carbon vacancy defects," *AIAA*, vol. 2012, 2012.

[52] C. Knox, J. Andzelm, J. Lenhart, A. Browning, and S. Christensen, "High strain rate mechanical behavior of epoxy networks from molecular dynamics simulations," in *Proc of 27th army science conf, Orlando, FL, GP-09*, 2010.

[53] V. Sundararaghavan and A. Kumar, "Molecular dynamics simulations of compressive yielding in cross-linked epoxies in the context of argon theory," *International Journal of Plasticity*, vol. 47, pp. 111–125, 2013.

[54] N. Fasanella and V. Sundararaghavan, "Molecular dynamics of SWNT/epoxy nanocomposites," in *56th AIAA/ASCE/AHS/ASC Structures, Structural Dynamics, and Materials Conference*, p. 0124, 2015.

[55] N. Fasanella and V. Sundararaghavan, "Atomistic modeling of thermomechanical properties of SWNT/epoxy nanocomposites," *Modelling and Simulation in Materials Science and Engineering*, vol. 23, no. 6, p. 065003, 2015.

[56] T. Kawamura, Y. Kangawa, and K. Kakimoto, "Investigation of thermal conductivity of nitride mixed crystals and superlattices by molecular dynamics," *physica status solidi (c)*, vol. 3, no. 6, pp. 1695–1699, 2006.

[57] Chantrenne, Raynaud, and Barrat, "Study of phonon heat transfer in metallic solids from molecular dynamic simulations," *Microscale Thermophysical Engineering*, vol. 7, no. 2, pp. 117–136, 2003.

[58] T. Terao, E. Lussetti, and F. Müller-Plathe, "Nonequilibrium molecular dynamics methods for computing the thermal conductivity: Application to amorphous polymers," *Physical Review E*, vol. 75, no. 5, p. 057701, 2007.

[59] V. Varshney, S. S. Patnaik, A. K. Roy, and B. L. Farmer, "Heat transport in epoxy networks: A molecular dynamics study," *Polymer*, vol. 50, no. 14, pp. 3378–3385, 2009.

[60] A. Kumar, V. Sundararaghavan, and A. Browning, "Study of temperature dependence of thermal conductivity in cross-linked epoxies using molecular dynamics simulations with long range interactions," *Modelling and Simulation in Materials Science and Engineering*, vol. 22, no. 2, p. 025013, 2014.

[61] R. Kubo, M. Toda, and N. Hashitsume, *Statistical physics II: nonequilibrium statistical mechanics*, vol. 31. Springer Science & Business Media, 2012.

[62] S. Shenogin, A. Bodapati, L. Xue, R. Ozisik, and P. Keblinski, "Effect of chemical functionalization on thermal transport of carbon nanotube composites," *Applied Physics Letters*, vol. 85, no. 12, pp. 2229–2231, 2004.

[63] T. C. Clancy and T. S. Gates, "Modeling of interfacial modification effects on thermal conductivity of carbon nanotube composites," *Polymer*, vol. 47, no. 16, pp. 5990–5996, 2006.

[64] S. T. Huxtable, D. G. Cahill, S. Shenogin, L. Xue, R. Ozisik, P. Barone, M. Usrey, M. S. Strano, G. Siddons, M. Shim, *et al.*, "Interfacial heat flow in carbon nanotube suspensions," *Nature materials*, vol. 2, no. 11, pp. 731–734, 2003.

[65] Z. Xu and M. J. Buehler, "Nanoengineering heat transfer performance at carbon nanotube interfaces," *ACS nano*, vol. 3, no. 9, pp. 2767–2775, 2009.

[66] M. Alaghemandi, F. Müller-Plathe, and M. C. Böhm, "Thermal conductivity of carbon nanotubepolyamide-6, 6 nanocomposites: Reverse non-equilibrium molecular dynamics simulations," *The Journal of chemical physics*, vol. 135, no. 18, p. 184905, 2011.

[67] V. Varshney, A. K. Roy, T. J. Michalak, J. Lee, and B. L. Farmer, "Effect of curing and functionalization on the interface thermal conductance in carbon nanotube–epoxy composites," *Jom*, vol. 65, no. 2, pp. 140–146, 2013.

[68] F. H. Gojny, M. H. Wichmann, B. Fiedler, I. A. Kinloch, W. Bauhofer, A. H. Windle, and K. Schulte, "Evaluation and identification of electrical and thermal conduction mechanisms in carbon nanotube/epoxy composites,"

[69] M. Biercuk, M. C. Llaguno, M. Radosavljevic, J. Hyun, A. T. Johnson, and J. E. Fischer, "Carbon nanotube composites for thermal management," *Applied physics letters*, vol. 80, no. 15, pp. 2767–2769, 2002.

[70] C. Liu and S. Fan, "Effects of chemical modifications on the thermal conductivity of carbon nanotube composites," *Applied Physics Letters*, vol. 86, no. 12, p. 123106, 2005.

[71] E. Choi, J. Brooks, D. Eaton, M. Al-Haik, M. Hussaini, H. Garmestani, D. Li, and K. Dahmen, "Enhancement of thermal and electrical properties of carbon nanotube polymer composites by magnetic field processing," *Journal of Applied physics*, vol. 94, no. 9, pp. 6034–6039, 2003.

[72] M. Bryning, D. Milkie, M. Islam, J. Kikkawa, and A. Yodh, "Thermal conductivity and interfacial resistance in single-wall carbon nanotube epoxy composites," *Applied Physics Letters*, vol. 87, no. 16, p. 161909, 2005.

[73] A. Moisala, Q. Li, I. Kinloch, and A. Windle, "Thermal and electrical conductivity of single-and multi-walled carbon nanotube-epoxy composites," *Composites science and technology*, vol. 66, no. 10, pp. 1285–1288, 2006.

[74] A. Bagchi and S. Nomura, "On the effective thermal conductivity of carbon nanotube reinforced polymer composites," *Composites science and technology*, vol. 66, no. 11, pp. 1703–1712, 2006.

[75] C. Yu, L. Shi, Z. Yao, D. Li, and A. Majumdar, "Thermal conductance and thermopower of an individual single-wall carbon nanotube," *Nano letters*, vol. 5, no. 9, pp. 1842–1846, 2005.

[76] N. Galamba, C. N. de Castro, and J. Ely, "Thermal conductivity of molten alkali halides from equilibrium molecular dynamics simulations," *The Journal of chemical physics*, vol. 120, no. 18, pp. 8676–8682, 2004.

[77] N. A. Fasanella and V. Sundararaghavan, "Thermal conductivity via atomistic modeling for epoxy-SWNT composites," in *57th AIAA/ASCE/AHS/ASC Structures, Structural Dynamics, and Materials Conference*, p. 0152, 2016.

[78] N. A. Fasanella and V. Sundararaghavan, "Atomistic modeling of thermal conductivity of epoxy nanotube composites," *JOM*, vol. 68, no. 5, pp. 1396–1410, 2016.

[79] L. V. Zhigilei, "MSE 4270/6270: Introduction to atomistic simulations," 2016.

[80] C. Li and T.-W. Chou, "Multiscale modeling of carbon nanotube reinforced polymer composites," *Journal of nanoscience and nanotechnology*, vol. 3, no. 5, pp. 423–430, 2003.

[81] S. Namilae and N. Chandra, "Multiscale model to study the effect of interfaces in carbon nanotube-based composites," *Journal of Engineering materials and technology*, vol. 127, no. 2, pp. 222–232, 2005.

[82] C. Li and T.-W. Chou, "Multiscale modeling of compressive behavior of carbon nanotube/polymer composites," *Composites science and technology*, vol. 66, no. 14, pp. 2409–2414, 2006.

[83] A. Liu, K. Wang, and C. E. Bakis, "Effect of functionalization of single-wall carbon nanotubes (swnts) on the damping characteristics of swnt-based epoxy composites via multiscale analysis," *Composites Part A: Applied Science and Manufacturing*, vol. 42, no. 11, pp. 1748–1755, 2011.

[84] G. D. Seidel and D. C. Lagoudas, "Micromechanical analysis of the effective elastic properties of carbon nanotube reinforced composites," *Mechanics of Materials*, vol. 38, no. 8, pp. 884–907, 2006.

[85] P. Spanos and A. Kontsos, "A multiscale monte carlo finite element method for determining mechanical properties of polymer nanocomposites," *Probabilistic Engineering Mechanics*, vol. 23, no. 4, pp. 456–470, 2008.

[86] K. Tserpes, P. Papanikos, G. Labeas, and S. G. Pantelakis, "Multi-scale modeling of tensile behavior of carbon nanotube-reinforced composites," *Theoretical and Applied Fracture Mechanics*, vol. 49, no. 1, pp. 51–60, 2008.

[87] M. Ionita, "Multiscale molecular modeling of swcnts/epoxy resin composites mechanical behaviour," *Composites Part B: Engineering*, vol. 43, no. 8, pp. 3491–3496, 2012.

[88] S. Yang, S. Yu, W. Kyoung, D.-S. Han, and M. Cho, "Multiscale modeling of size-dependent elastic properties of carbon nanotube/polymer nanocomposites with interfacial imperfections," *Polymer*, vol. 53, no. 2, pp. 623–633, 2012.

[89] S. Yang, S. Yu, J. Ryu, J.-M. Cho, W. Kyoung, D.-S. Han, and M. Cho, "Nonlinear multiscale modeling approach to characterize elastoplastic behavior of cnt/polymer nanocomposites considering the interphase and interfacial imperfection," *International Journal of Plasticity*, vol. 41, pp. 124–146, 2013.

[90] M. P. Allen and D. J. Tildesley, *Computer simulation of liquids*. Oxford university press, 1989.

[91] D. Frenkel and B. Smit, *Understanding molecular simulation: from algorithms to applications*, vol. 1. Academic press, 2001.

[92] J. Haile, "Molecular dynamics simulation: Elementary methods," *Computers in Physics*, vol. 7, no. 6, pp. 625–625, 1993.

[93] F. Ercolessi, "A molecular dynamics primer," *Spring college in computational physics, ICTP, Trieste*, vol. 19, 1997.

[94] D. Siegel, "Lecture notes in ME599," 2013.

[95] F. H. Stillinger and T. A. Weber, "Computer simulation of local order in condensed phases of silicon," *Physical review B*, vol. 31, no. 8, p. 5262, 1985.

[96] G. B. Bacskay, J. R. Reimers, and S. Nordholm, "The mechanism of covalent bonding," *Journal of Chemical Education*, vol. 74, no. 12, p. 1494, 1997.

[97] L. Verlet, "Computer" experiments" on classical fluids. i. thermodynamical properties of lennard-jones molecules," *Physical review*, vol. 159, no. 1, p. 98, 1967.

[98] C. W. Gear, *Numerical initial value problems in ordinary differential equations*. Prentice Hall PTR, 1971.

[99] W. C. Swope, H. C. Andersen, P. H. Berens, and K. R. Wilson, "A computer simulation method for the calculation of equilibrium constants for the formation of physical clusters of molecules: Application to small water clusters," *The Journal of Chemical Physics*, vol. 76, no. 1, pp. 637–649, 1982.

[100] A. Rahman, "Correlations in the motion of atoms in liquid argon," *Physical Review*, vol. 136, no. 2A, p. A405, 1964.

[101] C. W. Gear, "The numerical integration of ordinary differential equations," *Mathematics of Computation*, vol. 21, no. 98, pp. 146–156, 1967.

[102] J. Meller, "Molecular dynamics," *Encyclopedia of Life*, 2001.

[103] H. C. Andersen, "Molecular dynamics simulations at constant pressure and/or temperature," *The Journal of chemical physics*, vol. 72, no. 4, pp. 2384–2393, 1980.

[104] H. J. Berendsen, J. v. Postma, W. F. van Gunsteren, A. DiNola, and J. Haak, "Molecular dynamics with coupling to an external bath," *The Journal of chemical physics*, vol. 81, no. 8, pp. 3684–3690, 1984.

[105] P. H. Hünenberger, "Thermostat algorithms for molecular dynamics simulations," in *Advanced computer simulation*, pp. 105–149, Springer, 2005.

[106] S. Nosé, "A unified formulation of the constant temperature molecular dynamics methods," *The Journal of chemical physics*, vol. 81, no. 1, pp. 511–519, 1984.

[107] W. G. Hoover, "Canonical dynamics: equilibrium phase-space distributions," *Physical Review A*, vol. 31, no. 3, p. 1695, 1985.

[108] Q. Wang, B. K. Storm, and L. P. Houmøller, "Study of the isothermal curing of an epoxy prepreg by near-infrared spectroscopy," *Journal of applied polymer science*, vol. 87, no. 14, pp. 2295–2305, 2003.

[109] I. Yarovsky and E. Evans, "Computer simulation of structure and properties of crosslinked polymers: application to epoxy resins," *Polymer*, vol. 43, no. 3, pp. 963–969, 2002.

[110] D. R. Rottach, J. G. Curro, J. Budzien, G. S. Grest, C. Svaneborg, and R. Everaers, "Molecular dynamics simulations of polymer networks undergoing sequential crosslinking and scission reactions," *Macromolecules*, vol. 40, no. 1, pp. 131–139, 2007.

[111] D. R. Heine, G. S. Grest, C. D. Lorenz, M. Tsige, and M. J. Stevens, "Atomistic simulations of end-linked poly (dimethylsiloxane) networks: structure and relaxation," *Macromolecules*, vol. 37, no. 10, pp. 3857–3864, 2004.

[112] C. Wu and W. Xu, "Atomistic molecular modelling of crosslinked epoxy resin," *Polymer*, vol. 47, no. 16, pp. 6004–6009, 2006.

[113] S. Christensen, "Atomistically explicit molecular dynamics simulations of thermosetting polymers," in *Proc. of 39th ISTC SAMPE Conf*, 2007.

[114] D. Studio and I. Insight, "Accelrys software inc," *San Diego, CA*, vol. 92121, 2009.

[115] P. Dauber-Osguthorpe, V. A. Roberts, D. J. Osguthorpe, J. Wolff, M. Genest, and A. T. Hagler, "Structure and energetics of ligand binding to proteins: Escherichia coli dihydrofolate reductase-trimethoprim, a drug-receptor system," *Proteins: Structure, Function, and Bioinformatics*, vol. 4, no. 1, pp. 31–47, 1988.

[116] S. Plimpton, "Fast parallel algorithms for short-range molecular dynamics," *Journal of computational physics*, vol. 117, no. 1, pp. 1–19, 1995.

[117] S. Christensen, "Using molecular dynamics coupled with higher length scale simulations for the development of improved composite matrix materials," in *Proc. 17th Int. Conf. on Composite Materials (Edinburgh, UK)*, 2009.

[118] J. L. Stevens, A. Y. Huang, H. Peng, I. W. Chiang, V. N. Khabashesku, and J. L. Margrave, "Sidewall amino-functionalization of single-walled carbon nanotubes through fluorination and subsequent reactions with terminal diamines," *Nano Letters*, vol. 3, no. 3, pp. 331–336, 2003.

[119] Y. Zhao and E. V. Barrera, "Asymmmetric diamino functionalization of nanotubes assisted by boc protection and their epoxy nanocomposites," *Advanced Functional Materials*, vol. 20, no. 18, pp. 3039–3044, 2010.

[120] S. White, P. Mather, and M. Smith, "Characterization of the cure-state of dgeba-dds epoxy using ultrasonic, dynamic mechanical, and thermal probes," *Polymer Engineering & Science*, vol. 42, no. 1, pp. 51–67, 2002.

[121] S. R. Heinz and J. S. Wiggins, "Uniaxial compression analysis of glassy polymer networks using digital image correlation," *Polymer Testing*, vol. 29, no. 8, pp. 925–932, 2010.

[122] A. Tcharkhtchi, E. Gouin, and J. Verdu, "Thermal expansion of epoxide–amine networks in the glassy state," *Journal of Polymer Science Part B: Polymer Physics*, vol. 38, no. 4, pp. 537–543, 2000.

[123] A. Garg and S. B. Sinnott, "Effect of chemical functionalization on the mechanical properties of carbon nanotubes," *Chemical Physics Letters*, vol. 295, no. 4, pp. 273–278, 1998.

[124] Y.-K. Kwon, S. Berber, and D. Tománek, "Thermal contraction of carbon fullerenes and nanotubes," *Physical review letters*, vol. 92, no. 1, p. 015901, 2004.

[125] P. Calvert, "Nanotube composites: a recipe for strength," *Nature*, vol. 399, no. 6733, pp. 210–211, 1999.

[126] D. A. McQuarrie, *Statistical thermodynamics*. HarperCollins Publishers, 1973.

[127] A. J. Ladd, B. Moran, and W. G. Hoover, "Lattice thermal conductivity: A comparison of molecular dynamics and anharmonic lattice dynamics," *Physical Review B*, vol. 34, no. 8, p. 5058, 1986.

[128] S. Nose and M. L. Klein, "Constant pressure molecular dynamics for molecular systems," *Molecular Physics*, vol. 50, no. 5, pp. 1055–1076, 1983.

[129] J. Petravic, "Thermal conductivity of ethanol," *The Journal of chemical physics*, vol. 123, no. 17, p. 174503, 2005.

[130] D. M. Heyes, "Pressure tensor of partial-charge and point-dipole lattices with bulk and surface geometries," *Physical Review B*, vol. 49, no. 2, p. 755, 1994.

[131] B. A. Luty, I. G. Tironi, and W. F. van Gunsteren, "Lattice-sum methods for calculating electrostatic interactions in molecular simulations," *The Journal of chemical physics*, vol. 103, no. 8, pp. 3014–3021, 1995.

[132] M. Deserno and C. Holm, "How to mesh up ewald sums (ii): An accurate error estimate for the p3m algorithm," *arXiv preprint cond-mat/9807100*, 1998.

[133] S. Berber, Y.-K. Kwon, and D. Tománek, "Unusually high thermal conductivity of carbon nanotubes," *Physical review letters*, vol. 84, no. 20, p. 4613, 2000.

[134] J. R. Lukes and H. Zhong, "Thermal conductivity of individual single-wall carbon nanotubes," *Journal of Heat Transfer*, vol. 129, no. 6, pp. 705–716, 2007.

[135] E. J. Garboczi, *Finite element and finite difference programs for computing the linear electric and elastic properties of digital images of random materials*. Building and Fire Research Laboratory, National Institute of Standards and Technology, 1998.

[136] R. D. Cook *et al.*, *Concepts and applications of finite element analysis*. John Wiley & Sons, 2007.

[137] T. R. Chandrupatla, A. D. Belegundu, T. Ramesh, and C. Ray, *Introduction to finite elements in engineering*. Prentice Hall Upper Saddle River, 1997.

[138] C. A. Felippa, "Introduction to finite element methods," *Course Notes, Department of Aerospace Engineeing Sciences, University of Colorado at Boulder, available at http://www. colorado. edu/engineering/Aerospace/CAS/courses. d/IFEM. d*, 2004.

[139] Z. Xia, C. Zhou, Q. Yong, and X. Wang, "On selection of repeated unit cell model and application of unified periodic boundary conditions in micro-mechanical analysis of composites," *International Journal of Solids and Structures*, vol. 43, no. 2, pp. 266–278, 2006.

[140] J. Michel, H. Moulinec, and P. Suquet, "Effective properties of composite materials with periodic microstructure: a computational approach," *Computer methods in applied mechanics and engineering*, vol. 172, no. 1, pp. 109–143, 1999.

[141] V.-D. Nguyen, E. Béchet, C. Geuzaine, and L. Noels, "Imposing periodic boundary condition on arbitrary meshes by polynomial interpolation," *Computational Materials Science*, vol. 55, pp. 390–406, 2012.

[142] N. Recipes, "Wh press, sa teukolsky, wt vetterling, bp flannery," 1995.

[143] H.-J. Bunge, *Texture analysis in materials science: mathematical methods*. Elsevier, 2013.

[144] A. Heinz and P. Neumann, "Representation of orientation and disorientation data for cubic, hexagonal, tetragonal and orthorhombic crystals," *Acta Crystallographica Section A: Foundations of Crystallography*, vol. 47, no. 6, pp. 780–789, 1991.

[145] U. F. Kocks, C. N. Tomé, and H.-R. Wenk, *Texture and anisotropy: preferred orientations in polycrystals and their effect on materials properties*. Cambridge university press, 2000.

[146] B. L. Adams, A. Henrie, B. Henrie, M. Lyon, S. Kalidindi, and H. Garmestani, "Microstructure-sensitive design of a compliant beam," *Journal of the Mechanics and Physics of Solids*, vol. 49, no. 8, pp. 1639–1663, 2001.

[147] S. R. Kalidindi, J. R. Houskamp, M. Lyons, and B. L. Adams, "Microstructure sensitive design of an orthotropic plate subjected to tensile load," *International Journal of Plasticity*, vol. 20, no. 8, pp. 1561–1575, 2004.

[148] A. Kumar and P. Dawson, "Computational modeling of fcc deformation textures over rodrigues' space," *Acta Materialia*, vol. 48, no. 10, pp. 2719–2736, 2000.

[149] A. Kumar and P. R. Dawson, "Modeling crystallographic texture evolution with finite elements over neo-eulerian orientation spaces," *Computer methods in applied mechanics and engineering*, vol. 153, no. 3, pp. 259–302, 1998.

[150] H. R. Wenk, *Preferred Orientation in Deformed Metal and Rocks: An Introduction to Modern Texture Analysis*. Elsevier, 2013.

[151] P. R. Dawson and E. B. Marin, "Computational mechanics for metal deformation," *Advances in Applied Mechanics*, vol. 34, p. 77, 1997.

[152] R. M. Jones, *Mechanics of composite materials*. CRC press, 1998.

[153] I. M. Daniel, O. Ishai, I. M. Daniel, and I. Daniel, *Engineering mechanics of composite materials*, vol. 3. Oxford university press New York, 1994.

[154] S. Hirsekorn, "A review," *Textures and Microstructures*, vol. 12, pp. 1–14, 1990.

[155] H. Bunge, R. Kiewel, T. Reinert, and L. Fritsche, "Elastic properties of polycrystalsinfluence of texture and stereology," *Journal of the Mechanics and Physics of Solids*, vol. 48, no. 1, pp. 29–66, 2000.

[156] M. Aldridge, A. Wineman, A. Waas, and J. Kieffer, "In situ analysis of the relationship between cure kinetics and the mechanical modulus of an epoxy resin," *Macromolecules*, vol. 47, no. 23, pp. 8368–8376, 2014.

[157] M. J. Marks and R. V. Snelgrove, "Effect of conversion on the structure- property relationships of amine-cured epoxy thermosets," *ACS applied materials & interfaces*, vol. 1, no. 4, pp. 921–926, 2009.

[158] M. Abdalla, D. Dean, P. Robinson, and E. Nyairo, "Cure behavior of epoxy/mwcnt nanocomposites: The effect of nanotube surface modification," *Polymer*, vol. 49, no. 15, pp. 3310–3317, 2008.

[159] C. A. Dyke and J. M. Tour, "Overcoming the insolubility of carbon nanotubes through high degrees of sidewall functionalization," *Chemistry–A European Journal*, vol. 10, no. 4, pp. 812–817, 2004.

[160] H. Dai, "Carbon nanotubes: synthesis, integration, and properties," *Accounts of chemical research*, vol. 35, no. 12, pp. 1035–1044, 2002.

[161] E. A. Stefanescu, C. Daranga, and C. Stefanescu, "Insight into the broad field of polymer nanocomposites: from carbon nanotubes to clay nanoplatelets, via metal nanoparticles," *Materials*, vol. 2, no. 4, pp. 2095–2153, 2009.

[162] A. Kis, G. Csanyi, J.-P. Salvetat, T.-N. Lee, E. Couteau, A. Kulik, W. Benoit, J. Brugger, and L. Forro, "Reinforcement of single-walled carbon nanotube bundles by intertube bridging," *Nature materials*, vol. 3, no. 3, pp. 153–157, 2004.